



HAL
open science

From bench to bedside: in silico and ex vivo approaches for managing radiotherapy late toxicities

Liza Hettal

► To cite this version:

Liza Hettal. From bench to bedside: in silico and ex vivo approaches for managing radiotherapy late toxicities. Cancer. Université de Lorraine, 2021. English. NNT : 2021LORR0359 . tel-03855864

HAL Id: tel-03855864

<https://hal.univ-lorraine.fr/tel-03855864v1>

Submitted on 18 Sep 2023

HAL is a multi-disciplinary open access archive for the deposit and dissemination of scientific research documents, whether they are published or not. The documents may come from teaching and research institutions in France or abroad, or from public or private research centers.

L'archive ouverte pluridisciplinaire **HAL**, est destinée au dépôt et à la diffusion de documents scientifiques de niveau recherche, publiés ou non, émanant des établissements d'enseignement et de recherche français ou étrangers, des laboratoires publics ou privés.



**UNIVERSITÉ
DE LORRAINE**

**BIBLIOTHÈQUES
UNIVERSITAIRES**

AVERTISSEMENT

Ce document est le fruit d'un long travail approuvé par le jury de soutenance et mis à disposition de l'ensemble de la communauté universitaire élargie.

Il est soumis à la propriété intellectuelle de l'auteur. Ceci implique une obligation de citation et de référencement lors de l'utilisation de ce document.

D'autre part, toute contrefaçon, plagiat, reproduction illicite encourt une poursuite pénale.

Contact bibliothèque : ddoc-theses-contact@univ-lorraine.fr
(Cette adresse ne permet pas de contacter les auteurs)

LIENS

Code de la Propriété Intellectuelle. articles L 122. 4

Code de la Propriété Intellectuelle. articles L 335.2- L 335.10

http://www.cfcopies.com/V2/leg/leg_droi.php

<http://www.culture.gouv.fr/culture/infos-pratiques/droits/protection.htm>

Ecole Doctorale BioSE (Biologie-Santé-Environnement)

Thèse

Présentée et soutenue à huis clos pour l'obtention du titre de

DOCTEUR DE L'UNIVERSITE DE LORRAINE

Mention : « Sciences de la Vie et de la Santé »

par **Liza Hettal**

From bench to bedside: *in silico* and *ex vivo* approaches for managing radiotherapy late toxicities

Le 9 Juillet 2021

Membres du jury :

Rapporteurs :	Mme Michèle Martin	Directrice de recherche émérite, CEA, Evry
	Mme Ulrike Schick	Professeure des Universités – Praticien hospitalier, CHU de Brest, Brest
Examineurs :	Mr Jean-François Daisne	Professeur, Universitair Ziekenhuis Leuven, Leuven
Directeurs de thèse :	Mme Isabelle Behm-Ansmant	Chargée de recherche, CNRS, Nancy
	Mr Guillaume Vogin	Professeur des Universités – Praticien hospitalier, Centre François Baclesse, Esch-sur-Alzette

UMR 7365 CNRS-UL, Laboratoire IMoPA (Ingénierie Moléculaire et Physiopathologie articulaire)

Preface

In Europe, an estimated of 4.4 million new cancer cases and almost 2 million cancer deaths occurred in 2020. The increasing incidence of cancer make it a major public health concern, rising challenges in specific diagnostic, treatment, and follow-up. To date, cancer treatments rely on chemotherapy, radiotherapy (RT), immunotherapy, endocrine therapy and surgery. Around 50% cancer patients receive RT in Europe, a curative and palliative local treatment modality relying on the use of ionising radiations.(1)

Although effective, RT can lead to mild to severe specific toxicities. There is a real challenge in the prevention, diagnosis and management of secondary toxicities induced by RT. In this work, I focused on the diagnosis and management of late RT-induced adverse events. I will not address the treatments of these secondary toxicities.

The first part of this manuscript presents an innovative strategy for toxicity diagnosis. We will deal with an algorithm able to discriminate between tumour recurrence and radionecrosis, two very similar lesions on imaging, after stereotactic irradiation of brain metastases.

The second part of this manuscript tackles an innovative strategy for toxicity prediction. We will discuss the molecular determinants of radiation-induced fibrosis (RISF) and the functional differences between RISF-prone and RISF-patients' skin fibroblasts.

Abstract

Version française

En Europe, on estime que le cancer a touché 4,4 millions de nouveaux patients et a été à l'origine de près de 2 millions de décès en 2020. L'augmentation de l'incidence du cancer en fait un problème de santé publique majeur, imposant de nouveaux défis en matière de diagnostic, de traitement et de suivi des patients. À ce jour, les traitements du cancer associent la chimiothérapie, la radiothérapie (RT), l'immunothérapie et la chirurgie. Environ 50 % de tous les patients européens atteints de cancer reçoivent une RT, une modalité curative et palliative de traitement du cancer reposant sur l'utilisation de radiations ionisantes (RI). En effet, les cellules cancéreuses sont beaucoup plus sensibles aux RI que les cellules saines qui les entourent, ce qui permet l'action tumoricide des RI tout en préservant les tissus sains péri-tumoraux.

Bien qu'il s'agisse d'un outil hautement bénéfique, 10 à 15% des patients traités sont exposés à une toxicité aiguë inhabituelle et 5 à 20% à une toxicité tardive, entraînant des séquelles parfois létales, même en l'absence de déviation thérapeutique. Il existe un véritable défi dans la prévention, le diagnostic et la gestion des toxicités secondaires induites par la RT. Ce défi est le fil conducteur de mon projet doctoral. D'une part, nous avons développé un algorithme capable de discriminer la récurrence tumorale de la radionécrose cérébrale, deux lésions très similaires à l'imagerie, après irradiation stéréotaxique de métastases cérébrales. D'autre part, nous avons étudié les déterminants moléculaires de la fibrose cutanée radio-induite. Nous avons développé un test de pronostic pour prédire la propension des patientes à développer des toxicités tardives avant même d'avoir reçu leur traitement par RT. Nous avons également posé les premières bases de la compréhension des différences physiologiques entre les fibroblastes cutanés des patientes à risque (radiosensibles) et ceux des patientes sans risque (radiotolérantes) de développer des toxicités tardives après RT.

Radiomique et diagnostic des toxicités de la radiothérapie : une boîte noire pour ne plus percer les boîtes crâniennes

Contexte. La radiothérapie stéréotaxique (RTS) est recommandée pour le traitement de la maladie oligométastatique cérébrale (OMC) chez les patients dont le cancer primitif est contrôlé. Lorsqu'une prise de contraste réapparaît au cours du suivi post-RTS, il se pose la question de la distinction entre radionécrose et progression tumorale. Sans confirmation anatomo-pathologique (gold standard soumis à la problématique de l'échantillonnage), la prise de décision peut être inappropriée et retardée, entraînant une perte de chance pour le patient. Le suivi post-RTS de routine faisant appel à des examens d'imagerie, il serait intéressant d'en extraire et exploiter des paramètres quantitatifs : c'est la méthode radiomique.

Objectif. Nous proposons d'évaluer l'efficacité la méthode radiomique pour le diagnostic différentiel précoce de la radionécrose et de la progression tumorale après RTS d'OMC.

Matériel et méthodes. Vingt patients ayant reçu une RTS pour OMC, tous primitifs confondus, ont été inclus (8 radionécroses, 12 progressions, confirmées histologiquement). Nous avons évalué la pertinence clinique de 1766 paramètres radiomiques, extraits à l'aide du logiciel IBEX, à partir de la première IRM (pondération T1) après la RTS affichant une modification lésionnelle. Nous avons évalué la performance prédictive de 7 méthodes de sélection de variables couplées à 12 algorithmes de classification. La précision de la classification a été mesurée par le Kappa de Cohen.

Résultats. Le meilleur pouvoir prédictif atteint était un Kappa de Cohen de 0,68 (précision globale de 85%), exprimant une forte concordance entre la prédiction de l'algorithme et le gold standard histologique. La précision de prédiction pour la radionécrose était de 75 % et de 91 % pour la progression. L'aire sous la courbe a atteint 0,83 en utilisant un algorithme *Bagging* entraîné avec l'ensemble des variables sélectionnées à l'aide du score du Chi².

Conclusion. La méthode radiomique semble capable de distinguer la radionécrose de la progression de manière précise, précoce et non invasive. Cette étude prometteuse est une preuve de concept avant une étude de plus grande envergure visant à définir un modèle robuste pour aider à la prise de décision dans le cas de OMC.

Une plaque pour prédire toutes les toxicités ?

Contexte. Dans le cas du cancer du sein, la toxicité tardive se traduit, entre autres, par le développement d'une fibrose cutanée radio-induite chez 18% des patientes traitées. Chaque personne est caractérisée par sa propre sensibilité aux rayonnements. Ce concept est défini comme la radiosensibilité individuelle (RSI). Les bases moléculaires de la RSI restent largement inconnues.

La compréhension de l'origine de la RSI, ainsi que la prédiction fiable et non-invasive de la RSI pour chaque patient sont des enjeux majeurs de la RT. En effet, cela aiderait les oncologues à adapter les schémas thérapeutiques et en particulier les doses de RT afin d'optimiser le rapport thérapeutique individuel (bénéfice/toxicité). Ainsi, il serait possible de proposer une escalade de dose aux patients les plus radiotolérants ou, au contraire, une désescalade de dose, des techniques de RT protectrices (protonthérapie, curiethérapie) ou des traitements alternatifs évitant la RT (chirurgie non conservatrice) pour les patients les plus radiosensibles. Plus que guérir, la RT de demain doit assurer la guérison des patients sans séquelles en intégrant la RSI comme une variable clé.

Objectif. Nous cherchons à établir une signature transcriptomique constitutionnelle spécifique de la RSI, capable de prédire des toxicités tardives induite par la RT.

Matériel et méthodes. Des primocultures fibroblastiques ont été établies à partir de biopsies de peau saine de patientes radiosensibles ou radiotolérants inclus dans l'étude clinique SPLICI-Rad (NCT03000764). Les ARN totaux ont été extraits et hybridés sur les puces Affymetrix Clariom D. Une analyse bioinformatique quantitative a ensuite été réalisée, suivie d'une analyse fonctionnelle. Les variations mises en évidence ont ensuite été analysées et triées en fonction de leur pertinence fonctionnelle. Des tubes de sang, prélevés sur la même population de patientes radiotolérants (n=10) et radiosensibles (n=10) (étude SPLICI-Rad), ont été hybridés sur les mêmes puces Clariom D d'Affymetrix. Une analyse bioinformatique quantitative a ensuite été réalisée pour déterminer une signature sanguine RSI.

Résultats. La signature des fibroblastes de la peau développée à partir des analyses des puces comprend 35 gènes. Elle permet une très bonne discrimination des patients sur la base de leur seul transcriptome. Une signature sanguine a ensuite été proposée. Elle comprend 23 gènes et combine des marqueurs fibroblastiques de RSI, ainsi que des marqueurs purement sanguins. Elle permet une excellente discrimination des patients sur la base de leur seul transcriptome. Ces 23 gènes, ainsi que des contrôles soigneusement choisis, seront inclus sur une plaque de RT-qPCR proposée comme un test pour déterminer le statut RSI d'un patient.

Conclusion. Nous avons mis au point un test reposant sur la PCR quantitative qui peut prédire le statut de RSI d'un patient à partir d'un échantillon de sang. Ce test est non invasif, rapide et peu coûteux. À l'heure actuelle, la signature des fibroblastique est entièrement validée par qPCR. La validation de la signature sanguine sur les ARN des patients de SPLICI-Rad est en cours. Une collaboration avec le groupe UNITRAD a été initiée pour valider notre test sur le sang de plusieurs centaines de patients inclus dans l'essai prospectif HYPOG-01 (NCT03127995).

Cytokératines 7 et 18 : d'inattendus marqueurs dermiques d'une non moins inattendue toxicité tardive de la radiothérapie

Contexte. Les cytokératines constituent une sous-famille majeure de protéines de filaments intermédiaires. Elles sont principalement décrites dans les cellules épithéliales. Elles sont divisées en deux groupes, les cytokératines acides de type I codées par 28 gènes et les kératines basiques de type II codées par 26 gènes. Elles s'assemblent en bobines hélicoïdales double brin hétérodimériques composées d'une protéine de chaque groupe. La plupart de ces protéines sont spécifiques d'un type cellulaire ou d'un état de différenciation. Elles relient la membrane nucléaire à la membrane cytoplasmique. Parmi elles, les cytokératines-7 (CK7) et -18 (CK18) sont particulièrement associées à la fibrose. La CK7 est corrélée à l'expression de l' α -SMA dans la fibrose hépatique, et son expression peut prédire la sévérité de la fibrose hépatique alcoolique. La CK18 est particulièrement décrite dans la stéatose hépatique non alcoolique (NAFLD), une affection fibrotique du foie, et dans la fibrose hépatique de l'hépatite C.

Objectif. Nous étudions la pertinence de KRT7 et la KRT18 comme marqueurs prédictifs de la fibrose cutanée radio-induite.

Matériel et Méthodes. Les ARNm KRT7 et KRT18 ont été quantifiés par RT-qPCR dans des fibroblastes de peau saine provenant de patients radiosensibles ou radiotolérantes inclus dans l'étude clinique SPLICI-Rad (NCT03000764).

Résultats. Nous avons mis en évidence l'expression différentielle de 2 gènes, KRT7 et KRT18, dans les fibroblastes cutanés primaires de patients atteints de fibrose cutanée radio-induite (n = 7) par rapport à ceux qui ne sont pas sujets à la fibrose (n = 5). Les niveaux de transcription de KRT7 et KRT18 étaient respectivement 37,7 et 7 fois plus faibles dans les fibroblastes radiosensibles que dans les fibroblastes radiotolérants.

Conclusion. L'expression des gènes KRT18 et KRT7 apparaît comme un facteur pronostique potentiel de la fibrose cutanée radio-induite.

Substructure Analyzer : L'analyse de vos images en douceur

Contexte. Les dommages génomiques les plus critiques causés par les radiations ionisantes sont les cassures double brin (CDB) de l'ADN. Ces lésions génomiques, si elles ne sont pas réparées par les cellules saines, peuvent entraîner la mort cellulaire et la déstructuration des tissus ou l'adaptation/mutation cellulaire et la perturbation de l'homéostasie tissulaire. Dans tous les cas, une CDB non ou mal réparée entraînera l'apparition d'une toxicité de la radiothérapie. Par conséquent, la caractérisation de la RSI peut évaluer la capacité des cellules à réparer les CDB radio-induites par un marquage par immunofluorescence

indirecte des protéines de réparation de l'ADN telles que pATM ou 53BP1. Cette coloration donne lieu à des foci, marquant les CDB, qui disparaissent lorsque l'intégrité du génome est restaurée. Le comptage de ces foci est une étape fastidieuse et longue qui est entravée par le manque de reproductibilité intra- et inter-observateurs lorsqu'elle est effectuée manuellement. Cette observation peut être étendue à tout marquage intracellulaire nécessitant un traitement d'image.

Résumé. La dernière décennie a été caractérisée par des percées dans les techniques de microscopie à fluorescence, illustrées par l'amélioration de la résolution spatiale mais aussi dans l'imagerie des cellules vivantes et les techniques de microscopie à haut débit. Cela a conduit à une augmentation constante de la quantité et de la complexité des données de microscopie pour une seule expérience. Comme l'analyse manuelle des données de microscopie prend beaucoup de temps, est subjective et interdit les analyses quantitatives, l'automatisation de l'analyse des bioimages devient presque inévitable. Nous avons construit un flux de travail informatique appelé Substructure Analyzer pour automatiser entièrement l'analyse des signaux dans les bioimages obtenues par microscopie fluorescente. Ce workflow est développé sur la plateforme open-source collaborative Icy et est complété par des fonctionnalités d'ImageJ. Il comprend le prétraitement des images pour améliorer le rapport signal/bruit, la segmentation individuelle des cellules (détection des frontières cellulaires) et la détection/quantification des corps cellulaires enrichis dans des compartiments cellulaires spécifiques. L'avantage principal de ce flux de travail est de proposer des fonctionnalités complexes de bio-imagerie à des utilisateurs sans expertise en analyse d'images par le biais d'une interface facile d'utilisation. De plus, il est très modulaire et adapté à plusieurs problématiques allant de la caractérisation de la translocation nucléaire/cytoplasmique à l'analyse comparative de différents corps cellulaires dans différentes sous-structures cellulaires.

Caractérisation fonctionnelle des fibroblastes cutanés radiosensibles et radiotolérants

Contexte. Les fibroblastes de la peau produisent une riche matrice extracellulaire qui compose le derme. Divisés en deux phénotypes majeurs, les fibroblastes papillaires et les fibroblastes réticulaires, ils jouent un rôle clé dans l'intégrité structurelle et moléculaire de la peau.

Objectif. Les déterminants cellulaires de la fibrose cutanée radio-induite étant encore largement inconnus, il nous a semblé intéressant d'étudier la physiologie des fibroblastes cutanés de patients radiosensibles et radiotolérants.

Matériel et méthodes. Nous avons évalué les différentes fonctions cellulaires des fibroblastes radiosensibles (n = 5) et radiotolérants (n = 6) issus de l'étude SPLICI-Rad à l'état basal et au début du passage pour mieux se rapprocher de la physiologie des cellules *in vivo*.

Résultats. Nous avons démontré une homogénéité dans les sous-types de fibroblastes entre nos cultures radiosensibles et radiotolérantes, ce qui nous permet de conclure que les différences que nous mettons en évidence ne sont pas dues au déséquilibre de deux lignées fibroblastiques fonctionnellement différentes. Nous n'avons pas montré de différence significative entre la production de collagène des fibroblastes radiosensibles et radiotolérants après 3 jours de culture à confluence. Les fibroblastes radiosensibles ont présenté une vitesse de migration plus élevée, une prolifération plus importante et une réparation des DSB altérée par rapport aux fibroblastes radiotolérants.

English version

In Europe, 4.4 million new cancer cases and almost 2 million cancer deaths occurred in 2020. The increasing incidence of cancer make it a major public health concern, rising challenges in patients' diagnostic, treatment, and follow-up. To date, cancer treatments associate chemotherapy, radiotherapy (RT), immunotherapy, and surgery. Around 50% of all European cancer patients will receive RT(2), a curative and palliative modality of cancer treatment relying on the use of ionising radiations (IR). Indeed, cancer cells are much more sensitive to IR than the healthy ones embedding them, allowing irradiation to destroy tumours.

Although a wonderful and necessary tool in patients care, RT can be accompanied by mild to severe secondary toxicities. There is a real challenge in the prevention, diagnosis and management of secondary toxicities induced by RT. This challenge is the framework of my doctoral projet. On the one hand, we developed an algorithm able to discriminate between tumour recurrence and radionecrosis, two very similar lesions on imaging, after stereotactic irradiation of brain metastases. On the other hand, we studied the molecular determinants of radiation-induced skin fibrosis. We developed a prognostic test to predict patients' outcome before RT and laid the first bricks to understand the physiological differences between at-risk and non-at-risk patients' skin fibroblasts.

A sharp decision-support tool to stop slicing brains

Background. Stereotactic radiotherapy (SRT) is recommended for treatment of brain oligometastasis (BoM) in patients with controlled primary disease. Where contrast enhancement enlargement occurs during follow-up, distinguishing between radionecrosis and progression is a real challenge. Without pathological confirmation, decision-making may be inappropriate and delayed. Quantitative imaging features extracted from routinely performed examinations could be of interest. We proposed to explore the added value of the radiomics method for the differential diagnosis of these two entities.

Material and Methods. Twenty patients who received SRT for BoM, from any primary location, were included (8 radionecrosis, 12 progressions, pathologically confirmed). We assessed the clinical relevance of 1766 radiomics features, extracted with IBEX software, from the first T1-weighted postcontrast MRI after SRT showing a lesion modification. We evaluated 7 feature-selection methods and 12 classification methods in terms of respective predictive performance. The classification accuracy was measured with Cohen's Kappa after leave-one-out cross validation.

Results. The best predictive power reached was a Cohen's Kappa of 0.68 (overall accuracy of 85%), expressing a strong agreement between the algorithm prediction and the histological

gold standard. The prediction accuracy for radionecrosis was 75% and 91% for progression. The area-under-curve reached 0.83 using a bagging algorithm trained with the Chi-square score features set.

Conclusion. The radiomics method was able to discriminate radionecrosis from progression in an accurate, early, and non-invasive way. This promising study is a proof of concept prior to a larger study to define a robust model to support decision-making in BoM.

One plate to predict them all

Background. Out of 19 million new cases of cancer diagnosed per year worldwide, half are treated with RT. 10 to 15% of treated patients are exposed to unusual acute toxicity and 5 to 20% to late toxicity, leading to sequelae that are sometimes lethal in the absence of therapeutic deviation. In the case of breast cancer, such late toxicity results in the development of RISF in 18% of treated patients. Each person is characterised by his or her own sensitivity to radiation. This concept is defined as individual radiosensitivity (IRS). The molecular basis of IRS remains largely unknown.

The understanding of IRS origin, as well as the reliable and non-invasive IRS prediction for each patient are key issues in RT. Indeed, it would help oncologists in adapting the therapeutic schemes and in particular the RT doses in order to optimise the individual therapeutic ratio. Thus, it would be possible to propose dose escalation to the most radioresistant patients or, on the contrary, dose de-escalation, protective RT techniques (proton therapy, brachytherapy) or alternative local treatments avoiding RT (non-conservative surgery) for the most radiosensitive patients. More than just curing, tomorrow's RT must ensure that patients are cured without sequelae by integrating IRS as a key variable.

Aim. We are investigating a constitutional transcriptomic signature specific to IRS.

Material and Methods. Fibroblastic primocultures were established from healthy skin biopsies of radiosensitive or radioresistant patients included in SPLICI-Rad clinical study (NCT03000764). Total RNAs were extracted and hybridised on Affymetrix Clariom D chips. A quantitative bioinformatics analysis was then performed, followed by a functional analysis. The resulting variations were then analysed and sorted according to functional relevance. Blood tubes, taken from the same population of radioresistant (n=10) and radiosensitive (n=10) patients (SPLICI-Rad study), were hybridised on the same Affymetrix Clariom D chips. A quantitative bioinformatics analysis was then performed to determine a RSI blood signature.

Results. The skin fibroblast signature developed from the microarray analyses includes 35 genes. It allows a very good discrimination of patients based on their transcriptome alone. A blood signature was proposed. It comprises 23 genes and combines fibroblastic IRS markers,

as well as purely blood-based markers. It allows for excellent discrimination of patients based on their transcriptome alone. These 23 genes, along with accurate controls, will be turned into a plate-based RT-PCR assay for determining the IRS status of a patient.

Conclusion. We invented a PCR test that can predict IRS status based on a blood sample. This test is non-invasive, rapid and cost-effective. At this time, the fibroblast signature is fully validated by qPCR. The blood signature validation on the SPLICI-Rad patients' RNAs is ongoing. A collaboration with the UNITRAD group has been initiated to evaluate our test on blood from several hundred patients included in the prospective trial HYPOG-01 (NCT03127995).

Cytokeratins 7 and 18: unexpected dermis markers for an unexpected radiation-induced dermis toxicity

Background. Cytokeratins are a major subfamily of intermediate filament proteins. They are mainly described in epithelial cells. They are divided into two groups, the acidic type I cytokeratins encoded by 28 genes and the basic type II keratins encoded by 26 genes. They assemble into heterodimeric double-stranded coiled coils composed of one protein of each group. Most of these proteins are cell-type or differentiation-state specific. They connect the nuclear membrane to the cytoplasmic membrane. Among them, cytokeratin-7 (CK7) and -18 (CK18) are particularly associated with fibrosis. CK7 is correlated with the expression of α -SMA in hepatic fibrosis, and its expression can predict the severity of alcoholic liver fibrosis. CK18 is particularly described in non-alcoholic fatty liver disease (NAFLD), a fibrotic condition of the liver, and in hepatitis C liver fibrosis.

Aim. We are investigating KRT7 and KRT18 as predictive markers of radiation-induced skin fibrosis.

Material and Methods. KRT7 and KRT18 mRNA were quantified by RT-qPCR in healthy skin fibroblasts from radiosensitive or radioresistant patients included in the SPLICI-Rad clinical study (NCT03000764).

Results. We evidenced the differential expression of 2 genes, KRT7 and KRT18, in primary skin fibroblasts from fibrosis-prone patients (n = 7) compared to those fibrosis-free patients (n = 5). The levels of KRT7 and KRT18 transcripts were 37.7 and 7 times lower in fibroblasts from radiosensitive patients compared to radioresistant ones, respectively.

Conclusion. The expression of KRT18 and KRT7 genes may emerge as potential prognostic factor in RISF.

Substructure Analyzer: “Icy” cells of green, bright DAPI too...

Context. Ionizing radiations most critical genomic damage are DNA double-strand breaks. These genomic lesions, if not repaired, can lead to cell death and tissue destruction or cell mutation and disruption of tissue homeostasis. In any case, un- or poorly repaired DSB will lead to the onset of radiotherapy toxicity. Therefore, IRS characterisation must evaluate cells' ability to repair radiation-induced DSB through indirect immunofluorescence staining of DNA repair protein such as pATM or 53BP1. This staining results in foci, marking DSB, that disappear when genome integrity is restored. Counting these foci is a tedious and time-consuming step that is hampered by the lack of intra- and inter-observer reproducibility when done manually. This observation can be extended to every intracellular staining requiring image processing.

Summary. The last decade has been characterized by breakthroughs in fluorescence microscopy techniques illustrated by spatial resolution improvement but also in live-cell imaging and high-throughput microscopy techniques. This led to a constant increase in the amount and complexity of the microscopy data for a single experiment. Because manual analysis of microscopy data is very time consuming, subjective, and prohibits quantitative analyses, automation of bioimage analysis is becoming almost unavoidable. We built an informatics workflow called *Substructure Analyzer* to fully automate signal analysis in bioimages from fluorescent microscopy. This workflow is developed on the user-friendly open-source platform Icy and is completed by functionalities from ImageJ. It includes the pre-processing of images to improve the signal to noise ratio, the individual segmentation of cells (detection of cell boundaries) and the detection/quantification of cell bodies enriched in specific cell compartments. The main advantage of this workflow is to propose complex bio-imaging functionalities to users without image analysis expertise through a user-friendly interface. Moreover, it is highly modular and adapted to several issues from the characterization of nuclear/cytoplasmic translocation to the comparative analysis of different cell bodies in different cellular sub-structures.

Functional characterisation of radiosensitive and radioresistant skin fibroblasts

Background. Skin fibroblasts produce a rich extracellular matrix that composes the dermis. Divided in two major phenotypes, papillary fibroblasts and reticular fibroblasts, they play a key role in the structural and molecular integrity of the skin.

Aim. As the cellular determinants of RISF are still largely unknown, we deemed it interesting to study the physiology of skin fibroblasts from radiosensitive and radioresistant patients.

Material and methods. we evaluated the various cellular functions in fibroblasts from radiosensitive (n = 5) and radioresistant (n = 6) patients from SPLICI-Rad study at basal state and at early passage to better approximate the physiology of cells in vivo.

Results. We demonstrated a homogeneity in fibroblasts subtypes between our radiosensitive and radioresistant cultures, allowing us to conclude that the differences we are evidencing are not due to an imbalance of two functionally different skin fibroblast lineages. We showed no significant difference between fibroblasts from radiosensitive and radioresistant patients collagen production after 3 days at confluence. In our study, fibroblasts from radiosensitive patients exhibited a higher migration speed, a higher proliferation, and an impaired DSB repair compared to fibroblasts from radioresistant patients.

Acknowledgments

Acknowledgments

A mes encadrants

Je tiens à remercier le Dr Isabelle Behm-Ansmant et le Pr Guillaume Vogin, qui m'ont encadré tout au long de cette thèse et qui m'ont fait partager leurs brillantes intuitions. Isabelle, merci de m'avoir fait confiance, d'avoir eu la patience et la bienveillance d'accepter toutes mes manipulations ratées (et il y en a eu tellement...) m'avoir accompagnée pendant ces 4 années. Merci de m'avoir laissé la place de développer mes idées mais aussi de m'avoir su me guider quand il fallait. J'espère avoir un jour ta facilité à comprendre tous les sujets ! Guillaume, ça fait maintenant 6 années (!!!) qu'on travaille ensemble ! J'ai énormément appris à tes côtés, et j'espère bien continuer. Merci pour la confiance que tu m'as accordée, pour ton soutien constant et tes idées brillantes qui éclairent toujours les projets les plus sombres.

Aux membres de mon Jury

J'adresse tous mes remerciements Dr Michèle Martin ainsi qu'au Pr Ulrike Schick, de l'honneur qu'ils m'ont fait en acceptant d'être rapporteurs de cette thèse.

J'exprime ma gratitude au Pr Jean-François Daisne qui a accepté d'être examinateur de cette thèse.

Aux membres de mon comité de suivi de thèse

Je tenais à remercier tout particulièrement les Dr Michèle Martin et Martin Dutertre pour leur accompagnement durant ces 4 années de thèse. Vos questions et vos éclairages ont permis d'améliorer considérablement ce travail. Vos retours et votre bienveillance ont été d'un grand soutien, je vous en serai toujours reconnaissante.

A mes collègues, à mes amis, à ma famille

Je ne vous remercierai jamais assez pour votre soutien constant, votre bonne humeur, votre aide, et j'en passe. J'ai la chance de pouvoir dire que je me suis épanouie pendant mon doctorat, et c'est grandement grâce à vous ! 😊

Acknowledgments

List of Figures
and
Tables

Figure number	Title	Page
1	Percentage depth dose curves comparing carbon ion, proton and photon beams. The Bragg Peak corresponds to the maximum deposited dose	5
2	Schematic model for DSB repair	9
3	Overview of steps of a Radiomics analysis	24
4	The different types of RNA	41
5	Organisation of an intron between two exons	43
6	Simplified splicing mechanism	44
7	RNA response to DNA damage. RNA metabolism is affected in several ways, from transcription to post-transcriptional regulation	45
8	Patient with RISF on the left breast, following RT for breast cancer	47
9	Short- and long-term effects of the radiation response at the cellular and tissue levels	50
10	Cellular and molecular signals involved in transdifferentiation of myofibroblasts and fibrogenesis upon radiation exposure	51
11	Representative images for immunofluorescence 53BP1 staining of primary skin fibroblasts	84
12	Heatmap of differentially expressed biomarkers between fibroblasts from radioresistant and radiosensitive patients at basal state	70
13	RT-qPCR validation of gene expression variations in the skin fibroblast signature	71
14	Heatmap of differentially expressed blood biomarkers between radioresistant and radiosensitive patients at basal state	74
15	Principle of the individual radiosensitivity status test based on RT-qPCR analysis of blood signature gene expression	79
16	Principle of TaqMan real-time qPCR	81
17	Cytokeratin gene expression in our 12 primary human fibroblast cultures	132
18	Western blot showing representative results of CK7, CK18 and NCL loading control in total cell lysates from radioresistant and radiosensitive proteins	133
19	Expression of CK7 non-coding RNA vs CK7 mRNA in healthy dermal fibroblasts from radioresistant and radiosensitive patients	134
20	Subpopulation characterisation of primary adult skin fibroblast cultures	142
21	Relative collagen production and invasion of fibroblasts from radiosensitive patients compared to fibroblasts from radioresistant patients	142
22	Migration and proliferation of fibroblasts from radiosensitive and radioresistant patients	144
23	Proportion of live, early apoptotic, late apoptotic and dead fibroblasts from radiosensitive and radioresistant patients	145
24	DNA repair assessment through 53BP1 staining of fibroblasts from radioresistant and radiosensitive patients	146
25	Detail of subpopulation characterisation of primary fibroblast cultures	149

26	Heatmap of differentially expressed migration- and adhesion-related genes between fibroblasts from radioresistant and radiosensitive patients at basal state	151
27	Heatmap of differentially expressed migration- and adhesion-related genes between fibroblasts from radioresistant and radiosensitive patients at basal state	152

Table number	Title	Page
1	Hereditary diseases associated with IRS	12
2	Single nucleotide polymorphisms linked to the development of skin radiation-induced fibrosis	55
3	Summary of transcriptomic studies comparing skin fibroblasts from radiosensitive and radioresistant patients	57
4	Objectives and outcomes of SPLICI-Rad study	61
5	Inclusion criteria of SPLICI-Rad study	63
6	Exculsion criteria of SPLICI-Rad study	64
7	Gene list of skin fibroblast signature. The name and type (coding or non-coding) of each gene are indicated	69
8	List of differentially expressed genes between radiosensitive and radioresistant patients included in the blood signature	73
9	Patents on predicting individual radiosensitivity. The patent reference, the type of biological material used to perform the test and a brief description of the test are given	75
10	Summary of published studies from teams involved in competing companies to find an IRS signature	78
11	Composition of our primary fibroblast cultures in papillary, upper reticular and lower reticular lineages	141
12	Functional characterisation of radioresistant and radiosensitive skin fibroblasts	143

Table of contents

Introduction.....1

1. RADIOTHERAPY, AN ESSENTIAL WEAPON IN CANCER TREATMENT	3
1.1. HISTORY	3
1.1.1. <i>Late 1800.....</i>	<i>3</i>
1.1.2. <i>1900-1950.....</i>	<i>4</i>
1.1.3. <i>1946-1996.....</i>	<i>4</i>
1.1.4. <i>1996-2012.....</i>	<i>4</i>
1.1.5. <i>2012-Today.....</i>	<i>5</i>
1.2. MOLECULAR MECHANISMS	6
1.2.1. <i>Ionising radiation</i>	<i>6</i>
1.2.2. <i>Radiation effects</i>	<i>7</i>
2. RADIOTHERAPY, A POTENTIAL SOURCE OF TOXICITY FOR HEALTHY TISSUES	10
2.1. EPIDEMIOLOGY	10
2.2. COFACTORS OF TOXICITY	11
2.2.1. <i>Individual radiosensitivity and radiosensitive syndromes</i>	<i>11</i>
2.2.2. <i>Other cofactors.....</i>	<i>15</i>
2.3. CURRENT MANAGEMENT OF LATE EFFECTS	16
2.3.1. <i>Primary prevention</i>	<i>16</i>
2.3.2. <i>Secondary prevention</i>	<i>16</i>
2.3.3. <i>Tertiary prevention</i>	<i>17</i>
3. FROM BENCH TO BEDSIDE: IN SILICO AND EX VIVO APPROACHES FOR THE	18
MANAGEMENT OF LATE EFFECTS OF RADIOTHERAPY.....	18

Radiomics method for radiotherapy toxicity diagnosis.....19

4. INTRODUCTION	21
4.1. BRAIN METASTASES	21
4.1.1. <i>Epidemiology.....</i>	<i>21</i>
4.1.2. <i>Treatment of brain metastases.....</i>	<i>21</i>
4.2. POST-TREATMENT DILEMMA: RADIONECROSIS OR TUMOUR RECURRENCE?.....	22
4.2.1. <i>Radionecrosis</i>	<i>22</i>
4.2.2. <i>Differential diagnosis between radionecrosis and tumour recurrence</i>	<i>22</i>
4.2.3. <i>Therapeutic options for radionecrosis and tumour recurrence</i>	<i>22</i>
4.3. RADIOMICS: A HIGH THROUGHPUT APPROACH FOR MEDICAL IMAGING (85).....	23
4.3.1. <i>Overview</i>	<i>23</i>
4.3.2. <i>Workflow</i>	<i>23</i>
5. A SHARP DECISION-SUPPORT TOOL TO STOP SLICING BRAINS	24
5.1. ARTICLE	214
6. DISCUSSION AND CONCLUSION.....	37

Molecular and cellular approaches for radiotherapy toxicity prediction.....	35
7. INTRODUCTION.....	41
7.1. RNA: A SNAPSHOT OF THE CELL (90).....	41
7.1.1. RNA overview: a broad and diverse family of biomolecules.....	41
7.1.2. RNA Splicing: how to go from 60 000 genes to 240 000 transcripts?	43
7.1.3. RNA and DNA damage	44
7.1.4. RNA: your ideal biomarker	46
7.2. RADIATION-INDUCED SKIN FIBROSIS: THE UNPREDICTABLE TOXICITY OF RADIOTHERAPY FOR BREAST CANCER	46
7.2.1. Clinical aspect.....	46
7.2.2. Tissular aspect	48
7.2.3. Cellular aspect	49
7.2.4. Molecular aspects	50
7.2.5. RISF treatments	52
7.3. MOLECULAR DETERMINANTS OF SKIN RADIATION-INDUCED SKIN FIBROSIS	52
7.3.1. Introduction	53
7.3.2. Polymorphisms and haplotypes.....	54
7.3.3. Role of epigenetic marks.....	58
7.3.4. Conclusion	59
8. SPLICI-RAD STUDY	60
8.1. WHY DID WE NEED SPLICI-RAD STUDY?	60
8.2. OBJECTIVES AND ENDPOINTS	60
8.3. PATIENT SELECTION	62
8.3.1. Population	62
8.3.2. Inclusion criteria	62
8.3.3. Exclusion criteria	62
8.4. STUDY WORKFLOW	65
8.4.1. Sampling	65
8.4.2. Criteria for study termination	65
8.5. ETHICS AND REGULATORY GUIDELINES	66
8.5.1. Rules and regulations.....	66
8.5.2. Ethics Committee and regulatory authorities	66
8.5.3. Patient information and consent	66
9. A TRANSCRIPTOMIC TEST TO PREDICT THE ONSET OF RISF	67
9.1. WHY DO WE NEED A PROGNOSTIC TEST FOR RISF?.....	67
9.1.1. Strategies to prevent RT-related toxicities	67
9.1.2. A dire need for tests to personalise RT schemes.....	67
9.1.3. Philosophy behind the development of our prognostic test.....	68
9.2. HOW DID WE DEVELOP OUR PROGNOSTIC TEST FOR RISF?.....	68
9.2.1. Identification of an IRS signature in skin fibroblast.....	68
9.2.2. Construction of a blood IRS signature	72
9.3. WHAT ARE THE AVAILABLE TESTS FOR IRS?.....	75
9.4. WHAT ARE THE ADVANTAGES OF OUR TEST?	76
9.4.1. Non-invasive, quick, and cost-effective.....	76
9.4.2. Pathophysiologically accurate	76
9.4.3. Easily carried-out.....	76
9.5. WHAT ARE THE LIMITATIONS OF OUR TEST?	76
9.5.1. Limited number of patients in the development cohort.....	76
9.5.2. A prognostic test developed on post-RT samples.....	77

9.6. HOW WILL OUR TEST WORK?	79
9.6.1. <i>One plate to predict them all (173)</i>	79
9.6.2. <i>PaxGene Blood RNA Tube</i>	79
9.6.3. <i>Processing of extracted RNA</i>	80
9.6.4. <i>RNA quantification</i>	80
9.6.5. <i>Data processing and decision-making support system</i>	82
9.7. WHERE DO WE CURRENTLY STAND IN THE DEVELOPMENT OF THE TEST?	82
10. SUBSTRUCTURE ANALYZER: A USER-FRIENDLY WORKFLOW FOR RAPID EXPLORATION AND ACCURATE ANALYSIS OF CELLULAR BODIES IN FLUORESCENCE MICROSCOPY IMAGES	83
10.1. INTRODUCTION	83
10.2. ARTICLE	84
10.3. DISCUSSION AND CONCLUSION.....	111
11. CYTOKERATIN KRT7 AND KRT18 GENE EXPRESSION PREDICTS RISF	112
11.1. INTRODUCTION	112
11.2. ARTICLE	112
11.3. DISCUSSION AND CONCLUSION.....	132
12. FUNCTIONAL CHARACTERISATION OF RADIOSENSITIVE AND RADIORESISTANT SKIN FIBROBLASTS	135
12.1. INTRODUCTION	135
12.2. ARTICLE	135
12.2.1. <i>Introduction</i>	135
12.2.2. <i>Material and methods</i>	137
12.2.3. <i>Results</i>	141
12.2.4. <i>Discussion</i>	147
12.2.5. <i>Conclusion</i>	148
12.2.6. <i>Supplementary material</i>	149
12.3. COMPLEMENTARY RESULTS AND DISCUSSION	150
12.4. CONCLUSION.....	153
Discussion and perspectives	149
Conclusion	153
References	155

Introduction

In Europe, an estimated 4.4 million new cancer cases and almost 2 million cancer deaths occurred in 2020.(3) The increasing incidence of cancer makes it a major public health concern, rising challenges in specific diagnostic, treatment, and follow-up. To date, cancer treatments rely on chemotherapy, radiotherapy (RT), immunotherapy, endocrine therapy and surgery. Around 50% cancer patients receive RT in Europe (2), a curative and palliative local treatment modality relying on ionising radiations (IR).(1) Cancer cells are much more sensitive to IR than the healthy ones embedding them, allowing irradiation to inactivate tumours. Indeed, they combine greater genomic instability than healthy cells, inhibition of cell cycle checkpoints and hyperproliferation. Thus, they accumulate IR damage and continue to proliferate, precipitating them to death, while healthy cells focus on repairing this damage before dividing. Although effective, RT can lead to mild to severe specific toxicities.

1. Radiotherapy, an essential weapon in cancer treatment

1.1. History

1.1.1. Late 1800

In 1895, Wilhelm Conrad Röntgen discovered X-rays. (4) It was now possible to visualise the contents of the human body. The idea of using X-rays to treat cancers was first introduced in 1896 when Victor Depeignes treated a stomach tumour by irradiating it with what he called at the time "Rontgen rays". (5) This experiment signed the birth of RT. Since then, the discovery of natural radioactivity by Becquerel (6), followed by the isolation of radium by the Curies (7), provided the foundations for two RT techniques still in use today: external-beam RT (EBRT, radiation source outside of patient's body, directing its beam to specific body parts, used in SPLICI-Rad study detailed further) and brachytherapy (radiation source inside of patient's body, placed next to the area to be treated). (8) Since the beginning of its use, the aim of RT was, and still is, to deliver the highest possible radiation dose in the tumour volume while protecting the surrounding healthy tissues and organs at risk (OAR). (8)

1.1.2. 1900-1950

The first half of the XXth century saw the manufacturing of the first tools allowing the use of RT in routine cancer treatment. (9) The fundamental laws for cells and tissues sensitivity to radiation were described during this period as the "Bergonié-Tribondeau Law" (10):

“the sensitivity of cells to radiation varies directly with the reproductive capacity of the cells and inversely with their degree of differentiation”.

Henri Coutard later used this law to define the fractionated irradiation scheme of 2 Grays (Gy, joules/kg) per delivered fraction, five times a week (11), which is the basis of today standard irradiation schemes. This half-century also saw the birth of radioprotection, with the creation of the International Commission on Radiological Protection (12) in 1928. However, despite the promising results of RT, its use during this period was anecdotal.

1.1.3. 1946-1996

The second half of the XXth century was the one of RT democratisation with the development of safer and more powerful RT machines, the multiplication of clinical trials and the global recognition of RT as a standard cancer treatment. (8) The switch from radium to cobalt as a radioactive source allowed the delivery of 45-60 Gy to deep tumours while respecting the tolerance of the skin and the surrounding OAR. Cobalt machines were later replaced by linear accelerators, providing much easier waste management. Moreover, linear accelerators produce both photon and electron beams. (8) RT treatments became more precise, more accurate, safer and more standardised with the introduction of treatment planning systems (TPS) (13), 2D simulators, a defined framework for quality assurance (14) and the definition of dosimetric volumes such as gross tumour volume and planning target volumes. (12) Inclusion of RT in breast cancer treatment was proven to be highly beneficial by various randomised trials (15–17) allowing a rapid change of clinical practices.

1.1.4. 1996-2012

In early 2000, advances in imaging modalities (switch from 2D radiographies to 3D of computed tomography scans), planning algorithms (TPS substantiating beams), and machine design (multileaf collimators) pushed RT accuracy and safety to the next level. (8) This period was the birthplace of stereotactic RT (SRT), a RT modality able to deliver very high doses of radiation in a restricted volume, using multiple non-coplanar small beams. SRT allows hypofractionation and can be compared to a surgical burn of the targeted volume. Today, SRT

is delivered using dedicated machines, such as the Cyberknife[®], which is used to treat patients in the Lorraine Cancer Institute. TPS controlling RT and SRT machines are constantly improved, notably by the accounting of target movements created by patients' breathing during treatment, improving patients' care at the rhythm of technological innovation. (8)

1.1.5. 2012-Today

As TPS and RT machines are improving continuously, novel RT modalities are emerging. Here, I will briefly review 3 of them, from the most clinically advanced to the most preliminary ones: proton therapy, hadron therapy and flash therapy.

Proton therapy (PT) is blooming all over the world. (8) It uses proton beams, which main advantage, compared to conventional photon beams, is a greater sparing of OARs in selected clinical sites. Indeed, protons preferentially deposit energy at the end of their path through tissues. The maximum deposition occurs in Bragg Peak, which can be modulated to coincide with the tumour location. Only a few energy is deposited before the targeted area, and almost no energy is deposited after it (Figure 1). (18) Although very few randomised trials were conducted to assess PT efficiency, the excellent results for tumour control rates and toxicity profiles were considered sufficient to edit PT clinical indications. (18)

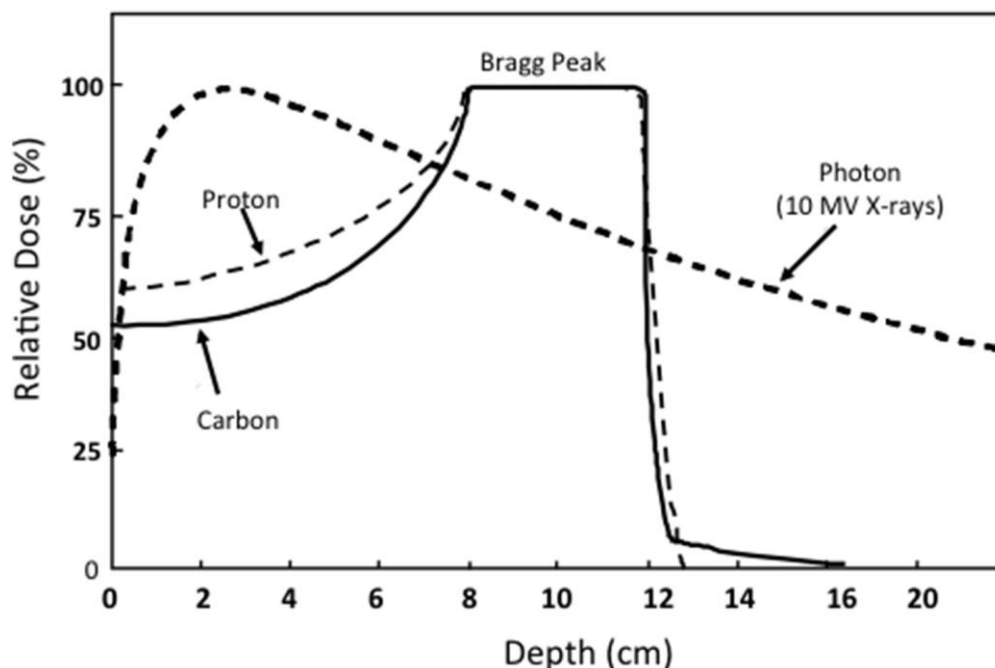


Figure 1. Percentage depth dose (PDD) curves comparing carbon ion, proton and photon beams. The Bragg Peak corresponds to the maximum deposited dose. (19)

Hadron therapy (HT), as PT, is a particle RT modality using carbon ions beams. As PT, its main advantage compared to conventional RT is an energy deposition sparing surrounding OARs (Figure 1). Fundamental experiments suggest that HT could be even more beneficial than PT, as the dose deposited before the maximum area is lower than for PT. (19) As per PT, there has not been any clinical trial to assess HT efficiency. To date, clinical evidence from phase II trials seems promising, but the level of proof is still insufficient to edit HT recommendations. (19) Both PT and HT suffer from their high cost and their lack of access. However, as their advantages in cancer treatment appear more and more obvious both in fundamental and clinical studies, one can expect that these modalities will progressively be included in patients' care.

Flash RT (FRT) is a photon-based RT modality. While conventional RT delivers 1 to 40 Gy per minute, FRT can deliver an average of 1 000 Gy per minute. It has been shown that it is possible to irradiate mice using FRT, without inducing any toxicities they would have developed with lower doses of conventional RT. (20) Although in its infancy, FRT carries great hopes of dose escalation and hypofractionation improving cancer control while preventing the onset of secondary toxicities.

1.2. Molecular mechanisms

1.2.1. Ionising radiation

1.2.1.1. Definition

Radiations are qualified as ionizing when inducing an electronic rearrangement of the target material. There are two types of radiation used in RT: particles and electromagnetic (or photonic) radiations. Physical and biological effects differ depending on the type of radiation. Only effects induced by photonic radiations are studied in this thesis.

1.2.1.2. Particle radiation

Particle radiation involves charged particles, such as α and β particles from radioactive decay, or accelerated nuclei or fragments of nuclei (carbon and hydrogen [protons] in particular). It can also use uncharged particles such as neutrons and electrons.

1.2.1.3. Electromagnetic radiation

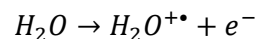
In RT, high-energy IR are used, involving either X-rays (wavelength between 10-12 m and 10-8 m) or gamma-rays produced by nuclei decay (wavelength inferior to 10-12). This type of radiation is involved in 99% of the treatment plans used in RT.

1.2.2. *Radiation effects*

1.2.2.1. Physical and chemical effects

The first interaction between IR and skin and treated tissues is the physical phase. During this phase, electrons are removed by ionisation of the tissues passed through. This phenomenon is achieved through the photoelectric effect (absorption of the incident photon by the atom and ejection of an electron) or the Compton effect (scattering of the incident photon by a weakly bound electron, which is itself removed).

These electrons have direct effects on the molecules of living organisms. The major described effect is the ionisation (or radiolysis) of water, producing free radicals. During ionisation:



The ejected electron can have enough energy to ionise other surrounding water molecules. The ionised water molecule is endowed with an unpaired electron noted by a dot \bullet . This first stage, which is very simple since there is no break in any chemical bond, happens whatever the nature and intensity of the radiation. It is followed by extremely rapid secondary reactions which finally lead to the formation of stable molecular products, dihydrogen H_2 and hydrogen peroxide H_2O_2 , and to the formation of free radicals or radical ions H^\bullet , $\bullet OH$, HO_2^\bullet , e^{-}_{aq} . These are atoms, molecules, or ions with an unpaired electron in a chemical bond. These free radicals cause oxidative stress within the cells, leading to critical damage to DNA, such as double-strand breaks.

1.2.2.2. Biological effects

After physical, physicochemical, and molecular reactions, ionizing radiations induce specific damages in the cell compartments – the most critical ones involving DNA.

DNA damage occurs in many different forms, the most common and harmful of which are double-strand breaks (DSB). DSB are complex lesions processed by a series of coordinated events within multi-protein complexes lead by the ATM protein (21). When DSB occurs, the MRN complex (Mre11/Rad50/Nbs1) is recruited from the damaged DNA site and in turn recruits the ATM protein (Figure 2). Physiologically present in the cell as an inactive dimer, ATM self-phosphorylates at the 1981 serine site, resulting in de-dimerization and activation. pATM then phosphorylates H2AX which recruits several proteins to the damaged DNA site that are subsequently phosphorylated by ATM, including 53BP1, BRCA1, Chk1 and Chk2.

These substrates will then induce cell cycle arrest and the activation of checkpoints prior to DNA repair. A contrario, ATM-dependent apoptosis may occur to prevent the cell from surviving. Along with other proteins such as GADD45 and p21, the phosphorylation of p53 disrupts cyclin-Cdk complexes causing the G1/S passage to stop or slow down. Ionizing radiation also causes G2 arrest and the accumulation of cells in the G2-M phase, the magnitude of which is generally proportional to the dose.

Homologous recombination uses DNA from the homologous chromosome as a template to faithfully repair the break. This first specific repair pathway takes place preferentially in the S and G2 phase and depends on RAD51 and BRCA proteins (22). Non homologous end joining (NHEJ) aims to join the flanking DNA strands without filling in the missing genetic information, therefore producing a loss of genetic information. Ku80 and Ku70 proteins associate, slide on the DNA to the level of the DSB. DNA-PKcs, is then recruited and the trimeric complex plays as a serine-threonine kinase activating ligase IV. NHEJ is the main DSB repair mechanism in humans (23).

Finally, the irradiated cell may either survive with accurate genetic information, survive with unrepaired lesions in more or less critical genes, die in the first generation, or even die after several mitoses. Radiation-induced death is the result of various contributions that can be described as different histological and eventually coexist – such as mitotic death, senescence and apoptosis (24).

Cancer cells are genetically more damaged than healthy cells, displaying a higher number of DSB at basal state. Hence, irradiating them rushes them to their death, as they accumulate more DNA damage than they can repair or survive with. Because of the physical properties of

photon beams, as well as the infiltrating nature of tumours into the surrounding healthy tissues, uncertainties in the repositioning of the patient, the movement of organs or tumour during treatment, the radiation oncologist must necessarily include a volume of healthy tissue around the target. This constraint, which cannot be totally reduced, is at the root of RT-induced toxicities.

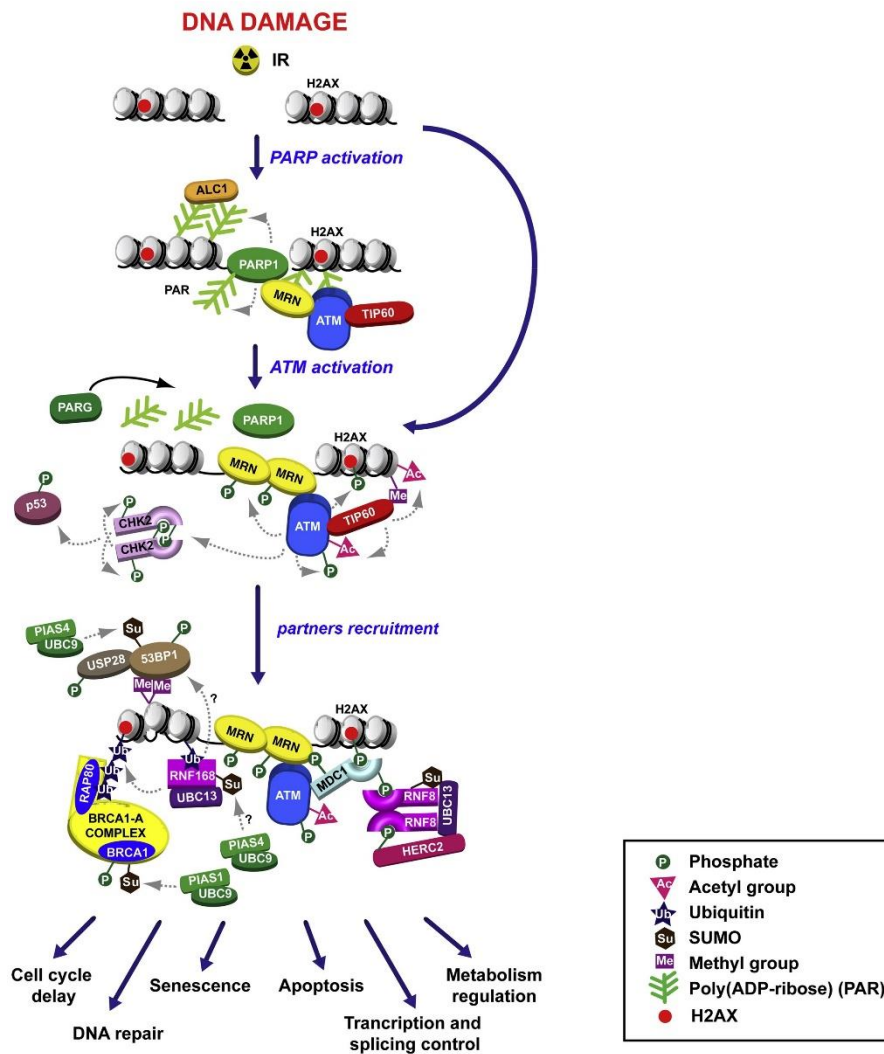


Figure 2. Schematic model for DSB repair, from Ciccia and Elledge (2010). Formation of DSBs after IR treatment activates PARP1, mediating the recruitment of the MRN/ATM complex. Activation of the ATM kinase activity by MRN and TIP60 leads to the phosphorylation of CHK2 and p53, in addition to a large number of other DDR factors, and the induction of the γ H2AX-dependent signaling cascade, which results in the recruitment of MDC1, RNF8, RNF168, BRCA1, and 53BP1 to DSBs. (25)

2. Radiotherapy, a potential source of toxicity for healthy tissues

2.1. Epidemiology

The risk and the severity of the sequelae are directly proportional to the dose received for a given tissue volume. Tumour and healthy tissues have their own radiation sensitivities - in principle ubiquitous for all the healthy tissues of the same individual, which makes it possible to characterize his/her individual radiosensitivity (IRS). When prescribing the treatment, the radiation oncologist usually applies constraints on OAR in the treated volume to inactivate the tumour cells with an “acceptable” risk of sequelae on OAR of the order of 5% at five years, assuming no particular individual over risk (26).

Overall, 3 to 18% of adults are estimated to suffer from late toxicity that can cause potentially serious sequelae in absence of therapeutic deviation (27,28). However, toxicity prevalence may be underestimated in absence of systematic dose-outcome correlations collections during the follow-up at populational level. Prospective clinical-dosimetric databases are emerging integrating patient-reported outcome in addition of the clinician one to offer a broader view (29). For instance, using an internet-based tool, 1 785 cancer survivors who underwent RT reported late effects they were experiencing. Of the whole cohort, the most common late effects reported were cognitive changes (58%), sexual changes (55%), changes in texture/color of skin (50%), and chronic pain/numbness/tingling (39%). Median time from diagnosis was 2.3 years. (30).

Ultimately, RT-induced morbidity exposes patients to additional morbidity such as fatigue, pain, aesthetic prejudice, depressive and anxiety disorders as well as an additional financial cost linked to healthcare consumption, discrimination, unemployment and poverty (31).

These late effects are characterized by a clinical latency during which intricated cellular and tissue events take place. These reactions appear more than 3 months even 6 months after the end of RT, especially in slowly renewing tissues (32). Various clinicopathological aspects are described: occlusions, stenoses, fibrosis, necrosis, neurodegeneration, atrophy, microangiopathy, endocrine hyosecretion..., which can occur in all organs and tissues, and causing often irreversible loss of function in absence of therapeutic deviation (33,34).

Furthermore, the functional tolerance of organs to irradiation depends on their ability to continue to function as an entity, and therefore on their functional architecture (35). The overall tolerance to irradiation of an organ integrates that of the different tissues that compose it: for example, the oesophagus has a mucous membrane (rapidly renewing tissue) responsible for

early esophagitis during irradiation and supporting connective tissue (slow-renewing tissue) which can lead to fibrosis and late radiation stenosis.

2.2. Cofactors of toxicity

2.2.1. Individual radiosensitivity and radiosensitive syndromes

The distribution of the individual propensity to develop tissue reactions after exposure to a standardized dose of ionizing radiation in the general population (i.e. IRS) follows a Gaussian curve (36). At the left-hand side of this curve, the patients may experience unusual severe tissue reactions although their phenotype appears grossly normal. However, a few very rare hereditary diseases are associated with IRS (Table 1). These pathologies most often have an autosomal recessive mode of transmission (37). Various phenotypes are described – sharing a poor tolerance to RT reflected by a poor SF2 (surviving fraction after 2 Gy; marker of individual radiosensitivity; the lower the value, the more radiosensitive the individual, normal value > 80%). They are induced either by chemotherapy or RT and are associated with abnormal DNA damage recognition or repair,. Human syndromes involving NHEJ defects would rather be associated with a strong immunodeficiency and a moderate to strong IRS while syndromes involving homologous recombination defects would rather be associated with a strong predisposition to cancer and a moderate to weak IRS. The human syndrome associated with the strongest IRS is homozygous ataxia telangiectasia (38). 1% of the world's population carries heterozygous ATM mutations leading to a weaker but still significant IRS (39,40). These hereditary diseases are far less prevalent than late toxicities of RT, suggesting the existence of other molecular determinants, yet to be deciphered.

Table 1: Hereditary diseases associated with IRS. SF2: Surviving fraction at 2 Gy, historical measure of cell sensitivity to ionizing radiations.

Disease	OMIM	Involved protein(s)	Role	SF2 (%)	Cancer predisposition	Associated phenotype
Ataxia telangiectasia	208900	ATM	recognition, signaling and repair of DSB	1-5	lymphomas, leukemias, breast cancer	ataxia, telangiectasia, immunodeficiency, mental retardation, premature aging, café au lait spots
Nijmegen breakage syndrome	251260	NBS1	MRN complex	2-6	lymphomas, gliomas	microcephaly, mental retardation, short stature, immunodeficiency, infertility
NBS-like syndrome	613078	RAD50	MRN complex	5-9	lymphomas	microcephaly, mental retardation, short stature, immunodeficiency
ATLD syndrome	604391	MRE11	MRN complex, endonuclease activity	15-40	lymphomas	AT phenotype without telangiectasia or immunodeficiency
ligase IV deficiency	606593	LIG4	NHEJ, VDJ recombination	5-9	lymphomas	Severe Combined Immune Deficiency (SCID), Pancytopenia, Growth Retardation, Facial Dysmorphism
DNA-PKcs deficiency		DNA-PKcs	NHEJ, VDJ recombination	8-20		SCID
Artémis syndrome	602450	Artemis	NHEJ, VDJ recombination	20-40		SCID, erythroderma, hepatosplenomegaly, lymphadenopathy, alopecia
Cernunnos syndrome	611291	XL/Cernunnos	NHEJ, VDJ recombination	20-40		SCID, microcephaly, growth retardation, facial dysmorphism
Omenn syndrome	603554	RAG1, RAG2	NHEJ, VDJ recombination	30-50		SCID, erythroderma, hepatosplenomegaly, lymphadenopathy, chronic inflammation
X-linked agammaglobulinemia (Bruton syndrome)	300755	BTK tyrosine kinase	NHEJ, VDJ recombination	30-50		SCID
Riddle syndrome	611943	RNF168	ubiquitine-ligase targeting H2A	10-20	hemopathies	microcephaly, mental retardation, short stature, immunodeficiency
Cornelia de Lange syndrome	122470	NIPBL, SMC1A, SMC3, RAD21	cohesin complex	20-70	hemangioendothelioma, nephroblastoma	facial dysmorphism, intellectual deficit, growth retardation malformations of the extremities and visceral (cardiac, renal ...), gastroesophageal reflux
Fanconi anemia	227650	FANC proteins incl. BRCA2	homologous recombination, cell cycle	20-40	Hemopathies, breast cancer, squamous cell carcinomas (H&N, esophagus, vulva)	chemosensitivity, bone marrow failure, microcephaly, visceral malformations, growth retardation, deafness, sterility, café au lait spots

BRCA1 syndrome	113705	BRCA1	homologous recombination, cell cycle	20-40	Cancers of the breast, ovary, colon, pancreas, prostate	
Progeria (Hutchinson-Gilford syndrome)	176670	Lamin A	organization of the nuclear lamina	8-19	/	premature aging, growth retardation, alopecia, lipodystrophy, scleroderma
Huntington's disease	143100	huntingtin	vesicular transport	18-30	/	neurodegeneration: chorea, dystonia, coordination disorders, cognitive decline, behavioral disorders
Usher syndrome	276900	USH proteins	?, cilia morphogenesis of sensory receptors	15-20	/	neurodegeneration: deafness-mutism, retinitis pigmentosa
Xeroderma pigmentosum	278700	XP proteins	Helicases, nucleases involved in NER	15-30	Skin basal cell carcinoma, squamous cell carcinoma, melanoma	photosensitivity, genodermatosis, deafness, microcephaly, keratitis, cataracts
Cockayne syndrome	216400	CS proteins	Helicases, nucleases involved in NER	15-30	/	photosensitivity, genodermatosis, growth retardation, retinitis pigmentosa, deafness, premature aging
Trichothiodystrophy	601675	TTD	Helicases, nucleases involved in NER	15-30	/	genodermatosis, photosensitivity, growth retardation, mental retardation
Gardner syndrome (Familial adenomatous polyposis),	175100	APC	MMR	20-30	intestinal cancers, thyroid, osteomas of the skull, epidermoid cysts, fibroids, desmoid tumors	genodermatosis
Turcot syndrome	276300	hMSH2	MMR	20-30	intestinal polyposis, brain tumors - medulloblastomas, hematologic malignancies, colorectal cancer, embryonic tumors, rhabdomyosarcomas	café au lait spots
Rothmund-Thomson syndrome	268400	RecQ4	RecQ Helicase	30-50	sarcomas, osteosarcomas	genodermatosis, premature aging, telangiectasias, hyper- and hypopigmentation, congenital skeletal abnormalities, growth retardation
Werner syndrome	277700	WRN	RecQ Helicase	30-50	sarcomas, osteosarcomas, melanomas, thyroid cancer	genodermatosis, premature aging, bilateral cataract, growth retardation, chemosensitivity

Bloom syndrome	210900	BLM	RecQ Helicase	30-50	sarcomas, all carcinomas, leukemias, lymphomas	genodermatosis, chemosensitivity, photosensitivity, telangiectasia, dwarfism, infertility, café au lait spots
Seckel syndrome	210600	ATR	Cell cycle, SSB and replication forks repair	60-80	/	Marked microcephaly, mental retardation, primordial dwarfism, facial dysmorphism
type 1 Neurofibromatosis	162200	neurofibromin	Ras inhibitor	30-60	neurofibromas, MPNST, gliomas	cafe au lait spots, genodermatosis, Lish nodules
basocellular naevomatosis (Gorlin syndrome)	109400	PTCH1	Sonic Hedgehog receptor (development)	80-100	medulloblastoma, basal cell carcinoma, breast cancer, colon cancer, odontogenic keratocystic tumors	genodermatosis, macrocephaly, skeletal abnormalities
Dysplastic nevus syndrome (FAMM)	155600	p16 & p14ARF	cell cycle regulation	80-100	melanoma, pancreatic cancer, breast cancer, myeloma	genodermatosis
Lewandowsky and Lutz dysplasia or epidermodysplasia verruciformis	226400	EVER1, EVER2	membrane proteins involved in zinc homeostasis (HPV barrier)	80-100	Skin cancers	genodermatosis
Dyskeratosis congenita	615190	RTEL1	helicase 1 regulating telomeric elongation	80-100	squamous cell carcinomas (H&N, esophagus, vagina or cervix)	genodermatosis, premature aging, tear atresia, infertility, growth retardation, microcephaly, immunodeficiency, bone marrow failure, cerebellar hypoplasia
Down syndrome	190685	DSCR1 & DYRK1A	inhibit the nucleoshuttling of NFATc transcription factors, which regulate development	80-100	myeloproliferative syndromes, leukemias	premature aging, mental retardation, heart and digestive malformations, growth retardation, microcephaly, hypotonia
Klinefelter syndrome	400045			80-100	Masculine breast cancer	premature aging, infertility, delayed puberty, gynecomastia, tall stature
Hereditary retinoblastoma	180200	RB1	negative cell cycle regulator (E2F)	80-100	retinomas, retinoblastomas, sarcomas	
Li Fraumeni syndrome	151623	P53, CHK2	apoptosis, cell cycle, DNA repair	80-100	breast cancer, glioma, acute leukemia, soft tissue sarcoma, osteosarcoma, adrenal cortex carcinoma	

2.2.2. Other cofactors

Other cofactors such as comorbidities, age, therapeutic parameters, severity of early toxicities, and concurrent treatments may predispose to the development of late RT toxicities. Indeed, some acquired conditions such as HIV infection (41), diabetes melitus (42), obesity (43), anemia, tobacco misuse, or systemic inflammatory diseases including connective tissue (44) and inflammatory bowel diseases may confer a slightly increased sensitivity to IR due respectively to immunodeficiency, microangiopathy or the development of autoantibodies directed against DNA repair proteins (45). Systemic scleroderma and fibrosing diseases in general, such as idiopathic retroperitoneal fibrosis, are very high-risk clinical situations with cases of lethal complications post RT repeatedly described in the literature (46).

Furthermore, individual sensitivity to radiation toxicity is a function of the developmental dynamics of the organ, its renewing potential, and ultimately the extent to which it has senesced (47). Growing organs and tissues in children may suffer from particular reactions compared to adults (48,49). At the other end, the susceptibility to late effects in the elderly seems to involve not only a decline in wound healing, but also a shift in the mechanisms of radiation-induced cell death towards senescence, interconnected with effects of comorbidities frequent in this age group.

Several therapeutic parameters are related with an increased risk of radiation sequelae. Due to the deterministic nature of non-carcinologic normal tissue effects, the total dose delivered is a major determinant of outcome. The variations in dose per session have a major impact on late effects, hypofractionation being much more toxic than the conventional fractionation for the same endpoint and the same volume of irradiated tissue (50). Similarly, high dose rate and low interval between fractions (inferior to 6 hours) may lead to an increased late toxicity by saturating DNA repair mechanisms in healthy tissue.

Associated treatments may alter the cell and tissue response to IR. Several examples can be given with concurrent chemotherapy in lung, breast or cervix cancer (51,52). Concurrent endocrine therapy may also be associated with an increased late radiation toxicity, e.g. lung fibrosis and subcutaneous fibrosis with tamoxifen or late gastrointestinal and genitourinary toxicity with androgen deprivation in men (53). While often the combination was well tolerated, increased toxicities have repeatedly been reported with some targeted therapies. (54) Finally checkpoint inhibitors may lead to higher incidence of immune-related pneumonitis in lung cancer patients who previously received RT. (55)

2.3. Current management of late effects

2.3.1. Primary prevention

The screening of constitutionally radiosensitive patients by means of IRS diagnostic tests could allow an a priori adaptation of their cancer treatment. It would thus be possible to recommend therapeutic alternatives, or to adapt the dose or volumes treated to the individual status, provided these modifications are validated in clinical trials. Several approaches are proposed (56): radiation induced lymphocyte apoptosis (57), quantification of radiation-induced pATM (58), TGF β 1 genetic variation (59), spontaneous transcriptomic signature targeting RNA involved in RT-induced fibrosis. However, there is currently no gold standard recommended for daily practice. Recommendations were recently published by the American Society for Radiation Oncology (60).

In order to improve the tolerance profile of RT, we can also raise various physical, technological and biological approaches. Hyperfractionation consists in delivering a dose per session lower than 1.8 Gy – eventually more than one session a day. The total dose is higher, but the total duration of treatment does not vary. This hyperfractionation has a protective effect on slowly renewing tissues affected by late toxicities, provided that a period of 4-6 hours is observed between the fractions (60).

Reducing the tissue volume irradiated at high doses also reduces the incidence of toxicities. Current techniques of EBRT, brachytherapy and HT meet this objective (8). Controlling patient and organ movements during or between RT sessions is also moving in this direction through the development of image-guided RT and adaptive RT. Protocols for partial irradiation of organs are being evaluated to reduce the tissue volume irradiated at high doses in selected indications, in particular in breast and bladder cancer (61).

2.3.2. Secondary prevention

Early diagnosis of toxicities is possible when subclinical biological or radiological signs appear in relation with unusual early or late toxicity events. Imaging methods are developing in that intent – such as radiomics and functional MRI (62–64). Biological biomarkers are also being studied, such as TGF- β 1 and IL-6 in prediction of radiation lung disease. (65)

2.3.3. Tertiary prevention

Radiation-induced late complications are generally considered irreversible with a complex pathophysiology involving chronic inflammation, micro vasculopathy, fibrosis, necrosis. When identified during the long-term follow-up, countermeasures may be proposed to mitigate these reactions. Depending on their severity and impact on survival quality, the current strategies include:

- Anti-inflammatory treatments (steroids or non-steroids) and angiotensin II receptor antagonists ; (66)
- Antioxidant treatments such as superoxide dismutase, tocopherol (vitamin E) preferably combined with pentoxifylline ; (67–69)
- Bevacizumab has been proposed as a treatment as it helps prevent angiogenesis by inhibiting VEGF and therefore slows the progression of radionecrosis in brain in particular; (70,71)
- Invasive conservative surgeries such as dilatation and stent implantation for stenoses (e.g. oesophagus, ureter), and surgical treatment of adhesions and strictures – keeping in mind that interventions potentially can worsen the underlying fibrosis, thereby exacerbating symptoms;
- Hypoxia reversion with hyperbaric oxygen (HBO); (72)
- Cell therapy has recently been shown to be effective in the context of severe accidental irradiation, consisting of injecting autologous mesenchymal stem cells in situ. (73)

3. From bench to bedside: in silico and ex vivo approaches for the management of late effects of radiotherapy.

RT is an effective tool, but like any treatment, it is not exempt from side effects. There is a real challenge in the prevention, diagnosis and management of secondary toxicities induced by RT. In this work, I focused on the diagnosis and management of late RT-induced adverse events. This manuscript will be divided in two parts, with some results presented as published or submitted scientific articles.

The first part of this manuscript addresses toxicities diagnosis applied to brain metastases. Brain metastases can be treated with SRT. During post-treatment follow-up, conducted using magnetic resonance imaging, physicians can identify a lesional evolution. The latter corresponds either to tumour recurrence or to brain radionecrosis, which is a late toxicity of SRT. Both diagnoses are equivocal on imaging and require the use of cerebral biopsy, which is an invasive, costly, and risk-prone examination for the patient. We propose to develop a decision support tool based on images from patient follow-up using the radiomics method, the analysis of quantitative parameters extracted from medical imaging.

The second part of this manuscript tackles an innovative strategy for toxicity prediction. For any organ treated by EBRT, IR must penetrate the skin. One of the most severe late skin toxicities induced by RT is radiation-induced skin fibrosis (RISF). Occurring unexpectedly, its emergence is not yet fully understood. Moreover, there is no predictive test to discriminate against patients at risk. In this work, we will study the molecular determinants of RISF, as well as the physiology of fibroblasts, the key cells of this disease, from both healthy and affected patients.

Radiomics method for radiotherapy toxicity diagnosis

4. Introduction

4.1. Brain metastases

4.1.1. Epidemiology

According to World Health Organisation, a brain metastasis (BM) is a tumour that originates from outside of the central nervous system and spreads to it, most commonly by a haematogenous pathway or by direct invasion of adjacent tissues. Here, we focus on parenchymal BMs. They represent most intracranial tumours. Fifteen to 40% of patients with cancer, all primary sites combined, will develop BMs. (74) The incidence of BM is increasing due to the effectiveness of new systemic treatments that extend patient survival, allowing cancer to spread to the brain. (75)

4.1.2. Treatment of brain metastases

Surgery and stereotactic radiotherapy (SRT) are the two cornerstones of focal treatment of oligometastatic patients with 1 to 5 BM. Management guidelines from the European Association of NeuroOncology (EANO) (76) and the Association des Neuro-Oncologues d'Expression Française (ANOCEF) (77) help in the decision making process. Surgery is a standard local treatment for BM, when the benefit-risk ratio is favourable. It can be associated with SRT. SRT is a high-precision technique using an association of tens to hundreds of fine converging photon beams, allowing the treatment of very small tumour volumes at high dose (hypofractionation) with a millimetric precision. The efficacy of SRT has been widely demonstrated in BM treatment with a local control rate of 70-90% at one year. (78)

Ten to 40% of patients experience complications after SRT. (79) Early reactions are transient, secondary to radiation-induced brain inflammation. They usually appear around the second week post- SRT: headache, nausea, vomiting sometimes indicating intracranial hypertension, seizures and worsening of pre-existing neurological deficits. Late side effects include risks of haemorrhage, neurocognitive disorders, leukoencephalopathy or radionecrosis (RN).

4.2. Post-treatment dilemma: Radionecrosis or Tumour recurrence?

4.2.1. Radionecrosis

RN is a vascular damage of the white matter developing in the irradiation field. It is secondary to the chronic inflammation of the brain parenchyma, with a tendency to spontaneous extension. (80) Its pathophysiology is not yet elucidated. RN is the most disabling late complication after SRT. Hypofractionation makes it more frequent as healthy tissue displays a greater difficulty to repair radiation-induced DNA damage. Two years after SRT, the incidence of RN reaches 34%, being symptomatic in 10-17% of cases. (81) RN typically occurs 10 to 16 months post-SRT and is rarely diagnosed in the first 3 months post-treatment, as it may be confused with pseudo-progression. RN symptoms are aspecific and depend on the irradiated functional area. (82)

4.2.2. Differential diagnosis between radionecrosis and tumour recurrence

The clinical and radiological features of RN are very similar to those of tumour recurrence (TR), making the discrimination between these two entities very challenging (Figure 1 in the article below). The gold standard for the diagnosis is anatomopathological analysis. However, cerebral biopsies are often not obtainable in clinical practice due to their invasive and risky character. In the absence of any possible histological documentation, clinical and imaging data are used to define the probability of RN or TR following the Response Assessment in Neuro-Oncology (RANO-BM) group criteria. (83) The evolution of each lesion is carefully measured. In the case of lesion progression, no pathognomonic signs on Magnetic resonance imaging (MRI) are available to distinguish RN from TR. Further radiological investigations would therefore be necessary, but no imaging criterion is currently validated to establish a reliable differential diagnosis.

4.2.3. Therapeutic options for radionecrosis and tumour recurrence

The first-line treatment for a suspected RN is corticosteroid therapy for at least 4 to 6 weeks before further MRI investigation. (84) If corticosteroid therapy fails, surgery is proposed, if possible, hence providing a definitive histological diagnosis. The treatment of TR is the same as in the management of the initial brain metastatic disease.

In summary, the differential diagnosis between RN and TR is challenging but essential as the therapeutic options for these two entities are very different. A delayed or erroneous diagnosis could be dramatic for patient' recovery.

4.3. Radiomics: a high throughput approach for medical imaging (85)

4.3.1. Overview

Radiomics is a recent and promising discipline. While the traditional analysis of imaging studies, such as MRI or positron emission tomography scans, is based on the visual interpretation of simple features - such as tumour size, general shape, contrast uptake or signal intensity - this new approach processes these imaging studies computationally and translates them into complex quantitative data. Radiomics is based on qualitative and quantitative analyses, combining numerical data from medical imaging with clinical and biological characteristics to obtain predictive and/or prognostic information about patients. Indeed, the study of cellular interaction within tissues and intrinsic characteristics of medical imaging reflect the physiology and pathophysiology of the affected organ. Radiomics have many advantages:

- They are non-invasive, as they rely on non-invasive imaging studies.
- They allow an evaluation of the studied tissues in their globality, thus characterising their spatial heterogeneity.
- They are an easy way to follow the patient over time, allowing to understand the changes throughout the history of the disease and the therapeutic sequence.

As this field is very new, no workflow has been implemented in standard clinical routines yet.

4.3.2. Workflow

A typical radiomics workflow follows 5 steps (Figure 3):

- 1) Data selection: choosing the image to analyse, the imaging protocol to use and the correlated outcome.
- 2) Imaging and segmentation with (semi-)automatic methods to improve reproducibility.
- 3) Feature extraction and selection with appropriated algorithms.
- 4) Modelling using available machine learning models.
- 5) Reporting results

Combining radiomics features with deep learning features or semantic features may be able to further improve prognostic performance. Several studies have proven the effectiveness of using these features independently in predictive modelling. For example, we can highlight Lucia *et al.* models, which are able to predict disease free survival and locoregional control in cervical cancer patients treated with chemoradiotherapy with an accuracy of 90% and 98%,

respectively. The use of these models in clinical practice would allow a personalised treatment with the prescription of more aggressive therapies for patients at higher risk of recurrence. (86)

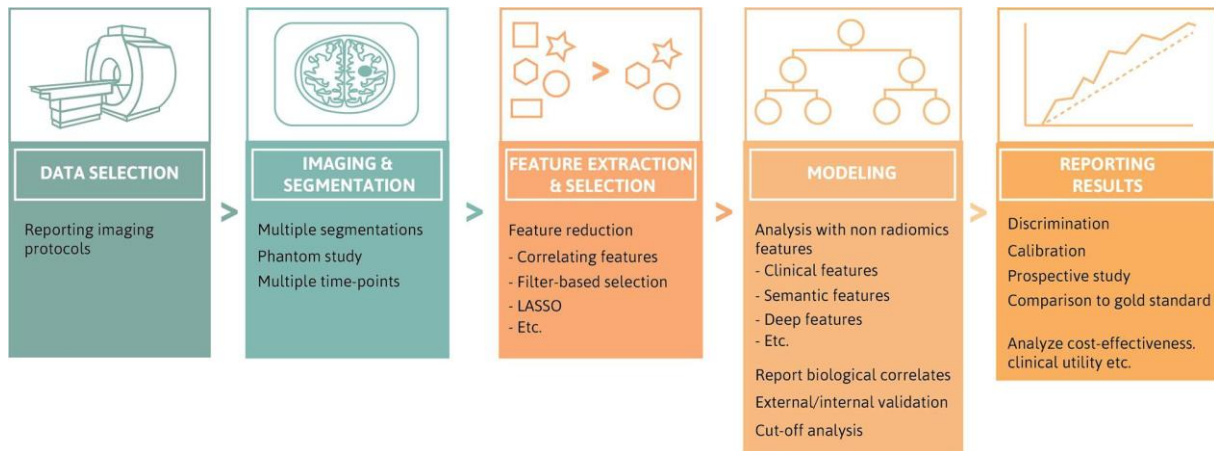


Figure 3: Overview of steps of a Radiomics analysis from Keek et al. (2018) (85)

5. A sharp decision-support tool to stop slicing brains

Radiomics can be applied to RT, and particularly to toxicities prediction. Therefore, it appeared interesting to use the radiomics approach in the early differential diagnosis of RN versus TR after SRT for BMs. Twenty patients who received SRT for brain oligometastases, from any primary location, were included (8 RN, 12 progressions, pathologically confirmed). We assessed the clinical relevance of 1766 radiomics features, extracted with IBEX software, from the first T1-weighted postcontrast MRI after SRT showing a lesion modification. We evaluated 7 feature-selection methods and 12 classification methods in terms of respective predictive performance. The classification accuracy was measured with Cohen's Kappa after leave-one-out cross validation. The best predictive power reached was a Cohen's Kappa of 0.68 (overall accuracy of 85%), expressing a strong agreement between the algorithm prediction and the histological gold standard. The prediction accuracy for RN was 75% and 91% for progression. The area-under-curve reached 0.83 using a bagging algorithm trained with the Chi-square score features set. The encouraging results of our study are detailed in the following article. (64)

5.1. Article

Radiomics Method for the Differential Diagnosis of Radionecrosis Versus Progression after Fractionated Stereotactic Body Radiotherapy for Brain Oligometastasis

Liza Hettal,^{a,1} Anais Stefani,^{b,1,2} Julia Salleron,^c Florent Courrech,^b Isabelle Behm-Ansmant,^a Jean Marc Constans,^d Guillaume Gauchotte^{e,f} and Guillaume Vogin^{a,b}

^a CNRS UMR 7365 IMoPA, Université de Lorraine, Biopôle, Vandoeuvre-Lès-Nancy, France; ^b Département de Radiothérapie, Institut de Cancérologie de Lorraine, Vandoeuvre-Lès-Nancy, France; ^c Cellule Data-biostatistiques, Institut de Cancérologie de Lorraine, Université de Lorraine, Vandoeuvre-lès-Nancy, France; ^d Département de NeuroRadiologie et Imagerie Médicale, CHU Amiens, France; ^e Département d'Anatomie et Cytologie Pathologiques, CHRU Nancy, France; and ^f INSERM U1256, Université de Lorraine, Nancy, France

Hettal, L., Stefani, A., Salleron, J., Courrech, F., Behm-Ansmant, I., Constans, J. M., Gauchotte, G. and Vogin, G. Radiomics Method for the Differential Diagnosis of Radionecrosis Versus Progression after Fractionated Stereotactic Body Radiotherapy for Brain Oligometastasis. *Radiat. Res.* **193**, 471–480 (2020).

Stereotactic radiotherapy (SRT) is recommended for treatment of brain oligometastasis (BoM) in patients with controlled primary disease. Where contrast enhancement enlargement occurs during follow-up, distinguishing between radionecrosis and progression presents a critical challenge. Without pathological confirmation, decision-making may be inappropriate and delayed. Quantitative imaging features extracted from routinely performed examinations are of interest in potentially addressing this problem. We explored the added value of the radiomics method for the differential diagnosis of these two entities. Twenty patients who received SRT for BoM, from any primary location, were included (8 radionecrosis, 12 progressions, pathologically confirmed). We assessed the clinical relevance of 1,766 radiomics features, extracted using IBEX software, from the first T1-weighted postcontrast magnetic resonance imaging (MRI) after SRT showing a lesion modification. We evaluated seven feature-selection methods and 12 classification methods in terms of respective predictive performance. The classification accuracy was measured using Cohen's kappa after leave-one-out cross-validation. In this work, the best predictive power reached was a Cohen's kappa of 0.68 (overall accuracy of 85%), expressing a strong agreement between the algorithm prediction and the histological gold standard. Prediction accuracy was 75% for radionecrosis, and 91% for progression. The area under a curve reached 0.83 using a bagging

algorithm trained with the chi-square score features set. These findings indicated that the radiomics method is able to discriminate radionecrosis from progression in an accurate, early and noninvasive way. This promising study is a proof of concept, preceding a larger prospective study for defining a robust model to support decision-making in BoM. In summary, distinguishing between radionecrosis and progression is challenging without pathology. We built a classification model based on imaging data and machine learning. Using this model, we were able predict progression and radionecrosis in, respectively, 91% and 75% of cases. © 2020 by Radiation Research Society

INTRODUCTION

Brain metastases are the most common brain tumors (1), with lung cancer as the leading primary (2). Patients with brain metastases experience variable survival and functional abilities according to well-known prognostic factors and the volume and location of the lesion(s) in the brain (3, 4). The concept of brain oligometastasis (BoM), defined by the presence of one to four or five brain metastases, has emerged, leading to considerations of alternative therapeutic approaches (5, 6). BoM can be managed with surgery, radiation, systemic therapy and/or supportive care, eventually combined (7, 8).

Stereotactic radiotherapy (SRT) has emerged as an alternative for selected patients with controlled primary disease, a significant life expectancy and appropriate target lesion(s) volume (7–9). The therapeutic ratio is achieved by precisely and accurately delivering a very high dose of radiation in one [stereotactic radiosurgery (SRS)] or a few [hypofractionated stereotactic radiotherapy (HSRT)] sessions to a limited, well-defined volume. Overall, SRT leads to a local control rate of 70–90% at 12 months (10). HSRT can be particularly beneficial for patients with large lesions or lesions located near critical structures (11–13).

Editor's note. The online version of this article (DOI: <https://doi.org/10.1667/RR15517.1>) contains supplementary information that is available to all authorized users.

¹ These authors contributed equally to this work.

² Address for correspondence: Academic Department of Radiation Therapy and Brachytherapy, Institut de Cancérologie de Lorraine - Alexis-Vautrin Comprehensive Cancer Center - Unicancer, 6 Avenue de Bourgogne - CS 30 519 Vandoeuvre-lès-Nancy Cedex, F-54 511, France; email: a.stefani@nancy.unicancer.fr.

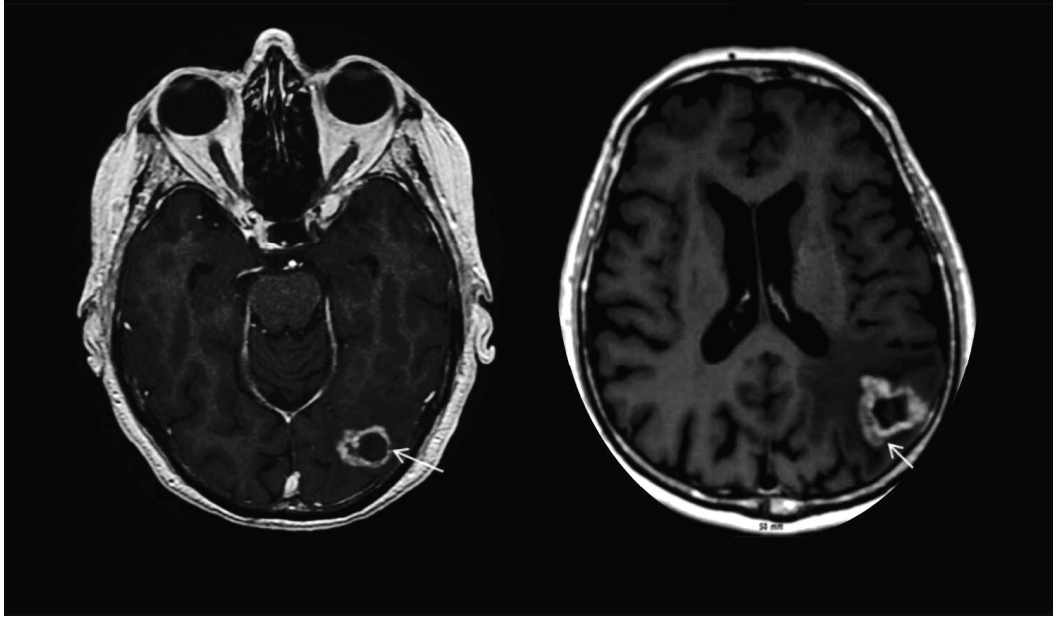


FIG. 1. Conventional MR images used in current clinical practice. Brain metastasis radionecrosis (left) and progression lesion (right) on T1-weighted post-contrast sequence are shown. Similar images are shown, with a peripheral enhancement of the lesion associated with perilesional edema.

The main complication after SRT is brain radionecrosis, a coagulative necrosis affecting mostly white matter. Radionecrosis is observed as a focal enlargement of an enhancing lesion occurring inside or in the margins of the radiation field after a free interval of several months. An actuarial incidence of radionecrosis of up to 34% two years after SRS was recently reported, which was symptomatic and sometimes lethal or severely debilitating in 10–17% of the patients (14). Radionecrosis incidence appears to be lower after HSRT (10, 12). Although the development of radionecrosis is currently unpredictable, the following risk factors have been identified: lesion volume and related volume of brain irradiated, total dose and fraction size and prior whole-brain radiotherapy (WBRT).

During follow-up after SRT for BoM, focal enlargement of a target lesion can be associated to either radionecrosis or tumor progression (Fig. 1). The two entities can moreover coexist in the same lesion (15). According to the Response Assessment in Neuro-Oncology Brain Metastases (RANO-BM) working group, none of the available standard morphologic imaging approaches, even combined, is accurate enough to distinguish between these two entities, exposing patients to an inadequate diagnostic hypothesis, treatment and outcome (16). Advanced imaging modalities, sometimes repeated, bring additional insights. Perfusion-weighted magnetic resonance imaging (MRI) appears to be efficient in differentiating between radionecrosis and progression. Dynamic susceptibility contrast PWI (DSC-PWI) became popular in clinical practice, with a specificity up to 96% (17).

Nonetheless, pathology is still best suited to this situation, but involves an invasive procedure with a debatable risk-

benefit ratio. Thus, the Association of French-speaking Neuro-Oncologists (ANOCEF) produced a diagnostic algorithm based on clinical and imaging criteria repeated over time (18).

More accurate noninvasive procedures are therefore needed. In the radiomics-based approach, raw imaging data, such as pixel intensity, shape and texture, are extracted from (standard-of-care) medical images to assess the characteristics of human tissue noninvasively (19). Specific molecular patterns can be expressed early in terms of macroscopic image-based features that can be captured on imaging. Radiomics has been successfully used to decipher prognostic features and, in healthy tissue, to facilitate patient-specific characterization of radiation-induced damage in lung (20, 21).

The applicability of this method has been studied in the field of neuroradiology (22). Zhang *et al.* and Peng *et al.* recently applied radiomics to distinguish radionecrosis from tumor progression after SRT, using different methods and with exceptional results (23, 24).

The goal of our study was to differentiate between radionecrosis and tumor progression using data extracted from the very first follow-up MRI collected after HSRT for BoM displaying lesion enhancement. We aimed to establish a proof of concept that the radiomics method could provide an earlier and more robust lesional diagnosis than current practices in that setting.

MATERIALS AND METHODS

Ethics

All patients were managed according to good clinical practice and all patients signed an informed consent form to be treated. This

retrospective study was approved by the local institutional review board on April 2017 and has been declared to the French National Data Protection Commission (CNIL).

Patients

We retrospectively selected patients who benefited from HSRT for BoM at the Lorraine Comprehensive Cancer Center, Nancy, France, from 2008 to 2017 and underwent surgery for their irradiated lesion. The inclusion criteria were: age >18 years old, newly diagnosed BoM from any primary location, irradiated with SRT, histological confirmation of the diagnosis, BoM defined by fewer than five brain metastases [at least one measuring 5 mm (or more) in the axial plane (short-axis diameter) but not exceeding 4 cm in the largest diameter], lesion modification defined on follow-up MRI, KPS \geq 70%, and (eventually) concurrent stable or decreasing dose of corticosteroids. WBRT (prior to, concurrent with or after SRT), chemotherapy and progression diagnosis obtained after reirradiation were accepted. Patients were excluded in the following cases: 1. no MRI follow-up; 2. radionecrosis diagnosis obtained after reirradiation. Pathologic specimens were reviewed blind by an external expert neuropathologist from the RENOP network (French network of pathologists involved in neuro-oncology). In the case of multiple brain lesions, only one was pathologically confirmed and therefore included.

SRT Conditions

BoM were treated using a Cyberknife™ G4 system (Accuray, Sunnyvale, CA) (6-MV energy beams). In our center, all brain metastases were treated with HSRT. A dose of 23.1 Gy in three fractions spread over three consecutive days was prescribed on the 70% isodose envelope, except in cases of reirradiation. In the latter case, a dose of 6 Gy in a single fraction was prescribed on the 80% isodose envelope. In our center, all brain metastases were treated with HSRT. A senior radiation oncologist with expertise in neuro-oncology manually delineated the gross tumor volume (GTV) on the planning CT scan, which was merged with a recent 3D axial gadolinium-enhanced T1-weighted postcontrast MR imaging (no specific planning MRI). A margin of 1–2 mm was applied to obtain the planning target volume (PTV).

MRI

All MR images were acquired with a 1.5T or 3T MRI system during routine quarterly follow-up visits in six centers. The morphological axial 3D gadolinium-enhanced T1-weighted postcontrast MRI sequences performed prior to SRT and during the follow-up were collected. The radiomics signature was obtained from imaging features extracted from a single high-quality standardized gadolinium-enhanced T1-weighted MRI. We analyzed the very first MRI displaying an enlargement of a pre-existing enhancing target lesion, or a suspected enhancement of the target lesion, inside or in the margins of the radiation field (event), before any outcome was stated either according to the clinical and MRI ANOCEF criteria for radionecrosis or according to the RANO group definition of progressive disease (16, 18).

Region-of-Interest Segmentation

A senior radiation oncologist, who is a member of ANOCEF and the European Organization for Research and Treatment of Cancer-Brain Tumor Group (EORTC-BTG) with 10 years' experience in neuro-oncology, manually delineated each evolving lesion using IBEX software on the reference axial T1-weighted MRI sequence blinded for each patient (25).

Image Preprocessing

Images were preprocessed using IBEX software (25) to make them comparable. We discretized the number of bins to 8 using BitDepthRescale_Range to standardize the intensity histograms and resampled the voxel size using Resample_VoxelSize to harmonize the size of voxels within each image.

Data Extraction

As shown in Fig. 2, a total of 1,766 variables characterizing tumor phenotype were extracted from MRI using IBEX software (25). According to Aerts *et al.* (20), these variables could be divided among four families: tumor intensity, shape, texture and gray-level features. Tumor intensity characteristics use first-order statistics, calculated from the histogram of all tumor voxel intensity values. Shape features consist of features based on the tumor shape (compactness, volume, etc.). Textural features quantify intratumor heterogeneity and are calculated in all three dimensions within the lesion volume. Gray-level features deal with the spatial relationships of given gray-level pixels within the original image. All features were standardized using Z-score normalization, to analyze them whatever their original scale. Features with a censorship rate greater than 50% were discarded.

Feature Selection

We used seven feature-selection methods based on filter approaches as ranking criterion. The filter approach is applied to prevent overfitting of the prediction to the sample (compared to wrapper or embedded methods) and due to its efficiency in terms of processing time. We computed seven univariate indexes (Fisher score, Relief, T-score, chi-square score, Wilcoxon, Gini index, mutual information maximization) reflecting the feature relevance while ignoring the feature redundancy.

Supervised Machine Learning

In machine learning, classification is considered as a supervised learning task of inferring a function from labeled training data (26). In our study, the training data consisted of an input vector represented by the features with the highest ranks extracted from MRI (see Feature Selection, above), and an output built with the outcome or histological analysis of their lesion. The classification algorithm (classifier) infers a function from the training data, which can be used for predicting the labels of unseen observations. We used 12 different classifiers: decision tree, naïve Bayesian, discriminant analysis, generalized linear models, multiple adaptive regression splines, nearest neighbors, neural networks, partial least square and principle component regression, random forests, support vector machines, bagging and boosting. These classifiers are trained using a leave-one-out cross-validation method. Publicly available implementations along with reported parameter configurations were used in the analysis, which ensured an unbiased evaluation of these methods (27). All classifiers were implemented using the R caret package (28).

Predictive Performance of Feature-Selection and Classification Methods

To investigate and compare different feature-selection and classification methods, we used a three-dimensional parameter grid for the analysis. For each of the seven feature-selection methods, we created three subsets of 1, 5 or 10 chosen variables among each feature family. These subsets were then evaluated by their kappa statistic computed with each machine-learning classifier and a leave-one-out cross-validation method. Cohen's kappa value was chosen over simple accuracy because it takes into account the possibility of the agreement between prediction and reality occurring by chance. The number of retained features within each family was assessed using a *t* test on the kappa values obtained in each condition.

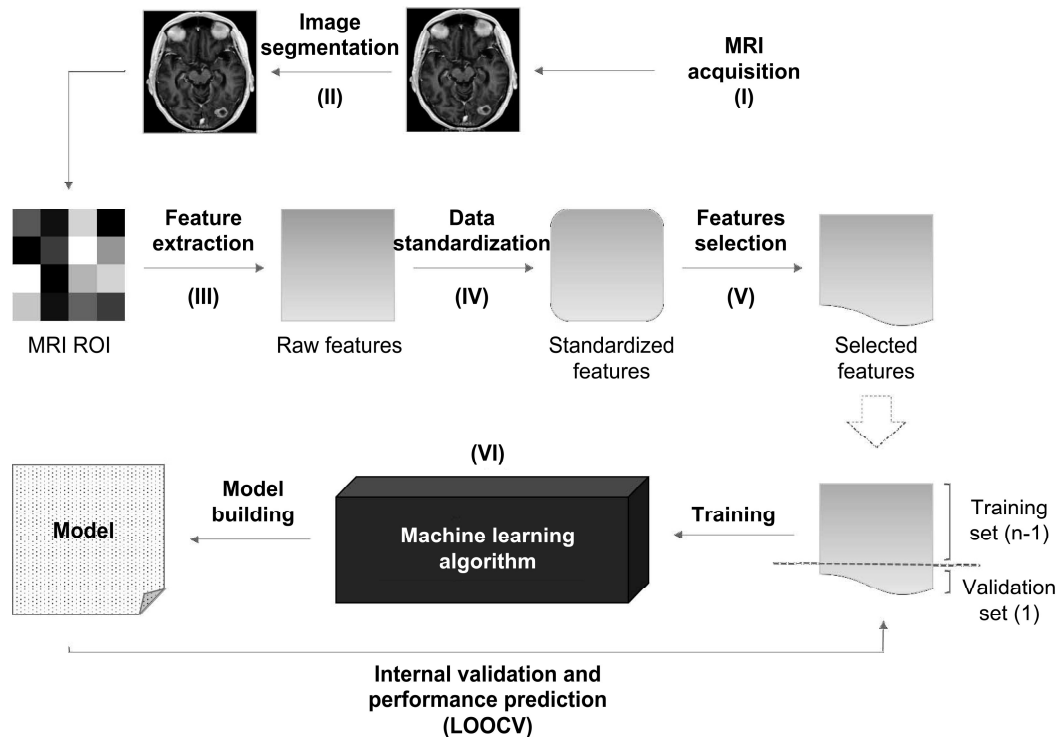


FIG. 2. Building the radiomics model. Workflow chart shows the following. I. MR images were acquired. II. Radiation oncologist contoured the lesion area on all T1-weighted post-contrast slices, designating the region of interest (ROI). III. Raw features were extracted from within the ROI, quantifying lesion intensity, shape, texture and gray-level features (the four families of variables, according to Aerts *et al.* (20)). IV. Data was standardized after image preprocessing: All features were standardized using Z-score normalization, to analyze them whatever their original range. V. Feature selection was performed. Seven feature-selection methods were used. VI. For feature analysis, the selected features were then analyzed for outcome correlation and compared to our pathological data. Twelve different classifiers were used; classifiers were trained using a leave-one-out cross-validation method. LOOCV = leave-one-out cross-validation.

Statistical Analysis

Best selected variables within each family of radiomic variables were compared within each group with a nonparametric Wilcoxon test to assess whether our two groups originated from the same distribution. All statistical analyses were conducted using R statistical language version 3.3.3.

Tumor Board Diagnoses

We retrospectively collected medical conclusions from multidisciplinary tumor boards (pathologists, neurologists, medical and radiation oncologists, neuroradiologists and neurosurgeons). Imaging reports edited by expert academic senior neuroradiologists (conventional MRI sequences \pm spectroscopic or perfusion sequences) were also gathered. Decision-making was based on all clinical and radiological available data, as in daily practice. Two types of conclusions were extracted from these data, radionecrosis and progression, and compared to our bioinformatic model.

RESULTS

Analyses were conducted on 20 patients: 8 radionecrosis and 12 progression. A summary of patient characteristics is provided in Table 1. The average follow-up before the occurrence of an event was 10.5 months. The median age in our sample was 57.6 years. At the time of HSRT, the

patients showed a KPS $\geq 70\%$. All patients had a diagnosis-specific graded prognostic assessment (DS-GPA) score ≥ 2.5 or ≥ 1.5 for breast cancer (29). The most common primary tumor location was non-small cell lung cancer. Patients were assigned to standard treatment, either HSRT alone ($n = 9$, 45%), HSRT with WBRT ($n = 2$, 10%), or HSRT after WBRT ($n = 9$, 45%). Only two patients received chemotherapy with HSRT ($n = 2$, 10%). In the radionecrosis cohort, the average preoperative GTVs and PTVs were $7.2 \text{ cc} \pm 8.2$ and $15.4 \text{ cc} \pm 12.7$; only one of the eight radionecrosis cases experienced a V18 Gy (healthy brain volume receiving 18 Gy) greater than 30.2 cc. In the progression cohort, the average preoperative GTVs and PTVs were $4.3 \text{ cc} \pm 3.8$ and $7.5 \text{ cc} \pm 6.1$, respectively; all progression cases presented a V18 Gy $< 22.8 \text{ cc}$ corresponding to a very low radionecrosis risk (12).

Eleven variables were discarded due to censorship before training. After selecting the best variable in each feature family (shape, intensity, texture, gray levels) according to each of the seven feature-selection scores, we subsequently obtained seven sets composed of four variables. The latter were used to predict the patient outcome, either radionecrosis or progression, through 11 supervised machine-learning algorithms. Power predictions of each model are

TABLE 1
Patient, Tumor(s) and Treatment(s) Characteristics
(n = 20)

Variable	Data
Age at SRT	56.6 (27.0–78.2) ^a
Sex	
Male	10
Female	10
Diagnosis (histology)	
Radionecrosis	8
Recurrence	12
Smoking	
Yes	5
No	6
Weaned	9
Comorbidities	
High blood pressure	9
Diabetes	2
Arteriopathy	3
Inflammatory disease	1
Primary histology	
Breast	2
Renal	1
Lung	15
Melanoma	1
Other	1
Brain metastasis (preoperative)	
Unique	15
>1	5
Volume (cc) PTV	10.67 (1–38.6) ^a
Extracerebral metastasis	
Yes	1
No	19
DS-GPA score	
≤1	0
1.5–2.5	2
≥3	18
BM treatment	
Prior surgery	3
Concomitant systemic treatment	2
Radiotherapy modality	
SRT alone	9
SRT after WBRT	9
SRT + WBRT	2
Interval between SRS and MRI modification (months)	10.5 (1.8–36.6) ^a
Interval between SRS and surgery (months)	15.3 (5.9–37.9) ^a

Notes. DS-GPA = diagnosis-specific graded prognostic assessment; PTV = planning target volume; SRT = stereotactic radiotherapy; WBRT = whole-brain radiotherapy.

^a Average (range).

shown in Supplementary Fig. S1 (<https://doi.org/10.1667/RR15517.1.S1>). A bagging algorithm trained with the chi-square score features set led to the best prediction power reached was Cohen's kappa of 0.68, expressing a strong agreement between the algorithm prediction and the patient's actual diagnosis assessed using the histological gold standard. The algorithm sensitivity for radionecrosis was 75% (6 out of 8 cases were predicted, specificity 91%), and 91% for progression (11 out of 12 cases were predicted, specificity 75%), for an area under the curve (AUC) of 0.83

[CI_{95%} = (0.65, 1)], (Fig. 3). This score was reached for a bagging algorithm trained with the chi-square score features set. Selecting five or ten features per family did not significantly improve the accuracy of the training ($P > 0.05$).

The selected variables in the chi-square score features set were roundness (shape), energy (intensity), complexity (texture) and difference entropy (gray levels). Their correlation is assessed in Supplementary Fig. S2 (<https://doi.org/10.1667/RR15517.1.S1>). There was no significant difference between each group for all selected variables (Fig. 4). Taken together, these results suggest that the highlighted variables are not able to discriminate radionecrosis from tumor progression on their own, only when they are input into models built with machine-learning algorithms.

Before surgery, only 11 out of 20 patients (55%) had an available diagnosis in their medical chart (see details in Table 2). Indeed, the medical team were unable to arrive at a diagnosis for the nine other patients, sending them directly to surgery. Of cases with a given diagnosis, the overall accuracy of the tumor board expertise was 54.5%. Progression was predicted in 100% of cases (6/6), whereas radionecrosis was never identified (0/5).

We applied the model based on delta-radiomics features, as defined by Zhang *et al.* (23) on 14 patients. Results as well as the comparison of the two methods are provided in the Supplementary Information (<https://doi.org/10.1667/RR15517.1.S1>).

DISCUSSION

Patients with BoM are eligible for an ablative and curative treatment such as SRT. To limit adverse events, HSRT rather than SRS is used on larger lesions.

One of the most disabling complications after SRT is cerebral radionecrosis. Due to the growing incidence of BoM in survivors and the widespread use of SRT, the prevalence of cerebral radionecrosis is increasing. Radionecrosis mimics the symptoms and MRI pattern of tumor recurrence, but their management differs greatly. The underlying mechanisms and the risk of developing radionecrosis have not yet been fully elucidated. Radionecrosis should be suspected in patients with enlarging lesions more than three months after SRT.

Differentiating between radionecrosis and progression is a highly challenging in current practice. The gold standard remains pathology, but very few patients are eligible for the required intervention. Other quantitative MRI approaches have been developed, such as spectroMRI, perfusion and diffusion MRI, (30) but also other imaging techniques such as amino-acid PET, with 11C-methyl-L-methionine (31), O-(2-[18F]fluoroethyl)-L-tyrosine, (32) or L-3,4-dihydroxy-6-[18F]-fluorophenylalanine (33). These advanced imaging modalities provide notable help without totally solving the differential diagnosis issue, because there are no current

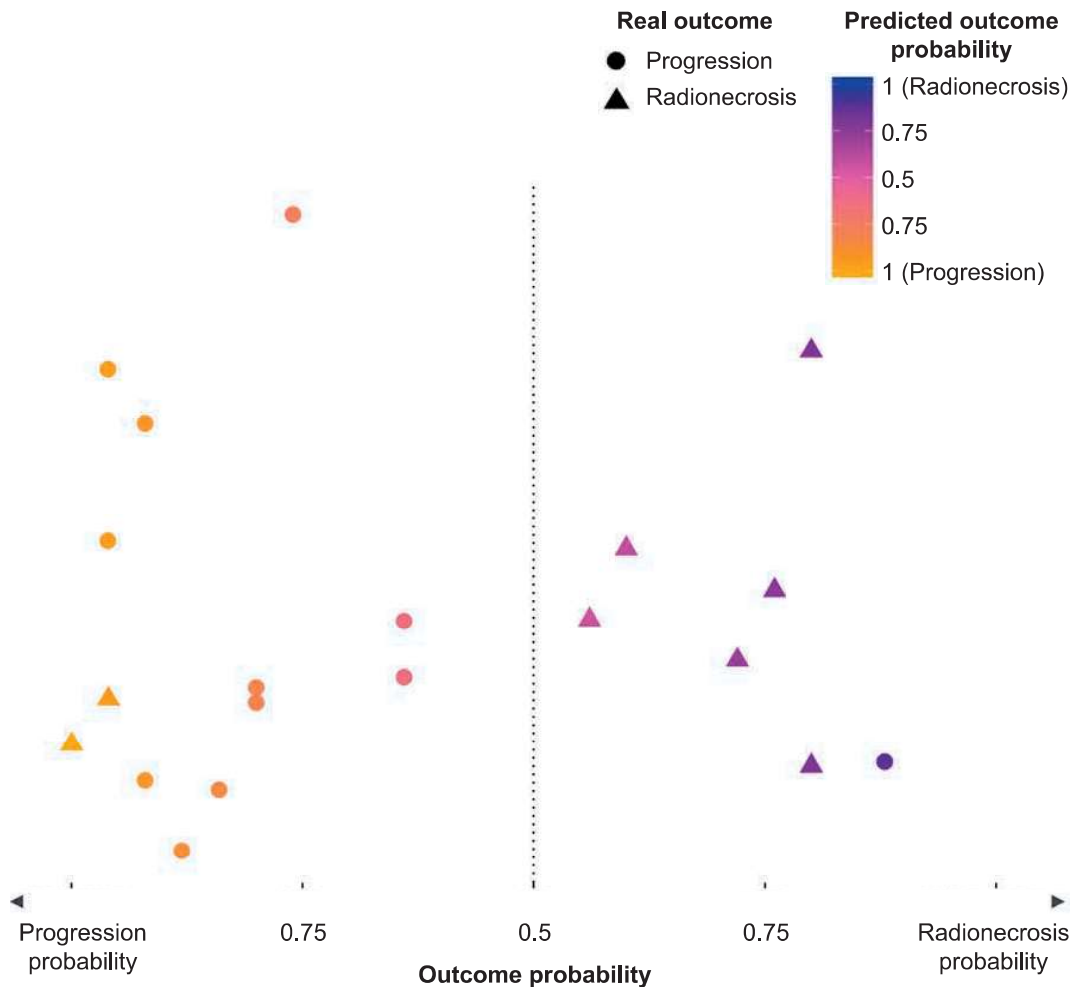


FIG. 3. Best performance of predicting outcome probability compared to actual histological outcome. Training was performed with one feature per family.

standardized discriminating criteria (34). A diagnosis algorithm was proposed after a U.S. survey was performed on the management of radionecrosis (35) and by the ANOCEF in France (18). Moreover, additional examinations result in increased cost and can lead to delay in treatment due to the lack of availability of certain examinations in daily practice.

In this proof of concept, we evaluated the performance of the radiomics approach to distinguish between radionecrosis and progression after HSRT in BoM management, using T1-weighted post-contrast MRI sequences. First radiomics studies in brain tumors, focusing particularly on primary tumors, have used this methodology for diagnosis, prognosis or classification of brain tumor subtypes (22). To our knowledge, only three studies have been undertaken to evaluate this method for the differential diagnosis of radionecrosis and progression on MRI in BoM. Other teams have used different imaging techniques for the same purpose, such as Lohmann *et al.* (36), who demonstrated, in a retrospective study, that textural feature analysis based on O-(2-[18F]fluoroethyl)-L-tyrosine PET helps to improve

discrimination between progression and radionecrosis with an accuracy of 85%

Our goal was to obtain an effective model, especially earlier in the natural history of the disease, to enhance both diagnostic probability and bring about earlier appropriate treatment. Our method is based on that of Aerts *et al.* (20) highlighted in lung cancer. In our study, the highest accuracy in classification was obtained by combining the chi-square variable selection score with a bagging algorithm (37) for learning (AUC = 0.83). Our method appears able to differentiate between radionecrosis and progression with a prediction of the patient's status in strong agreement with the actual (histological) status of the patient (Cohen's kappa 0.68).

We accepted WBRT and Cyberknife reirradiation to best reflect current clinical practice. However, currently treatment of BoM patients with SRT alone is preferred because of the lack of improvement in overall survival and a deterioration of cognitive functions when WBRT is associated (38). A meta-analysis of three randomized controlled trials comparing SRS alone versus SRS and WBRT in patients with one to four brain metastases

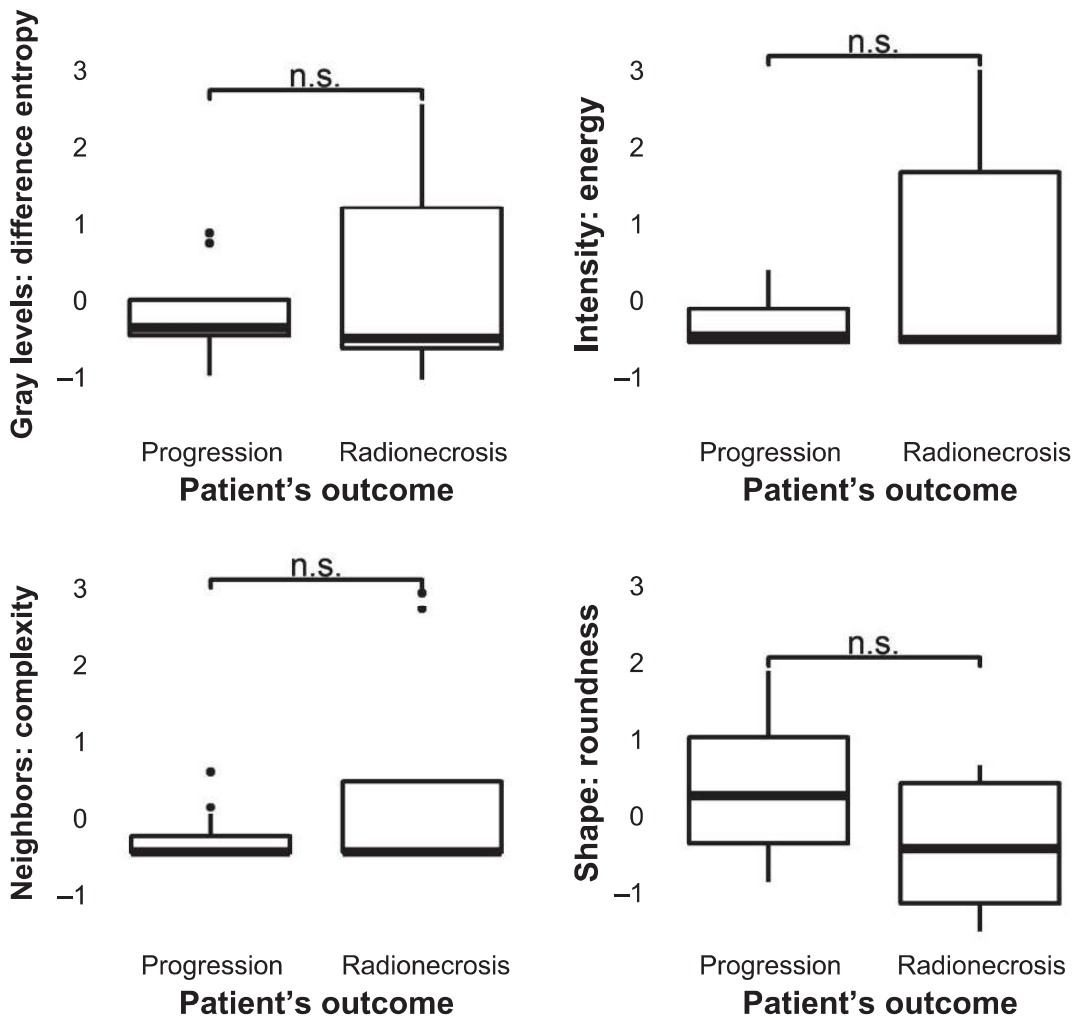


FIG. 4. Histograms show the accuracy of selected variables in discriminating progression from radionecrosis. Selected variables in the chi-square score features set are: roundness (shape), energy (intensity), complexity (texture) and difference entropy (gray levels). Analysis was performed with one variable per family.

confirmed that the omission of WBRT did not adversely affect distant brain relapse rates (39). All patients in our study were treated with HSRT. However, no standard exists for decision-making between SRS and HSRT, (11–13), although HSRT appears to be a safe and efficient alternative treatment to SRS. Concerning Cyberknife reirradiation, two patients with a recurrence were reirradiated by Cyberknife

TABLE 2
Comparison of our Algorithm to the Medical Team’s Conclusions

	Our algorithm	Medical team
Dataset	Our cohort	Our cohort (11/20)
Data used	T1-w MRI at 1 time point	All available data ^a
Radionecrosis sensitivity	75% ($P = 0.02$)	0%
Progression sensitivity	91% (ns)	100%

Notes. T1-w MRI = T1-weighted postcontrast magnetic resonance imaging; ns = non-significant.

^a Radiological and clinical data.

before surgery. Our model, based on the very first suspicious MRI, performed before the second irradiation, was able to allocate the right diagnosis to our patients several weeks or months before surgery. This demonstrates a strong point of our analysis, which is the precocity of the diagnosis.

We compared the performance of our method to the decision made by senior neuroradiologists in the weekly multidisciplinary brain tumor board. Unlike Tiwari *et al.* (40), who analyzed the feasibility of differentiating radionecrosis from progression using computer-extracted texture features, our medical team exploited all available clinical and imaging data, and not only the image of interest. Under these conditions, 100% of progression were predicted but no radionecrosis. Considering these results, a bioinformatics model could be a very useful tool in clinical practice to bolster decision-making.

Compared to other published studies (23, 41), one of the strengths of our study was the confirmation of radionecrosis or progression for all patients by pathology, the gold

standard which allowed for a definitive diagnosis. In some cases, pathology samples display a coexistence of tumor and necrosis, making diagnosis difficult. As with Peng *et al.* (24), we chose a simplified labeling of mixed pathology specimens as true progression, which can disrupt the model's performance. They did a similar study of 66 patients, using a hybrid feature selection and classification algorithm with good performance (AUC 0.81). The pathological status of most of the patients was confirmed by clinical and radiological follow-up after surgery. Indeed, only two patients pathologically classified as radionecrosis relapsed compared with more than 50% of patients pathologically classified as progression (7/12 progression). The homogeneity of the delivered dose by HSRT in our cohort should be noted, suggesting the type of entity that develops (radionecrosis and/or tumor progression) is independent of the therapeutic modalities of HSRT. Notably, the HSRT scheme reported here (23.1 Gy in three fractions on 80% isodose) is equivalent to that reported by Minniti *et al.* when adjusting the prescription isodose (10). Historically, we opted for prescription scheme from the commissioning of our machine (42) as part of a prospective medico-economic study. The fractionation scheme reported in this study was developed in 2004 as part of a prospective French medico-economic study. It should be noted that we modified our prescription in 2018 by allowing a dose escalation stratified according to the lesion volume.

The risk of radionecrosis increases with dose and target volume size. The volume of healthy brain tissue that is irradiated with a dose of 18 Gy (three fractions) is a predictor of brain radionecrosis (12). In our study, the preoperative PTV did not bias the result, as all patients but one presented a $V_{18Gy} < 30.2$ cc, corresponding to an estimated radionecrosis risk $< 6\%$ at one year; the patient in question consequently developed radionecrosis (10, 12).

There are some limitations to our study. First, this was a retrospective and monocentric study with non-standardized imaging procedures and a small patient sample due to the rarity of the two pathologic entities and the requirement for histological evidence. One must keep in mind that the use of small cohorts can lead to overfitting of the output model and overoptimistic predictive statistics, particularly when the leave-one-out cross-validation method is used, despite it being the standard with this type of cohort. Accurate performance statistics can only be computed on an external validation cohort. We chose not to use data augmentation to keep our data as close as possible to the clinical reality.

Another possible limitation is that the MRI follow-up procedure was variable between imaging centers, including unequal posttreatment delay, different vendors, uncalibrated parameters leading to variability in image acquisition, etc., because of the retrospective aspect of the study. This well reflects the reality of clinical practice, but is not ideal in model development, as it may add confounding factors. To compensate for this heterogeneity, we preprocessed the images, by resampling all the intensity diagrams to the same

number of bits and by harmonizing the number of voxels. The sequences analyzed in this study were acquired using 1.5T and 3T MRI systems. Increasing the force of the magnetic field in magnetic nuclear resonance techniques leads to increasing the resolution of the reconstructed images, affecting extracted radiomics parameters. To overcome this issue, we resampled the number of voxels of the studied sequences to the lowest among the latter. To date, there is still no consensus in MR image standardization (43) and we deliberately chose to keep the harmonization simple for easier comparison and further development. Nevertheless, we did not alter the lesion images in any other way; notably, we did not edit the borders of the delineated lesions, following the methodology of Aerts *et al.* (20). We chose to include only the T1-weighted post-contrast MRI in this study as this modality is frequently used in current practice. It is clear that additional quantitative MRI sequences could be informative to find a combination model, which could be more powerful for our objective.

Finally, as in other similar studies, lesion segmentation was performed manually, and thus may be biased by interindividual and intraindividual variability.

One of the main challenges when applying artificial intelligence to health is the use of nonexplicit models. Indeed, unlike any regression model, which displays all its variables and coefficients, and which can be easily understood, machine-learning algorithms may appear to be obscure black boxes without any sense of the phenomenon mechanistics (44). Nevertheless, their power in image classification has been largely documented (45) and can improve patient care. Moreover, these models can be easily integrated into various treatment planning system software programs. Once the radiomics module is installed on the image processing console, the radiomics analysis is almost instantaneous; it only requires manual delineation of the lesion.

CONCLUSIONS

Our model is able to discriminate between radionecrosis and progression in an accurate, early and noninvasive way. This tool may help decision-making in cases of lesional contrast enlargement after SRT. Nevertheless, this model must be considered as a proof of concept, since, to date, its robustness has not been assessed on an external validation cohort. Our project paves the way to build bigger databases for developing a reliable signature for discriminating between these two outcomes.

SUPPLEMENTARY INFORMATION

Additional information. Comparison of our model to the method of Zhang *et al.*, based on delta-radiomics features, considering feature changes over time between two images.

Fig. S1. Heatmap illustrating the Cohen's kappa of each of the feature-selection methods (rows) and classification algorithms (columns) for the best variable selected by family of radiomic features.

Fig. S2. Correlation between each feature (variable) assessed with Pearson correlation coefficient.

ACKNOWLEDGMENTS

We thank Prof. Philippe Lambin, Arthur Jochems and Simon Keek (Maastricht University, Maastricht, The Netherlands) for fruitful discussions on radiomics and help in data interpretation. We acknowledge Dr. Joy Zhang (MD Anderson Cancer Center, Mansfield, OH) for her assistance in image preprocessing, Prof. Claude Alain Maurage (Lille University Hospital Center, Lille, France) for pathological specimen blind review and Dr. Louise Ball for language assistance. This research did not receive any specific grant from funding agencies in the public, commercial, or not-for-profit sectors.

Received: September 16, 2019; accepted: January 31, 2020; published online: March 11, 2020

REFERENCES

- Patel TR, Knisely JPS, Chiang VLS. Management of brain metastases: surgery, radiation, or both? *Hematol Oncol Clin North Am* 2012; 26:933–47.
- Nussbaum ES, Djalilian HR, Cho KH, Hall WA. Brain metastases. Histology, multiplicity, surgery, and survival. *Cancer* 1996; 78:1781–8.
- Sperduto PW, Yang TJ, Beal K, Pan H, Brown PD, Bangdiwala A, et al. Estimating survival in patients with lung cancer and brain metastases. *JAMA Oncol* 2017; 3:827–31.
- Sperduto PW, Jiang W, Brown PD, Braunstein S, Sneed P, Wattson DA, et al. Estimating survival in melanoma patients with brain metastases: An update of the graded prognostic assessment for melanoma using molecular markers (Melanoma-molGPA). *Int J Radiat Oncol Biol Phys* 2017; 99:812–6.
- Kocher M, Soffiatti R, Abacioglu U, Villa S, Fauchon F, Baumert BG, et al. Adjuvant whole-brain radiotherapy versus observation after radiosurgery or surgical resection of one to three cerebral metastases: results of the EORTC 22952-26001 Study. *J Clin Oncol* 2011; 29:134–41.
- Maclean J, Fersht N, Singhera M, Mulholland P, McKee O, Kitchen N, et al. Multi-disciplinary management for patients with oligometastases to the brain: results of a 5 year cohort study. *Radiat Oncol* 2013; 8:156.
- Soffiatti R, Abacioglu U, Baumert B, Combs SE, Kinhult S, Kros JM, et al. Diagnosis and treatment of brain metastases from solid tumors: guidelines from the European Association of Neuro-Oncology (EANO). *Neuro Oncol* 2017; 19:162–74.
- Le Rhun E, Dhermain F, Noel G, Reyns N, Carpentier A, Mandonnet E, et al. ANOCEF guidelines for the management of brain metastases. *Cancer Radiother* 2015; 19:66–71. (Article in French)
- Mehta MP, Tsao MN, Whelan TJ, Morris DE, Hayman JA, Flickinger JC, et al. The American Society for Therapeutic Radiology and Oncology (ASTRO) evidence-based review of the role of radiosurgery for brain metastases. *Int J Radiat Oncol Biol Phys* 2005; 63:37–46.
- Minniti G, D'Angelillo RM, Scaringi C, Trodella LE, Clarke E, Matteucci P, et al. Fractionated stereotactic radiosurgery for patients with brain metastases. *J Neurooncol* 2014; 117:295–301.
- Kim Y-J, Cho KH, Kim J-Y, Lim YK, Min HS, Lee SH, et al. Single-dose versus fractionated stereotactic radiotherapy for brain metastases. *Int J Radiat Oncol Biol Phys* 2011; 81:483–9.
- Minniti G, Scaringi C, Paolini S, Lanzetta G, Romano A, Cicone F, et al. Single-fraction versus multifraction (3×9 Gy) stereotactic radiosurgery for large (greater than 2 cm) brain metastases: A comparative analysis of local control and risk of radiation-induced brain necrosis. *Int J Radiat Oncol Biol Phys* 2016; 95:1142–8.
- Fokas E, Henzel M, Surber G, Kleinert G, Hamm K, Engenhart-Cabillic R. Stereotactic radiosurgery and fractionated stereotactic radiotherapy: comparison of efficacy and toxicity in 260 patients with brain metastases. *J Neurooncol* 2012; 109:91–8.
- Kohutek ZA, Yamada Y, Chan TA, Brennan CW, Tabar V, Gutin PH, et al. Long-term risk of radionecrosis and imaging changes after stereotactic radiosurgery for brain metastases. *J Neurooncol* 2015; 125:149–56.
- Telera S, Fabi A, Pace A, Vidiri A, Anelli V, Carapella CM, et al. Radionecrosis induced by stereotactic radiosurgery of brain metastases: results of surgery and outcome of disease. *J Neurooncol* 2013; 113:313–25.
- Lin NU, Lee EQ, Aoyama H, Barani IJ, Barboriak DP, Baumert BG, et al. Response assessment criteria for brain metastases: Proposal from the RANO group. *Lancet Oncol* 2015; 16:e270–8.
- Wang B, Zhao B, Zhang Y, Ge M, Zhao P, Na Sun null, et al. Absolute CBV for the differentiation of recurrence and radionecrosis of brain metastases after gamma knife radiotherapy: a comparison with relative CBV. *Clin Radiol* 2018; 73:758.e1–e7.
- Le Rhun E, Dhermain F, Vogin G, Reyns N, Metellus P. Radionecrosis after stereotactic radiotherapy for brain metastases. *Expert Rev Neurother* 2016; 16:903–14.
- Lambin P, Leijenaar RTH, Deist TM, Peerlings J, de Jong EEC, van Timmeren J, et al. Radiomics: the bridge between medical imaging and personalized medicine. *Nat Rev Clin Oncol* 2017; 14:749–62.
- Aerts HJWL, Velazquez ER, Leijenaar RTH, Parmar C, Grossmann P, Carvalho S, et al. Decoding tumour phenotype by noninvasive imaging using a quantitative radiomics approach. *Nat Commun* 2014; 5:4006.
- Cunliffe A, Armato SG, Castillo R, Pham N, Guerrero T, Al-Hallaq HA. Lung texture in serial thoracic computed tomography scans: correlation of radiomics-based features with radiation therapy dose and radiation pneumonitis development. *Int J Radiat Oncol Biol Phys* 2015; 91:1048–56.
- Zhou M, Scott J, Chaudhury B, Hall L, Goldof D, Yeom KW, et al. Radiomics in brain tumor: Image assessment, quantitative feature descriptors, and machine-learning approaches. *AJNR Am J Neuroradiol* 2017; 39:208–16.
- Zhang Z, Yang J, Ho A, Jiang W, Logan J, Wang X, et al. A predictive model for distinguishing radiation necrosis from tumour progression after gamma knife radiosurgery based on radiomic features from MR images. *Eur Radiol* 2017; 28:2255–63.
- Peng L, Parekh V, Huang P, Lin DD, Sheikh K, Baker B, et al. Distinguishing true progression from radionecrosis after stereotactic radiation therapy for brain metastases with machine learning and radiomics. *Int J Radiat Oncol Biol Phys* 2018; 102:1236–43.
- Zhang L, Fried DV, Fave XJ, Hunter LA, Yang J, Court LE. IBEX: an open infrastructure software platform to facilitate collaborative work in radiomics. *Med Phys* 2015; 42:1341–53.
- Mohri M, Rostamizadeh A, Talwalkar A. *Foundations of machine learning*. Cambridge, MA: MIT Press; 2012.
- Fernandez-Delgado M, Cernadas E, Barro S, Amorim D. Do we need hundreds of classifiers to solve real world classification problems? *J Mach Learn Res* 2014; 15:3133–81.
- Kuhn M. Building predictive models in R using the caret package. *J Stat Softw* 2008; 28. (<https://bit.ly/2SjF1Jb>)
- Sperduto PW, Kased N, Roberge D, Xu Z, Shanley R, Luo X, et al. Summary report on the graded prognostic assessment: an accurate and facile diagnosis-specific tool to estimate survival for patients with brain metastases. *J Clin Oncol* 2012; 30:419–25.
- Chuang M-T, Liu Y-S, Tsai Y-S, Chen Y-C, Wang C-K.

- Differentiating radiation-induced necrosis from recurrent brain tumor using mr perfusion and spectroscopy: A meta-analysis. *PLoS One* 2016; 11:e0141438.
31. Terakawa Y, Tsuyuguchi N, Iwai Y, Yamanaka K, Higashiyama S, Takami T, et al. Diagnostic accuracy of 11C-methionine PET for differentiation of recurrent brain tumors from radiation necrosis after radiotherapy. *J Nucl Med* 2008; 49:694–9.
 32. Galldiks N, Stoffels G, Filss CP, Piroth MD, Sabel M, Ruge MI, et al. Role of O-(2-(18)F-fluoroethyl)-L-tyrosine PET for differentiation of local recurrent brain metastasis from radiation necrosis. *J Nucl Med* 2012; 53:1367–74.
 33. Cicone F, Minniti G, Romano A, Papa A, Scaringi C, Tavanti F, et al. Accuracy of F-DOPA PET and perfusion-MRI for differentiating radionecrotic from progressive brain metastases after radiosurgery. *Eur J Nucl Med Mol Imaging* 2015; 42:103–11.
 34. Chao ST, Ahluwalia MS, Barnett GH, Stevens GHJ, Murphy ES, Stockham AL, et al. Challenges with the diagnosis and treatment of cerebral radiation necrosis. *Int J Radiat Oncol Biol Phys* 2013; 87:449–57.
 35. Stockham AL, Ahluwalia M, Reddy CA, Suh JH, Kumar A, Vogelbaum MA, et al. Results of a questionnaire regarding practice patterns for the diagnosis and treatment of intracranial radiation necrosis after SRS. *J Neurooncol* 2013; 115:469–75.
 36. Lohmann P, Stoffels G, Ceccon G, Rapp M, Sabel M, Filss CP, et al. Radiation injury vs. recurrent brain metastasis: combining textural feature radiomics analysis and standard parameters may increase 18F-FET PET accuracy without dynamic scans. *Eur Radiol* 2017; 27:2916–27.
 37. Breiman L. Bagging predictors. *Mach Learn* 1996; 24:123–40.
 38. Chang EL, Wefel JS, Hess KR, Allen PK, Lang FF, Kornguth DG, et al. Neurocognition in patients with brain metastases treated with radiosurgery or radiosurgery plus whole-brain irradiation: a randomised controlled trial. *Lancet Oncol* 2009; 10:1037–44.
 39. Sahgal A, Aoyama H, Kocher M, Neupane B, Collette S, Tago M, et al. Phase 3 trials of stereotactic radiosurgery with or without whole-brain radiation therapy for 1 to 4 brain metastases: individual patient data meta-analysis. *Int J Radiat Oncol Biol Phys* 2015; 91:710–7.
 40. Tiwari P, Prasanna P, Wolansky L, Pinho M, Cohen M, Nayate AP, et al. Computer-extracted texture features to distinguish cerebral radionecrosis from recurrent brain tumors on multi-parametric MRI: A feasibility study. *AJNR Am J Neuroradiol* 2016; 37:2231–6.
 41. Larroza A, Moratal D, Paredes-Sanchez A, Soria-Olivas E, Chust ML, Arribas LA, et al. Support vector machine classification of brain metastasis and radiation necrosis based on texture analysis in MRI. *J Magn Reson Imaging* 2015; 42:1362–8.
 42. Buchheit I, Aget H, Boisserie G, Brunet G, Bard J-J, Santoro L, et al. Procedure quality control in the framework of STIC 2004 program “Radiotherapy in Stereotaxic Conditions of Brain Metastases”. *Cancer Radiother* 2007; 11:389. (Article in French)
 43. Shinohara RT, Sweeney EM, Goldsmith J, Shiee N, Mateen FJ, Calabresi PA, et al. Statistical normalization techniques for magnetic resonance imaging. *Neuroimage Clin* 2014; 6:9–19.
 44. Castelvechi D. Can we open the black box of AI? *Nature* 2016; 538:20–3.
 45. Krizhevsky A, Sutskever I, Hinton GE. ImageNet classification with deep convolutional neural networks. In: Pereira F, Burges CJC, Bottou L, Weinberger KQ, editors. *Advances in neural information processing systems* 25. Red Hook, NY: Curran Associates, Inc.; 2012. p. 1097–105. (<https://bit.ly/2wovNEC>)

Supplementary material

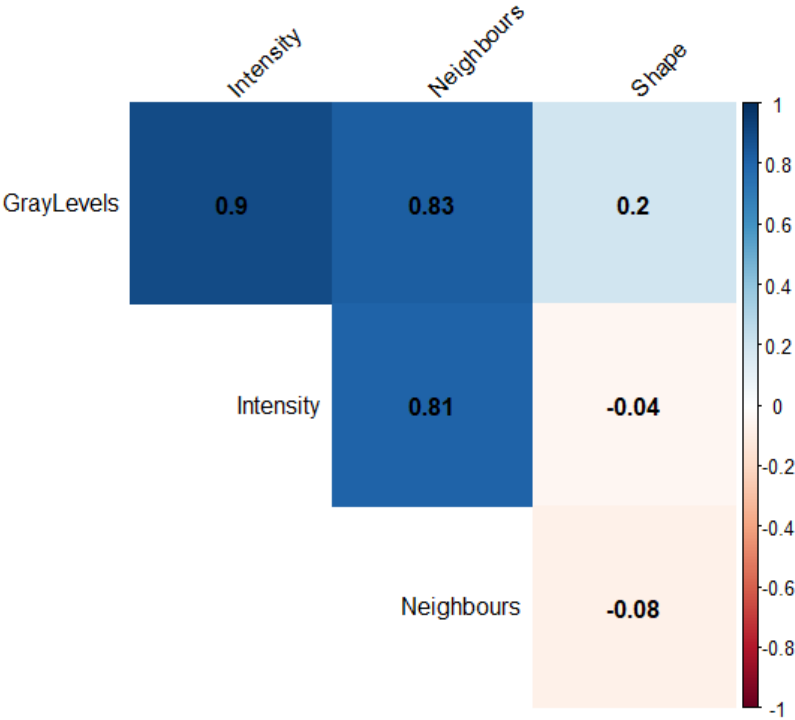
Supplementary data 1 Heatmap illustrating the Cohen's kappa of each of the feature-selection methods (rows) and classification algorithms (columns) for the best variable selected by family of radiomic features.

Abbreviations: BAG = Bagging; BST = Boosting; BY = Naïve Bayesian classifier; CHSQ = Chi-square score; DA = Discriminant analysis; DT = Decision tree; FSCR = Fisher score; GINI = Gini index; GLM = Generalized linear models; MARS = Multiple adaptive regression splines; MIM = Mutual information maximization; NN = Nearest neighbors; NNet = Neural networks; PLSR = Partial least square and principle component regression; RELF = Relief; RF = Random forests; SVM = Support vector machines; TSCR = T-score; WLCX = Wilcoxon.

	<i>DT</i>	<i>BST</i>	<i>BY</i>	<i>DA</i>	<i>BAG</i>	<i>RF</i>	<i>NNet</i>	<i>SVM</i>	<i>NN</i>	<i>PLSR</i>	<i>GLM</i>	<i>MARS</i>
<i>CHSQ</i>	0.08	0.26	0.11	0.22	0.68	0.44	0.31	0.09	-0.03	0.00	0.14	-0.10
<i>FSCR</i>	0.06	-0.05	0.05	-0.15	0.04	0.17	0.17	0.04	-0.25	0.00	-0.19	-0.10
<i>GINI</i>	-0.05	0.00	-0.32	-0.44	-0.17	-0.19	-0.16	-0.28	-0.10	0.00	-0.48	0.00
<i>MIM</i>	-0.14	-0.10	-0.22	-0.30	0.20	0.14	-0.30	-0.52	-0.21	0.00	-0.33	0.00
<i>RELF</i>	-0.16	-0.28	-0.18	0.13	0.04	0.16	0.32	0.05	0.12	0.00	0.20	-0.10
<i>TSCR</i>	0.48	0.57	0.32	0.17	0.47	0.47	0.15	0.29	0.15	0.00	0.24	0.51
<i>WLCX</i>	0.00	0.00	-0.07	-0.52	-0.17	-0.36	-0.24	-0.10	-0.18	0.00	-0.52	0.00

Abbreviations: BAG = Bagging; BST = Boosting; BY = Naïve Bayesian classifier; CHSQ = Chi-square score; DA = Discriminant analysis; DT = Decision tree; FSCR = Fisher score; GINI = Gini index; GLM = Generalized linear models; MARS = Multiple adaptive regression splines; MIM = Mutual information maximization; NN = Nearest neighbors; NNet = Neural networks; PLSR = Partial least square and principle component regression; RELF = Relief; RF = Random forests; SVM = Support vector machines; TSCR = T-score; WLCX = Wilcoxon.

Supplementary data 2 Correlation between each feature (variable) assessed with Pearson correlation coefficient.



Appendix : Delta-radiomics signature.

Delta-radiomics signature. We applied the model based on delta-radiomics features as defined by Zhang et al. on 14 patients.(Zhang et al., 2017) Using IBEX, we extracted four variables (energy and variance from direct intensity features, and high grey-level run emphasis and short-run high grey-level emphasis from a 2.5D grey-level run-length matrix) from two consecutive follow-up T1-weighted MRIs. The first image set was the one used in our model, and the second was the one that was available immediately after. Delta-radiomics features were normalized in order to take into account the diversity in time differences between the two MRI. Next, we input these variables into a RUSBoost algorithm implemented on R, using the RUSBoost package(Seiffert et al., 2010) tuned with 150 learners and proportions of RN and P in each iteration similar to the cohort's (respectively 40% and 60%). We were not able to add the HOG skewness feature extracted from T2-weighted MRI to the model as this sequence is not routinely performed in our center and was available for very few patients. Performance comparison was assessed using a Chi-square test.

Zhang et al.(Zhang et al., 2017) were able to show that a combination of several radiomic textural features (direct intensity and intensity histogram, grey-level co-occurrence matrix, grey-level run-length matrix, geometric shape, neighborhood grey-tone difference matrix, histogram of oriented gradients) from T1-weighted postcontrast and T2-weighted MRI scans had great potential for the best prediction for distinguishing RN from P in patients treated with Gamma Knife radiosurgery (AUC=0.73), with a better accuracy prediction for P. Our model did not take into account feature changes over time between two images (delta-radiomics). We applied their model to a cohort of 14 patients (6 RN and 8 P) in our study (details in Table 2) with an available valid T1-weighted postcontrast MRI. Despite a 100% P prediction accuracy, this model could not predict any of the RN we documented (AUC=0.5). These results suggest that our model is better for RN prediction and is equally good at predicting P (Chi-square test, $p = 0.02$ and $p = 0.30$, respectively). Nevertheless, despite the T2-extracted feature being the less informative, we were not able to include it in this validation as the sequences were available for very few patients. Indeed, this sequence is not routinely performed in our centers; T2-FLAIR sequences are preferred. Moreover, we did not use the same analytical software and the small sample size of our cohort may have led to overfitting of our model. Thus, these results must be taken with caution

6. Discussion and conclusion

The differential diagnosis between RN and TR after SRT of BM is a real daily challenge in clinical practice. Indeed, distinguish these 2 entities is of major importance in patients' treatment because their management differs radically. Delay or even misdiagnosis can dramatically impact the patient's quality of life and sometimes even survival. Our objective was to investigate the radiomics methodology in the early differential diagnosis of RN versus TR after SRT of brain oligometastases.

This original pilot study demonstrates that our radiomics model can differentiate RN from TR in an accurate, early and non-invasive way. Indeed, the prediction of our model, based on the very first lesion change on follow-up MRI, allows a very early diagnosis in the course of the disease. For example, we were able to correctly predict the diagnosis of 2 progressing patients several weeks to several months before surgery. These results, like those already described in the literature, are very encouraging. (87–89) Nevertheless, the interpretation of these conclusions must remain cautious, as this study is a proof of concept.

The study design and the results provide food for thought on how to improve the performance and accuracy of our radiomics method. On the one hand, it is important to ensure the homogeneity of the images included in the analysis. Image pre-processing methods are probably insufficient to overcome too much image heterogeneity. Therefore, it is essential to set up a standardisation of MRI image acquisition protocols to obtain homogeneous and reproducible data, facilitate algorithm learning and improve the algorithm's prediction. On the other hand, it would also be interesting to use other MRI sequences (T2, perfusion) or amino acid PET imaging, which are relevant in the distinction between RN and TR. Combining several sequences and different imaging modalities would improve the diagnostic performance of our model and lead to more robust results. In order to confirm our results, a collaboration with Prof. Lambin's team (Maastrro Clinic, Maastricht) is in progress. This collaboration would allow us to validate our model on the hundreds of RN and TR MRI studies from their database.

In conclusion, in case of the discovery of lesion progression on a standard follow-up MRI after SRT for BM, our radiomics method could, in the long term, help in discriminating between RN and TR, the MRI-twins. Our algorithm could easily be integrated into TPS software to assist radiation oncologists in early decision making. Early and accurate diagnosis of RT-toxicity is very beneficial for patient. However, no toxicity would be even better than an early-detected toxicity. Following the ancient saying of Hippocrates: 'prevention is better than cure', the following section of this manuscript will tackle the prevention of late RT-induced adverse reactions.

**Molecular and cellular
approaches for
radiotherapy toxicity
prediction**

7. Introduction

7.1. RNA: A snapshot of the cell (90)

7.1.1. RNA overview: a broad and diverse family of biomolecules

The transcriptome is defined as the complete set of transcripts in a cell, and their quantity, for a specific developmental stage or physiological condition. It is dynamic and a good representative of the cellular state. There are different types of expressed RNAs in human cells as shown in Figure 4.

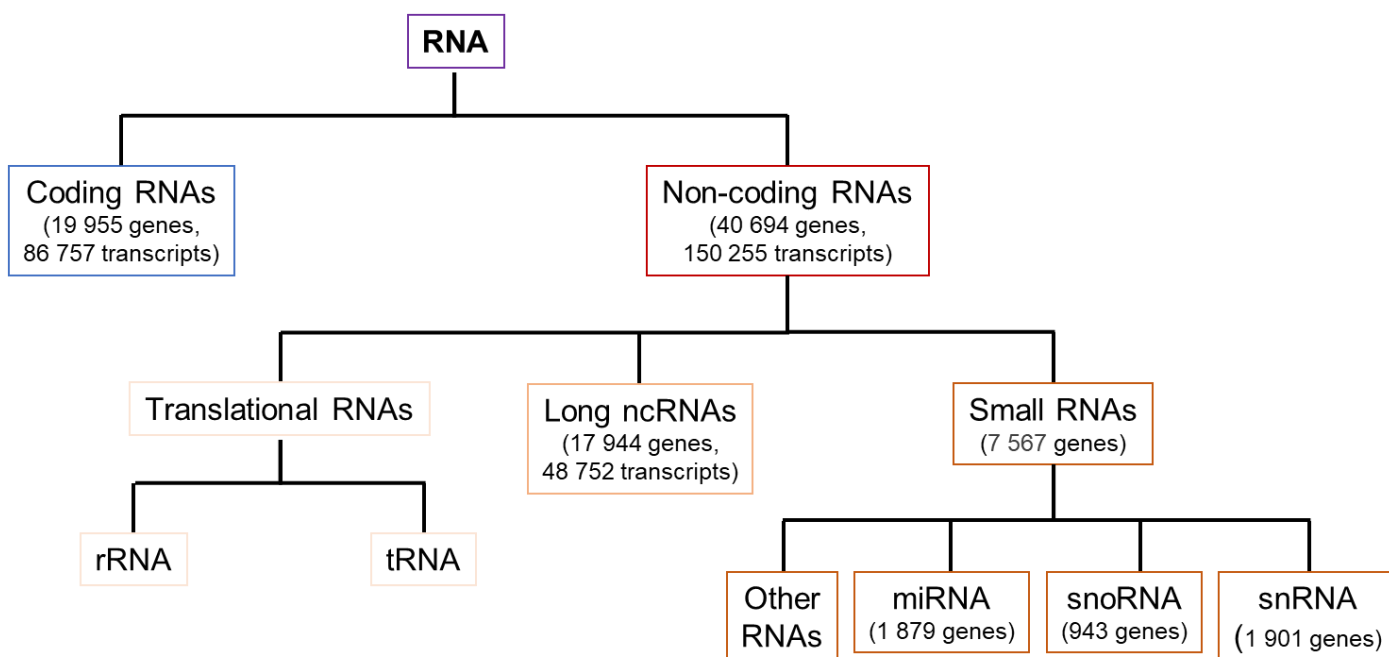


Figure 4. The different types of RNA, according to data from GENCODE GRCh38.p13 (May 2021) (91)

7.1.1.1. Coding RNA : Messenger RNA (mRNA)

Pre-mRNA are synthesised by RNA polymerase II from a DNA template. These single-stranded molecules have specific sequences such as exons separated by introns, a reading frame, splicing regulatory sequences, export sequences, stability regulation sequences, etc. During their maturation, a cap (7-methyl-guanosine) is added at the 5' end at the beginning of transcription, then introns and alternative exons are removed (splicing), along with the addition of a polyadenylation tail at the 3' end. The mature form of these transcripts, called messenger RNA, is exported to the cytoplasm to be translated into protein with the help of transfer RNAs (tRNAs) and ribosomes (rRNAs).

7.1.1.2. Non-coding RNA (ncRNA)

ncRNAs are also transcribed RNA polymerase II. These RNAs that have little or no ability to code for proteins. (92) They are divided into two families based on size. Long ncRNAs (lncRNAs) exceed 200 nucleotides whereas small ncRNAs are smaller than 200 nucleotides.

As transcribed by the same polymerase as mRNAs, most characterised lncRNAs share some properties of mRNAs. For example, they are produced as primary transcripts with multi-exonic structure, are polyadenylated and have a cap at their 5' end. LncRNAs are also defined by their relative location with respect to the nearest coding gene: they are said to be either intragenic if they partially overlap, in sense or antisense direction, with the sequences of a coding gene, or intergenic, if located between two coding genes. Although the study of lncRNAs functions is still in its infancy, an important role for these RNAs in the regulation of gene expression is already emerging, in particular through chromatin remodelling, direct regulation of transcription, alternative splicing or translation. Their effects may be mediated by their secondary structure, their complementarity to specific sequences or their ability to recruit partner proteins or RNAs (sponge). (93)

Small ncRNAs are divided into several functional families. MicroRNAs bind to a target mRNA in the cytoplasm to repress its translation or cause its degradation. Ribosomal RNAs (rRNAs) are components of ribosomes. Small nuclear RNAs (snRNAs) are the RNA components of the spliceosome and thus participate in the splicing of primary transcripts. Small nucleolar RNAs (snoRNAs) participate in the maturation of ribosomes and the spliceosome by introducing post-transcriptional modifications within rRNAs and snRNAs. The tRNAs, through their secondary structure, and with the help of the large subunit of the ribosome, participate in the translation of transcripts into proteins.

7.1.2. RNA Splicing: how to go from 60 000 genes to 240 000 transcripts?

During their maturation, the introns of primary transcripts are excised by the splicing process carried out by a nucleoprotein macrocomplex, the spliceosome. This excision is enabled by the recognition of specific sequences at the exon/intron junctions called splice sites. These splice sites are called donor or acceptor sites depending on whether they are located 5' or 3' from the intron to be excised. As shown in Figure 5, the donor site (5' splice site) is composed of a terminal GU dinucleotide. The acceptor site (3' splice site) has three particularly conserved sequence elements: a branch box with an adenine residue (branchpoint), a polypyrimidine sequence, and a terminal AG dinucleotide.

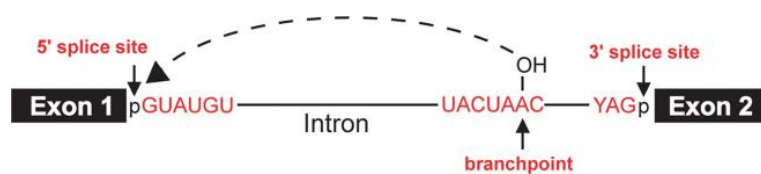


Figure 5. Organisation of an intron between two exons, from Chen & Cheng (2012) (94)

The aforementioned sequences will be recognised by five small nuclear ribonucleoproteins (snRNPs) that constitute the spliceosome: U1, U2, U4, U5 and U6. The spliceosome catalyses the two transesterification steps leading to intron excision, as illustrated in Figure 6. In the first step, the 2'-OH group of the conserved adenine of the branch box will attack the phosphate of the donor site. This leads to a cleavage of the 5' end of the intron being excised, and a concomitant ligation of the 5' end of the intron to the 2'-hydroxyl group of the branch point, forming a lariat. The second transesterification step consists of an attack of the 3'-OH group of the cleaved exon on the phosphate at the 3' end of the intron. This second step allows the two exons to be linked together and releases the intron still in the lariat configuration.

In humans, splicing regulatory sequences can promote or inhibit splicing. They are found in introns and exons. Their use can lead to the splicing of some exons, known as alternative. This mechanism allows the production of a very large diversity of mRNAs or ncRNAs from primary transcripts and contributes to the diversity of the proteome and transcriptome found in our cells. Alternative splicing plays a crucial role in the life of the cell, notably in growth and differentiation, but also in its adaptation to its environment, and in particular in the response to stress. (95)

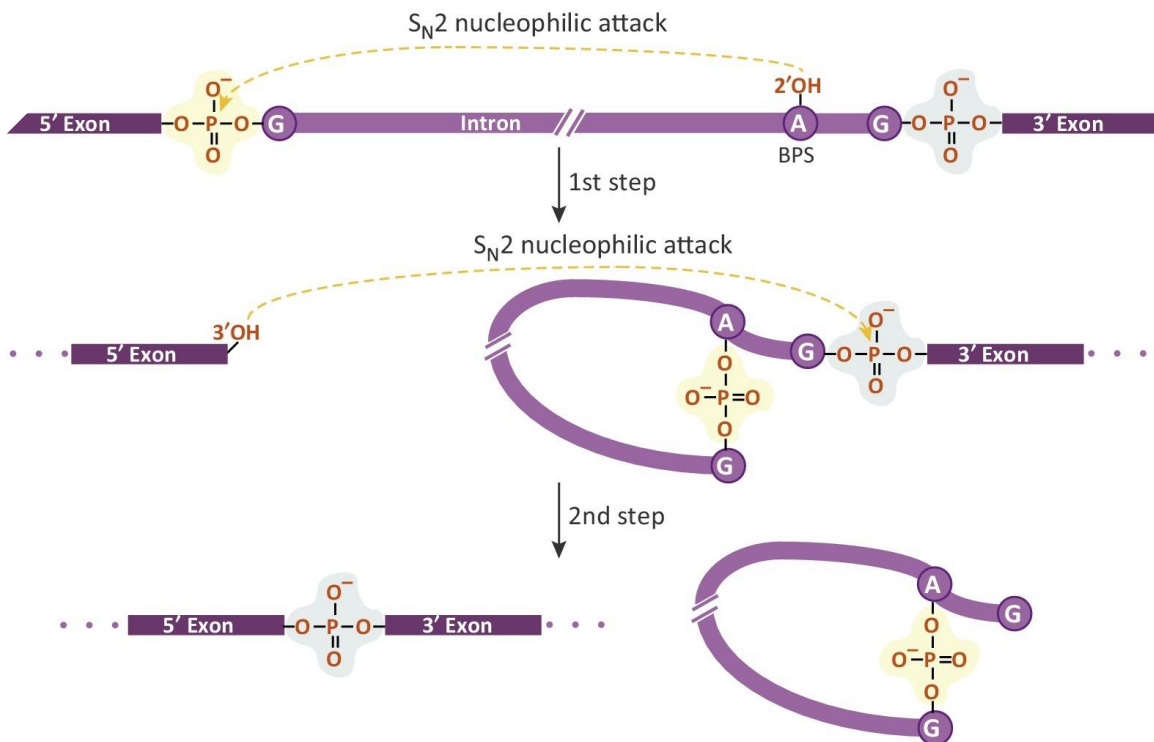


Figure 6. Simplified splicing mechanism, from Papasaikas et Valcárcel (2016) (96)

7.1.3. RNA and DNA damage

The transcriptome is dynamic and adapts swiftly when the cell is stimulated, such as in case of DNA damage after exposition to IR, as illustrated in Figure 7. IR impacts RNA metabolism at several levels.

IR regulates gene expression in a dose-dependent manner, inducing the differential expression of genes ranging from regulatory mechanisms such as signal transduction-associated genes for small doses, to apoptosis-related genes for higher doses. (97) Several lncRNAs have been implicated in the transcriptional regulation of cell cycle genes during the DDR such as ncRNA_{CCND1}. ncRNA_{CCND1}, through the recruitment of FUS/TLS – an RNA binding protein involved in transcription, RNA processing, and DNA repair – inhibited CBP acetyltransferase activity and therefore repressed the transcription of the cyclin D1 gene. (98)

On a translational level, microarray analysis of polysome-bound versus total RNA showed that, both in human astrocytes and brain tumour cells, 10 times more genes were found regulated through their recruitment to polysomes compared to those transcriptionally modulated. Interestingly, some of these genes were involved in transcription regulation and RNA metabolism, even after an irradiation of 7 Gy. (99)

Regarding RNA splicing, Forrester *et al.* used exon arrays to evaluate IR-induced splicing changes induced. They characterised the use of alternative promoters in GADD45G and VWCE transcription. (100) The activity of splicing factors is regulated during the DNA damage response at the level of transcription, splicing, post-translational modification, subcellular localization, and protein–protein interaction. These factors are greatly reviewed in (101) As it is not the main focus of this thesis, I will only mention the IR-modulation of various SRSF and hnRNP proteins, which are of utmost importance in the splicing mechanism, suggesting a global splicing mechanism yet to be deciphered.

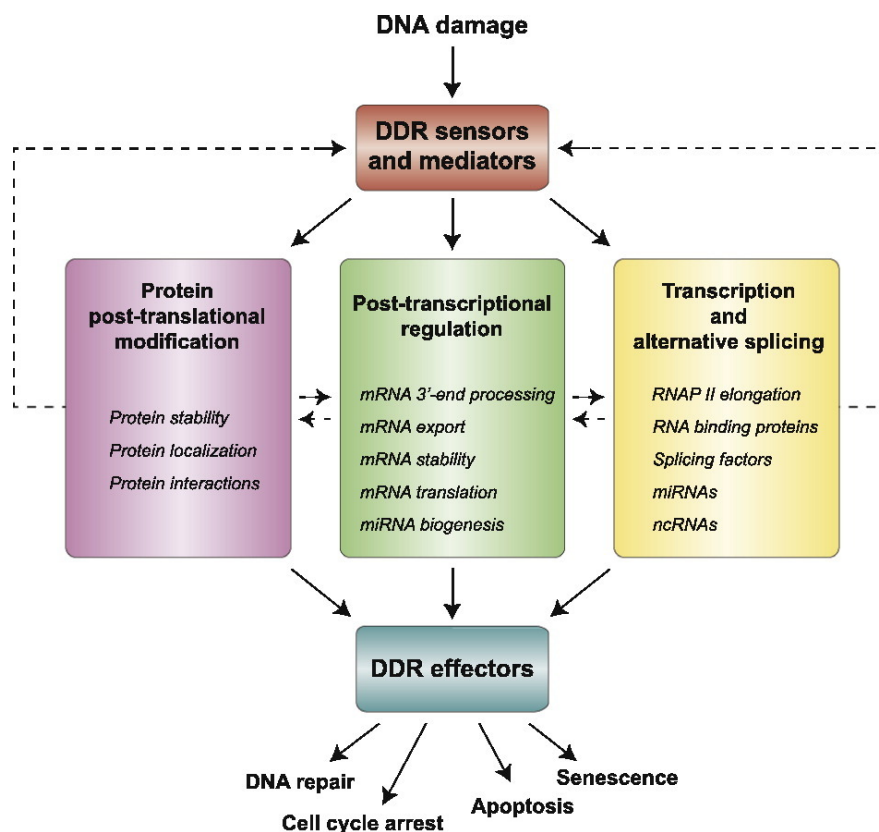


Figure 7. RNA response to DNA damage. RNA metabolism is affected in several ways, from transcription to post-transcriptional regulation, from *Giono et al.* (2016) (102)

7.1.4. RNA: your ideal biomarker

There is a major challenge in looking into the transcriptome of a cell. Unlike the genome, it is a dynamic indicator that evolves swiftly in response to changes in the cell's environment, both in response to various stresses and to the early and late development of pathologies. The transcriptome carries more information than the proteome, since no more than 4% of the transcribed genome is translated into proteins. This type of study made it possible to demonstrate, among other things, the role of ANRIL, a lncRNA, in the development of atherosclerosis (103,104), as well as the role of miR-155 in inflammatory diseases. (105,106) Moreover, RNAs have the unique feature of being present in all biological fluids, which allows non-invasive analysis of their expression. It would be interesting to use this approach in the prediction of RT toxicities.

7.2. Radiation-induced skin fibrosis: the unpredictable toxicity of radiotherapy for breast cancer

Female breast cancer is the most prevalent cancer, with an estimated 2.3 million new cases worldwide responsible for 6.9% of cancer deaths. (3) Eighty percent of newly diagnosed non-metastatic breast cancers or ductal carcinoma in situ are treated with radiotherapy (RT), especially in a conservative approach. (17,107) However, more than 80% of patients receiving RT on breast will experience some degree of skin toxicity from mild reversible burns to late and severe adverse events such as secondary malignancies. (108,109). RT toxicities are mainly explained by deterministic rather than stochastic consequences of irradiation. (110) In this work, we will focus on radiation-induced skin fibrosis (RISF), which even with good dose management, is estimated to occur in up to 18% of breast cancer patients 3 years post-RT (28). The following paragraphs will review the clinical, tissular, cellular and molecular aspects of RISF. (111,112)

7.2.1. Clinical aspect

RISF is a late adverse event of the skin developed from 6 months after RT, in an unpredictable manner and without therapeutic deviation. Its occurrence is correlated with total dose and delivered dose per session in terms of frequency and severity. Fibrotic lesions are limited to the irradiated volume. They have a polymorphic appearance and are manifested, in increasing order of severity, by less elastic irradiated skin, retractile sclerosis (Figure 8), and finally, spontaneous ulceration. These superficial aspects may be associated with fibronectin manifestations of the underlying tissues.



Figure 8. Patient with RISF on the left breast, following RT for breast cancer.

The spontaneous evolution of RISF occurs in stages of progressive worsening over several years, leading to an irreversible sequela. This evolution can be summarised in 3 phases:

- 1) An initial pre-fibrotic phase, which occurs during the 6 to 24 months following irradiation. Often asymptomatic, it may show signs of chronic aspecific and localised inflammation such as local oedema, redness, pain, heat and itching.
- 2) A phase of organised fibrous sequelae, where signs of local inflammation have disappeared. Remodelling of underlying tissues occurs: epithelia thin, underlying tissues thicken and indurate, and telangiectasias appear.
- 3) A late phase of fibrotic disease, where the connective swelling is replaced by a retractile atrophy of stone-like consistency, with progressive destruction of the healthy tissue.

7.2.2. Tissular aspect

The histological aspects of RISF vary according to the progression of the disease. They mainly concern the dermis, the intermediate connective layer of the skin. As its clinical presentation, the tissue presentation can be divided into three phases:

- 1) An initial pre-fibrotic phase characterised by chronic aspecific inflammation in which endothelial cells appear to play a crucial role. The inflammation is classically characterised by increased vascular permeability, leading to extravasation of serum proteins resulting in oedema. Collagen and fibronectin degradation fragments attract local connective, epithelial and blood cells. The endothelium is destroyed, activating connective cells, especially dermal fibroblasts, by exposure to inflammatory stimuli.
- 2) A phase of organised fibrous sequelae where the fibrotic tissue is mainly composed of fibroblasts that transdifferentiate into myofibroblasts producing an excessively rich in collagens extracellular matrix. Immune cells are recruited to the tissue and act as enhancers. The formed fibrosis is characterised by an alternance of areas of active fibrosis (composed of a high density of hyperproliferative myofibroblasts and an inorganised layer of extracellular matrix), with areas of paucicellular fibrosis (composed of senescent fibroblasts of low proliferation and longitudinally oriented collagen fibres clusters organised in dense and regular trabeculae). Thus, the densification of the fibrotic tissue is established by successive remodelling of the deposited extracellular matrix. Collagen renewal is dependent on cells that secrete degradation enzymes such as macrophages and fibroblasts. Growth factors such as PDGF or TGF β amplify this phenomenon. Sequestered in the extracellular matrix, they are then released locally from matrix receptors and allow persistent local stimulation.
- 3) In the advanced stage, the tissues are friable, with little vascularity and few fibroblasts. In this remodelled fibrotic tissue, the matrix increases in density and stability. However, the scarred irradiated zone remains fragile, subject to late inflammatory relapses reactivated by any physicochemical trauma.

The vicious circle of permanent remodelling of fibrous tissue reflects the dysregulation of fibroblast proliferation, and the loss of homeostasis between synthesis and degradation of extracellular matrix. It is clearly at odds with the clinical perception of fixedness of RISF.

7.2.3. Cellular aspect

Physiologically, the fibroblast is the keystone of the dermis. It has a variable morphology with its degree of activity and its different stages of differentiation: from the quiescent fibrocyte found in mature connective tissue to the hyperactive myofibroblast. The fibroblast is a secretory cell that manufactures the constituents of the extracellular matrix (collagen, fibronectin, etc.) and the degradation enzymes (proteinases, collagenases, etc.), thus ensuring the maintenance of the extracellular matrix by rigorous homeostasis between synthesis and degradation. The fibroblast can produce growth factors (TGF β , interleukins, PDGF, and so on) and prostaglandins. Thus, it plays a regulatory role for neighbouring mesenchymal cells.

Under the influence of an inflammatory reaction or wound healing, fibroblasts transdifferentiate into myofibroblasts with contractile and secretory properties. In a physiological healing process, such as after irradiation, myofibroblasts disappear after filling the wound and the inflammation disappearance. However, in RISF, they persist and remain present in the late stages of constituted fibrosis (Figure 9). They show increased proliferation and altered matrix secretion associated with an overall decrease in matrix metalloproteinases. This process corresponds to the histological description of active hypercellularised fibrosis patches, and to the clinical observation of radiation-induced fibrous swellings.

The fate of irradiated fibrocytes is thought to be accelerated senescence followed by premature cell death. The progressive cell depletion associated with incomplete cell replacement would correspond to the patches of paucicellular fibrosis described at the tissular level.

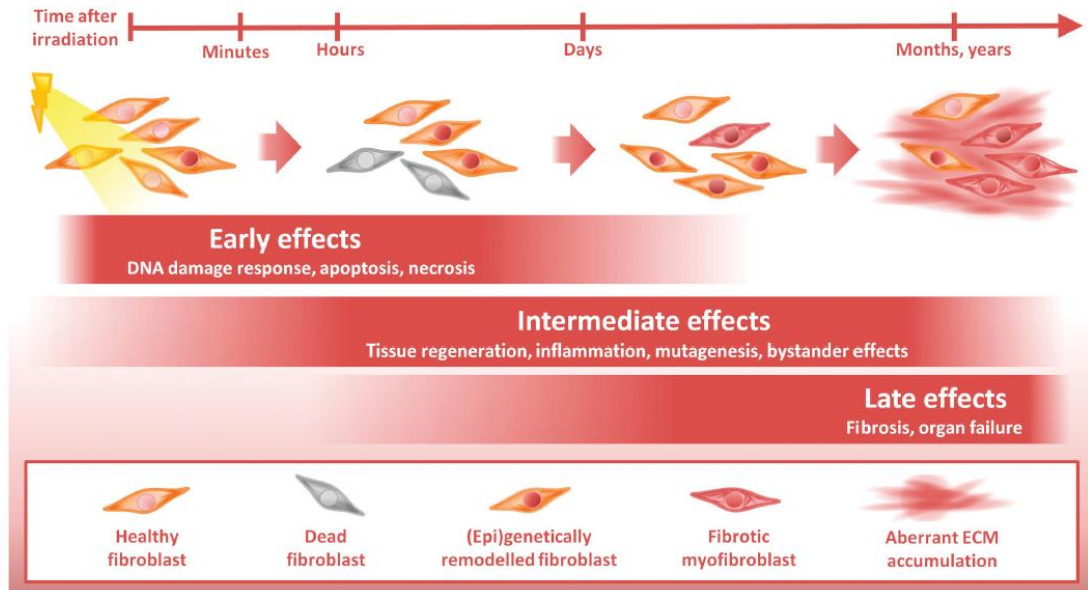


Figure 9. Short- and long-term effects of the radiation response at the cellular and tissue levels, from Weigel *et al.* (2016)

7.2.4. Molecular aspects

7.2.4.1. Genetic and protein regulations

Persistent self-sustaining cell activations characterise fibrosis. Physiological healing is interrupted by termination signals when the skin lesion is repaired. Thus, myofibroblasts and inflammatory cells disappear. In RISF, this feedback does not occur (Figure 10) due to chronic activation through the continuous production of pro-inflammatory mediators such as growth factors and reactive oxygen species.

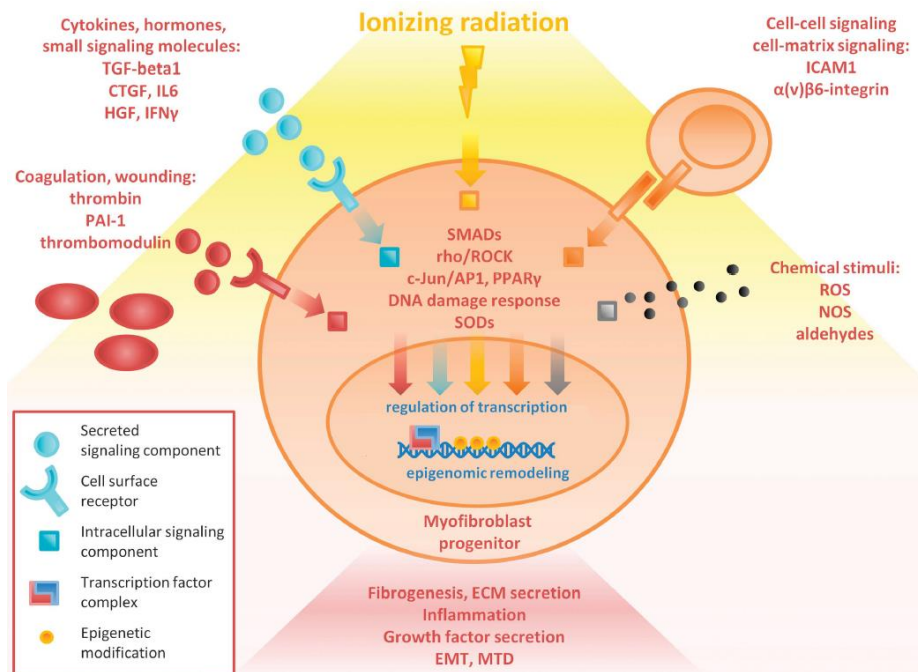


Figure 10. Cellular and molecular signals involved in transdifferentiation of myofibroblasts and fibrogenesis upon radiation exposure, from Weigel *et al.* (2016) (113)

As previously described, the interaction of IR with the tissues generates ROS at the origin of the initial inflammatory outbreak. During the subsequent serum exudation, polynuclear cells and macrophages are stimulated via the contact with collagen degradation products, thus releasing further waves of pro-inflammatory cytokines. The process is then self-sustaining in a chronic inflammatory area where homeostasis is disrupted. Any further oxidative stress may increase the production of pro-inflammatory molecules, contributing to the extension and densification of fibrosis. In the extracellular environment, oxidative stress mediates matrix degradation, leukocyte chemotaxis and phagocytosis, and fibroblast activation. In the intracellular environment, the adaptive reactions secondary to oxidative stress involve the activation of genes and proteins specific to the stress response, which trigger a series of processes such as DNA repair, cell cycle arrest or the secretion of growth factors (TNF α , PDGF, IL-1). Finally, superoxide ions O $_2^{\cdot-}$ can interfere with biological membranes through lipid peroxidation inducing gene modulations via transcription factors sensitive to the redox state of the cell such as NF-kB.

Thus, the regulation of the fibrotic process occurs at several levels: chemotaxis, fibroblast proliferation, metabolism and secretion of extracellular matrix constituents. Indeed, the expression and activity of many growth factors are modified, exerting a direct or indirect role in the formation and maintenance of the fibrotic process. Among these factors, TGF β is now considered to be the cytokine mainly involved in the fibrotic process.

7.2.4.2. Focus on the role of TGFβ1 in RISF (112,114)

TGFβ1 is a growth factor in the form of a large latent complex whose activation is under the control of proteases. It binds to specific membrane receptors TβRI and TβRII. Further propagation of the signal within the cell is mediated by the direct substrates of these receptors, the SMAD proteins, which are transcription factors that enable the active complexes formed to move from the cytoplasm to the nucleus.

TGFβ1 is involved in epithelial and endothelial cell proliferation (G1-S phase stalling), apoptosis, activation of fibroblasts into myofibroblasts, synthesis of extracellular matrix components, and expression of integrins that play a major role in cell-matrix interactions.

TGFβ1 is the mastermind of the fibrotic process. It is primarily responsible for the initiation, development and maintenance of fibrosis such as atherosclerosis, kidney, liver or lung fibrosis, and of course RISF. During acute inflammation, TGFβ secreted by platelets can initiate a series of events, including the recruitment and activation of macrophages, which in turn secrete chemotactic and mitogenic factors for fibroblasts. In the extension and chronic phase of fibrosis, circulating TGFβ and TGFβ synthesised by the myofibroblasts themselves, contribute to the self-maintenance of the fibrotic process.

7.2.4.3. Epigenetic regulations (113)

Epigenetic regulations of RISF are discussed in the following review.

7.2.5. RISF treatments

Current RISF curative or preventive treatments are limited, with most therapeutic strategies showing only moderate benefits in high level-of-proof clinical trials. (115,116) Therefore, prevention by the identification of accurate predictive markers may be a key to protect at-risk patients.

7.3. Molecular determinants of skin radiation-induced skin fibrosis

The following section is a manuscript in preparation for submission in *RNA Biology*.

7.3.1. Introduction

7.3.1.1. Radiotherapy (RT) as a treatment for breast cancer and radiation toxicities

Female breast cancer is the most prevalent cancer, with an estimated 2.3 million new cases worldwide being responsible for 6.9% of cancer deaths. (3) 80% of newly diagnosed non-metastatic breast cancers or ductal carcinoma in situ are treated with radiotherapy (RT), especially in a conservative approach. (17,107) However, more than 80% of patients receiving RT on breast will experience some degree of skin toxicity, which includes early frequent and reversible erythema and dry desquamation, and/or late and debilitating fibrosis or secondary cancers. (108,109). RT toxicities are mainly explained by deterministic rather than stochastic consequences of irradiation. (110) Even with a good dose management, 3 years after being treated with RT, radiation-induced skin fibrosis (RISF) is estimated to occur in up to 18% of breast cancer patients (28). Furthermore, current RISF curative or preventive treatments are limited, with most therapeutic strategies showing only minimal benefit in high level-of-proof clinical trials. (115,116) Therefore, prevention may be a key to protect at-risk patients. In addition to well-known comorbidities or RT-related factors, the propensity to develop such toxicities is linked to individual radiosensitivity (iRS), defined as any constitutional enhanced tissue or cell reaction following exposure to ionizing radiations compared to that of the majority of individuals. (117) Underlying mechanism of iRS are yet to be fully deciphered. In this review, we provide an overview of the molecular determinants of iRS involved in the development of RISF. We summarise the implication of SNPs and haplotypes, stressing the importance of ethnically diverse cohorts. Then, we outline the association of gene expression and alternative splicing of skin fibroblasts in the onset of RISF. Lastly, we cover the recent advances in the epigenetics of RISF.

7.3.1.2. Skin radiation induced fibrosis

RISF is a late adverse event developed from 6 months after RT in an unpredictable manner and without therapeutic deviation. There is a correlation with total dose and dose/session in terms of frequency and severity. At the tissue level, RISF is characterised by connective tissue hyperplasia resulting in excess extracellular matrix, parenchymal impoverishment with excess production of myofibroblasts, and reduced vascularisation. (109) This pathogenic state is reached after a succession of key steps resembling a disrupted healing process. (118) First, irradiation initiate an inflammatory response, cytokine production, and subsequent recruitment of innate immune cells. A conjugated response from neutrophils, monocytes and lymphocytes will increase this inflammatory response by producing pro-inflammatory factors such as interleukin (IL)-1, IL-6, PDGF, TGF- α but especially TGF- β , which is strongly involved in the

development of RISF. (114,118) The secretion of PDGF will induce the recruitment of fibroblasts which will transdifferentiate into myofibroblasts under the action of the TGF- β . (109,119,120) The acquisition of this phenotype, together with the presence of TGF- β , will lead to excess production of collagen, fibronectin, and proteoglycans by the myofibroblasts, disrupting tissue integrity. These cells have a contractile capacity, notably through the production of α -Smooth muscle actin, which contributes to skin remodelling. (114) This process is crucial to the initial response to radiation but fails to end in radiosensitive patients; hence creating a self-sustained inflammation and fibroblast activation. Weigel *et al.* suggested that epigenetic marks, such as miRNA expression and histone modification play a role in fibrosis development notably by being long-term determinants of gene expression, allowing the cells to perpetuate fibrogenesis well after irradiation. (113) The association of all aforementioned mechanisms will lead to a clinically injured breast skin, displaying a loss of elasticity and a severe induration sometimes to the point of limitation in arm movement (121,122). Clinical and aesthetical symptoms are doubled by the psychological burden of bearing a life-long painful scar of a cancer. (123) In this review, we will define radiosensitive patients as patients developing RISF, and radioresistant patients as RISF-free patients after RT for breast cancer.

7.3.2. Polymorphisms and haplotypes

Genome-wide association studies have been widely used to identify associations between commonly occurring variations in DNA sequence, such as single nucleotide polymorphisms (SNP) and human traits.(124) A few single nucleotide polymorphisms (SNP) have been linked to RISF (Table 2), most of them belonging to the DNA damage response (DDR) pathway. ATM, a central kinase in the initiation of DDR (125), was particularly investigated. Ho *et al.* have demonstrated that the presence of any ATM variant in patients treated with RT for breast cancer led to a greater risk of developing RISF.(126) The widely studied missense ATM SNP rs1801516 (c.5557G > A, p.Asp1853Asn) was evaluated in over 5000 breast cancer patients (127) and is the most promising SNP candidate in predicting RISF. It was also recently associated with increased overall toxicity after RT for prostate cancer.(128) Interestingly, ATM IVS22-77 T>C/IVS48 + 238 C>G (129) and XRCC3 rs861539 (130) SNPs confer their respectively radioprotective and radiosensitising effect only at heterozygous state. To our knowledge, only these 8 SNPs were significantly associated with the development of RISF, most probably because of the lack of availability of cohorts big enough to reach the appropriate power. To overcome this obstacle, Zschenker *et al.* proposed a composite risk score based on 6 risk alleles : rs1801516 (ATM, codon 158), rs1695 (GSTP1, codon 105), rs4880 (SOD2, codon 16), rs1800469 (TGFB1, position -509), rs13181 (XPD, codon 751), and rs25487 (XRCC1, codon 399).(131) Although, no individual SNP reached significance, they evidenced

that the more risk allele the patient was bearing, the greater were the odds of developing RISF (2.09 per risk allele, CI_{95%} = [1.32,3.55], p = 0.0005).

Mitochondrial haplogroups are also associated with radiosensitivity. Terrazzino *et al.* demonstrated the radioprotective effect of mitochondrial haplogroup H (132), which is mostly represented in Indo-European populations (133). In contrast, patients bearing haplogroups J and U, mostly Indo-Europeans, are at higher risk of developing RISF. (132) As ethnicity rises as potential risk factor, there is an high interest in screening amongst different ethnic group, as highlighted in Ho *et al.*(126)

Gene	Reference SNP	OR [CI _{95%}]	Localisation	Type of mutation	Ref.
ATM	rs1801516	1.23 [1, 1.51] 1.27 [1.02, 1.58]	Exonic	Missense (D>N)	(127,134)
ATM	IVS22-77 T>C	0.45 [0.24, 0.85]	Intronic	-	(129)
ATM	IVS48+238 C>G	0.50 [0.27, 0.94]	Intronic	-	(129)
DNMT1	rs2228611	0.26 [0.10, 0.71]	Exonic	Synonymous	(135)
TGFB1	rs1800469	- 3.40 [1.38, 8.40]	Upstream	-	(136,137)
TGFB1	rs1800470	- 2.37 [0.99, 5.60]	Exonic	Missense (P>L)	(136,137)
XRCC1	rs1799782 + rs25487	4.33 [1.24, 15.12]	Exonic	Missense (R>W + Q>R)	(138)
XRCC3	rs861539	1.17 [1.09, 1.26]	Exonic	Missense (T>M)	(130)

Table 2. Single nucleotide polymorphisms linked to the development of skin radiation-induced fibrosis.

7.3.2.1. Gene expression and alternative splicing: an invisible burden that matters

The interest in the predictive power of skin transcriptome emerged in the early 2000's, when Quarmby *et al.* studied the differential expression of cytokines between radiosensitive and radioresistant breast cancer patients. (139) As fibrosis is mainly defined as an excess of collagen in the extracellular matrix, they decided to study tissue-specific collagen producing cells which are skin fibroblasts. They highlighted an overexpression of PDGFB in fibroblasts from radiosensitive patients, whose homodimers stimulate fibroblast collagen production, and whose overexpression in tissues has been implicated in the development of fibrosis. (140) As RISF develops only on irradiated skin, few years later Alsner *et al.* hypothesized that iRS determinants would lie in an impaired radiation response of skin fibroblasts (Table 3). (141,142) These studies were the first to identify an *in vitro* transcriptomic signature for iRS in RISF. The pointed predictive genes were associated with cellular functions such as TGF β pathway, particularly extracellular matrix remodelling, apoptosis, proliferation, and reactive oxygen species scavenging (142). These *in vitro* findings paved the way to predictive tests for personalized medicine. (143,144) However, these tests failed to detect patients at risk, but they efficiently identified patients displaying a resistance to radiation-induced fibrosis. (143,144) This limitation was faced by Azria *et al.*, who were trying to predict RISF using radiation-induced CD8 T-lymphocyte apoptosis. (145,146) Thereby, since radiation-induced response did not appear relevant anymore for patients at-risk discrimination, Forrester *et al.* proposed to unravel iRS by studying the basal transcriptome of radiosensitive patients compared to radioresistant patients. (147)

Team	RS patients	RR patients	Radiation scheme	Selected differentially expressed genes	Assay used for gene selection	Ref.
Quarmby <i>et al.</i>	3	3	Not irradiated	FMLP-R-I, TNF α , NGFR, EPHB2, PDGFB, NTRK1, LFNG, DDR1; IFNGR1	Cytokine array	(139)
Alsner <i>et al.</i>	22	4	3 * 3.5 Gy over 3 days, RNA extracted 2h after last irradiation.	CDC6, CDON, CXCL12, FAP, FBLN2, LMNB2, LUM, MT1X, MXRA5, SLC1A3, SOD2, SOD3, WISP2	15K cDNA microarray (148)	(141)
Rødninge <i>n et al.</i>	10	4	3 * 3.5 Gy over 3 days, RNA extracted 2h after last irradiation.	PLAGL1, CCND2, CDC6, DEGS1, CDON, CXCL12, MXRA5, LUM, MT1X, MT1F, MT1H, C1S, NF1, ARID5B, SCL1A3, TM4SF10, MGC33894, ZDHHC5/MFGE8	15K cDNA microarray	(142)
Forrester <i>et al.</i>	6	8	Not irradiated	FBN2, FST, GPRC5B, NOTCH3, PLCB1, DPT, DDIT4L, SGCG	GeneChip Human Exon 1.0 ST Array	(147)

Table 3. Summary of transcriptomic studies comparing skin fibroblasts from radiosensitive and radioresistant patients. RS : Radiosensitive, RR : Radioresistant

For the first time, Forrester *et al.* showed the existence of a basal transcriptomic signature that discriminated patients prone to develop RISF using health fibroblasts extracted from healthy skin. (147) This signature has been patented, presumably for the purpose of developing a predictive test for RISF. (149) Only a minute part of differentially expressed genes identified with Human Exon 1.0 ST Array has been shown in the article. Overall, 1577 genes were differentially expressed between fibroblasts from radiosensitive and radioresistant patients. These genes were associated with collagen metabolism gene ontology terms. FST, coding for follistatin, a protein neutralising the actions of the TGF β family of proteins (150) was shown to be under-expressed in fibroblasts from radiosensitive patients (Fold-change = - 1.9). These findings led to testing this protein as primary prevention in mice, showing that subcutaneous injections of follistatin before irradiation attenuated the radiation-induced fibrotic response. (151)

Phenotype-specific splicing events have also been highlighted. 152 genes have been found to be alternatively spliced between fibroblasts from radiosensitive and radioresistant patients. As for those differentially expressed, they were associated with gene ontology terms linked to

fibrosis pathogenesis such as integrin-mediated signalling pathway (152) and extracellular matrix disassembly. It is worth noting that they are also associated with transcription regulation functions (GO:0042789). Only half of alternatively spliced genes and 5% of differentially expressed genes are common, suggesting independent regulatory mechanisms that are in play. Interestingly, these alterations in gene expression and alternative splicing exist in the absence of any macroscopic difference between radiosensitive and radioresistant patients' healthy skins. This phenotypically similar skin is not surprising as the observed fold-changes remain modest. Taken together, the altered gene expression and gene splicing between the two phenotypes suggest the existence of clinically invisible, subtle molecular differences before irradiation, that would be determinant in tissue fate after irradiation.

7.3.3. Role of epigenetic marks

Epigenetic modifications include histone modifications such as acetylations and methylations, DNA methylation, particularly on CpG island, non-coding RNAs and three-dimensional chromatin organization. (153) As a relatively new field, only few studies have been conducted on the epigenetic regulations of skin fibrosis, mainly on miRNAs (reviewed elsewhere (154)). Moreover, Phenylbutyrate, a histone deacetylase inhibitor, was correlated with suppression of the aberrant expression of radiation-induced TGF β and TNF α , subsequently reducing RISF. Hence, histone modifications were shown to be involved in RISF pathophysiology (155) To our knowledge, only Weigel *et al.* have conducted a whole genome epigenetic analysis on radiosensitive and radioresistant skin fibroblasts. (156) They evaluated the methylation state of genome-wide CpG islands using Infinium Methylation Assays. (156) In this study, 12 968 differentially methylated CpG islands covering 9 060 genes have been identified. Interestingly, a Gene Ontology analysis revealed that they have been associated with transcription regulation functions, such as regulation of transcription by RNA polymerase II and mRNA splicing via spliceosome, and with fibrosis-linked functions, such as extracellular matrix organization or integrin-mediated signalling pathway. Cross-analysis with Forrester *et al.* expression data evidenced that 53% of differentially expressed genes were differentially methylated between radiosensitive and radioresistant skin fibroblasts. However, CpG island differential methylation was not significantly associated with differential gene expression in Forrester *et al.*'s dataset, suggesting that CpG island methylation may not be the main regulatory mechanism of the globally observed differential expression between Forrester *et al.*'s radiosensitive and radioresistant skin fibroblasts. However, these conclusions remain rough since the epigenetic study and the transcriptomic study were not conducted on the same patients. Extensive epigenetic and transcriptomic studies on the same patients are required to describe more precise mechanisms. Nevertheless, at the scale of a single gene, the differential methylation of the CpG islands was shown to be a key factor in the expression of this given

gene. Weigel *et al.* particularly demonstrated that the differential methylation of a diacylglycerol kinase alpha (DGKA) enhancer led to the recruitment of EGR1, facilitating radiation-induced DGKA transcription in cells from patients later developing fibrosis. (156) DGKA is involved in processes critical in fibrogenesis such as immune response, lipid signalling, exosome production, and migration as well as cell proliferation. (157) This discovery may provide novel preventive therapies that improve RT as Valinciute *et al.* have recently shown that PFI-1, a BET-bromodomain inhibitor, suppressed DGKA induction in bleomycin-treated fibroblasts, leading to a less severe fibrosis phenotype (158)

7.3.4. Conclusion

With almost one woman over five facing clinically significant RISF after RT for breast cancer, prevention of this late radiation toxicity emerges as a high priority issue within the frame of personalised medicine. For two decades, molecular and functional approaches have followed one another in an attempt to predict the occurrence of RISF but have only met with moderate success. (58,145,146,159,160) Though in its infancy, the hypothesis of the existence of basal molecular differences is slowly arising, shedding light on the importance of alternative splicing and epigenetic regulations, and opening promising new leads for late toxicity management.

8. SPLICI-Rad study

8.1. Why did we need SPLICI-Rad study?

As previously presented, RISF is a severe and irreversible side effect following RT for breast cancer. SPLICI-Rad is a clinical study investigating for a RISF prognostic signature in healthy skin fibroblasts, as well as understanding the effect of ionising radiation on the transcriptome of these cells.

Improving the management of complications and sequelae was part of the general objectives of the Cancer Plan III 2014-2019, a French nation-wide health program. Radiation-induced morbidity, most often mediated by fibrosis, exposes patients and society to additional costs. Screening individuals predisposed to pathological radiation-induced fibrosis would allow the personalisation of cancer treatments. Therefore, a molecular characterisation of this RISF and the search for a specific prognostic signature appeared essential.

The following summarizes SPLICI-Rad's trial specifications (NCT03000764).

8.2. Objectives and endpoints

The objectives and endpoints of this study are introduced in Table 4.

Objectives

Endpoints

Primary	<p>Comparing the overall expression and splicing profiles of mRNAs and ncRNAs in healthy dermal fibroblasts between 2 groups of patients treated with RT:</p> <ul style="list-style-type: none"> - Patients with RISF, CTCAE v4.0 grade ≥ 3 (so-called radiosensitive) - Patients without RISF, CTCAE v4.0 grade ≤ 3 (so-called radioresistant) 	<ul style="list-style-type: none"> - Variations in gene expression - Frequency of inclusion of individual exons within the set of RNA isoforms (global splicing profiles),
Secondary	<ul style="list-style-type: none"> - Defining a predictive transcriptomic signature of RISF based on inter-individual comparisons of global mRNA and ncRNA expression profiles, - Applying the signature obtained on healthy fibroblasts to blood, - Comparing within the same individual the overall RNA expression and splicing profiles between healthy dermal fibroblasts and fibroblasts harvested from the irradiated skin, - Detecting specific circulating HSP proteins in each patient group that are potentially predictive of pathological radiation-induced fibrosis, - Investigating potential interactions between DNA repair proteins involved in radiation-induced double strand breaks. 	<ul style="list-style-type: none"> - Number of residual micronuclei 24 hours after ex vivo irradiation, - Number of double strand breaks, evaluated through indirect immunofluorescence staining of 53BP1 and pATM proteins after ex vivo irradiation, - ELISA blood determination of candidate biomarkers: HSP70, HSP27, HSP $\alpha\beta$-crystalline

Table 4. Objectives and outcomes of SPLICI-Rad study.

8.3. Patient selection

8.3.1. Population

The SPLICI-Rad study was conducted in two groups of patients:

- 10 patients with unusual late radiation-induced skin or soft tissue toxicity (CTCAE v4.0 grade ≥ 3 dermatitis, fibrosis, atrophy) 6 months after RT for breast cancer (radiosensitive patients)
- 10 patients previously treated with conservative surgery and postoperative RT for localized breast cancer with CTCAE v4.0 ≤ 1 late radiation-induced skin or soft tissue toxicity, more than 4 years after RT (radioresistant patients).

8.3.2. Inclusion criteria

To be included in the study, patients had to meet the inclusion criteria presented in Table 5.

8.3.3. Exclusion criteria

Patients meeting any criteria described in Table 6 were not included in the study.

<p>Both groups</p>	<ul style="list-style-type: none"> - Female, - Age ≥ 18 years and < 70 years, - Non-metastatic disease, - Performance status: 0-1, - Bra size ≤ 110 cm and Cup size <D, - No previous history of breast reconstructive surgery, - Ability to undergo the various blood samples: haematological conditions allowing this sampling, - Non-progressive carcinological disease, - No systemic inflammatory disease (other than scleroderma if applicable) or diabetes - No previous history of inflammatory or infectious signs at the biopsy sites at inclusion, - Patient informed that signed an informed consent, - Registration to a social security regime, - History of breast disease (adenocarcinoma in situ or invasive)
<p>Radioresistant group</p>	<ul style="list-style-type: none"> - Postoperative radiotherapy completed for 4 years or longer, - Late radiation-induced skin or soft tissue toxicity of CTCAE v4.0 grade ≤1.
<p>Radiosensitive group</p>	<ul style="list-style-type: none"> - Post-operative radiotherapy completed at least 6 before the onset of late radiation-induced toxicity, - Unusual late radiation-induced skin or soft tissue toxicity (dermatitis, fibrosis, atrophy) of CTCAE v4.0 grade ≥ 3.

Table 5. Inclusion criteria of SPLICI-Rad study.

<p>Both groups</p>	<ul style="list-style-type: none"> - Age <18 years or >70 years, - Metastatic or progressing disease, - Performance status > 1, - Cup size ≥ D or Bra size > 110 cm, - History of breast reconstructive surgery, - Radiation therapy that delivered an overdose > 110% of the prescribed dose, - Presence of systemic inflammatory disease or diabetes, - Presence of inflammatory or infectious signs at the biopsy sites at inclusion, - Ulceration in the treated breast, - Pregnant or likely to be pregnant within 6 months, - No registration to a social security regime, - Patients under guardianship (including curatorship) - Patients with anaemia - Patients under anti-coagulation treatment
<p>Radioresistant group</p>	<ul style="list-style-type: none"> - Postoperative radiotherapy completed for less than 4 years, - Late radiation-induced skin or soft tissue toxicity of CTCAE v4.0 grade > 1
<p>Radiosensitive group</p>	<ul style="list-style-type: none"> - Post-operative radiotherapy completed less than 6 before the onset of late radiation-induced toxicity, - Unusual late radiation-induced skin or soft tissue toxicity (dermatitis, fibrosis, atrophy) of CTCAE v4.0 grade < 3.

Table 6. Exclusion criteria of SPLICI-Rad study.

8.4. Study workflow

8.4.1. Sampling

After inclusion, patients participating in the trial underwent the following sample collection:

- a skin biopsy (12-gauge punch, under local anaesthesia by lidocaine and prilocaine patch) in healthy non-irradiated skin,
- a skin biopsy (12-gauge punch, under local anaesthesia by lidocaine and prilocaine patch) in the RT field (in fibrotic areas for radiosensitive patients),
- a 10 mL blood sample in EDTA K2 tube
- a 2.5 mL blood sample in PAXgene Blood RNA tube
- 2 x 4 ml blood samples in EDTA K2 tube.

After sampling, patients were followed up according to the recommendations for breast cancer. The radiation oncologist contacted the patients 7 days after the samples were taken to detect any adverse event and, depending on the case, decided on an additional visit.

8.4.2. Criteria for study termination

The study could have been suspended or stopped by the promoter in agreement with the coordinator or at the request of the regulatory authority and/or the ethics committee (committee for the protection of individuals) for the following reasons:

- Unexpected frequency and/or severity of toxicity,
- Insufficient patient recruitment,
- Insufficient quality of data collection.

8.5. Ethics and regulatory guidelines

8.5.1. Rules and regulations

The study was conducted in agreement with:

- the ethics guidelines of the latest version of the Declaration of Helsinki,
- the Good Clinical Practices of November 24th, 2006 defined by the International Conference on Harmonisation (ICH-E6, 17/07/96), the Huriet-Serusclat law (n° 88-1138) of December 20th, 1988 concerning the protection of individuals undergoing biomedical research and modified by the Public Health Orientation law (n° 2004-806) of August 9th, 2004,
- the Data Protection Act No. 78-17 of January 6th, 1978 as amended by Act No. 2004-801 of August 6th, 2004 on the protection of individuals with regard to the processing of personal data,
- the bioethics law n° 2004-800 of August 6th, 2004
- the regulation of clinical trials modified by the law of August 9th, 2004 (n° 2004-806) relative to public health policy, and by its application decree of April 26th, 2006 (N°2006-477),
- the European Directive (2001/20/EC) on the conduct of clinical trials.

8.5.2. Ethics Committee and regulatory authorities

The study was submitted to the French Commission for the Protection of Personal Data (CNIL) for authorisation. Individual data communicated to the promoter were anonymised. Informed consents were sent to the promoter in a sealed envelope.

The protocol was submitted to the ethics committee (CCP EST III) which issued a positive report on September 6th, 2016.

The protocol was submitted to the national drug safety agency (HAS), which issued a positive report on May 27th, 2016.

8.5.3. Patient information and consent

Prior to the study, the free, informed, and written consent of the patients was obtained after comprehensive information had been provided by the investigator during a consultation and after sufficient time for reflection.

9. A transcriptomic test to predict the onset of RISF

Thanks to the transcriptomic analyses of SPLICI-Rad study samples, we were able to develop a candidate prognostic test able to predict the onset of RISF. Our team is currently being supported by SATT Sayens (innovation support organism) to carry this project to the industrialisation phase. To date, the patent registration procedure is ongoing. The following section summarises the invention disclosure on which this patent is based.

9.1. Why do we need a prognostic test for RISF?

9.1.1. Strategies to prevent RT-related toxicities

To prevent the occurrence of early and late toxicities, emphasis has been placed on improving RT techniques to reduce the volume of healthy tissue irradiated, and on the search for predictive biomarkers. The first proposed IRS tests are based on the quantification of radiation-induced cell death in fibroblasts (clonogenicity (161), DNA repair, micronuclei (162), patents...), but their use in clinical practice has been limited by the need for a skin biopsy, cell culture time, and cost and lack of reproducibility. More recently, a blood test based on the rate of radiation-induced apoptosis of lymphocytes has been proposed (patent WO_2018041960 (146)). The results of the latter, coupled with smoking status and the presence of hormone therapy, are very effective in identifying patients at no risk of RISF (NPV = 93.5%). On the other hand, they struggle to discriminate patients at risk, with a positive predictive value of only 20.9% and a specificity of 48.7%, notably due to the existence of confounding pathologies associated with lymphocyte apoptosis.

9.1.2. A dire need for tests to personalise RT schemes.

The understanding of IRS origin, as well as the reliable and non-invasive IRS prediction for each patient are key issues in RT. Indeed, it would help oncologists in adapting the therapeutic schemes and in particular the RT doses in order to optimise the individual therapeutic ratio. Thus, it would be possible to propose dose escalation to the most radioresistant patients or, on the contrary, dose de-escalation, protective RT techniques (proton therapy, brachytherapy) or alternative local treatments avoiding RT (non-conservative surgery) for the most radiosensitive patients. More than just curing, tomorrow's RT must ensure that patients are cured without sequelae by integrating IRS as a key variable.

9.1.3. Philosophy behind the development of our prognostic test

We are investigating the identification of a constitutional transcriptomic signature specific to IRS:

- **Transcriptomic**, because coding and non-coding RNAs are, due to their diversity, the molecules most likely to discriminate 2 individuals (163)
- **Constitutional**, because IRS is an individual phenotypic characteristic. It does not a priori require irradiation to be revealed.
- **Specific** to the IRS, in order to ensure powerful discrimination between individuals.

The identification of this signature is based on the comparative analysis of the blood (non-invasive and faster for a predictive test) and fibroblast transcriptomes (as it reflects the origin of the IRS) of 10 radiosensitive and 10 radioresistant patients from SPLICI-Rad study. The fibroblast signature is used to improve the understanding of the molecular basis of IRS and to bring specificity to the blood signature for the development of our **blood predictive test**.

9.2. How did we develop our prognostic test for RISF?

9.2.1. Identification of an IRS signature in skin fibroblast

For the development of this invention, we took as a model radiation-induced skin fibrosis, a frequent late toxicity occurring after breast cancer treatment by RT. The development of a fibroblast signature is particularly interesting because it allows the identification of functionally relevant markers, since these cells are central to the pathophysiology of radiation-induced skin fibrosis. Fibroblastic primocultures were established from healthy skin biopsies of radiation-sensitive or radiation-tolerant patients in the SPLICIRAD clinical study (NCT03000764). Total RNAs were extracted and hybridised on Affymetrix Clariom D chips. These high-definition chips cover not only the exons of coding and non-coding transcripts, i.e. 670 402 exons, but also the known exon-exon junctions (339 146 junctions). A quantitative bioinformatics analysis was then performed, followed by a functional analysis (gene ontology). The resulting variations were then analysed and sorted according to functional relevance.

The skin fibroblast signature developed from the microarray analyses includes 35 genes (Table 7). As illustrated by the heatmap of the expression of these 35 genes, it allows a very good discrimination of patients based on their transcriptome alone (Figure 12).

Gene name	Type	Gene name	Type
ABCA5	Coding	LINC00882	Non-Coding
ACTR3	Coding	NDNF	Coding
APOBEC3B	Coding	NR3C2	Coding
BACE2-IT1	Non-Coding	NRSN2	Coding
BVES	Coding	NTNG1	Coding
CADPS	Coding	PDCD1LG2	Coding
CAP1P2	Coding	PERP	Coding
CFL1	Coding	PSPHP1	Coding
ERG	Coding	PTMS	Coding
ESYT1	Coding	PTPRN	Coding
GGH	Coding	RN7SKP234	Non-Coding
GPC4	Coding	SPOCD1	Coding
HIST1H2BM	Coding	STK32B	Coding
IFI27	Coding	SV2A	Coding
IGF2BP3	Coding	TMSB4XP1	Coding
KCNQ5	Coding	TNXA	Non-Coding
KCNQ5-IT1	Non-Coding	TUBA1A	Coding
LAMA2	Coding		

Table 7. Gene list of skin fibroblast signature. The name and type (coding or non-coding) of each gene are indicated.

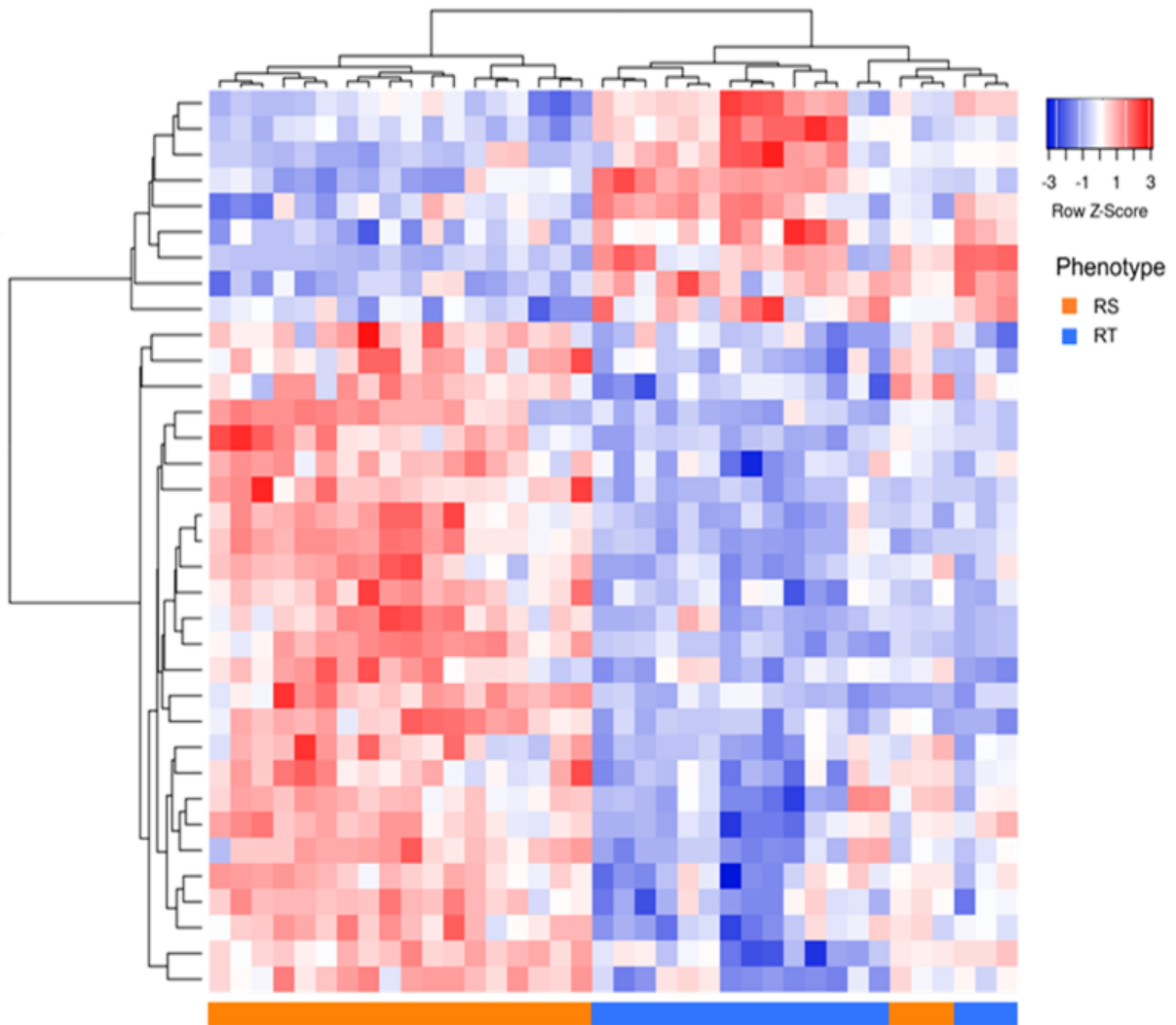
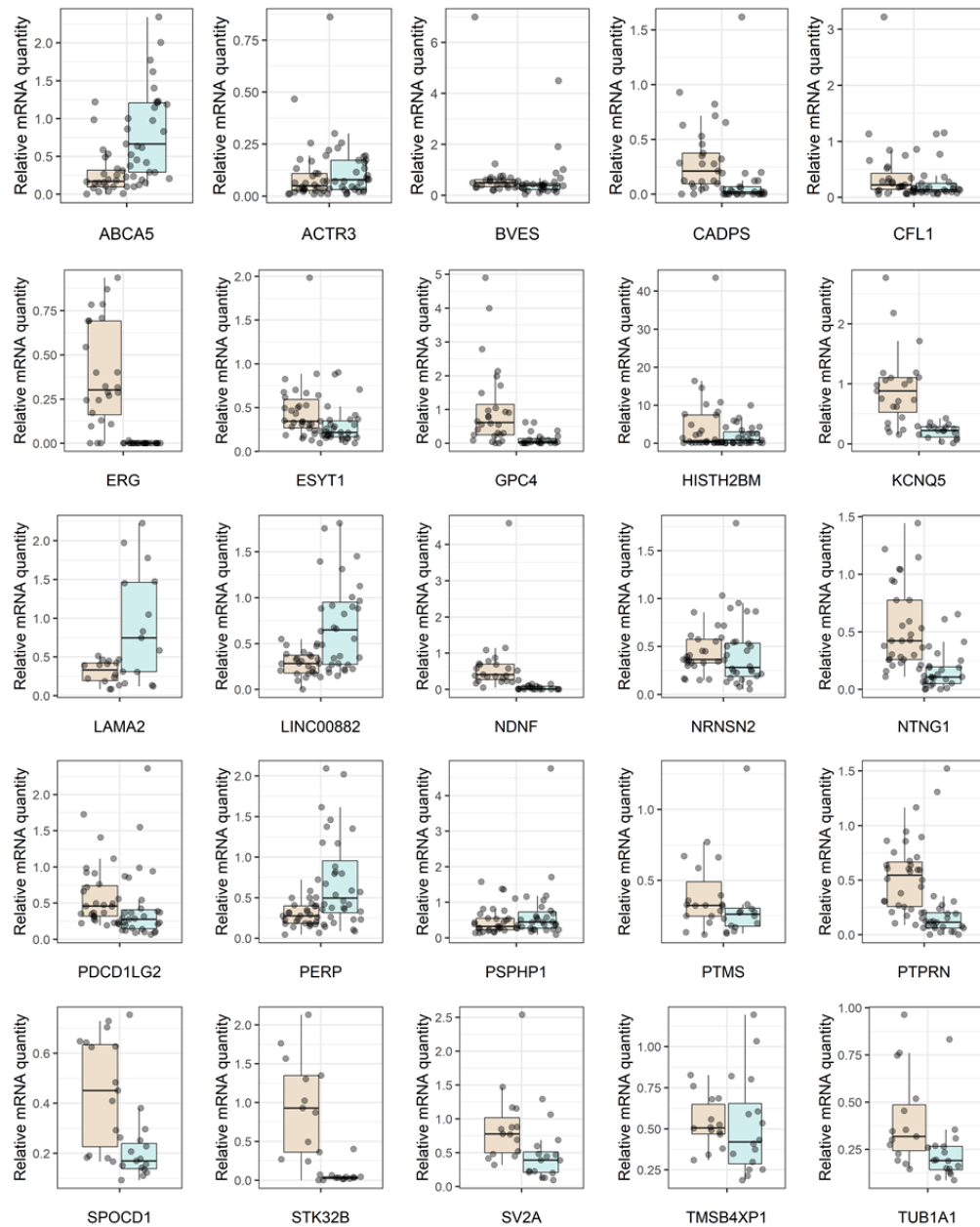




Figure 12. Heatmap of differentially expressed biomarkers between fibroblasts from radioresistant and radiosensitive patients at basal state (FDR p-val < 0.01, $n_{RR} = 7$, $n_{RS} = 6$)

Observed expression variations for the genes of our fibroblastic signature were validated by quantitative RT-qPCR (Figure 13). Of the 35 genes in our signature, 25 were analysed by RT-qPCR and 18 expression variations were validated (p -value < 0.05).



Genes	Fold-Change	p-value
ABCA5	-3.002119	3.90E-05
ACTR3	1.055617	2.81E-01
BVES	1.300851	2.26E-04
CADPS	2.263239	5.35E-04
CFL1	1.595952	1.32E-01
ERG	594.0286	1.91E-08
ESYT1	1.624741	3.17E-03
HIST1H2BM	2.428645	1.89E-01
GPC4	8.316211	1.08E-05
KCNQ5	4.42425	1.95E-06
LAMA2	-2.987494	1.37E-02
LINC00882	-2.490385	3.29E-04
NDNF	14.14861	4.89E-08
NRSN2	1.029267	2.68E-01
NTNG1	3.296888	1.14E-06
PDCD1LG2	1.328483	1.08E-02
PERP	-2.336001	1.03E-03
PSPHP1	-1.401858	2.51E-01
PTMS	1.249808	1.10E-01
PTPRN	2.285627	1.03E-05
SPOCD1	1.955217	2.31E-03
STK32B	15.34731	4.42E-04
SV2A	2.030542	2.34E-03
TMSB4XP1	1.028651	4.48E-01
TUB1A1	1.725558	1.06E-02

Figure 13. RT-qPCR validation of gene expression variations in the skin fibroblast signature. Non-validated expression variations (p-value >0.05) are shown in gray.

 Radioresistant
 Radiosensitive

9.2.2. Construction of a blood IRS signature

Because IRS is constitutional, it is possible to identify a person's IRS from any of its tissues. However, the ubiquity of IRS markers is often associated with their low expression and makes them complex to identify regarding tissue-specific expressed genes. It is therefore interesting to identify functionally relevant genes in the tissue and cell type subject to toxicity - in this case, skin fibroblasts, and then to assess their detection and differential expression in easily accessible and analysable samples - in this case, blood. RNA extracted from PaxGene RNA Blood tubes, taken from the same population of radioresistant (n=10) and radiosensitive (n=10) patients (SPLICI-Rad study), were hybridised on the same Affymetrix Clariom D chips. Based on the transcriptome analysis of the patients in these 2 groups, a blood signature was proposed. It comprises 23 genes (Table 8) and combines fibroblastic IRS markers (10 of the 35 genes, chosen based on the level of expression and detectability in blood), as well as purely blood-based markers (13 genes). It allows for excellent discrimination of patients based on their transcriptome alone (Figure 14). Variations in gene expression have not yet been validated and should be validated by quantitative RT-PCR.

Gene name	Type	Origin
ABCA5	Coding	Fibroblasts
AC109829.1	Coding	Blood
APOBEC3B	Coding	Fibroblasts
CBX2	Coding	Blood
CCSAP	Coding	Blood
CDX4	Coding	Blood
ENPP7P11	Coding	Blood
GGTA2P	Coding	Blood
IFI27	Coding	Fibroblasts
IGKV1D-42	Coding	Blood
LL0XNC01-250H12.3	Non-Coding	Blood
NR3C2	Coding	Fibroblasts
NTNG1	Coding	Fibroblasts
OR7E13P	Coding	Blood
PDCD1LG2	Coding	Fibroblasts
PLG	Coding	Blood
PSPHP1	Coding	Fibroblasts
PTPRN	Coding	Fibroblasts
RP11-159D12.8	Non-Coding	Blood
RP11-404P21.5	Non-Coding	Blood
RSPRY1	Coding	Blood
TNXA	Non-Coding	Fibroblasts
TUBA1A	Coding	Fibroblasts

Table 8. List of differentially expressed genes between radiosensitive and radioresistant patients included in the blood signature.

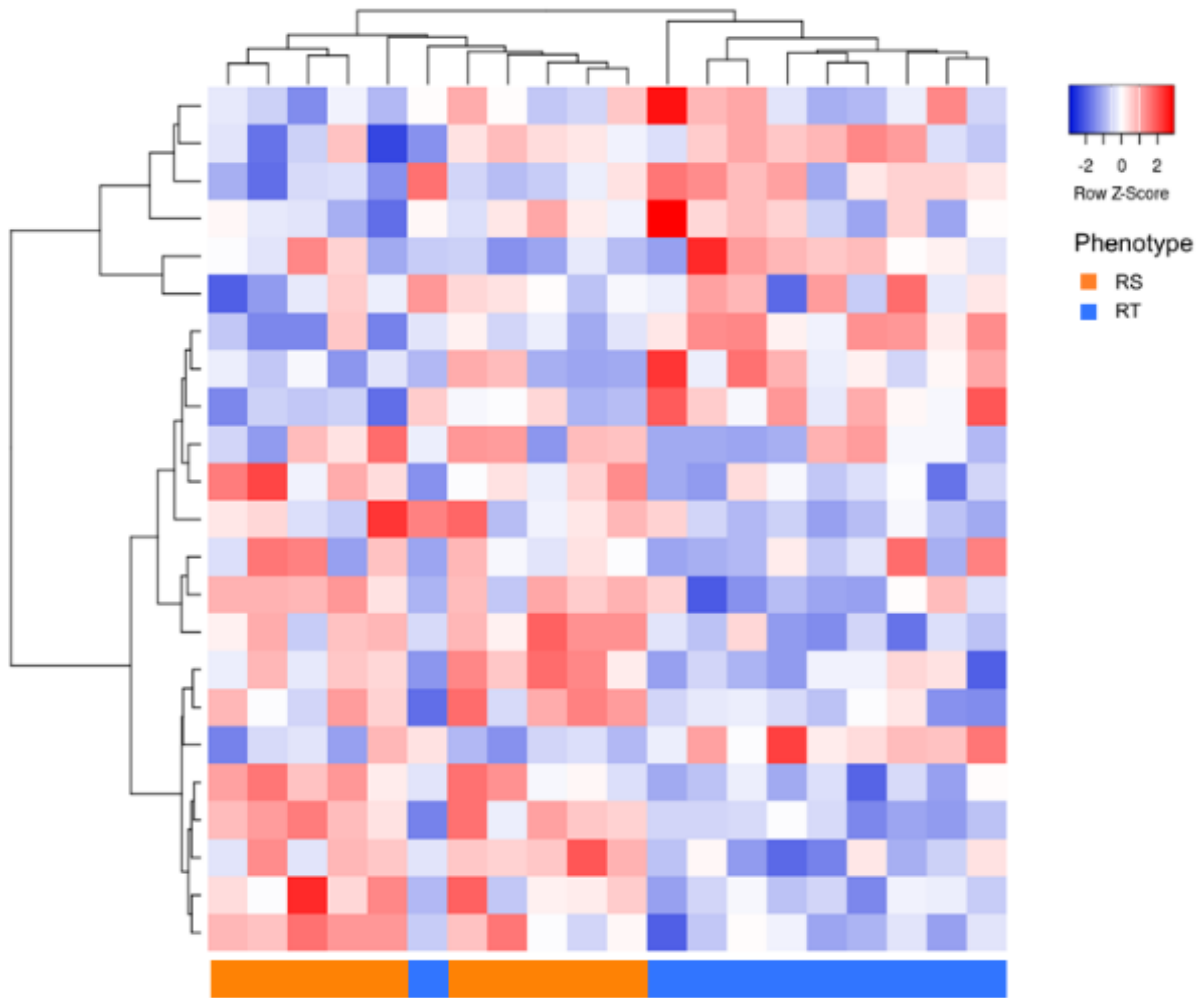


Figure 14. Heatmap of differentially expressed blood biomarkers between radioresistant and radiosensitive patients at basal state ($n_{RR} = 10$, $n_{RS} = 10$)

9.3. What are the available tests for IRS?

So far, only a few teams have been interested in developing a predictive test for individual radiosensitivity. Most of these teams have adopted RISF as their model. Competitors' patents for IRS prediction tests are listed in Table 9.

Patent reference	Inventors	Biological sample used	Description	Ref.
FR_3017625	Foray et al. UCBL	Skin fibroblasts	Predicting a patient's radiosensitivity using the number of basal and residual γ H2AX foci after irradiation (~24h).	(164)
WO_2015121596	Foray et al. UCBL	Skin fibroblasts	Predicting the severity of a patient's post-radiation response using the number of basal and residual γ H2AX foci after irradiation (~ 24h).	(159)
WO_2018229439	Pereira Neolys	Skin fibroblasts	Predicting patient radiosensitivity using basal pATM foci counts.	(160)
WO_2014154854	Azria et al. CHU Montpellier	T Cells	Predicting RT-induced toxicities (grade CTCAE > 2) quantifying radiation-induced lymphocyte apoptosis and 5 proteins (AK2, IDH2, ANX1, APEX1 et HSC70)	(165)
WO_2017032865	Schmitz et al. CEA	Various biological fluids	Predicting acute RT-induced toxicities using assessment of TRAIL/TNFSF10 rs3815496 and rs1131532 SNPs and those in strong linkage disequilibrium with them.	(166)
WO_2018041960	Azria et al. IRCM	T Cells	Predicting radiation-induced late toxicities in breast cancer treatment using radiation-induced T cell apoptosis, smoking status and endocrine therapy use.	(146)
WO_2011006214	Sprung & Mckay McCallum	Blood / Skin fibroblasts	Assessing susceptibility to radiation-induced toxicity by measuring the expression of several genes in blood or skin fibroblasts, with or without ex vivo irradiation.	(149)
WO_2014184028	Lambin et al. Maastricht University	Various biological fluids	Assessing proneness to radiation-induced lung toxicity by measuring mitochondrial SNPs.	(167)

Table 9. Patents on predicting individual radiosensitivity. The patent reference, the type of biological material used to perform the test and a brief description of the test are given. (**Black:** Breast cancer, **Gray:** All cancers)

9.4. What are the advantages of our test?

9.4.1. Non-invasive, quick, and cost-effective

Our invention is a PCR test that can be performed on a blood sample. It is therefore non-invasive, rapid and cost-effective. It is easy to use and can be automated, since the technique and equipment required to perform it are common in medical laboratories.

9.4.2. Pathophysiologically accurate

Conceptually, our test is distinguished by its pathophysiological relevance as its development was focused on the cell type involved in the phenotype of interest, using human samples, and in realistic experimental conditions. We also used an integrative approach based on functionally relevant molecular events.

9.4.3. Easily carried-out

From a methodological point of view, no ex-vivo irradiation is required. As IRS is constitutional, we decided to develop our test on native patients' samples.

9.5. What are the limitations of our test?

9.5.1. Limited number of patients in the development cohort

Our development cohort has a limited number of patients. In addition to the well-known lack of power associated with small cohorts, the use of high-throughput techniques on few patients involves a risk of an over-fit of the selected markers. The genes we identified, despite all the methodological precautions taken, could be proved to be false positives, unable to discriminate radiosensitive from radioresistant patients. Consequently, this signature requires validation on a larger cohort. A collaboration with the UNITRAD group has been initiated to evaluate our test on blood from several hundred patients included in the prospective trial HYPOG-01 (NCT03127995).

In addition, we could further investigate the impact of the test results for different dose ranges in other anatomical locations e.g. from primocultures and blood samples from the CRYOTOX collection (NCT03980977).

9.5.2. A prognostic test developed on post-RT samples

IRS is assumed to be constitutional and ubiquitous for all cells and tissues of the same person. This is the postulate of our test which, in its method and contrary to competing approaches, does not require *ex vivo* irradiation of samples. However, it can be argued that the patients included in our pilot study have, by definition, received RT prior to the study as they were included based on the development of late RT toxicities. Is our test influenced by this body irradiation (partial at high dose/quasi-total at low dose)? In other words, can pre-study RT change our constitutional signature of IRS?

It is worth mentioning that the skin samples are taken from an area that received an anecdotal dose during RT, several years after the end of treatment, which is accepted in several published studies (Table 10) and competing patents (Table 10) as a basal state.

Few studies have been performed on the persistence of a radiation response in blood over time, at therapeutically relevant delivered doses. However, Port et al (168) showed in 18 baboons irradiated (whole body) at 2.5 or 5 Gy that few of the genes differentially expressed immediately after irradiation were still expressed 106 days post-irradiation and that these genes are mainly related to the response to irradiation (168). In our study, the patients' transcriptome was analysed from samples (skin or liquid biopsy) taken 5 years post-irradiation from a non-irradiated area. Gene expression of our chosen markers did not vary in response to irradiation (transcriptomic analysis after irradiation at 2 Gy performed *ex-vivo* on primary fibroblast cultures from SPLICI-Rad patients). It is therefore highly unlikely that the expression of our blood signature genes was affected by the patients' RT treatment. It should also be noted that the blood cells, given their lifespan (from a few hours to a few months) had all been renewed at the time of collection and that the progenitors of the blood cells are located in organs at risk, specifically protected by irradiation scheme designs. Furthermore, Dr David Azria's team lymphocyte apoptosis test, although developed on blood samples taken post-irradiation, confirmed its effectiveness by similar results on blood samples taken before RT.

Finally, designing a *de novo* prospective clinical study to evaluate IRS before RT using our approach requires the recruitment of several hundred patients and a delay of at least 5 years to characterise the IRS phenotype. Feasibility and cost seem difficult to bear at this stage. In the aforementioned prospective trial HYPOG-01 (NCT03127995), blood samples were taken before the start of RT. To date, some of the included patients had sufficient follow-up to characterise their IRS status. This study would provide an avenue to explore the robustness of our signature.

Team	Type of test	Biological sample used	Discovery phase			Validation phase		
			Sample size	Study design	Samples taken prior or post-RT?	Sample size	Study design	Samples taken prior or post-RT?
Foray et al. (169)	Indirect immunofluorescence	Skin fibroblasts	12 (cases) + 100 (controls)	Retrospective	Post-RT			
Azria et al. (170)	T cell apoptosis	T cells	12 (cases) + 105 (controls)	Retrospective	Post-RT	415	Prospective	Prior to RT
Alsner et al. (171,172)	RNA quantification	Skin fibroblasts	14	Retrospective	Post-RT	214	Prospective	Post-RT

Table 10. Summary of published studies from teams involved in competing companies to find an IRS signature.

9.6. How will our test work?

9.6.1. One plate to predict them all (173)

Our test consists of a plate-based RT-qPCR assay for determining the IRS status of a patient through the expression analysis of the genes constituting our IRS blood signature (Figure 15).

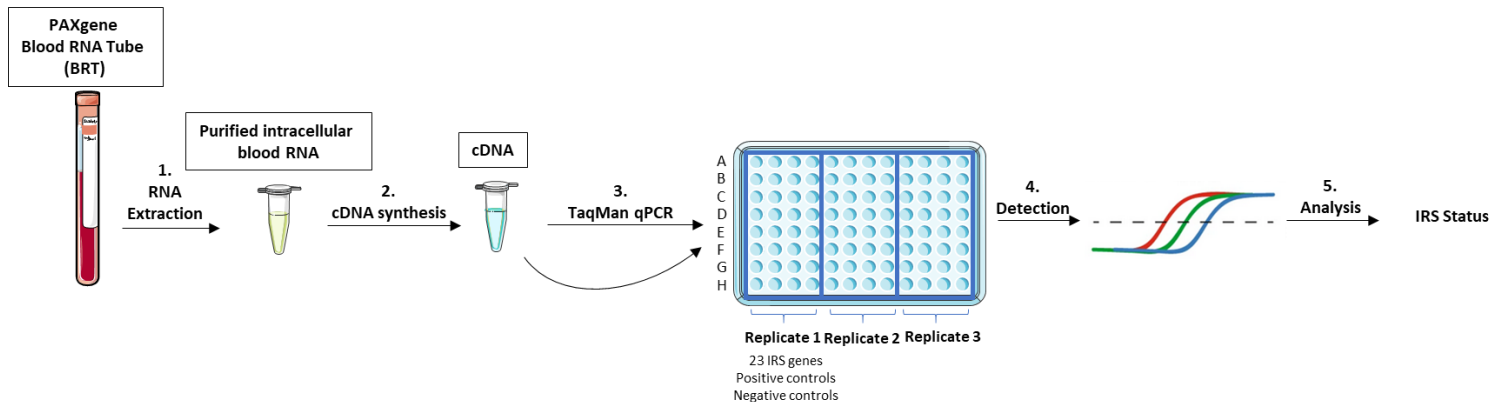


Figure 15. Principle of the individual radiosensitivity status test based on RT-qPCR analysis of blood signature gene expression.

The protocols of the different steps are summarised in the following sections.

9.6.2. PaxGene Blood RNA Tube

PAXgene Blood RNA Kit will be used for the purification of intracellular RNA from whole blood collected in the PAXgene Blood RNA Tube.

PAXgene Blood RNA Tubes (BRT) contain a specific reagent based on a patented RNA stabilisation technology. This reagent protects RNA molecules from degradation by RNases and minimises ex vivo changes in gene expression. PAXgene BRTs stabilise cellular RNAs for up to 3 days at 18-25°C, up to 5 days at 2-8°C and for at least 11 years when the stabilised blood is stored at -20°C or -70°C. This system allows the preparation of purified intracellular RNA of good quality that can be used for RT-qPCR based molecular diagnostic tests.

9.6.3. Processing of extracted RNA

The extracted RNAs will then be measured by spectrophotometry at 260 nm. Contamination by proteins or phenolic compounds/salts will be estimated by measuring the absorbance ratios 260/280 and 260/230, respectively. If these ratios are found to be unsatisfactory (ratios ≤ 1.7), a phenol-chloroform extraction followed by absolute ethanol precipitation in the presence of 0.15 M sodium acetate will be performed in order to remove phenol and protein residues and to optimise the quality of total RNA. RNA quality and non-contamination by genomic DNA will be assessed by capillary electrophoresis (Bioanalyzer or Tape Station system).

The reverse transcription reaction will be performed on a minimum of 200 ng of total RNA using a random primer mix (High capacity cDNA reverse transcription Kit, Life Technologies or SuperScript™ III First-Strand Synthesis System, Invitrogen) according to the supplier's protocol.

9.6.4. RNA quantification

Expression of the blood signature genes will be analysed by real-time PCR based on TaqMan chemistry, which is currently used in many molecular diagnostic assays and whose principle is described in Figure 16. As with other quantitative PCR methods, the detected fluorescent signal allows for a quantitative measurement of the exponential product accumulation over the course of the PCR cycles. Moreover, the TaqMan method allows a significant increase in the specificity of detection. For each IRS blood signature gene a specific primer pair and TaqMan probe will be optimised. Thus, 96-well PCR plates already containing the specific primers and the TaqMan probe will be custom-produced and will allow the parallel analysis of blood RNA from 3 patients.

A set of 32 wells (1/3 of the plate) will be dedicated to the analysis of a sample:

- 23 wells correspond to the IRS signature genes (variable according to the number of genes retained in the final signature after validation in the blood samples),
- 4 wells for housekeeping genes that will be used for data normalisation
- Several wells will be dedicated to negative controls: H₂O control and non-retro-transcribed control (RT-)

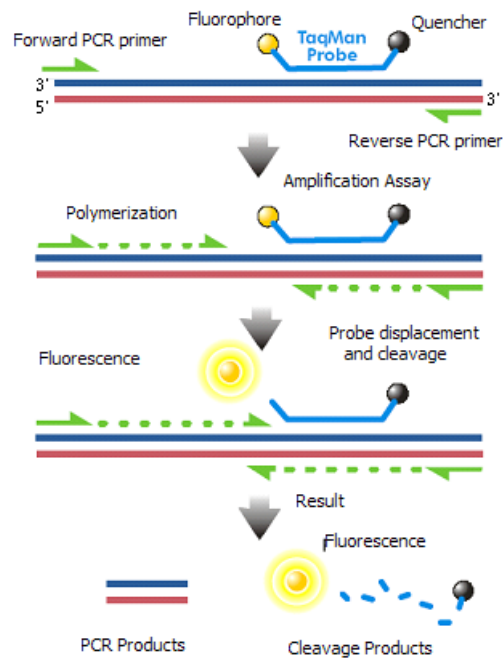


Figure 16. Principle of TaqMan real-time qPCR. This method is based on the 5' → 3' exonuclease activity of Taq Polymerase. Each TaqMan probe is designed to hybridise to a specific region of DNA amplified by a specific primer pair. The probe, with a total length of approximately 20-30 nucleotides, has a reporter fluorochrome at its 5' end and a quencher fluorochrome at its 3' end. Within the probe, the spatial proximity of the quencher and the reporter inhibits fluorescence emission. During the synthesis of the amplification product by the Taq polymerase (using Forward and Reverse primers), the TaqMan probe is hydrolysed releasing the fluorophore whose fluorescence becomes detectable and can be measured at the end of each elongation cycle.

9.6.5. Data processing and decision-making support system

The IRS status of the tested patient can be established by two methods. The most efficient one will be chosen after blood signature validation.

1) Unsupervised classification method: dendrogram, mathematically implicit model

A dendrogram (classification tree) discriminating the two IRS phenotypes will be constructed using a hierarchical clustering algorithm on SPLICI-Rad patients' gene expression levels. Then, we will integrate the data from the analysis of a new patient, with an unknown IRS status, into this dendrogram. Depending on the "branch" into which this patient is projected, it will be possible to establish her radiosensitivity status. Examples of dendrograms are shown in the upper parts of figures 12 and 14.

2) Score and threshold method: mathematically explicit model

For each gene, we will establish expression thresholds using the expression levels of SPLICI-Rad patients (known IRS status). From these thresholds, a risk score will be calculated to define the radiosensitivity status of the newly analysed patients. Clinical parameters may be considered in order to improve the accuracy of this score.

9.7. Where do we currently stand in the development of the test?

At this time, the fibroblast signature, defined after microarray analysis, is fully validated by qPCR. The TaqMan probes as well as the forward and reverse primers specific to the blood signature are being designed. The blood signature validation on the SPLICI-Rad patients' RNAs will be performed in the weeks following the publication of this manuscript. Once this signature is validated, we will establish the qPCR plate design of our prognostic test, as well as the data analysis model. In parallel to the product development, the blood IRS signature will be validated on a larger cohort to assess its robustness. This will enable us to provide physicians with a complete decision-support product for them to propose safer cancer treatment for their patients.

For the sake of proposing an optimised prognostic test, we focused on ~ 30 discriminating genes between radiosensitive and radioresistant patients. However, many interesting genes have been left aside. The following section describes the contribution of KRT7 and KRT18 expression in the prediction of RISF onset after RT.

10. Substructure Analyzer: A User-Friendly Workflow for Rapid Exploration and Accurate Analysis of Cellular Bodies in Fluorescence Microscopy Images

10.1. Introduction

As stated before, ionizing radiations most critical genomic damage are DNA double-strand breaks. These genomic lesions, if not repaired, can lead to cell death and tissue destruction or cell mutation and disruption of tissue homeostasis. In any case, un- or poorly repaired DSB will lead to RT toxicity. Therefore, IRS characterisation must evaluate cells ability to repair radiation-induced DSB. To do so, it is possible to follow DSB repair through staining of DNA repair proteins involved in this mechanism, such as pATM or 53BP1. (25) These staining reveals foci, marking DSB. These foci disappear when the DSB is repaired as DNA repair protein leave (Figure 11). Counting these foci is a tedious and time-consuming step that is hampered by the lack of intra- and inter-observer reproducibility when done manually. This observation can be extended to every intracellular staining requiring image processing. It was from this observation that Dr. Géraud Heckler, a former PhD student in our team, developed an image analysis module. (174) Substructure Analyzer is a workflow that allows the automation of image analysis of intracellular bodies in order to increase the reproducibility and decrease the analyses bias. I contributed through extensive testing of the workflow, bug correction, code cleaning and voice dubbing of the protocol video. The workflow, developed for Icy, an open-source image processing software, is described in the following article.

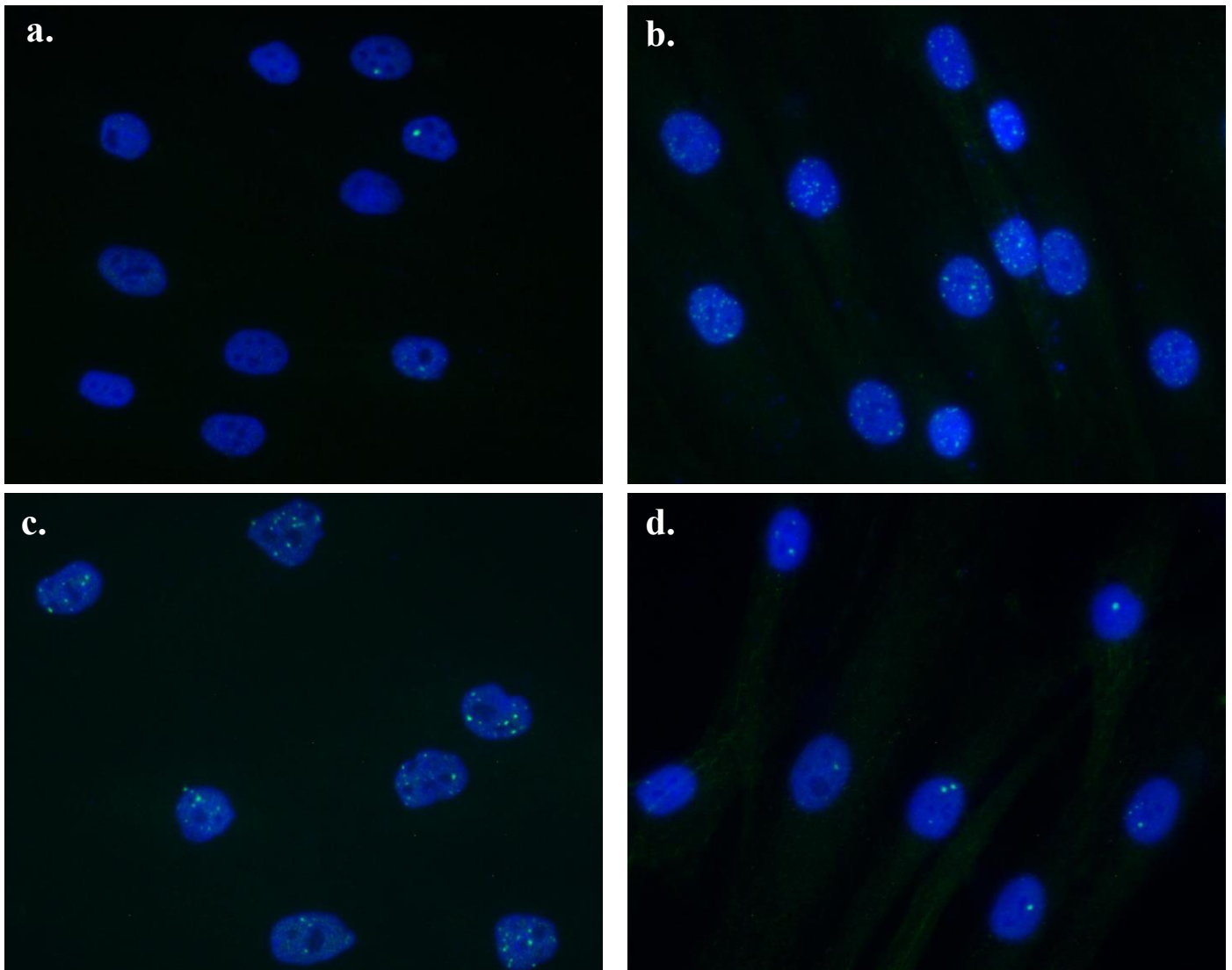


Figure 11. Representative images for immunofluorescence 53BP1 staining of primary skin fibroblasts **a.** unirradiated or after **b.** 1h, **c.** 4h or **d.** 24h post-2Gy irradiation.

10.2. Article

Substructure Analyzer: A User-Friendly Workflow for Rapid Exploration and Accurate Analysis of Cellular Bodies in Fluorescence Microscopy Images

Géraud Heckler¹, Christelle Aigueperse¹, Liza Hettal¹, Quentin Thuillier¹, Fabrice de Chaumont², Stéphane Dallongeville², Isabelle Behm-Ansmant¹

¹ Université de Lorraine, CNRS, IMoPA F54000 Nancy France ² Institut Pasteur, BioImage Analysis Unit, CNRS UMR 3691, Paris, France.

Corresponding Authors

Christelle Aigueperse

christelle.aigueperse@univ-lorraine.fr

Isabelle Behm-Ansmant

isabelle.behm@univ-lorraine.fr

Citation

Heckler, G., Aigueperse, C., Hettal, L., Thuillier, Q., de Chaumont, F., Dallongeville, S., Behm-Ansmant, I. Substructure Analyzer: A User-Friendly Workflow for Rapid Exploration and Accurate Analysis of Cellular Bodies in Fluorescence Microscopy Images. *J. Vis. Exp.* (161), e60990, doi:10.3791/60990 (2020).

Date Published

July 15, 2020

DOI

10.3791/60990

URL

jove.com/video/60990

Abstract

The last decade has been characterized by breakthroughs in fluorescence microscopy techniques illustrated by spatial resolution improvement but also in live-cell imaging and high-throughput microscopy techniques. This led to a constant increase in the amount and complexity of the microscopy data for a single experiment. Because manual analysis of microscopy data is very time consuming, subjective, and prohibits quantitative analyses, automation of bioimage analysis is becoming almost unavoidable. We built an informatics workflow called *Substructure Analyzer* to fully automate signal analysis in bioimages from fluorescent microscopy. This workflow is developed on the user-friendly open-source platform Icy and is completed by functionalities from ImageJ. It includes the pre-processing of images to improve the signal to noise ratio, the individual segmentation of cells (detection of cell boundaries) and the detection/quantification of cell bodies enriched in specific cell compartments. The main advantage of this workflow is to propose complex bio-imaging functionalities to users without image analysis expertise through a user-friendly interface. Moreover, it is highly modular and adapted to several issues from the characterization of nuclear/cytoplasmic translocation to the comparative analysis of different cell bodies in different cellular sub-structures. The functionality of this workflow is illustrated through the study of the Cajal (coiled) Bodies under oxidative stress (OS) conditions. Data from fluorescence microscopy show that their integrity in human cells is impacted a few hours after the induction of OS. This effect is characterized by a decrease of coilin nucleation into characteristic Cajal Bodies, associated with a nucleoplasmic redistribution of coilin into an increased number of smaller foci. The central role of coilin in the exchange between CB components and the surrounding

nucleoplasm suggests that OS induced redistribution of coilin could affect the composition and the functionality of Cajal Bodies.

Introduction

Light microscopy and, more particularly, fluorescence microscopy are robust and versatile techniques commonly used in biological sciences. They give access to the precise localization of various biomolecules like proteins or RNA through their specific fluorescent labeling. The last decade has been characterized by rapid advances in microscopy and imaging technologies as evidenced by the 2014 Nobel Prize in Chemistry awarding Eric Betzig, Stefan W. Hell and William E. Moerner for the development of super-resolved fluorescence microscopy (SRFM)¹. SFRM bypasses the diffraction limit of traditional optical microscopy to bring it into the nanodimension. Improvement in techniques like live-imaging or high throughput screening approaches also increases the amount and the complexity of the data to treat for each experiment. Most of the time, researchers are faced with high heterogeneous populations of cells and want to analyze phenotypes at the single-cell level.

Initially, analyses such as foci counting were performed by eye, which is preferred by some researchers since it provides full visual control over the counting process. However, manual analysis of such data is too time consuming, leads to variability between observers, and does not give access to more complex features so that computer-assisted approaches are becoming widely used and almost unavoidable². Bioimage informatics methods substantially increase the efficiency of data analysis and are free of the unavoidable operator subjectivity and potential bias of the manual counting analysis. The increased demand in this field and the improvement of computer power led to the

development of a large number of image analysis platforms. Some of them are freely available and give access to various tools to perform analysis with personal computers. A classification of open access tools has been recently established³ and presents Icy⁴ as a powerful software combining usability and functionality. Moreover, Icy has the advantage of communicating with ImageJ.

For users without image analysis expertise, the main obstacles are to choose the appropriate tool according to the problematic and correctly tune parameters that are often not well understood. Moreover, setup times are often long. Icy proposes a user-friendly point-and-click interface named “Protocols” to develop workflow by combining some plugins found within an exhaustive collection⁴. The flexible modular design and the point-and-click interface make setting up an analysis feasible for non-programmers. Here we present a workflow called *Substructure Analyzer*, developed in Icy’s interface, whose function is to analyze fluorescent signals in specific cellular compartments and measure different features as brightness, foci number, foci size, and spatial distribution. This workflow addresses several issues such as quantification of signal translocation, analysis of transfected cells expressing a fluorescent reporter, or analysis of foci from different cellular substructures in individual cells. It allows the simultaneous processing of multiple images, and output results are exported to a tab-delimited worksheet that can be opened in commonly used spreadsheet programs.

The *Substructure Analyzer* pipeline is presented in **Figure 1**. First, all the images contained in a specified folder are pre-processed to improve their signal to noise ratio. This step

increases the efficiency of the following steps and decreases the running time. Then, the Regions of Interest (ROIs), corresponding to the image areas where the fluorescent signal should be detected, are identified and segmented. Finally, the fluorescent signal is analyzed, and results are exported into a tab-delimited worksheet.

Object segmentation (detection of boundaries) is the most challenging step in image analysis, and its efficiency determines the accuracy of the resulting cell measurements. The first objects identified in an image (called primary objects) are often nuclei from DNA-stained images (DAPI or Hoechst staining), although primary objects can also be whole cells, beads, speckles, tumors, or whatever stained objects. In most biological images, cells or nuclei touch each other or overlap causing the simple and fast algorithms to fail. To date, no universal algorithm can perform perfect segmentation of all objects, mostly because their characteristics (size, shape, or texture) modulate the efficiency of segmentation⁵. The segmentation tools commonly distributed with microscopy software (such as the MetaMorph Imaging Software by Molecular Devices⁶, or the NIS-Elements Advances Research software by Nikon⁷) are generally based on standard techniques such as correlation matching, thresholding, or morphological operations. Although efficient in basic systems, these overgeneralized methods rapidly present limitations when used in more challenging and specific contexts. Indeed, segmentation is highly sensitive to experimental parameters such as cell type, cell density, or biomarkers, and frequently requires repeated adjustment for a large data set. The *Substructure Analyzer* workflow integrates both simple and more sophisticated algorithms to propose different alternatives adapted to image complexity and user needs. It notably proposes the marker-based watershed algorithm⁸ for

highly clustered objects. The efficiency of this segmentation method relies on the selection of individual markers on each object. These markers are manually chosen most of the time to get correct parameters for full segmentation, which is highly time consuming when users face a high number of objects. *Substructure Analyzer* proposes an automatic detection of these markers, providing a highly efficient segmentation process. Segmentation is, most of the time, the limiting step of image analysis and can considerably modify the processing time depending on the resolution of the image, the number of objects per image, and the level of clustering of objects. Typical pipelines require a few seconds to 5 minutes per image on a standard desktop computer. Analysis of more complex images can require a more powerful computer and some basic knowledge in image analysis.

The flexibility and functionality of this workflow are illustrated with various examples in the representative results. The advantages of this workflow are notably displayed through the study of nuclear substructures under oxidative stress (OS) conditions. OS corresponds to an imbalance of the redox homeostasis in favor of oxidants and is associated with high levels of reactive oxygen species (ROS). Since ROS act as signaling molecules, changes in their concentration and subcellular localization affect positively or negatively a myriad of pathways and networks that regulate physiological functions, including signal transduction, repair mechanisms, gene expression, cell death, and proliferation^{9, 10}. OS is thus directly involved in various pathologies (neurodegenerative and cardiovascular diseases, cancers, diabetes, etc.), but also cellular aging. Therefore, deciphering the consequences of OS on the human cell's organization and function constitutes a crucial step in the understanding of the roles of OS in the onset and development of human pathologies. It has been established that OS regulates gene expression by

modulating transcription through several transcription factors (p53, Nrf2, FOXO3A)¹¹, but also by affecting the regulation of several co- and post-transcriptional processes such as alternative splicing (AS) of pre-RNAs^{12, 13, 14}. Alternative splicing of primary coding and non-coding transcripts is an essential mechanism that increases the encoding capacity of the genomes by producing transcript isoforms. AS is performed by a huge ribonucleoprotein complex called spliceosome, containing almost 300 proteins and 5 U-rich small nuclear RNAs (UsnRNAs)¹⁵. Spliceosome assembly and AS are tightly controlled in cells and some steps of the spliceosome maturation occur within membrane-less nuclear compartments named Cajal Bodies. These nuclear substructures are characterized by the dynamic nature of their structure and their composition, which are mainly conducted by multivalent interactions of their RNA and protein components with the coilin protein. Analysis of thousands of cells with the *Substructure Analyzer* workflow allowed characterization of never described effects of OS on Cajal Bodies. Indeed, obtained data suggest that OS modifies the nucleation of Cajal Bodies, inducing a nucleoplasmic redistribution of the coilin protein into numerous smaller nuclear foci. Such a change of the structure of Cajal Bodies might affect the maturation of the spliceosome and participate in AS modulation by OS.

Protocol

NOTE: User-friendly tutorials are available on Icy's website <http://icy.bioimageanalysis.org>.

1. Download Icy and the *Substructure Analyzer* protocol

1. Download Icy from the Icy website (<http://icy.bioimageanalysis.org/download>) and download

the **Substructure Analyzer** protocol: <http://icy.bioimageanalysis.org/protocols?sort=latest>.

NOTE: If using a 64-bit OS, be sure to use the 64-bit version of Java. This version allows for increasing the memory allocated to Icy (**Preferences | General | Max memory**).

2. Opening the protocol

1. Open Icy and click on **Tools** in the **Ribbon** menu.
2. Click on **Protocols** to open the **Protocols Editor** interface.
3. Click on **Load** and open the protocol **Substructure Analyzer**. Protocol loading can take a few seconds. Be sure that the opening of the protocol is complete before using it.

NOTE: The workflow is composed of **13 general blocks** presented in **Figure 2a**. Each block works as a pipeline composed of several boxes performing specific subtasks.

3. Interacting with the workflow on Icy

NOTE: Each block or box is numbered and has a specific rank within the workflow (**Figure 2b**). By clicking on this number, the closest possible position to the first is assigned to the selected block/box then the position of the other blocks/boxes is re-organized. Respect the right order of the blocks when preparing the workflow. For example, Spot Detector block needs pre-defined ROIs so that Segmentation blocks have to run before Spot Detector blocks. Do not modify the position of boxes. Do not use "." in the image's name.

1. By clicking on the upper left corner icon, collapse, expand, enlarge, narrow, or remove the block (**Figure 2b**).
2. Each pipeline of the workflow is characterized by a network of boxes connected via their input and output

(**Figure 2b**). To create a connection, click on **Output** and maintain until the cursor attains an input. Connections can be removed by clicking on the **Output** tag.

4. Merging of the channels of an image

1. Use the block **Merge Channels** to generate merged images. If necessary, rename the files so that sequences to be merged have the same name's prefix followed by a distinct separator. For example, sequences of individual channels from an Image A are named: ImageA_red, ImageA_blue.

NOTE: For the separator, do not use characters already present in the image's name.

2. In the same folder, create one new folder per channel to merge. For example, to merge red, green, and blue channels, create 3 folders, and store the corresponding sequences in these folders.
3. Only use the block **Merge Channels**, remove the other blocks, and save the protocol as **Merge Channels**.

1. Access the boxes to set parameters. For each channel, fill the boxes **Channel number X** (boxes 1, 5 or 9), **Folder channel number X** (boxes 2, 6 or 10), **Separator channel number X** (boxes 3, 7 or 11) and **Colormap channel nb X** (boxes 4, 8 and 12) respectively.

NOTE: These boxes are horizontally grouped by four, each line corresponding to the same channel. In each line, a display is also available (boxes 23, 24, or 25) to directly visualize the sequence of the corresponding channel.

1. In the box **Channel number X**, choose which channel to extract (in classical RGB images, 0=Red, 1=Green, 2=Blue). The user quickly

accesses the different channels of an image within the **Inspector** window of Icy, in the **Sequence** tab. Write the smallest channel's value in the upper line and the highest one in the bottom line.

2. In the box **Folder channel number X**, write the \Name of the folder containing images of channel X.
3. In the box **Separator channel number X**, write the separator used for the image's name (in the previous example: "_red", "_green" and "_blue").
4. In the box **Colormap channel nb X**, indicate with a number which colormap model to use to visualize the corresponding channel in Icy. The available colormaps are visible in the **Sequence** tab of the **Inspector** window.
5. In the box **Format of merged images** (box 28), write the extension to save merged images: .tif, .gif, .jpg, .bmp or .png.

NOTE: To merge only 2 channels, do not fill the four boxes corresponding to the third channel.

2. On the upper left corner of the **Merge Channels** block, click on the link directly to the right of **Folder**. In the **Open** dialog box which appears, double-click on the folder containing sequences of the first channel that has been defined in the box **Folder channel number 1** (box 2). Then, click on **Open**.
3. Run the protocol by clicking on the black arrow in the upper left corner of the **Merge Channels** block (see part 7 for more details). Merged images are saved in a **Merge** folder in the same directory as the folders of individual channels.

5. Segmentation of the regions of interest

NOTE: Substructure Analyzer integrates both simple and more sophisticated algorithms to propose different alternatives adapted to image complexity and user needs.

1. Select the adapted block.
 1. If objects do not touch each other, or the user does not need to differentiate clustered objects individually, use the block **Segmentation A: Non clustered objects**.
 2. When objects do not touch each other, but some of them are close, use the block **Segmentation B: Poorly clustered objects**.
 3. For objects with a high clustering level and a convex shape, use the block **Segmentation C: Clustered objects with convex shapes**.
 4. If objects present a high clustering level and have irregular shapes, use the block **Segmentation D: Clustered objects with irregular shapes**.
 5. Use the block **Segmentation E: Clustered cytoplasm** to segment touching cytoplasm individually using segmented nuclei as markers. This block imperatively needs segmented nuclei to process.

NOTE: Blocks adapted for primary object segmentation process independently so that several blocks can be used in the same run to compare their efficiency for a particular substructure or to segment different types of substructures. If the clustering level is heterogeneous within the same set of images, then process small and highly clustered objects separately in the adapted blocks.

2. Link the **output0** (File) of the block **Select Folder** to the **folder** input of the chosen segmentation block.
 3. Set parameters of the chosen segmentation block.
 1. Segmentation A: Non clustered objects and Segmentation C: Clustered objects with convex shapes
 1. In box **Channel signal** (box 1), set the channel of the objects to segment.
 2. As an option, in box **Gaussian filter** (box 2), increase the X and Y sigma values if the signal inside objects is heterogeneous. The Gaussian filter smooths out textures to obtain more uniform regions and increases the speed and efficiency of nuclei segmentation. The smaller the objects, the lower the sigma value is. Avoid high sigma values. Set default values to 0.
 3. In box **HK-Means** (box 3), set the **Intensity classes** parameter and the approximate minimum and maximum sizes (in pixels) of objects to be detected.
- NOTE:** For intensity classes, a value of 2 classifies pixels in 2 classes: background and foreground. It is thus adapted when the contrast between the objects and the background is high. If foreground objects have different intensities or if the contrast with the background is low, increase the number of classes. The default setting is 2. Object size can be quickly evaluated by drawing a ROI manually around the object of interest. Size of the ROI (Interior in pixels) appears directly on the image when pointing it with the cursor or can be accessed in the **ROI statistics** window (open it from the search bar). Optimal parameters detect

each foreground object in a single ROI. They can be manually defined in Icy (**Detection and Tracking | HK-Means**).

4. In the box **Active Contours** (box 4), optimize the detection of object borders. Exhaustive documentation for this plugin is available online: http://icy.bioimageanalysis.org/plugin/Active_Contours. Correct parameters can also be manually defined in Icy (**Detection and Tracking | Active Contours**).
 5. During the process, a folder is automatically created to save images of segmented objects. In the box **Text** (box 6), name this folder (ex: Segmented nuclei). To set the format for saving images of segmented objects (Tiff, Gif, Jpeg, BMP, PNG), fill the box **format of images of segmented objects**. The folder is created in the folder containing merged images.
 6. Run the workflow (for details, see part 7).
2. Segmentation B: Poorly clustered objects
1. Follow the same steps as in 5.3.1 to set parameters of boxes **Channel signal**, **HK-Means**, **Active Contours**, **Extension to save segmented objects** and **Text** (Boxes ranks are not the same as in step 5.3.1).
 2. In the box **Call IJ plugin** (box 4), set the **Rolling** parameter to control background subtraction. Set this parameter to at least the size of the largest object that is not part of the background. Decreasing this value increases background removal but can also induce loss of foreground signal.

3. In the box **Adaptive histogram equalization** (box 6), improve the contrasts between the foreground objects and the background. Increasing the slope gives more contrasted sequences.

4. Run the workflow (for details, see part 7).

3. Segmentation D: Clustered objects with irregular shapes

NOTE: Three different methods of segmentation apply to each image: firstly, **HK-means clustering** combined with the **Active Contours method** is applied. Then, the **classical watershed algorithm** (using the Euclidian distance map) is applied to previously mis-segmented objects. Finally, a **marker-based watershed algorithm** is used. Only HK-means and marker-based watershed methods need user intervention. For both methods, the same parameters can be applied for all images (fully automated version) or be changed for each image (semi-automated version). If the user is not trained in these segmentation methods, the semi-automated processing is highly recommended. During the processing of this block, manual intervention is needed. When a segmentation method is finished, the user must manually remove mis-segmented objects before the beginning of the next segmentation method. Successfully segmented objects are saved and not considered in the next step(s). This block has to be connected with the block **Clustered/heterogeneous shapes primary objects segmentation Dialog Box** to work correctly.

1. Download the ImageJ collection MorphoLibJ on <https://github.com/ijpb/>

MorphoLibJ/releases. The MorphoLibJ 1.4.0 version is used in this protocol. Place the file **MorphoLibJ_-1.4.0.jar** in the folder `icy/ij/plugins`. More information about the content of this collection is available on <https://imagej.net/MorphoLibJ>.

2. Follow the same steps as in step 5.3.1 to set parameters of boxes **Channel signal**, **Gaussian filter**, **Active Contours**, **Extension to save segmented objects** and **Text**. Boxes ranks are not the same as in step 5.3.1.
3. Set parameters of the box **Adaptive histogram equalization** (see step 5.3.2.3).
4. To activate **Subtract Background**, write **yes** in **Apply Subtract Background?** (box 5). Else, write **No**. If the plugin is activated, set the rolling parameter (see step 5.3.2), in the box **Subtract Background parameter** (box 7).
5. **Automatization of HK-means:** To apply the same parameters for all images (fully automated processing), set the **Nb of classes** (box 11), the **Minimum size** (box 12), and the **Maximum size** (box 13) (see step 5.3.1). These parameters must be set to select a maximum of foreground pixels and to optimize the individualization of foreground objects. For the semi-automated processing version, no intervention is needed.
6. **Automatization of marker extractions:** for the fully-automated version, expand the box **Internal Markers extraction** (box 27) and set the value of the “dynamic” parameter in line 13 of the script. For the semi-automated processing version, no intervention is needed.

NOTE: Markers are extracted by applying an extended-minima transformation on an input image controlled by a “dynamic” parameter. In the marker-based watershed algorithm, flooding from these markers is simulated to perform object segmentation. For the successful segmentation of foreground objects, one single marker per foreground object should be extracted. The setting of the “dynamic” parameter for optimal markers extraction depends mostly on the resolution of images. Thus, if being not familiar with this parameter, use the semi-automated version.

7. Run the workflow (for details, see part 7).
8. At the beginning of the processing, dialog boxes **HK-means parameters** and **Marker-based watershed** successively open. To apply the same parameters for all images (fully-automated version), click on **YES**. Otherwise, click on **NO**. An information box opens, asking to “Determine optimal ROIs with HK-Means plugin and close image”. Click on **OK** and manually apply the HK-Means plugin (**Detection and Tracking|HK-Means**) on the image, which automatically opens. Select the **Export ROIs** option in the HK-Means plugin box. Apply the best parameters to have ROIs containing a maximum of foreground pixels and to optimize the individualization of foreground objects. When optimal ROIs are found, directly close the image.
9. At the end of the first segmentation method, an information box opens and asks to “Remove unwanted ROIs and close image”. These ROIs correspond to the borders of the segmented

objects. Select **OK** and remove ROIs of mis-segmented objects in the image, which automatically opens. An ROI can be easily removed by placing the cursor on its border and using the “Delete” button of the keyboard. Close the image. Repeat the same procedure after completion of the second segmentation step.

10. At this stage, if the YES button was selected for the full-automatization of the marker-based watershed algorithm, the previously set parameters will be applied to all images.
11. If the NO button was selected, an information box opens, asking to “Determine and adjust internal markers”. Click on **OK** and within the ImageJ interface of Icy, go to **Plugins | MorphoLibJ | Minima and Maxima|Extended Min & Max**. In Operation, select **Extended Minima**.
12. Select **Preview** to pre-visualize on the automatically opened image the result of the transformation. Move the dynamic until optimal markers are observed. Markers are groups of pixels with a value of 255 (Not necessarily white pixels). Optimal parameters lead to one marker per object. Focus on the remaining objects that have not been well segmented with the two previous segmentation methods.
13. If necessary, improve the markers by applying additional morphological operations like “Opening” or “Closing” (**Plugins | MorphoLibJ | Morphological Filters**). When getting the final image of markers, keep it open and close all the other images ending with the image initially used as an input for the **Extended Minima** operation.

Click on **No** if an ImageJ box asks to save changes on this image.

14. In the box **Nb of images with Information Box** (box 14), determine how many images with Information Boxes should appear.

4. Segmentation E: Clustered cytoplasm

NOTE: This block uses previously segmented nuclei as individual markers to initiate cytoplasm segmentation. Be sure that the block of nuclei segmentation has processed before using it.

1. In the box **Channel cytoplasm** (box 1), set the channel of the cytoplasmic signal.
2. In the box **Extension segmented nuclei** (box 2), write the format used to save images of segmented nuclei (tif, jpeg, bmp, png). The default format is tif.
3. In the box **Text** (box3), write the \Name of the folder containing segmented nuclei.
4. In the box **Format of images of segmented cytoplasms** (box 4), set the format to use for saving segmented objects images (Tiff, Gif, Jpeg, BMP, PNG).
5. During the process, a folder is automatically created to save images of segmented cytoplasms. In the box **Text** (box 5), name this folder (ex: Segmented cytoplasms). The folder is created in the folder containing merged images.
6. Follow the same steps as in step 5.3.1 to set parameters of boxes **Gaussian filter** and **Active Contours** (Be careful, box ranks are not the same as in step 5.3.1).
7. Run the workflow (for details, see part 7).

6. Fluorescent signal detection and analysis

1. Select the adapted block.
 1. In the block **Fluorescence Analysis A: 1 Channel**, perform detection and analysis of foci in one channel inside one type of segmented object: detection of coilin foci (red channel) within the nucleus.
 2. In the block **Fluorescence Analysis B: 2 Channels in the same compartment**, perform detection and analysis of foci in two channels inside one type of segmented object: detection of coilin (red channel) and 53BP1 (green channel) foci within the nucleus.
 3. In the block **Fluorescence Analysis C: 2 Channels in two compartments**, perform detection and analysis of foci in one or two channels, specifically inside the nuclei and their corresponding cytoplasm: detection of Coilin foci (red channel) both within the nucleus and its corresponding cytoplasm or detection of Coilin foci (red channel) within the nucleus and G3BP foci (green channel) within the corresponding cytoplasm.
 4. In the block **Fluorescence Analysis D: Global Translocation**, calculate the percentage of signal from one channel in two cellular compartments (a and b). For example, in a cytoplasm/nucleus translocation assay, export calculated percentages of nuclear and cytoplasmic signals for each image in the final “Results” spreadsheet. The formula used to calculate the nuclear signal percentage is shown below. This block can be used for any subcellular compartment:

$$\% \text{ nuclear signal} = \frac{\text{Sum of all nuclei signals} \times 100}{(\text{Sum of all nuclei signals} + \text{Sum of all cytoplasmic signals})}$$
 5. In the block **Fluorescence Analysis E: Individual Cell Translocation**, calculate the percentage of

signal from one channel in two cellular compartments for each cell. This block is specially optimized for nucleus/cytoplasm translocation assay at the single-cell level.

NOTE: Because the block **Fluorescence Analysis E: Individual Cell Translocation** performs analysis at the single-cell level, efficient segmentation of nucleus and cytoplasm is needed.

2. Link the **output0** (File) of the block **Select Folder** (block 1) to the **folder** input (white arrows in black circles) of the chosen block.
3. Set the parameters of the chosen block.
 1. Fluorescence Analysis A: 1 Channel, Fluorescence Analysis B: 2 Channels in the same compartment and Fluorescence Analysis C: 2 Channels in two compartments
 1. In the box **Folder images ROI**, write the name of the folder containing images of segmented objects preceded by a backslash. (For example: \Segmented nuclei).
 2. In the box **Format of images of segmented objects** (box 2), write the format used to save images of segmented objects (tif, jpeg, bmp, png). The default format is tif.
 3. In the box **Kill Borders?**, write **Yes** to remove border objects. Otherwise, write **No**. The installation of the MorphoLibJ collection of ImageJ is required to use this function (see step 5.3.3).
 4. In the box(es) **Channel spots signal**, set the channel where spots have to be detected. In classical RGB images, 0=Red, 1=Green, and 2=Blue.

5. In the boxes **Name of localized molecule**, write the name of the molecule localizing into the spots. The number of fields to enter depends on the number of molecules.
 6. In the box(es) **Wavelet Spot Detector Block**, set spot detection parameters for each channel. Set the scale(s) (referred to spot size), and the sensitivity of the detection (a smaller sensitivity decreases the number of detected spots, the default value being 100 and the minimum value being 0). Exhaustive documentation of this plugin is available online: http://icy.bioimageanalysis.org/plugin/Spot_Detector. Parameters can also be manually defined in Icy (**Detection and Tracking | Spot Detector**).
 7. As an option, in the box **Filter ROI by size**, filter the segmented objects where spots are detected by setting an interval of size (in pixels). This step is especially useful to remove under- or over-segmented objects. To manually estimate the size of objects, see step 5.3.1. Default parameters do not include the filtering of ROIs by size. The block 2 Channels in two compartments contains two boxes: Filter nuclei by size (box 19) and Filter cytoplasm by size (box 46).
 8. Optionally, in the box **Filter spots by size**, filter the detected spots according to their size (in pixels) to remove unwanted artifacts. To manually estimate spot size, click on **Detection and Tracking** and open the **Spot detector** plugin. In **Output** options, select **Export to ROI**. Be careful that default parameters do not include filtering of spots by size, and that filtered spots are not taken into account for the analysis. The number of fields to enter depends on the number of channels.
 9. Optionally, in the box **Filter spots**, apply an additional filter (contrast, homogeneity, perimeter, roundness) on the detected spots. Be careful that default parameters do not include spot filtering and that filtered spots are not taken into account for the analysis. The number of fields to enter depends on the number of channels.
 10. Optionally, in the boxes **Spot size threshold**, set a threshold for the area (in pixels) of analyzed spots. The number of counted spots below and above this threshold is exported in the final **Results** spreadsheet. The number of boxes to be informed depends on the number of channels.
 11. Run the workflow (for details, see part 7). Data are exported in a **Results** spreadsheet saved in the folder containing merged images.
2. Fluorescence Analysis D: Global Translocation and Fluorescence Analysis E: Individual Cell Translocation:
 1. In the boxes **Folder images** (boxes 1 and 2), write the \Name of the folder containing images of segmented objects. In the block **Fluorescence Analysis D: Global Translocation**, the two types of ROI are identified as ROI a and ROI b. For the block **Fluorescence Analysis E: Individual Cell Translocation**, in **Folder images segmented nuclei** and **Folder images segmented cytoplasms** boxes, write the name

of the folder containing segmented nuclei and cytoplasms, respectively.

2. In the box **Channel signal** (box 3), enter the channel of the signal.
3. In the box **Format of images of segmented objects** (box 4), write the format used to save images of segmented objects (tif, jpeg, bmp, png). The default format is tif. The **Kill Borders** option is also available to remove border objects (see step 6.3.1).
4. Optionally, in boxes **Filter ROI by size**, filter the segmented objects by setting an interval of size (in pixels). This step could be useful to remove under- or over-segmented objects. To manually estimate object size, see step 5.3.1. There are two fields to enter, one per channel. Default parameters do not include ROI filtering by size.
5. Run the workflow (for details, see part 7). Export data in a spreadsheet **Results** saved in the folder containing merged images.

7. Run the protocol

1. To process one block in a run, remove the connection between the selected block and the block **Select Folder**. Place the wanted block at the 1st rank. On the upper left corner of the wanted block, click on the link directly to the right of **folder**. In the **Open** dialog box which appears, double-click on the folder containing the merged images. Then, click on **Open**. Click on **Run** to start the workflow. The processing can be stopped by clicking on the **Stop** button.
2. To process different blocks in a run, keep connections of chosen blocks with the block **Select Folder** (block 1).

Make sure that their rank allows the good processing of the workflow. For example, if a specific block needs segmented objects to process, be sure that the segmentation block processes before. Before running the workflow, remove unused blocks and save the new protocol with another name.

3. Click on **Run** to start the workflow. When the open dialog box appears, double-click on the folder containing the merged images. Then, click on **Open**. The workflow automatically runs. If necessary, stop the processing by clicking on the **Stop** button.
4. At the end of the processing, check that the message **The workflow executed successfully** appeared in the lower right-hand corner and that all the blocks are flagged with a green sign (**Figure 2b**). If not, the block and the inside box presenting the error sign indicate the element to correct (**Figure 2b**).

NOTE: After the workflow executed successfully, a new run cannot be directly started, and to process the workflow again, at least one block should be flagged with the sign “ready to process”. To change the state of a block, either delete and re-create a link between two boxes inside this block or simply close and re-open the protocol. If an error occurs during the processing, a new run can directly be started. During a new run, all the blocks of the pipeline are processed, even if some of them are flagged with the green sign.

Representative Results

All the described analyses have been performed on a standard laptop (64-bit, quad-core processor at 2.80 GHz with 16 GB random-access memory (RAM)) working with the 64-bit version of Java. Random-access memory is an important parameter to consider, depending on the amount

and the resolution of images to analyze. Using the 32-bit version of Java limits the memory to about 1300 MB, which could be unsuitable for big data analysis, whereas the 64-bit version allows increasing the memory allocated to Icy. **Figure 3** reports the time needed for segmentation for different types of images and different resolutions. It confirms that high resolution substantially increases the time of primary object segmentation.

The data presented in the next paragraphs demonstrate that the *Substructure Analyzer* workflow can be used to solve most of the common problematics encountered in cellular and molecular biology (cell counting, foci counting and analysis, translocation analysis).

Measurement in numerous cells of the precise proportion of molecules concentrated within a given compartment or the change of localization across subcellular domains can be a very cumbersome and error-prone task, especially when it is performed manually. **Figure 4** illustrates the ability of the workflow to rapidly and precisely quantify the well-described nuclear translocation of the transcription factor NFκB in response to TNFα stimulation. Images used for the analysis were graciously compiled by Ilya Ravkin (<http://www.ravkin.net/SBS/Image-Library.htm>) and are publicly available at the Broad Bioimage Benchmark Collection¹⁶. This set contains images of MCF7 and A549 cell lines treated with increasing concentrations of TNFα. The analysis has been performed on more than 40,000 cells and 96 images (48 images for each channel) from the MCF7 cell line (**Figure 4a**). The whole analysis (from the import of images to data saving) took 26 minutes. Each image corresponds to a specific TNFα concentration. The nuclear/cytoplasmic proportions of NFκB were homogeneous across all cells for a given image. For this reason, for each

image, the values of all nuclear or cytoplasmic pixels were summed to calculate the nuclear and cytoplasmic proportions of NFκB, and individualization of touching nuclei/cytoplasm during their segmentation was not required. DAPI images were processed in the **Segmentation C: Clustered objects with convex shapes** block to segment nuclei and the green channel was used to delineate the cytoplasm with the **Segmentation E: Clustered cytoplasm** block (**Figure 4b**). The **Fluorescence Analysis D: Global Translocation** block was used to export the sum of nuclear and cytoplasmic pixel values. The obtained data are represented in a dose-response curve (**Figure 4c**) and illustrate the increase of NFκB nuclear proportion after stimulation with increasing concentrations of TNFα.

The workflow not only analyzes the global intensity signal in different sub-cellular compartments but can also be used to detect foci and extract specific information about their features. **Figure 5a** illustrates the detection of P-bodies in individual cells by localizing the enhancer of mRNA decapping 4 (EDC4) protein. The **Segmentation A: Non clustered objects** block was used to segment nuclei that present a low level of clustering, the **Segmentation E: Clustered cytoplasm** block to delineate the cytoplasm and the **Fluorescence Analysis C: 2 channels in two compartments** to detect EDC4 foci. Segmented objects are identified (Segmented nuclei_0, Segmented cytoplasm_0), and multiple information is collected into the corresponding worksheet (Segmented nuclei Information and Segmented cytoplasm Information) like the EDC4 mean intensity or the number/size of detected bodies in each ROI (**Figure 5b**). Before being analyzed, detected bodies can be preliminarily filtered according to their area, which can be useful to exclude objects below the resolution power of the microscope. To estimate the size

of conserved objects, an additional area threshold can be introduced. Areas of all the detected bodies are reported in dedicated worksheets (Segmented nuclei_Distribution foci size, Segmented cytoplasms_Distribution foci size). In this example, we highlight the analysis of two cells (Segmented nuclei_0 and_1 and Segmented cytoplasm_0 and_1), where cytoplasmic EDC4 foci are detected. Note that even though the signal of the EDC4 protein is detected in both the nuclear and cytoplasmic compartments, only the cytoplasmic foci correspond to P-bodies. The nuclear signal most likely results from the cross-reactivity of the antibody used to perform immunofluorescence experiments. The size in pixels of each of the foci is given.

Then, as the effect of oxidative stress (OS) on Cajal Bodies was still unknown, we took advantage of the versatility of the workflow to study it during time kinetics (2 to 20 hours after OS induction with 500 μM H_2O_2) (**Figure 6**). Cajal Bodies are dynamic structures nucleating and dissolving within the nucleoplasm under the control of specific parameters like the transcription rate or cell cycle progression. Cajal Bodies were visualized by localizing their main structural and functional component, the coilin protein. Information about the number and the size of Cajal bodies were collected by studying 2300 individual cells from high-resolution images (3840X3072) containing 3 channels: DAPI (blue), 53BP1 (green) and coilin (red) (**Figure 6a**). Full processing took less than 1 h. Because nuclei presented convex shape and some of them were clustered, the block **Segmentation C: Clustered objects with convex shapes** was chosen to perform the segmentation. As OS is known to induce DNA double-strand breaks (DDSBs), the p53-binding protein 1 (53BP1), known to be an essential effector of DNA damage signaling pathways, was used as a marker to discriminate between stressed and non-stressed cells. Indeed, in the absence of DNA damages,

53BP1 is homogeneously distributed within the nucleoplasm, whereas following DNA damages, it concentrates on DDSBs, which form easily distinguishable foci in microscopy. The number and the size of both 53BP1 and coilin nuclear foci in each cell were analyzed by using the block **Fluorescence Analysis B: 2 Channels in the same compartment**. Firstly, the analysis of 53BP1 data helped to determine for each time point of the kinetics the best threshold to classify cells according to their stress status. Among the whole kinetics, OS induces a significant increase of the 53BP1 foci number with an 11-fold increase at 2, 4, and 8 h after the induction of OS (**Figure S1**). This effect is less pronounced at 6 h (6.5-fold) because of a higher initial level of DSB in non-stressed cells. Even after 20 h, a sustained increase remains (almost 6-fold). These data reflect the efficiency of the treatment to induce the OS and establish 53BP1 as an efficient stress-marker for both early and late observations in microscopy. On the other hand, a small proportion of stressed-cells with a low level of DDSBs was observed at each time point of the kinetics, suggesting that cells are not homogeneously stressed, enforcing the importance of using a stress marker in stress experiments. Based on the ROC analysis, an overall threshold of 17 53BP1 foci was selected to discriminate between stressed and unstressed cells throughout the kinetics (**Figure S1**).

Then the number and size of nuclear foci of coilin were analyzed according to the cell's stress status. A significant increase in the number of foci was observed 2, 4, and 6 h after stress induction (**Figure 6b**). The most sustained effect is observed at 2 h, the number of cells having more than 10 foci increasing from 0% in the unstressed cells to 75% in the stressed cells. Moreover, more than 25% of stressed cells of that time point had more than 20 coilin foci. This effect progressively decreases until 8 h. At 20 h, a small increase of the first and the third quartiles is observed, but data also

show that 84% and 80% of cells present less than 8 foci in non-stressed and stressed cells, respectively. These data show that OS also has late effects on parameters controlling the nucleation of Cajal Bodies, which might be different from early effects. Interestingly, careful analysis of the features of the coilin nuclear foci revealed that the observed increase of the number of coilin foci associates with a decrease in their size (**Figure 6c**). For instance, 2 h after OS induction, the proportion of coilin foci with an area below $0.2 \mu\text{m}^2$ increases from 26% to 64%. This effect decreases until 8 h, but, unlike Cajal Bodies' number, no significant change is observed at 20 h. This might reflect that early and late nucleoplasmic redistribution of Cajal Bodies are different events.

Altogether these data strongly suggest that OS changes the nucleation power of Cajal Bodies, inducing a nucleoplasmic redistribution into numerous smaller nuclear foci. Since nucleation of Cajal Bodies is driven by their protein and RNA components, this suggests that the OS effect might change the composition of Cajal Bodies. Within Cajal Bodies, the coilin protein interacts with several different protein partners such as components of the SMN complex and Sm proteins. These interactions often involved phosphodomains of coilin, and one can imagine that a modification of the structure of Cajal Bodies could be linked to changes in the phosphorylation status of coilin. Moreover, recent works demonstrated that Cajal Bodies are not randomly localized within the nucleus, and can affect gene expression through proximal association with specific gene loci¹⁷. Given all these facts, it would not be surprising if an effect on Cajal bodies' functionality would accompany changes in their structure. From these results, we can also ask if such Cajal Bodies' remodeling is a passive consequence of OS or participates

in the response by interacting with specific gene loci, for example.

To test if a change in coilin expression could alter its localization and change the nucleation of Cajal Bodies, we overexpressed an exogenous GFP-coilin fusion protein. Nuclei were not clustered, so segmentation was performed with the block **Segmentation A: Non clustered objects**. Then, to precisely quantify the number and size of the coilin foci (red signal, channel 1) according to the level of GFP-coilin (green signal, channel 2) overexpression, the block **Fluorescence Analysis B: 2 Channels in the same compartment** was used. The level of GFP-coilin was reflected by the mean intensity of the GFP signal in individual nucleus (**Figure 7a**). In cells with medium or high level of GFP-coilin overexpression (GFP intensity higher than 10), the number of Cajal Bodies per nucleus significantly increases with some nuclei displaying up to 21 foci (**Figure 7b**). We also noticed that the brightness (mean intensity) of Cajal Bodies considerably increases in parallel with the overexpression level leading to intensity saturation. Such saturated regions might thus mask the presence of smaller and fainter foci. In cells overexpressing a medium or high level of GFP-coilin, the size of Cajal Bodies also significantly increases, the median values rising from 1 to $2 \mu\text{m}^2$ (**Figure 7c**). Moreover, more than 25% of cells with a high GFP-coilin expression level present foci with an area larger than $2.5 \mu\text{m}^2$, whereas it never exceeds $0.8 \mu\text{m}^2$ in non-transfected cells. In conclusion, GFP-Coilin overexpression leads to a significant increase in both the number and size of Cajal Bodies. Since OS increases the number of Cajal Bodies but reduces their size, these data might reflect that OS effect on the structure of Cajal Bodies is most probably induced by a

change of their composition rather than by an effect on the cellular amount of coilin.

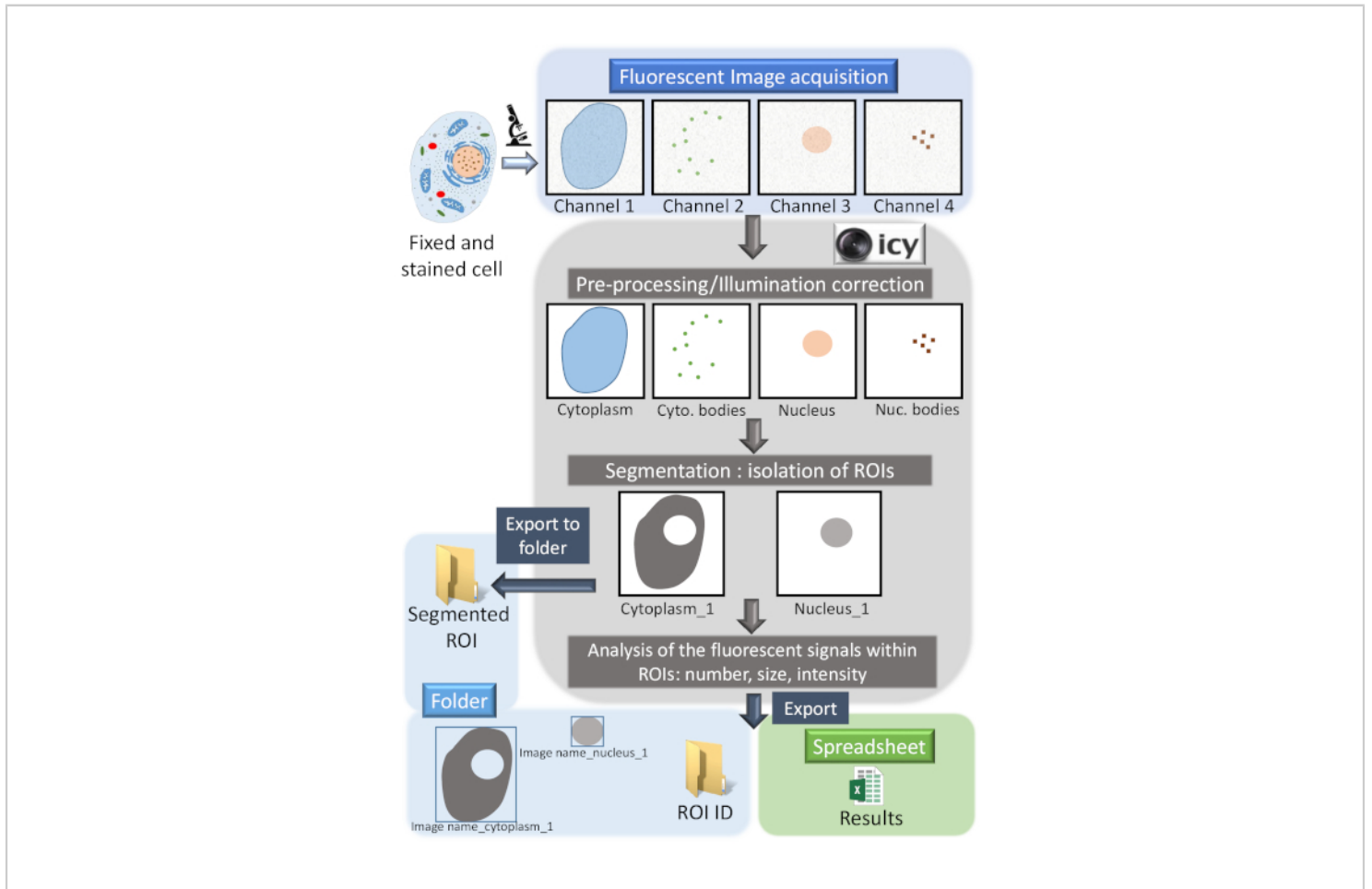


Figure 1: The *Substructure Analyzer* pipeline

The workflow is developed in Icy, an open community platform for bioimage informatics, and performs automatic analysis of multiple fluorescence microscopy images. Firstly, multi-channel images are automatically loaded within the protocol and pre-processed to improve, if necessary, the signal to noise ratio and to remove imaging artifacts. Then, image segmentation isolates regions of interest (ROIs) from the background. Several methods of segmentation are available depending on the level of clustering and the nature of the objects of interest. Segmented objects are saved with a specific descriptor (for example, Image name_Nucleus_1) in a specific folder and can be used/re-used for subsequent analysis. Fluorescent signals like spots are then analyzed within the ROIs and multiple features (location, size, shape, intensity, texture, spot number, and size) are exported into an automatically created spreadsheet. All the measured features, like the number of detected spots, are reported to the descriptor of the corresponding ROI. [Please click here to view a larger version of this figure.](#)

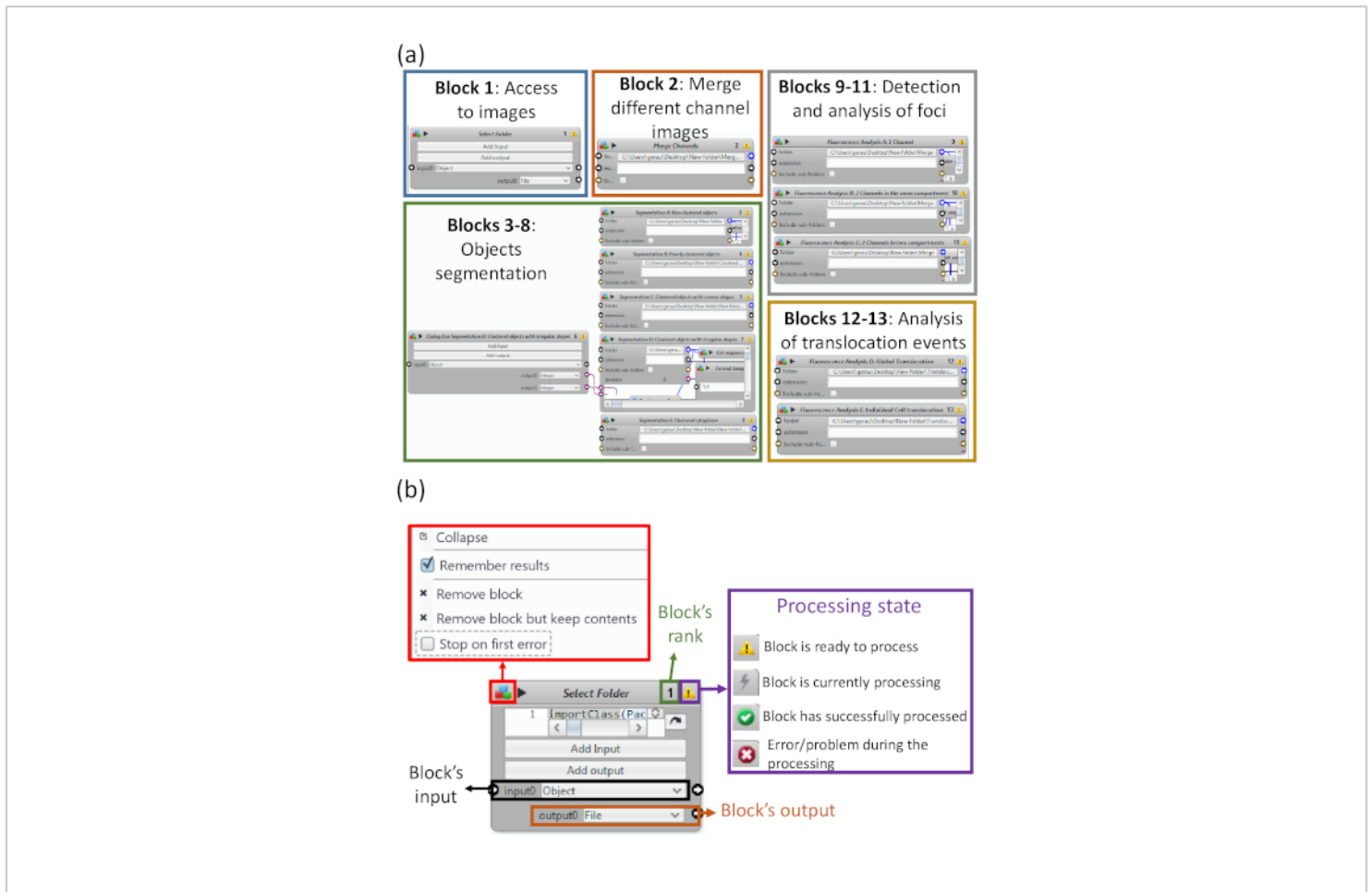


Figure 2: Graphical interface of the Icy workflow

(a) The workflow is composed of 13 general blocks, which can be grouped according to their general function: **Select Folder** (block 1) allow access to images; **Merge Channels** (block 2) is used to merge different channels of images. Blocks 3 to 8 are dedicated to object segmentation, each one being adapted for a specific context: **Segmentation A: Non clustered objects**, **Segmentation B: Poorly clustered objects**, **Segmentation C: Clustered objects with convex shapes**, **Segmentation D: Clustered objects with irregular shapes** (block 7, works in association with block 6), **Segmentation E: Clustered cytoplasms**. Blocks 9 to 11 are used to count/analyze foci within subcellular compartments: **Fluorescence Analysis A: 1 Channel**, **Fluorescence Analysis B: 2 Channels in the same compartment** and **Fluorescence Analysis C: 2 Channels in two compartments**. Blocks 12 and 13 are adapted for the analysis of translocation events: **Fluorescence Analysis D: Global Translocation** and **Fluorescence Analysis E: Individual Cell Translocation**. (b) Global presentation of a block architecture. [Please click here to view a larger version of this figure.](#)

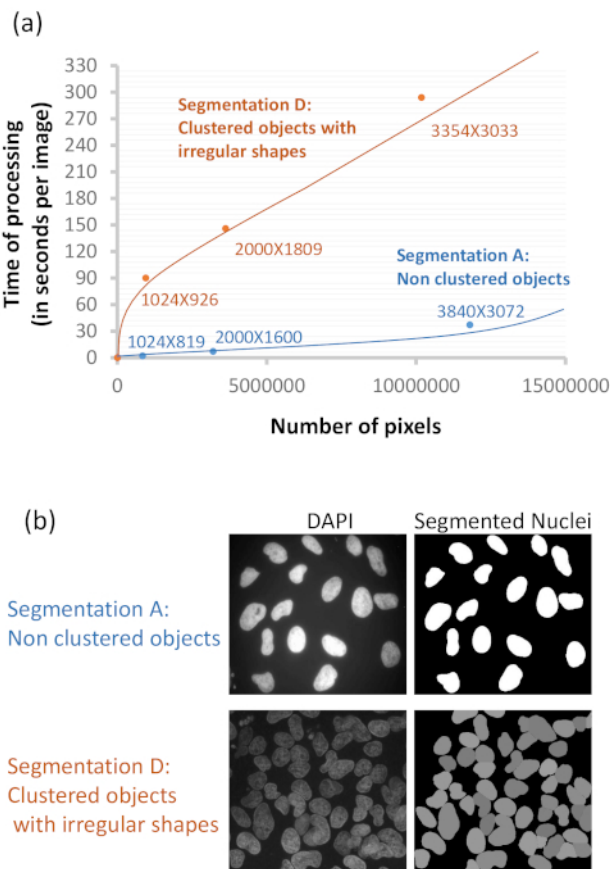


Figure 3: Time needed for segmentation as a function of image resolution and object clustering level

(a) Graphical illustration of the time needed to perform segmentation depending on image resolution and clustering level. Two different segmentation blocks have been tested: **Segmentation A** (for non-clustered objects) and **Segmentation D** (for clustered objects with irregular shapes). The time of processing (in seconds per image) is plotted as a function of image resolution (number of pixels). (b) Example of images analyzed with either **Segmentation A** or **Segmentation D** block. DAPI staining and segmented nuclei are indicated. [Please click here to view a larger version of this figure.](#)

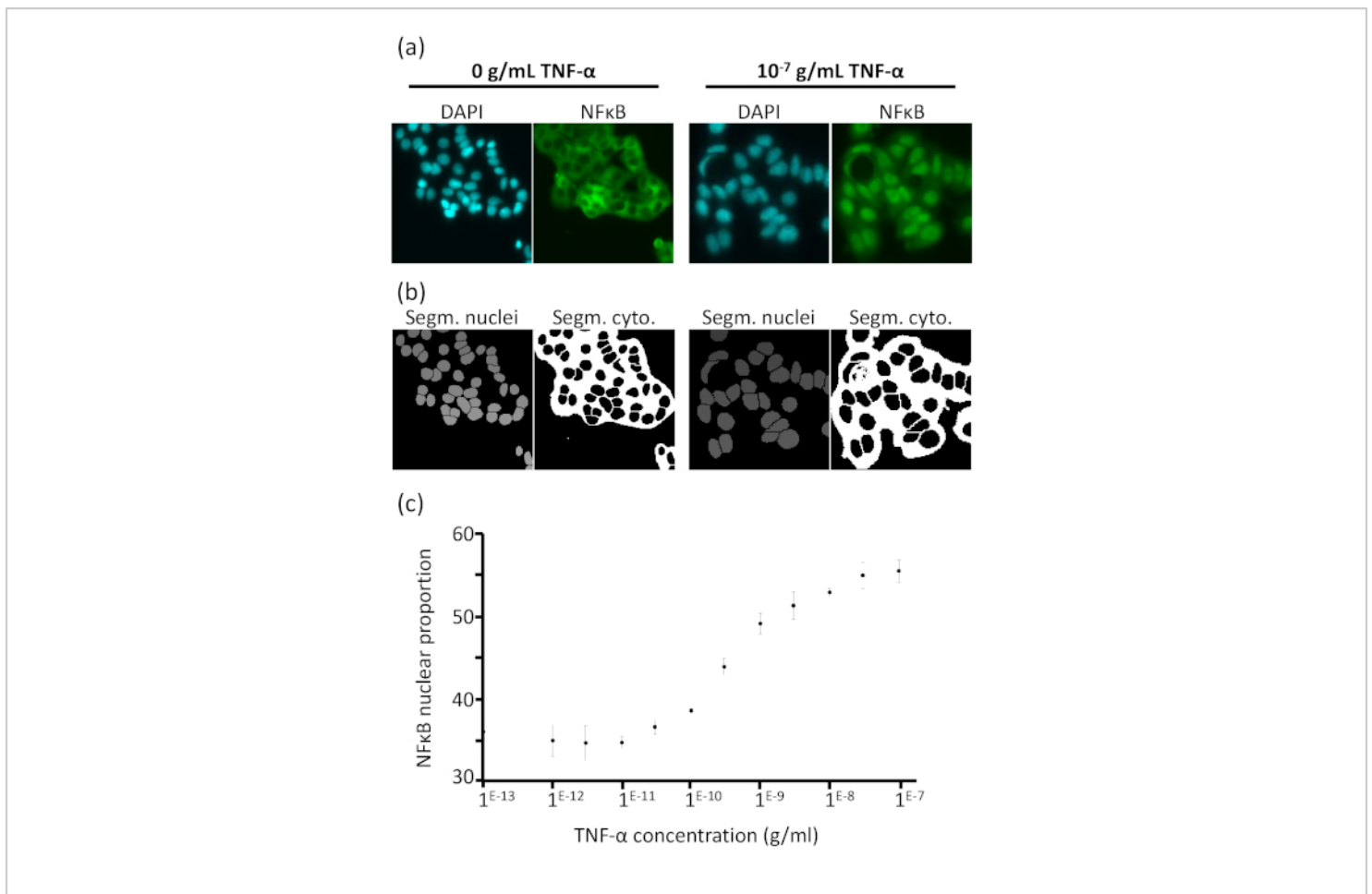


Figure 4: Workflow analysis of an NF κ B nuclear translocation assay in response to TNF α stimulation

(a) Example of images of human MCF7 cells (human breast adenocarcinoma cell line) treated with TNF α from the BBBC014 image set (Broad Bioimage Benchmark Collection)¹². Localization of the transcription factor NF κ B has been studied in cells treated with 12 increasing concentrations of TNF α (from 0 to 10⁻⁷ g/mL). For each concentration, 4 replicates were done. DAPI images (blue channel) were processed in the **Segmentation C: Clustered objects with convex shapes** block to segment nuclei, and then NF κ B staining with FITC (green channel) was used to delineate the cytoplasm with the **Segmentation E: Clustered cytoplasm** block. The **Fluorescence Analysis D: Global Translocation** block was used to export the sum of nuclear and cytoplasmic pixel values. (b) Segmented nuclei (grey) and cytoplasm (white) are used to determine the total intensity of the NF κ B fluorescent signal in each compartment. (c) The dose-response curve obtained from data analysis illustrates the increase of NF κ B nuclear proportion as TNF α concentration increases. Images are in an 8-bit BMP format, and the image size is 1360 x 1024 pixels. For each concentration, the standard deviation between the 4 replicates is calculated and illustrated as error bars. [Please click here to view a larger version of this figure.](#)

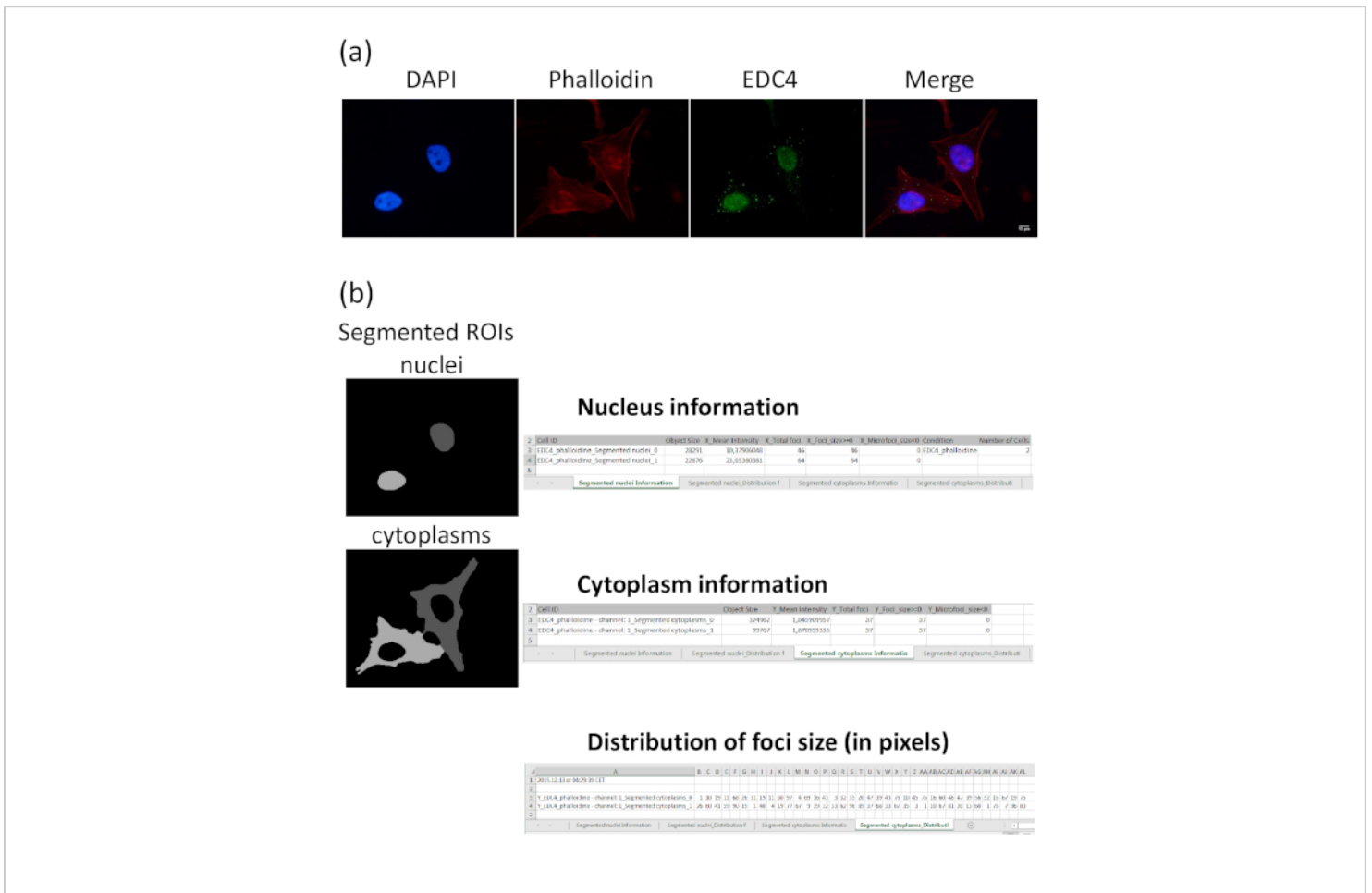


Figure 5: Quantification of EDC4 foci (P-bodies) within the cytoplasm in individual cells

(a) Co-staining with DAPI (blue channel) and Phalloidin (red channel) allows the segmentation and identification of cell nuclei and F-actin, respectively. The EDC4 protein (green channel) is used as a marker for the detection of P-bodies known to be exclusively cytoplasmic. Scale bar, 10 μ m. (b) Foci are counted, and several features (here their area in pixels) are exported to the *Results* spreadsheet structured in several sheets. Two sheets are dedicated to the analysis of nuclei and two to the analysis of cytoplasm. Each row embeds the information of a specific ROI. In *Nucleus/Cytoplasm Information* sheets, the characteristics of segmented objects are exported (ROI ID, size, and mean intensity), followed by the number of detected foci within each ROI. If necessary, a size threshold (100 pixels in this example) can be added, and the number of foci below and above this threshold is reported in the two last columns. In *Nucleus/Cytoplasm_Distribution of foci size* sheets, the area (in pixels) of all the detected foci is reported in the row of the corresponding ROI. In this example, we highlight the analysis of two cells (Segmented cytoplasm_0 and_1), where cytoplasmic EDC4 foci have been detected. The size in pixels of each of the foci is also given. [Please click here to view a larger version of this figure.](#)

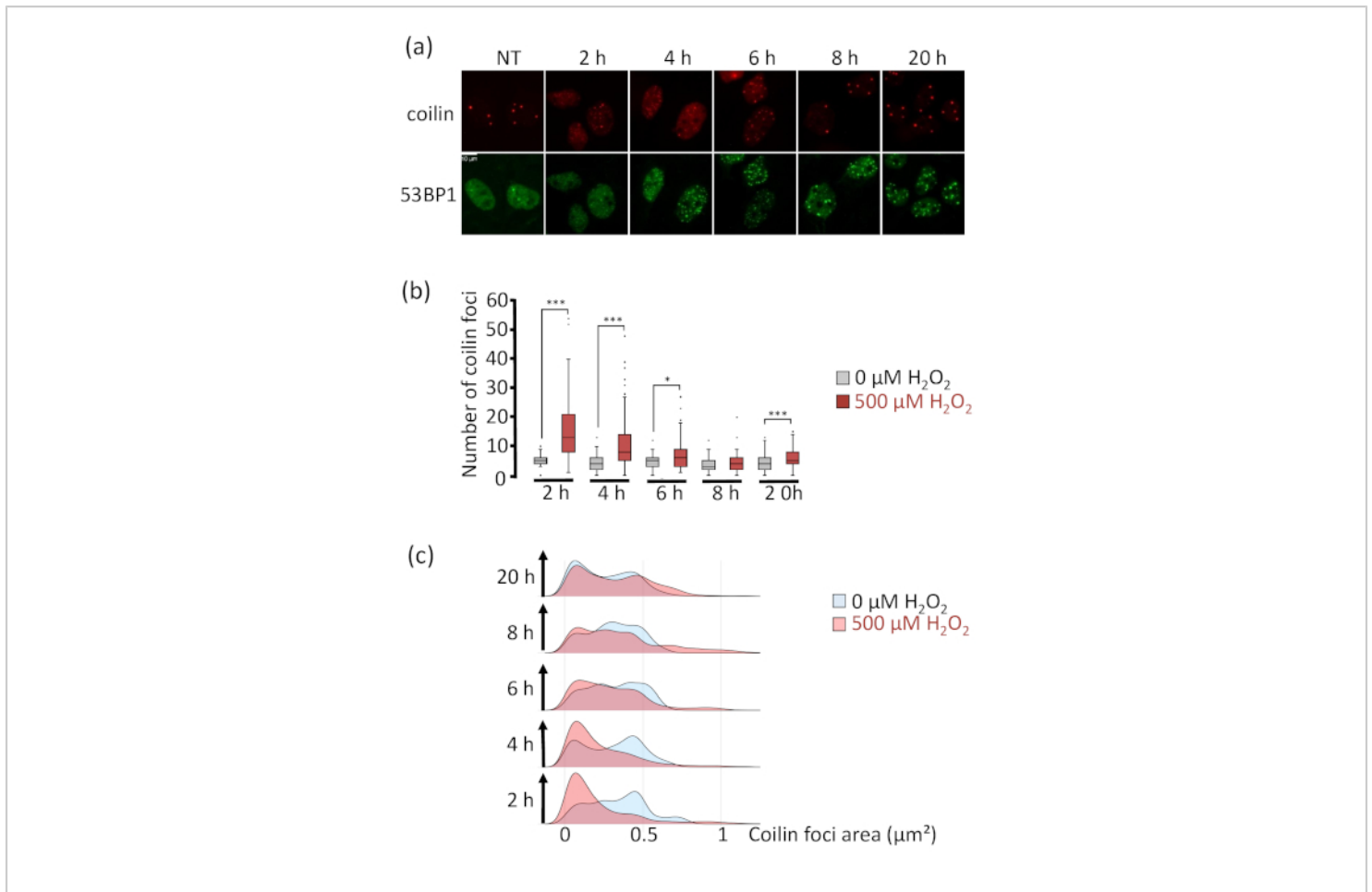


Figure 6: Kinetics of coilin and 53BP1 nucleoplasmic distribution after oxidative stress

The analysis of the number and size of foci was based on more than 110 individual cells for each time point from 3 independent kinetics. **(a)** Immunofluorescence detection of coilin and 53BP1 foci in HeLa S3 cells throughout treatment kinetics with 500 μM H_2O_2 . 53BP1 concentrates on DNA Double-Strand Break sites and is used to assess the efficiency of the treatment on each cell. Coilin is enriched in Cajal Bodies. Cells were fixed 2, 4, 6, 8, and 20 h after oxidative stress induction and co-stained with anti-coilin (red channel) and anti-53BP1 (green channel) antibodies. Scale bar, 10 μm . **(b)** The number of coilin nuclear foci after oxidative stress. Results are shown as box plots, where the central mark is the median, the lower and upper edges of the box are the 25th and 75th percentiles. In cells treated with H_2O_2 , a significant increase in the number of coilin foci is detected and is maximal after 2 and 4 h of treatment. Wilcoxon - Mann Whitney test analysis demonstrates a significant difference between untreated and H_2O_2 treated cells (*, $p < 0.05$; **, $p < 0.01$; ***, $p < 0.001$). **(c)** The proportion of cells in function of the coilin foci area (μm^2). Most foci have a smaller area at 2 h and 4 h time points as compared to the control. [Please click here to view a larger version of this figure.](#)

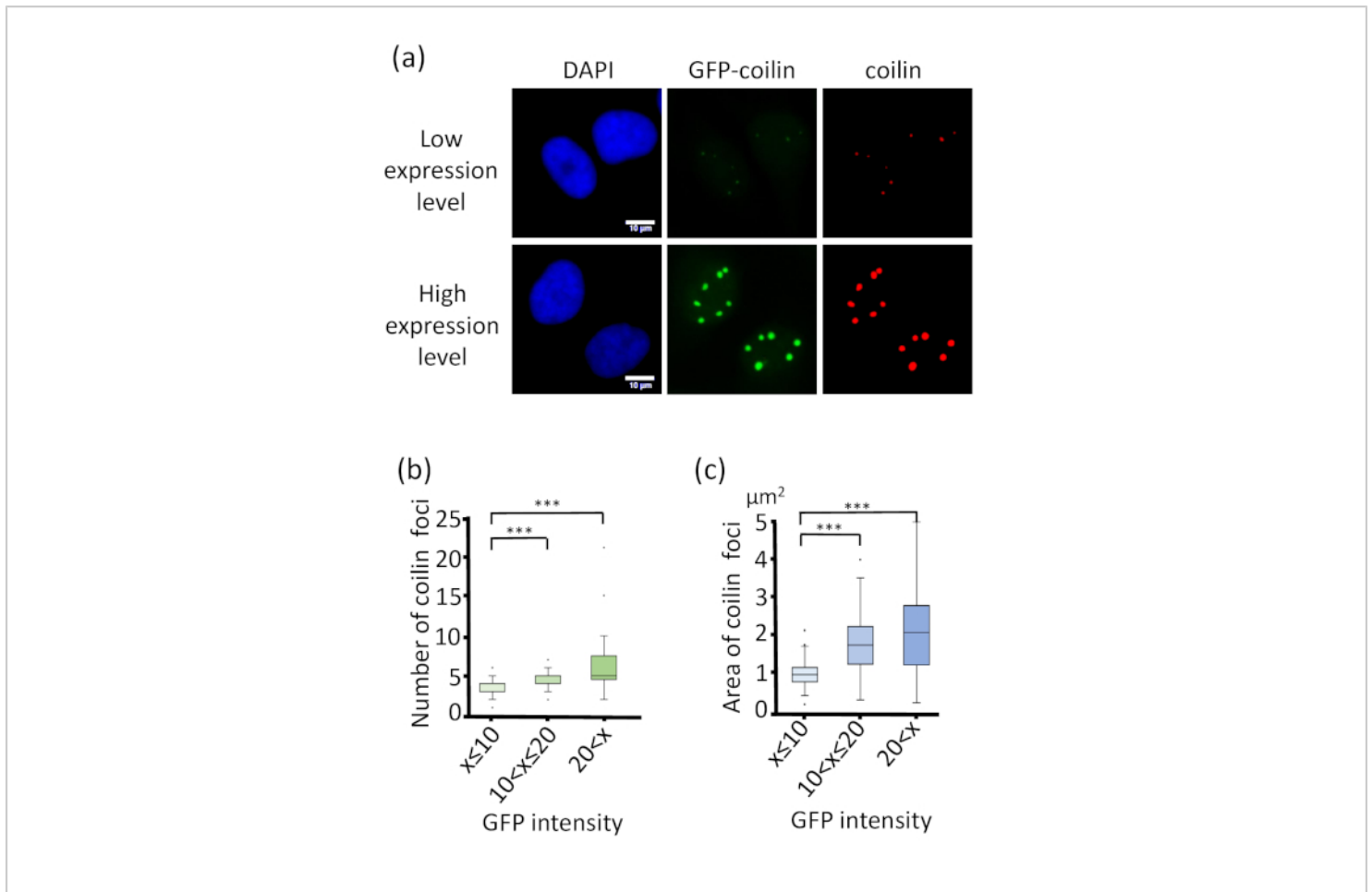


Figure 7: Study of Cajal Bodies' nucleation in cells overexpressing a GFP-coilin fusion protein

(a) HeLa S3 cells were transiently transfected in biological triplicates with 500 ng of a plasmid expressing a GFP-Coilin fusion protein using a standard procedure following the manufacturer's recommendations. After 48 h, cells were fixed and stained with an antibody against coilin. DAPI (blue channel) permits to segment nuclei. For these analyses, more than 100 cells were analyzed. GFP signal reflects ectopic coilin-GFP protein (green channel) localization, whereas the coilin signal (red channel) corresponds to both endogenous and exogenous protein localization. For each nucleus, the mean intensity of the GFP signal reflects the level of coilin expression. According to this parameter, the features of Coilin foci have been analyzed using the block **Fluorescence Analysis B: 2 Channels in the same compartment**. Scale bar, 10 μm . (b) Relationship between the number of coilin foci and mean GFP intensity per nucleus. Results are shown as box plots, where the central mark is the median, the lower and upper edge of the box are the 25th and 75th percentiles. Wilcoxon - Mann Whitney test analysis demonstrates a significant increase of the number of foci for a GFP intensity >10 (*, $p < 0.05$; **, $p < 0.01$; ***, $p < 0.001$). (c) Relationship between the area of coilin foci and mean GFP intensity per nucleus. Results are shown as box plots, where the central mark is the median, the lower and upper edge of the box are the 25th and 75th percentiles. Wilcoxon - Mann Whitney

test analysis demonstrates a significant increase of the area of coilin foci for a GFP intensity >10 (*, $p < 0.05$; **, $p < 0.01$; ***, $p < 0.001$). [Please click here to view a larger version of this figure.](#)

Figure S1: Kinetics of 53BP1 nucleoplasmic distribution after oxidative stress

(a) Quantification of 53BP1 nuclear foci in untreated or H₂O₂ treated cells after different incubation times. Results are shown as box plots, where the central mark is the median, the lower and upper edge of the box are the 25th and 75th percentiles. Wilcoxon - Mann Whitney test analysis demonstrates a significant difference between untreated and H₂O₂ treated cells (*, $p < 0.05$; **, $p < 0.01$; ***, $p < 0.001$). (b) For each time point of the kinetics, a ROC (Receiver Operating Characteristic) curve has been established to determine the best threshold to discriminate between stressed and unstressed cells. The parameters of each test are reported in the table (Sensitivity, specificity, TP: true positive, TN: true negative, FP: false positive, FN: false negative). From these data, a global threshold of 17 53BP1 foci was determined to discriminate stressed from non-stressed cells through the kinetics. [Please click here to download this file.](#)

Discussion

An increasing number of free software tools are available for the analysis of fluorescence cell images. Users must correctly choose the adequate software according to the complexity of their problematic, to their knowledge in image processing, and to the time they want to spend in their analysis. Icy, CellProfiler, or ImageJ/Fiji are powerful tools combining both usability and functionality³. Icy is a stand-alone tool that presents a clear graphical user interface (GUI), and notably its “Protocols” point and click interface through which workflows can be easily designed or manipulated⁴. The functionality of this software is enhanced by supporting and utilizing ImageJ

plug-ins, and a lot of documentation is available thanks to its large community of users. We used this strong combination of usability and functionality of the Icy software to develop the *Substructure Analyzer* workflow. Its main objective is to propose an automated solution to perform a full analysis of cell fluorescent signal from multiple images. The analysis encompasses image pre-processing, object segmentation, and fluorescent signal analysis.

Several protocols are gratefully shared on the Icy website and propose to use Icy functionalities to detect and analyze fluorescent signals like cellular foci. However, some of these protocols only process one image per run, do not export the results in a specific file or analyze a single channel. Others do not contain preliminary segmentation to determine regions of interest (ROIs) or propose simple algorithms like “HK-means” that are not suited for the segmentation of highly clustered objects. *Substructure Analyzer* automates all the steps of the image analysis from image pre-processing to the segmentation of objects and the detection/analysis of fluorescent signals. The protocol also proposes simple or more complex methods for object segmentation and export of the data (names of the segmented objects, foci analysis) is realized in optimized outputs adapted to the problematic. CellProfiler also proposes powerful pipelines composed of modules that encapsulate functionalities^{18, 19}. The available pipelines are well adapted to specific problems. Icy workflows are a network of different boxes, each of them performing a specific task. Through the “Protocols” interface, boxes composing the network are intuitive and easy to manipulate. *Substructure Analyzer* is adapted to several contexts like the simple merging of channels, the quantification of fluorescent

signals distribution between two subcellular compartments, the analysis of foci in one or several channels from one or two cellular compartments in individual cells. Several displays allow visualizing the intermediate results during each run to control the processing. Moreover, Icy presents icon bars that group the methods by topic and from which functionalities found in the workflow can be separately manipulated to manually test specific parameters on some images before using them on a whole image set.

Like in the bioimage analysis field, the most critical step of this protocol is the object segmentation. The protocol proposes the segmentation of primary objects, which are most of the time cell nuclei, and also contains another block which task is to segment a second type of objects within the cell. Nuclei segmentation can be difficult when the objects are highly clustered so that they touch or overlap together. Different alternatives for the segmentation of primary objects are contained in the protocol, according to the shape of the objects and the level of clustering even if to date no universal algorithm success in the full segmentation of highly clustered objects. The segmentation process is mainly limited by the determination of correct parameters that could successfully segment a part of the objects but lead to under- or over-segmentation of another part. The user would have to perform different runs with different parameters to get a final correct segmentation, especially for clustered objects presenting heterogeneous and non-convex shapes.

This protocol is mostly limited by the segmentation step, which could be highly time consuming and need powerful computer configuration for the most complex cases. More specifically, the more numerous or complex the images are (clustered objects to segment, a high number of pixels in the images), the more random-access memory (RAM) the

user will require. Globally, for any problematic, the user will need to run the protocol on a 64 bits Java Runtime Environment (freely available on Java website) and to use a 64 bits operating system (OS) to increase the available memory used by Icy (memory is limited to 1300 MB for 32 bits JRE). Because of the script, the protocol does not work correctly on a Mac computer. Moreover, the number of parameters increases with the complexity of the problem and will require more knowledge in image analysis. Concerning the functionality criteria, this protocol has not yet been adapted for the analysis of stacked images (time stacks, z-stacks) even if Icy efficiently performs analysis on this type of data.

Future updates will be realized notably to improve the segmentation of complex clustered objects. Additional blocks will be developed to adapt the segmentation to clustered cellular structures with irregular non-convex shapes. We will also adapt the workflow for the analysis of time and z-stacks (for live imaging and 3D data).

Disclosures

The authors have nothing to disclose.

Acknowledgments

G.H. was supported by a graduate fellowship from the Ministère Délégué à la Recherche et aux Technologies.

L.H. was supported by a graduate fellowship from the Institut de Cancérologie de Lorraine (ICL), whereas Q.T. was supported by a public grant overseen by the French National Research Agency (ANR) as part of the second “Investissements d’Avenir” program FIGHT-HF (reference:

ANR-15-RHU4570004). This work was funded by CNRS and Université de Lorraine (UMR 7365).

References

1. Möckl, L., Lamb, D.C., Bräuchle, C. Super-resolved fluorescence microscopy: Nobel Prize in Chemistry 2014 for Eric Betzig, Stefan Hell, and William E. Moerner. *Angewandte Chemie*. 53 (51), 13972-13977 (2014).
2. Meijering, E., Carpenter, A.E., Peng, H., Hamprecht, F.A., Olivo-Marin, J.-C. Imagining the future of bioimage analysis. *Nature Biotechnology*. 34 (12), 1250-1255 (2016).
3. Wiesmann, V., Franz, D., Held, C., Münzenmayer, C., Palmisano, R., Wittenberg, T. Review of free software tools for image analysis of fluorescence cell micrographs. *Journal of Microscopy*. 257 (1), 39-53 (2015).
4. de Chaumont, F. et al. Icy: an open bioimage informatics platform for extended reproducible research. *Nature Methods*. 9 (7), 690-696 (2012).
5. Girish, V., Vijayalakshmi, A. Affordable image analysis using NIH Image/ImageJ. *Indian J Cancer*. 41(1):47 (2004).
6. Zaitoun, N. M., Aqel, M. J. Survey on image segmentation techniques. *Procedia Computer Science*. 65, 797-806 (2015).
7. Devices, M. *MetaMorph Microscopy Automation and Image Analysis Software*. <https://www.moleculardevices.com/products/cellular-imaging-systems/acquisition-and-analysis-software/metamorph-microscopy> (2018).
8. Nikon. *NIS-Elements Imaging Software*. https://www.nikon.com/products/microscope-solutions/lineup/img_soft/nis-element (2014).
9. Meyer, F., Beucher, S. Morphological segmentation. *Journal of Visual Communication and Image Representation*. 1 (1), 21-46 (1990).
10. Schieber, M., Chandel, N.S. ROS Function in Redox Signaling and Oxidative Stress. *Current Biology*. 24 (10), R453-R462 (2014).
11. D'Autréaux, B., Toledano, M.B. ROS as signalling molecules: mechanisms that generate specificity in ROS homeostasis. *Nature Reviews. Molecular Cell Biology*. 8 (10), 813-824 (2007).
12. Davalli, P., Mitic, T., Caporali, A., Lauriola, A., D'Arca, D. ROS, Cell Senescence, and Novel Molecular Mechanisms in Aging and Age-Related Diseases. *Oxidative Medicine and Cellular Longevity*. 2016, 3565127 (2016).
13. Disher, K., Skandalis, A. Evidence of the modulation of mRNA splicing fidelity in humans by oxidative stress and p53. *Genome*. 50 (10), 946-953 (2007).
14. Takeo, K. et al. Oxidative stress-induced alternative splicing of transformer 2 β (SFRS10) and CD44 pre-mRNAs in gastric epithelial cells. *American Journal of Physiology - Cell Physiology*. 297 (2), C330-C338 (2009).
15. Seo, J. et al. Oxidative Stress Triggers Body-Wide Skipping of Multiple Exons of the Spinal Muscular Atrophy Gene. *PLOS ONE*. 11 (4), e0154390 (2016).
16. Will, C.L., Luhrmann, R. Spliceosome Structure and Function. *Cold Spring Harbor Perspectives in Biology*. 3 (7), a003707-a003707 (2011).

17. Ljosa, V., Sokolnicki, K.L., Carpenter, A.E. Annotated high-throughput microscopy image sets for validation. *Nature Methods*. 9 (7), 637-637 (2012).
18. Wang, Q. et al. Cajal bodies are linked to genome conformation. *Nature Communications*. 7 (2016).
19. Carpenter, A.E. et al. CellProfiler: image analysis software for identifying and quantifying cell phenotypes. *Genome Biology*. 7, R100 (2006).
20. McQuin, C. et al. CellProfiler 3.0: Next-generation image processing for biology. *PLoS Biology*. 16 (7), e2005970 (2018).

10.3. Discussion and conclusion

Substructure Analyzer is a highly modular workflow that could become an essential tool to every biologist. The feedback from users has highlighted a sometimes complex learning curve due to the unfamiliarity of the Icy interface. However, after a short training, users quickly become autonomous.

Substructure Analyzer has been extensively used to analyse the imaging experiments of the functional characterisation of fibroblasts from radiosensitive and radioresistant patients described in the following section.

11. Cytokeratin KRT7 and KRT18 gene expression predicts RISF

11.1. Introduction

Cytokeratins are a major subfamily of intermediate filament proteins. They are mainly described in epithelial cells. They are divided into two groups, the acidic type I cytokeratins encoded by 28 genes and the basic type II keratins encoded by 26 genes. They assemble into heterodimeric double-stranded coiled coils composed of one protein of each group. (175) Most of these proteins are cell-type or differentiation-state specific. They connect the nuclear membrane to the cytoplasmic membrane.

Among them, cytokeratin-7 (CK7) and -18 (CK18) are particularly associated with fibrosis. (176–181) CK7 is correlated with the expression of α -SMA in hepatic fibrosis (176,178) , and its expression can predict the severity of alcoholic liver fibrosis. (177) CK18 is particularly described in non-alcoholic fatty liver disease (NAFLD) (179,181), a fibrotic condition of the liver, and in hepatitis C liver fibrosis. (180)

Dogmatically described in epithelia, we were surprised to detect KRT7 and KRT18 mRNA in skin fibroblasts from SPLICI-Rad study patients after microarray analysis. Moreover, we evidenced the differential expression of 2 genes, KRT7 and KRT18, in primary skin fibroblasts from fibrosis-prone patients (n = 7) compared to those fibrosis-free patients (n = 5). The levels of KRT7 and KRT18 transcripts were 37.7 and 7 times lower in fibroblasts from radiosensitive patients compared to radioresistant ones, respectively, suggesting a role in RISF onset. The following article summarises our work regarding KRT7 and KRT18 expression as predictive markers of RISF. (182)

11.2. Article

[Article Full Title]

Cytokeratin KRT7 and KRT18 gene expression predicts radiation-induced skin fibrosis

[Short Running Title]

KRT7 & KRT18 predict skin fibrosis

[Author Names]

Liza Hettal¹, MSc, Raphaël Rouget¹, PhD, Quentin Thuillier¹, BSc, Elise Cérimèle², BSc, Priscillia Tosti³, PhD, Aurélie François², MSc, Isabelle Behm-Ansmant^{1*}, PhD, and Guillaume Vogin^{1,2,4*}, MD, PhD.

[Author Institutions]

¹ Université de Lorraine, CNRS, IMoPA, F-54000 Nancy, France

² Institut de Cancérologie de Lorraine, CNRS, Université de Lorraine, 6 Avenue de Bourgogne, 54519, Vandoeuvre-lès-Nancy, France.

³ Clinical Trials Promotion Unit, Institut de Cancérologie de Lorraine, Vandoeuvre-Les-Nancy, France

⁴ Centre François Baclesse, Centre National de Radiothérapie du Grand-Duché du Luxembourg, Esch Sur Alzette, Luxembourg

[Corresponding Author Name & Email Address]

Isabelle Behm-Ansmant: isabelle.behm@univ-lorraine.fr

Guillaume Vogin: guillaume.vogin@univ-lorraine.fr

[Author Responsible for Statistical Analysis Name & Email Address]

Liza Hettal: liza.hettal@univ-lorraine.fr

[Conflict of Interest Statement for All Authors]

All authors declare no conflict of interest.

[Funding Statement]

This work was supported by funding from the Institut de Cancérologie de Lorraine and the Ligue contre le Cancer (Fibroscreen project).

[Clinical trial information]

SPLICI-Rad study is registered in Clinical Trial.gov under NCT03000764. SPLICI-Rad study was approved by the national ethical committee (CPP EST III 16.05.01). All the patients were informed and gave a signed consent according to the ethics recommendations.

[Data Availability Statement for this Work]

Research data are stored in an institutional repository and will be shared upon request to the corresponding authors.

[Acknowledgements]

We thank members of the 'RNA-RNP team' and Michele Martin (LGRK – CEA) for helpful discussions and technical advice. We thank Foray's lab (U1296 - Inserm) for the generous gift of radiosensitive primary cells. The Flow Cytometry-Cell Biology Core Facility of UMS2008 IBSLor is thanked for the access to the Gallios flow cytometer. CNRS and Université de Lorraine are also thanked for their institutional support.

[Article Full Title]

Cytokeratin KRT7 and KRT18 gene expression predicts radiation-induced skin fibrosis

[Short Running Title]

KRT7 & KRT18 predict skin fibrosis

[Author Names]

XXX

[Author Institutions]

XXX

[Corresponding Author Name & Email Address]

XXX

[Author Responsible for Statistical Analysis Name & Email Address]

XXX

[Conflict of Interest Statement for All Authors]

All authors declare no conflict of interest.

[Funding Statement]

This work was supported by funding from XXX and XXX.

1
2
3
4
5
6
7
8
9
10
11
12

[Clinical trial information]

XXX is registered in Clinical Trial.gov under NCTXXX. XXX was approved by the national ethical committee (XXX). All the patients were informed and gave a signed consent according to the ethics recommendations.

13
14

[Data Availability Statement for this Work]

15
16
17
18
19
20
21
22

Research data are stored in an institutional repository and will be shared upon request to the corresponding authors.

23
24
25

[Acknowledgements]

26
27
28
29
30
31
32
33
34
35
36
37
38
39
40
41
42
43
44
45
46
47
48
49
50
51
52
53
54
55
56
57
58
59
60
61
62
63
64
65

We thank members of XXX and Michele Martin (LGRK – CEA) for helpful discussions and technical advice. We thank XXX for the generous gift of radiosensitive primary cells. The Flow Cytometry-Cell Biology Core Facility of XXX is thanked for the access to the Gallios flow cytometer. XXX and XXX are also thanked for their institutional support.

Abstract

Radiation-induced skin fibrosis (RISF) is a severe and irreversible skin late effect after radiotherapy. Here, we identified KRT7 and KRT18, as differentially expressed between healthy skin fibroblasts from patients with or without RISF. Their expression can discriminate patients at risk for RISF and may predict the onset of RISF.

Introduction

Breast cancer is the most frequently diagnosed cancer in women, with about 685 000 associated deaths worldwide and 2.3 million new cases yearly. ¹ Adjuvant radiotherapy (RT) is indicated in 80% of newly diagnosed non-metastatic breast cancers or ductal carcinoma in situ to improve local control and overall survival. ² However up to 48% and 18% of the patients experience grade ≥ 2 early and late skin toxicity respectively even with up-to-date RT techniques^{3,4}.

In particular, radiation-induced skin fibrosis (RISF) - the most clinically apprehensible and uncomfortable skin late effect - is characterised by an excess of collagen in the dermis, resulting in an irreversible increase of connective tissue stiffness with a loss of tissue function at the irradiated site. Predicting the onset of RISF with accurate risk factors is complex and challenging to achieve personalised cancer treatment.

Cytokeratins are a major subfamily of intermediate filament proteins. They are mainly described in epithelial cells. They are divided into two groups, the acidic type I cytokeratins encoded by 28 genes and the basic type II keratins encoded by 26 genes. They assemble into heterodimeric double-stranded coiled coils composed of one protein of each group. ⁵ Most of these proteins are cell-type or differentiation-state specific. They connect the nuclear membrane to the cytoplasmic membrane. Among them, cytokeratin-7 (CK7) and -18 (CK18) are particularly associated with fibrosis. ⁶⁻¹¹ CK7 is correlated with the expression of α -SMA in hepatic fibrosis ^{6,8}, and its expression can predict the severity of alcoholic liver fibrosis. ⁷ CK18 is particularly described in non-alcoholic fatty liver disease (NAFLD) ^{9,11}, a fibrotic condition of the liver, and in hepatitis C liver fibrosis. ¹⁰

Here, we identified their respective coding genes, KRT7 and KRT18, as differentially expressed between healthy skin fibroblasts from patients with or without RISF. Their expression can discriminate patients at risk for RISF and may predict the onset of RISF.

Material and methods

This study was conducted on 12 primary adult skin fibroblast cultures. Ten primary fibroblast cultures, including 6 primary cultures derived from radioresistant patients (RISF-free) and 4 primary cultures derived from radiosensitive patients (RISF-prone), originated from XXX (NCTXXX). Two primary radiosensitive cultures were generously gifted.¹² Detailed clinical characteristics of the patients are listed in Table 1. Clinical data on tumour characteristics and therapy regimens were extracted from the medical records.

Clinical Radiosensitivity status of the primary cells

Radiosensitive primary cells were derived from patients with severe RISF (grade ≥ 3 , CTCAE v4.0 scale¹³) between 6 months and 5 years after the completion of RT while radioresistant cultures were raised from patients with no skin toxicity at 5 years after RT (grade ≤ 1 , CTCAE v4.0 scale).

Skin biopsy procedure

Skin biopsy specimens have been collected from the arm opposite to the irradiated breast (unirradiated area), using a 12G dermal punch after local anaesthesia. After sampling, fibroblast primary cultures were derived according to standard procedures.¹²

Cell culture

All fibroblast primary cultures were grown in DMEM medium (Dulbecco's Modified Eagle Medium, Sigma-Aldrich) supplemented with 20% FBS (Fetal Bovine Serum, Dutscher), 10U/ml penicillin/streptomycin (Sigma-Aldrich), and 2.9 mg/ml of L-glutamine (Sigma-Aldrich).

Reverse Transcription Quantitative Polymerase Chain Reaction (RT-qPCR)

1
2
3 Total RNA was isolated from early passage primary fibroblasts using TRIzol (Invitrogen) as described
4
5 elsewhere.¹⁴ DNase digestion was performed on 2 µg of total RNA using RQ1 DNase (Promega)
6
7 according to the manufacturer's recommendations. cDNA was prepared from 2 µg of total RNA using
8
9 Superscript III first strand synthesis kit (Invitrogen), in the presence of 40 U of Ribolock™. qRT-PCR was
10
11 performed on ViiA-7 Real-Time PCR system (Applied Biosystems) using SYBR Green-based detection
12
13 (iQ SYBR green supermix, Bio-Rad Laboratories) and oligonucleotides described in Table 2. The relative
14
15 quantification of mRNA expression was performed using the standard curve method. The expression
16
17 of the target gene was normalized to the expression of GAPDH.
18
19
20
21

Statistical analysis

22
23
24
25 All analyses were performed using R software (version 4.0.5). Radiosensitive and radioresistant groups
26
27 were compared using Mann-Whitney non-parametric tests. Association between a variable and a
28
29 phenotype was assessed using Chi² or Fisher's Exact tests. The significance threshold was set to $p <$
30
31 0.05. The classification performances were characterized on by five parameters: AUC, sensitivity index,
32
33 specificity index, the PPV and the negative predicted value (NPV) using the ROCit package¹⁵.
34
35
36
37
38
39
40
41
42
43
44
45
46
47
48
49
50
51
52
53
54
55
56
57
58
59
60
61
62
63
64
65

Results

We first took advantage of freely available transcriptomics data to check for cytokeratin gene expression in healthy primary fibroblasts.¹⁶ We found that a large panel of cytokeratin genes, encoding both type I and type II cytokeratins, is expressed in fibroblasts (Fig. 1A). Moreover, we evidenced the differential expression of 2 genes, KRT7 and KRT18, in primary skin fibroblasts from patients with RISF (n = 6) compared to those fibrosis-prone (n = 6). The levels of KRT7 and KRT18 transcripts were 37.7 and 7 times lower in radiosensitive fibroblasts compared to radioresistant ones, respectively (Fig. 1B-1C). Higher expression of KRT7 and KRT18 genes is significantly associated with a protection against the development of RISF (Chi² test, p < 0.05). The prognostic test associating the mRNA levels of KRT7 and KRT18 displays an AUC of 0.83 (Fig. 2). The test's performance metrics for the specificity, sensitivity, PPV and NPV were: 1.00, 0.71, 1.00 and 0.78, respectively.

Discussion

1
2
3
4 According to the critical need of personalised cancer treatments, the RT community is awaiting
5
6 prognostic biomarkers for individual propensity to develop high grade RISF.¹⁷ Here, we identified KRT7
7
8 and KRT18 gene expression as accurate and promising prognostic markers of RISF onset. Although
9
10 cytokeratin expression has never been reported in healthy fibroblasts to date, we are fully confident
11
12 that our data are not artefacts. Indeed, cytokeratin gene expression was established from both
13
14 previously published transcriptomics data and our primary skin fibroblast cultures for which cell
15
16 lineage contamination by keratinocytes was excluded after phenotype analysis by flow cytometry
17
18 (Supplementary Fig. 1). In epithelial cells, cytokeratins work as heterodimeric proteins enabling cells
19
20 to withstand mechanical stress. CK7 and CK18 dimerize with CK17 and CK8, respectively.¹⁸ Although
21
22 expressed in healthy fibroblasts (Fig. 1A), no significant variation in neither of these dimeric partners
23
24 was found in our data (data not shown), hinting a function of these proteins in monomeric or non-
25
26 canonical heterodimeric states in primary skin fibroblasts. Concerning the molecular bases of KRT7 and
27
28 KRT18, data from the study of Weigel *et al.*¹⁹ showed the absence of CpG methylation difference
29
30 around KRT7 and KRT18 genes, suggesting that it relies on another regulatory mechanism. Further
31
32 investigations will also be required to assess their contribution, if any, to RISF pathophysiology.
33
34 Recently, CK18 was shown to play a role in modulating the activation of PI3K/Akt/NF- κ B pathway
35
36 proteins under genotoxic stress in hepatocytes, which is an interesting lead regarding the effects of
37
38 RT.²⁰

39
40 We must underline that our findings rely on a limited number of patients due to the rarity of RISF
41
42 primary cell collections. National and European consortia appear necessary to gather large and diverse
43
44 biological collections to allow the validation of candidate biomarkers in RT toxicity prediction.
45
46
47
48
49
50
51
52
53
54
55
56
57
58
59
60
61
62
63
64
65

1
2
3
4
5
6
7
8
9
10
11
12
13
14
15
16
17
18
19
20
21
22
23
24
25
26
27
28
29
30
31
32
33
34
35
36
37
38
39
40
41
42
43
44
45
46
47
48
49
50
51
52
53
54
55
56
57
58
59
60
61
62
63
64
65

Conclusion

The expression of the KRT18 and KRT7 genes may emerge as potential prognostic factor in RISF. Evaluated individually prior RT, this marker could support RT prescription to prevent the occurrence of RISF. According to the invasive nature and processing time of skin biopsy, the assessment of KRT7 and KRT18 expression in circulating fluids, such as blood, is currently investigated in larger cohorts, to offer a quicker risk assessment.

1. Sung H, Ferlay J, Siegel RL, et al. Global cancer statistics 2020: GLOBOCAN estimates of incidence and mortality worldwide for 36 cancers in 185 countries. *CA Cancer J Clin.* n/a(n/a). doi:<https://doi.org/10.3322/caac.21660>
2. Veronesi U, Cascinelli N, Mariani L, et al. Twenty-Year Follow-up of a Randomized Study Comparing Breast-Conserving Surgery with Radical Mastectomy for Early Breast Cancer. *N Engl J Med.* 2002;347(16):1227-1232. doi:10.1056/NEJMoa020989
3. Pignol J-P, Olivetto I, Rakovitch E, et al. A multicenter randomized trial of breast intensity-modulated radiation therapy to reduce acute radiation dermatitis. *J Clin Oncol Off J Am Soc Clin Oncol.* 2008;26(13):2085-2092. doi:10.1200/JCO.2007.15.2488
4. Sperk E, Welzel G, Keller A, et al. Late radiation toxicity after intraoperative radiotherapy (IORT) for breast cancer: results from the randomized phase III trial TARGIT A. *Breast Cancer Res Treat.* 2012;135(1):253-260. doi:10.1007/s10549-012-2168-4
5. Hesse M, Zimek A, Weber K, Magin TM. Comprehensive analysis of keratin gene clusters in humans and rodents. *Eur J Cell Biol.* 2004;83(1):19-26. doi:10.1078/0171-9335-00354
6. Qiu B-F, Zhang G-Q, Xu F-M, Xu Q, Xu T. Effect of the transdifferentiation of BECs into myofibroblasts on the pathogenesis of secondary cholestatic hepatic fibrosis. *Exp Ther Med.* 2019;17(4):2769-2776. doi:10.3892/etm.2019.7234
7. Ren C, Paronetto F, Mak KM, Leo MA, Lieber CS. Cytokeratin 7 staining of hepatocytes predicts progression to more severe fibrosis in alcohol-fed baboons. *J Hepatol.* 2003;38(6):770-775. doi:10.1016/S0168-8278(03)00144-2
8. Bateman AC, Hübscher SG. Cytokeratin expression as an aid to diagnosis in medical liver biopsies. *Histopathology.* 2010;56(4):415-425. doi:<https://doi.org/10.1111/j.1365-2559.2009.03391.x>
9. Fitzpatrick E, Mitry RR, Quaglia A, Hussain MJ, deBruyne R, Dhawan A. Serum Levels of CK18 M30 and Leptin Are Useful Predictors of Steatohepatitis and Fibrosis in Paediatric NAFLD. *J Pediatr Gastroenterol Nutr.* 2010;51(4):500-506. doi:10.1097/MPG.0b013e3181e376be
10. Jazwinski AB, Thompson AJ, Clark PJ, Naggie S, Tillmann HL, Patel K. Elevated serum CK18 levels in chronic hepatitis C patients are associated with advanced fibrosis but not steatosis. *J Viral Hepat.* 2012;19(4):278-282. doi:<https://doi.org/10.1111/j.1365-2893.2011.01546.x>
11. Kaswala DH, Lai M, Afdhal NH. Fibrosis Assessment in Nonalcoholic Fatty Liver Disease (NAFLD) in 2016. *Dig Dis Sci.* 2016;61(5):1356-1364. doi:10.1007/s10620-016-4079-4
12. XXX
13. Common Terminology Criteria for Adverse Events (CTCAE). Published online 2009:79.
14. Rio DC, Ares M, Hannon GJ, Nilsen TW. Purification of RNA using TRIzol (TRI reagent). *Cold Spring Harb Protoc.* 2010;2010(6):pdb.prot5439. doi:10.1101/pdb.prot5439
15. ROCit: An R Package for Performance Assessment of Binary Classifier with Visualization. Accessed May 4, 2021. <https://cran.r-project.org/web/packages/ROCit/vignettes/my-vignette.html>

16. Chiarelli N, Carini G, Zoppi N, Ritelli M, Colombi M. Transcriptome analysis of skin fibroblasts with dominant negative COL3A1 mutations provides molecular insights into the etiopathology of vascular Ehlers-Danlos syndrome. *PloS One*. 2018;13(1):e0191220. doi:10.1371/journal.pone.0191220
17. Gomolka M, Blyth B, Bourguignon M, et al. Potential screening assays for individual radiation sensitivity and susceptibility and their current validation state. *Int J Radiat Biol*. 2020;96(3):280-296. doi:10.1080/09553002.2019.1642544
18. Hatzfeld M, Franke WW. Pair formation and promiscuity of cytokeratins: formation in vitro of heterotypic complexes and intermediate-sized filaments by homologous and heterologous recombinations of purified polypeptides. *J Cell Biol*. 1985;101(5):1826-1841. doi:10.1083/jcb.101.5.1826
19. Weigel C, Veldwijk MR, Oakes CC, et al. Epigenetic regulation of diacylglycerol kinase alpha promotes radiation-induced fibrosis. *Nat Commun*. 2016;7(1):10893. doi:10.1038/ncomms10893
20. Mayemba CN. Rôle de la phosphorylation des kératines 8/18 dans la modulation de la voie de survie PI3K/AKT/NF-KB en réponse au stress cytotoxique. Published online 2019. <http://depot-e.uqtr.ca/id/eprint/9089/1/032314919.pdf>

Tables

Table 1. Clinical and treatment characteristics of radioresistant and radiosensitive patients included in this study. Values are given as: median (range). CTV: Clinical Target Volume, NA: Not applicable.

Table 2. KRT7 and KRT18 expression qPCR oligonucleotides.

1
2
3
4
5
6
7
8
9
10
11
12
13
14
15
16
17
18
19
20
21
22
23
24
25
26
27
28
29
30
31
32
33
34
35
36
37
38
39
40
41
42
43
44
45
46
47
48
49
50
51
52
53
54
55
56
57
58
59
60
61
62
63
64
65

Figures

1
2
3
4 **Figure 1.** Expression of KRT7 and KRT18 mRNAs in healthy dermal primary fibroblasts from
5
6 radioresistant and radiosensitive patients. a. Cytokeratin gene expression in 9 healthy primary human
7
8 fibroblast cultures (data extracted from GSE117680). The relative expression in log2 of representative
9
10 type I and type II cytokeratins as well as the expression of fibroblastic-specific genes is illustrated. b.
11
12 Boxplot of the relative quantity of the KRT7 mRNA normalised to GAPDH mRNA expression. c. Boxplot
13
14 of the relative quantity of the KRT18 mRNA normalised to GAPDH mRNA expression. * : $p < 0.05$, ***
15
16 : $p < 0.001$
17
18
19
20

21 **Figure 2.** Receiver Operating Characteristic (ROC) curve of KRT7 and KRT18 mRNA levels as predictors
22
23 of RISF. AUC = 0.83. TPR : True positive rate. FPR : False positive rate.
24
25
26
27
28
29
30
31
32
33
34
35
36
37
38
39
40
41
42
43
44
45
46
47
48
49
50
51
52
53
54
55
56
57
58
59
60
61
62
63
64
65

Table 1

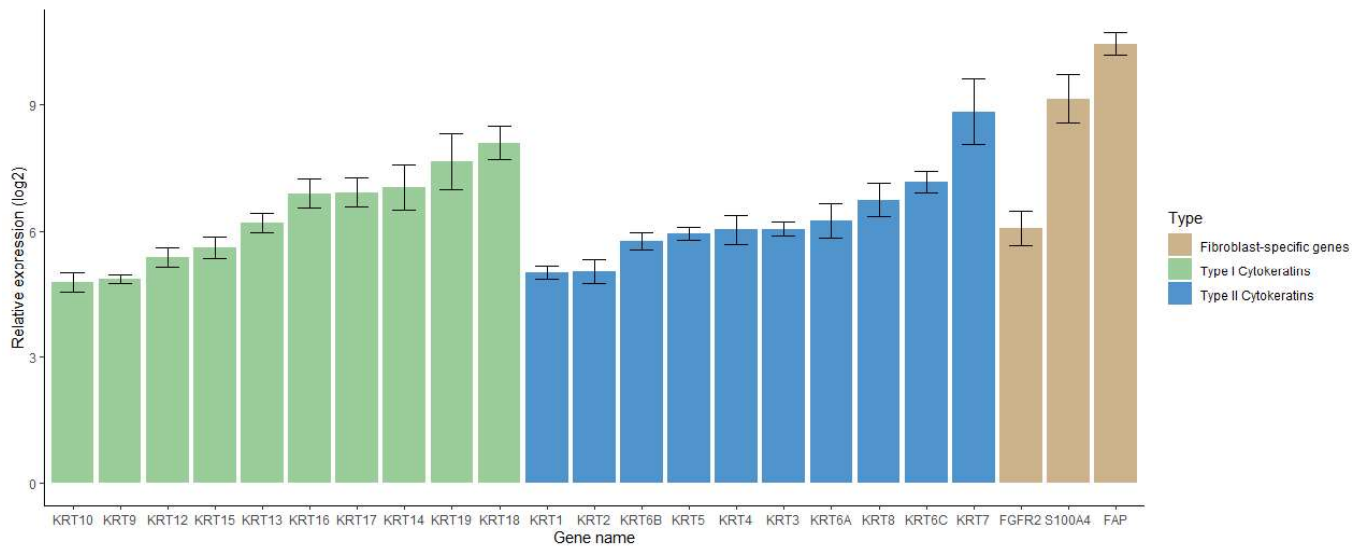
Gene	Radioresistant patients	Radiosensitive patients	p-value
Number of patients	5	7	NA
Patient-related factors			
<i>Age</i>	59 (43-67)	59 (55-70)	0.37
<i>Smoking</i>	2 (40%)	1 (14%)	0.52
<i>Bra size (cm)</i>	90 (85-105)	105 (90-110)	0.09
<i>Bra cup</i>			NA
A	1 (20%)	0	
B	2 (40%)	0	
C	1 (20%)	4 (57%)	
D	1 (20%)	1 (14%)	
Unknown	0	2 (29%)	
Radiotherapy parameters			
<i>Delivered dose (Gy)</i>	48 (48-50)	48 (48-50)	0.83
<i>Number of sessions</i>	24 (24-25)	24.5 (24-25)	0.83
<i>Mean CTV dose (Gy)</i>	51 (50-59)	55 (53-58)	0.71
<i>D2% (Gy)</i>	54 (54-70)	64 (62-68)	0.71
<i>Boost (Yes)</i>	0	4 (57%)	0.08
<i>Boost mean CTV dose (Gy)</i>	-	13.5 (10-15)	NA
<i>Sequential Chemotherapy</i>	1 (20%)	2 (29%)	1
<i>Sequential Endocrine therapy</i>	0	4 (57%)	0.08
Late effects			
<i>RISF</i>			
CTCAE v4 ≤ 1	5 (100%)	0	0.001
CTCAE v4 ≥ 3	0	7 (100%)	0.001
<i>Deep connective breast tissue fibrosis</i>	0	6 (88%)	0.02
<i>Breast atrophy</i>	0	4 (57%)	0.08
Comorbidities			
<i>Diabetes mellitus</i>	0	0	1
<i>Genetic DNA repair disease</i>	0	0	1

Table 2

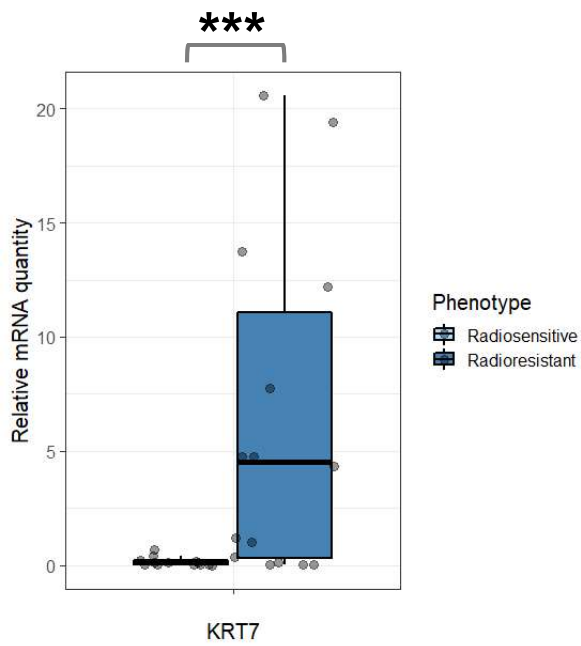
Gene	Use	Forward primer	Reverse primer
CK7	mRNA	5'-CGGCATCATCGCTGAGGTCAA-3'	5'-GCCTGGAGGGTCTCAAACCTGG-3'
CK18	mRNA	5'-CCAGTCTGTGGAGAACGACA-3'	5'-GAGCAGCTCCTCCTTGAGAG-3'

Figure 1

a.



b.



c.

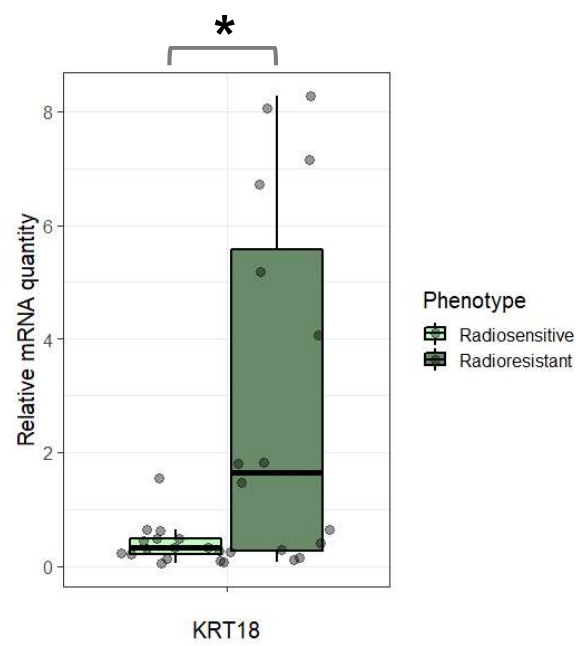
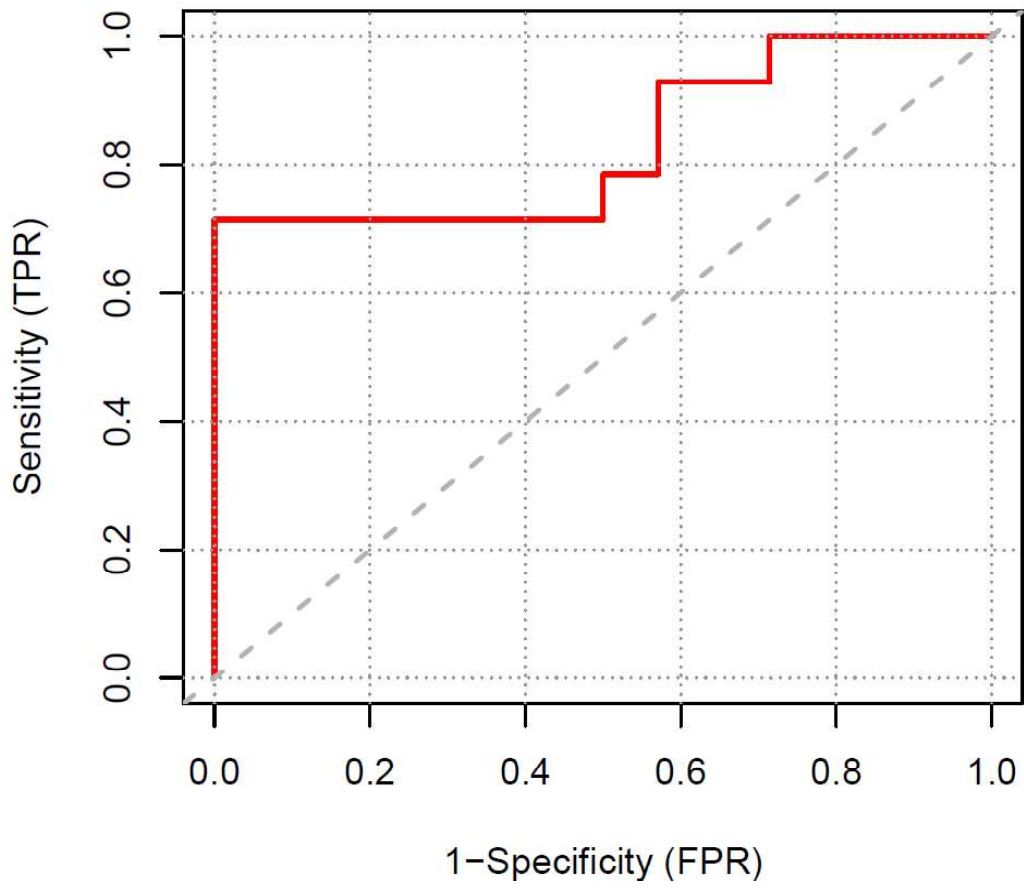


Figure 2



11.3. Discussion and conclusion

For intellectual property considerations, we were unable to show our data associated with the keratin genes in the article. Figure 17 summarises the expression of the main keratin genes in fibroblasts from radiosensitive and radioresistant patients from the SPLICI-Rad study. As in Chiarelli *et al.* (183), KRT7 and KRT18 are the two most expressed keratins in our fibroblasts (Figure 17). Interestingly, the genes encoding the partners of CK7 and CK18, KRT17 and KRT8 respectively, are not differentially expressed between the two phenotypes ($FC_{KRT17} = -1.03$, $p_{KRT17} > 0.1$, $FC_{KRT8} = 1.17$, $p_{KRT8} > 0.1$), suggesting an effect of CK7 or CK18 in the monomeric or homodimeric state. CK7 and CK18 were observed in protein extracts from fibroblasts from radioresistant patients (Figure 18), allowing protein explorations to identify CK7 and CK18 partners in fibroblasts.

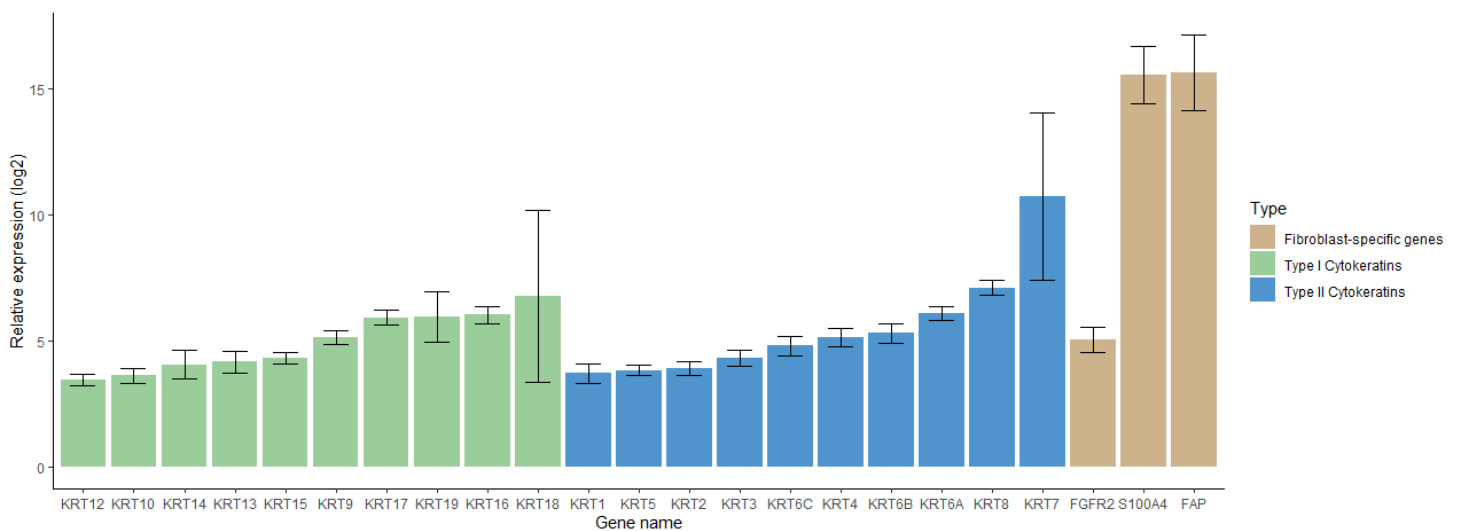


Figure 17. Cytokeratin gene expression in our 12 primary human fibroblast cultures The relative expression in log2 of representative type I and type II cytokeratins as well as the expression of fibroblastic-specific genes is illustrated. Data are plotted as mean and standard deviation.

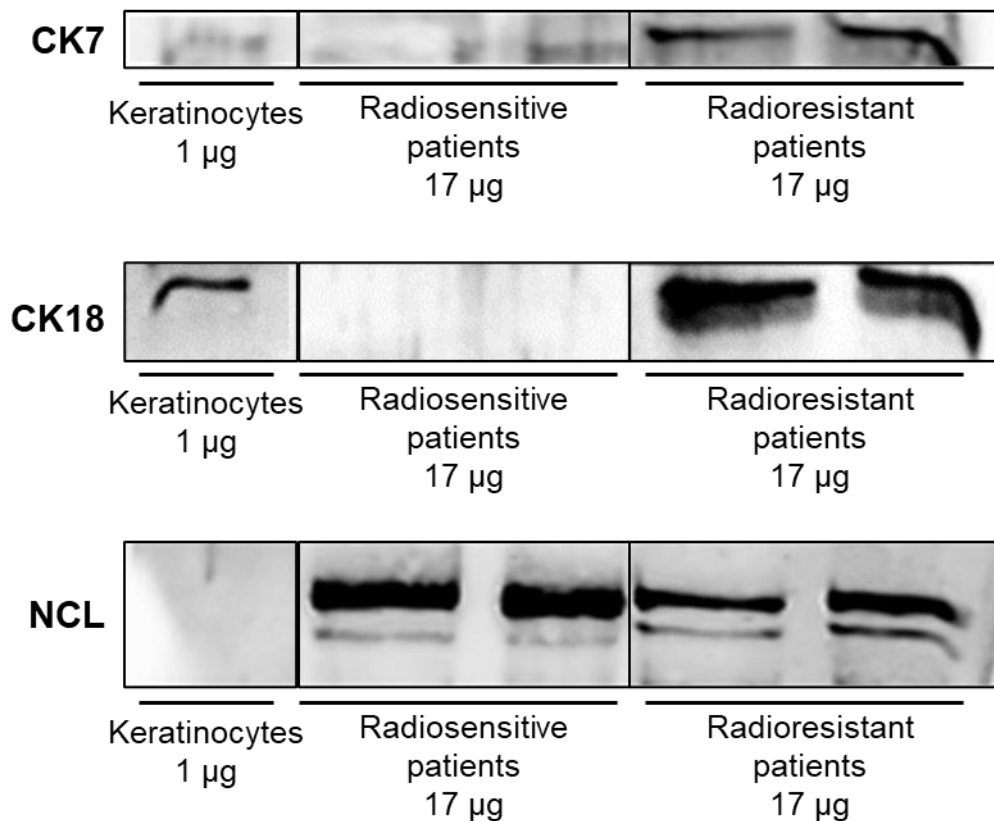


Figure 18. Western blot showing representative results of CK7, CK18 and NCL loading control in total cell lysates from radioresistant and radiosensitive proteins.

In addition, data from microarray analysis suggested splicing variations, and in particular intron retention, which would lead to the preferential transcription of non-coding isoforms of KRT7 and KRT18 in fibroblasts from radiosensitive patients and would partly explain the absence of CK7 and CK18 in these cells. We tested these splicing events by RT-qPCR, but they were found to be statistically not significant (Figure 19). This lack of significance can be explained by three factors. First, the quantified non-coding isoforms of KRT7 and KRT18 are weakly expressed, making them largely undetectable and preventing accurate quantitative analysis. Specific reverse transcription of these genes could overcome this obstacle. Then, the number of patients included in this analysis remains modest. These two elements together lead to a lack of statistical power that prevents us from completely excluding the participation of splicing mechanisms in the protein regulation of CK7 and CK18. It would be interesting to reproduce these experiments on other samples in order to refute or confirm this hypothesis. Finally, non-coding isoforms are transient and more prone to degradation, making them harder to detect. Indeed, in case of nuclear ncRNAs, they can be degraded by the nuclear exosome; in case of ncRNAs exported in the cytoplasm, they can be degraded through nonsense mediated decay. As we do not have any data on whether these non-coding isoforms are exported in the cytoplasm or sequestered in the nucleus therefore, we would have to try blocking either or

both of the aforementioned degradation pathways to stabilise them. Inhibition of the nuclear exosome and the nonsense mediated decay mechanisms can be achieved through RRP46 and UPF1 knock-down respectively.

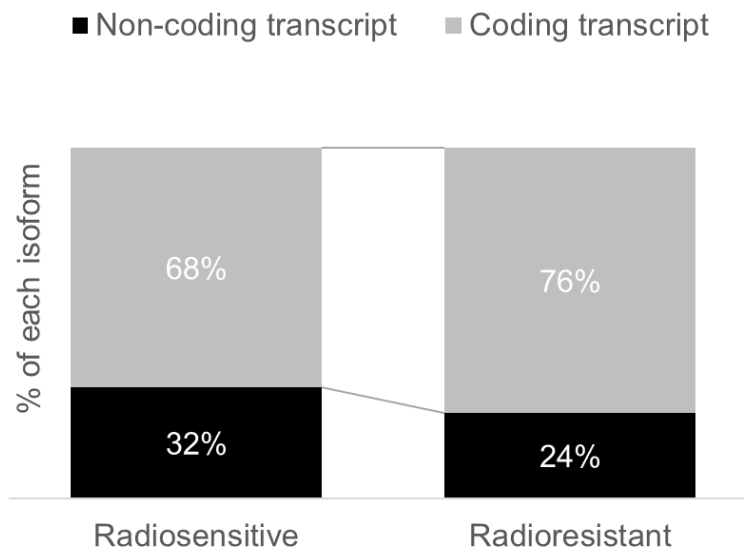


Figure 19. Expression of CK7 non-coding RNA vs CK7 mRNA in healthy dermal fibroblasts from radioresistant and radiosensitive patients.

Microarray analysis revealed massive alternative splicing of a large majority of the of the two keratin gene clusters. This observation is still very preliminary and requires validation by RT-PCR or RT-qPCR. It would be interesting to perform a sequence analysis in the vicinity of the validated events in order to highlight potential cryptic splice sites, as well as potential nucleotide motifs specific to splicing factor docking. The cluster-wide distribution of these splicing differences could also suggest a more global epigenetic regulation.

Our study suggests that KRT7 and KRT18 may have a protective role in the development of RISF. Apart from this first hypothesis, the role of keratins in fibroblasts is still completely unknown. Moreover, the two keratin clusters seem to be strongly alternatively spliced between fibroblasts from radiosensitive and radioresistant patients. These preliminary observations have paved the way for a whole field of research, ranging from the very specific pathophysiology of RISF to the very general structure of the skin.

Molecular approaches, although indispensable, are only a glimpse of IRS and RISF. They can be combined with cellular approaches that provide a first insight into the functional differences between fibroblasts from radiosensitive and radioresistant patients. The following section describes a cellular approach to IRS and RISF.

12. Functional characterisation of radiosensitive and radioresistant skin fibroblasts

12.1. Introduction

Skin fibroblasts produce a rich extracellular matrix that composes the dermis. Divided in two major phenotypes, papillary fibroblasts and reticular fibroblasts, they play a key role in the structural and molecular integrity of the skin as described in section 7.2.3 *Cellular aspect*. To improve our understanding of RISF onset, we evaluated the various cellular functions in fibroblasts from radiosensitive (n = 5) and radioresistant (n = 6) patients from the SPLICI-Rad study at basal state and at early passage to better approximate the physiology of cells *in vivo*.

We demonstrated a homogeneity in fibroblasts subtypes between our radiosensitive and radioresistant cultures, allowing us to conclude that the differences we are evidencing are not due to an imbalance of two functionally different skin fibroblast lineages. We showed no significant difference between fibroblasts from radiosensitive and radioresistant patients collagen production after 3 days at confluence. In our study, fibroblasts from radiosensitive patients exhibited a higher migration speed, a higher proliferation, and an impaired DSB repair compared to fibroblasts from radioresistant patients. Complete results are presented in the following manuscript in preparation for *Journal of Investigative Dermatology*.

12.2. Article

12.2.1. Introduction

Female breast cancer is the most prevalent cancer, with an estimated 2.3 million new cases worldwide responsible for 6.9% of cancer deaths. (3) 80% of newly diagnosed non-metastatic breast cancers or ductal carcinoma *in situ* are treated with radiotherapy (RT), especially in a conservative approach. (17,107) However, more than 80% of patients receiving RT on the breast will experience some degree of skin toxicity from mild reversible burns to late and severe adverse events such as secondary malignancies. (108,109). RT toxicities are mainly explained by deterministic rather than stochastic consequences of irradiation. (110) In this work, we will focus on radiation-induced skin fibrosis (RISF) which, even with good dose management, is estimated to occur in up to 18% of breast cancer patients 3 years post-RT (28). Patients developing RISF are said radiosensitive, while RISF-free patients are radioresistant.

RISF is a late adverse event of the skin developed from 6 months after RT, in an unpredictable manner and without therapeutic deviation. Its occurrence is correlated with total dose and

delivered dose per session in terms of frequency and severity. Fibrotic lesions are limited to the irradiated volume. They have a polymorphic appearance and are manifested, in increasing order of severity, by less elastic irradiated skin, retractile sclerosis, and finally, spontaneous ulceration. These superficial aspects may be associated with fibronecrotic manifestations of the underlying tissues. (112)

Skin fibroblasts produce a rich extracellular matrix that composes the dermis. They play a key role in the structural and molecular integrity of the skin. Physiologically, the fibroblast is the keystone of the dermis. It has a variable morphology with its degree of activity and its different stages of differentiation: from the quiescent fibrocyte found in mature connective tissue to the hyperactive myofibroblast. The fibroblast is a secretory cell that manufactures the constituents of the extracellular matrix (collagen, fibronectin, etc.) as well as the degradation enzymes (proteinases, collagenases, etc.), thus ensuring the maintenance of the extracellular matrix by a rigorous homeostasis between synthesis and degradation. The fibroblast can produce growth factors (TGF β , interleukins, PDGF, etc.) and prostaglandins. Thus, it plays a regulatory role for neighbouring mesenchymal cells. (112)

In adult human skin, the dermis is divided into two parts: the superficial part is referred to as papillary dermis and the deeper part as reticular dermis. These two subparts are characterised by distinct composition and organisation of the extracellular matrix elements and specific properties of the resident fibroblasts. Fibroblasts from the papillary dermis, or papillary fibroblasts, differ from fibroblasts from the reticular dermis, or reticular fibroblasts, in their shapes, functions and gene expression profile. (184) While papillary fibroblasts are spindle-shaped, reticular fibroblasts exhibit a more flattened appearance (185,186) Regarding their functions, papillary and reticular fibroblasts from adult human skin exhibit different growth and contractile capacities, and do not have equivalent capacities for promoting epidermal reconstruction. (185) Reticular fibroblasts display a greater collagen lattice contraction capacity than papillary fibroblasts (185), although papillary fibroblasts promote a better epidermis organisation and differentiation during wound healing. (187) The latter years have seen the rise of papillary and reticular fibroblasts transcriptome characterisation. (188–190) Regarding the pathophysiology of RISF, we can specifically highlight the overexpression of the myofibroblast marker α -smooth muscle actin (α -SMA) in reticular fibroblasts. (185) The latter also exhibit different collagens expression pattern, and notably COL11A1 which is was found to be 100 times more expressed in reticular fibroblasts than in papillary fibroblasts in Nauroy *et al.* work. (188) All together, these observations suggest that papillary and reticular fibroblasts can be considered as two distinct functional entities, whose proportions must be determined prior to any functional analysis of entire dermis fibroblasts population.

As the cellular determinants of RISF are still largely unknown, we deemed it interesting to study the physiology of skin fibroblasts from radiosensitive and radioresistant patients. In this study, we characterized the major functions of fibroblasts from radiosensitive and radioresistant patients in order to identify possible defects predictive of the occurrence of RISF.

12.2.2. *Material and methods*

This study was conducted on 11 primary adult skin fibroblast cultures. Ten primary fibroblast cultures, including 6 primary cultures derived from radioresistant patients (RISF-free) and 3 primary cultures derived from radiosensitive patients (RISF-prone), originated from the SPLICI-Rad study (NCT03000764). Two primary radiosensitive cultures were generously gifted. (191).

12.2.2.1. Clinical Radiosensitivity status of the primary cells

Radiosensitive primary cells were derived from patients with severe RISF (grade ≥ 3 , CTCAE v4.0 scale(192)) between 6 months and 5 years after the completion of RT while radioresistant cultures were raised from patients with no skin toxicity at 5 years after RT (grade ≤ 1 , CTCAE v4.0 scale).

12.2.2.2. Skin biopsy procedure

Skin biopsy specimens have been collected from the arm opposite to the irradiated breast (unirradiated area), using a 12G dermal punch after local anaesthesia. After sampling, fibroblast primary cultures were derived according to standard procedures. (191)

12.2.2.3. Cell culture

All fibroblast primary cultures were grown in DMEM medium (Dulbecco's Modified Eagle Medium, Sigma-Aldrich) supplemented with 20% FBS (Fetal Bovine Serum, Dutscher), 10U/ml penicillin/streptomycin (Sigma-Aldrich), and 2.9 mg/ml of L-glutamine (Sigma-Aldrich). All the following experiments were performed between passage 3 and passage 6.

12.2.2.4. Irradiation protocol

Primary cells were irradiated in the Radiotherapy Department of the Institut de Cancérologie de Lorraine. The irradiations were performed using a Clinac iX VARIAN linear accelerator according to the following parameters: posterior beam (180° arm); 6 MV photons at a rate of 200UM/min; 40x40 cm fields; 1.5 cm thick Plexiglas bolus; single fraction dose of 2 Gy or 8 Gy; distance from the source of 100 cm; ambient temperature.

12.2.2.5. Fibroblast lineage determination

Fibroblasts lineage determination was performed as described elsewhere.(193) Briefly, living cells were incubated 1 h at room temperature with anti-human FAP APC (1:100, FAB3715A-100, R&D), anti-human CD90 AF700 (1:100, 328119, BioLegend), and then washed twice with PBS/BSA 0.1%. Twenty thousand cells of each sample were subsequently acquired on Gallios cytometer (Beckman-Coulter), where live cells have been kept based on their propidium iodide exclusion and revealed according to their FAP and CD90 fluorescent signal. FlowJo® software (Becton-Dickinson Biosciences) was used to analyse and generate the bivariate plots.

12.2.2.6. Invasion assay

Cell migration was evaluated using in vitro transwell inserts (8 µm pores) (Costar®). Fibroblasts were plated in triplicate (200,000 cells/well) in serum-free media on a layer of Matrigel® (Corning) (2 mg/ml) for invasion. (194) Outer wells contained DMEM with 20% FBS cell culture media. After 24 h, cells that migrated through the insert were fixed with 4% formaldehyde (28908, Thermo scientific) and stained with Crystal Violet. The inner transwell membrane was delicately cleaned using a cotton swab. The remaining Crystal Violet on the outer membrane was solubilised in ethanol. This solution's absorbance was measured at 570 nm, reflecting the quantity of cells having reached the outer membrane. A coated but unseeded transwell, treated in the same conditions, was used as blank. These experiments have been performed in duplicate, with a technical duplicate every time.

12.2.2.7. Collagen production assay

300 000 cells were seeded in a 6-well plate well, mimicking confluence. After 72h hours of culture, cells are fixed using 70% ethanol. Fixed cells were stained with Sirius Red (0.1% in picric acid) for 1h. (194) Cells were washed with PBS to remove Direct Red 80 and air dried at room temperature. To quantitate staining intensity, 0.1 M NaOH was used to free bound Direct Red 80. The absorbance of the dye suspension was measured at 540 nm. These experiments have been performed in duplicate, with a technical duplicate every time.

12.2.2.8. Proliferation assay

Briefly, slides were seeded with 10 000 cells and cultured for 24h. Then cells were fixed in 4 % paraformaldehyde at room temperature for 10 minutes. Cells were permeabilised in 0.5%Triton X-100 at room temperature for 10 minutes. Permeabilisation was followed by an incubation with rabbit anti-human Ki67 (1:500, ab15580, Abcam) at room temperature for 1h, then secondary Alexa Fluor488 goat anti-rabbit IgG antibody (1:100, A11008, Invitrogen) was added at room temperature for 45 minutes in the dark. Between each of the steps, cells were washed three time. Cells were counterstained with DAPI. Foci counting was performed on at least one 100 nuclei per patient and condition using Substructure Analyzer protocol on Icy. (174) These experiments have been performed in triplicate, with a technical duplicate every time.

12.2.2.9. Wound healing assay

Two-wells inserts (80209, Ibidi) were placed in a 6-well plate well, one per well, and seeded with 20,000 cells (in a maximum volume of 70 μ l) per chamber. The next day, the insert is removed, creating a gap between the two insert wells, representing the starting point of the migration assay ($t = 0$ h). Cells were then covered with 2 ml of complete medium and pictures are taken with a phase-contrast microscope after 6h and 24h of culture. The distance covered by the fibroblast migration front was evaluated using ImageJ. These experiments have been performed in duplicate, with a technical duplicate every time.

12.2.2.10. Apoptosis assay

Apoptosis has been measured with Annexin-V-FITC Apop kit (eBioscience, Invitrogen) according to manufacturer instructions. Briefly, 2.106 cells have been sequentially stained with recombinant human Annexin-V and propidium iodide (PI). For each sample, 20 000 cells have been acquired with a Gallios cytometer (Beckman-Coulter) and discriminated according FITC and PI intensities with the following gating strategy for quantification, using FlowJo software (Becton-Dickinson): Lower-Left and Lower-Right quadrants represent live (based-on PI exclusion) and early apoptotic cells respectively. Upper-Left and Upper-Right quadrants contained late apoptotic and necrotic cells respectively. Each quadrant quantification, indicated by percentage of cells, has been plotted using R.

12.2.2.11. 53BP1 staining

Briefly, slides were seeded with 10 000 cells and irradiated at 2 Gy (or not) the next day. 1h, 4h ou 24h post-irradiation, cells were fixed in 4 % paraformaldehyde at room temperature for 10 minutes. Cells were then permeabilised in 0.5%Triton X-100 at room temperature for 10 minutes. Permeabilisation was followed by an incubation with rabbit anti-human 53BP1 (1:200, ab36823, Abcam) at room temperature for 1h, then secondary Alexa Fluor488 goat anti-rabbit IgG antibody (1:100, A11008, Invitrogen) was added at room temperature for 45 minutes in the dark. Between each of the steps, cells were washed three time. Cells were counterstained with DAPI. Foci counting was performed on at least one 100 nuclei per patient and condition using Substructure Analyzer protocol on Icy. (174) These experiments have been performed in triplicate, with a technical duplicate every time.

12.2.2.12. Statistical analysis

All analyses were performed using R software (version 4.0.5). Radiosensitive and radioresistant groups were compared using Mann-Whitney non-parametric tests. Association between a variable and a phenotype was assessed using Barnard's tests. The significance threshold was set to $p < 0.05$.

12.2.3. *Results*

12.2.3.1. Homogenous distribution of fibroblasts subpopulations between fibroblasts from radiosensitive and radioresistant patients

Using flow cytometry, we characterised the fibroblastic subpopulations (papillary, upper reticular, lower reticular) of 5 primary adult skin fibroblast cultures, 3 derived from radioresistant patients, 2 derived from radiosensitive patients, according to their FAP and CD90 status as described in Figure 20a. Detailed sub-population characteristics are described in Table 11 and detailed in Figure 25. We found no significant differences in fibroblastic lineage proportion between radioresistant and radiosensitive primary cells (Figure 20b). Hence, we conclude that our radiosensitive and radioresistant primary adult skin fibroblast cultures are homogenous regarding their fibroblastic subpopulations' composition. The functional similarities and differences described in this work can therefore be imputed to the specific physiology of fibroblasts from radiosensitive and radioresistant patients, excluding a disequilibrium in fibroblastic subpopulations that could have led to a global change in the behaviour of our primary cultures.

	Fibroblasts from RR patients (n = 3)	Fibroblasts from RS patients (n = 2)
Upper reticular lineage	95.1 (85.4 – 95.5)	82.95 (74.8 – 91.1)
Lower reticular lineage	4.82 (4.29 – 14.3)	16.90 (8.69 – 25.1)
Papillary lineage	0.021 (0 – 0.24)	0.0475 (0.042 – 0.053)

Table 11. Composition of our primary fibroblast cultures in papillary, upper reticular and lower reticular lineages. Results are given as median (range) percentage of the whole primary culture population. RR: Radioresistant. RS: Radiosensitive.

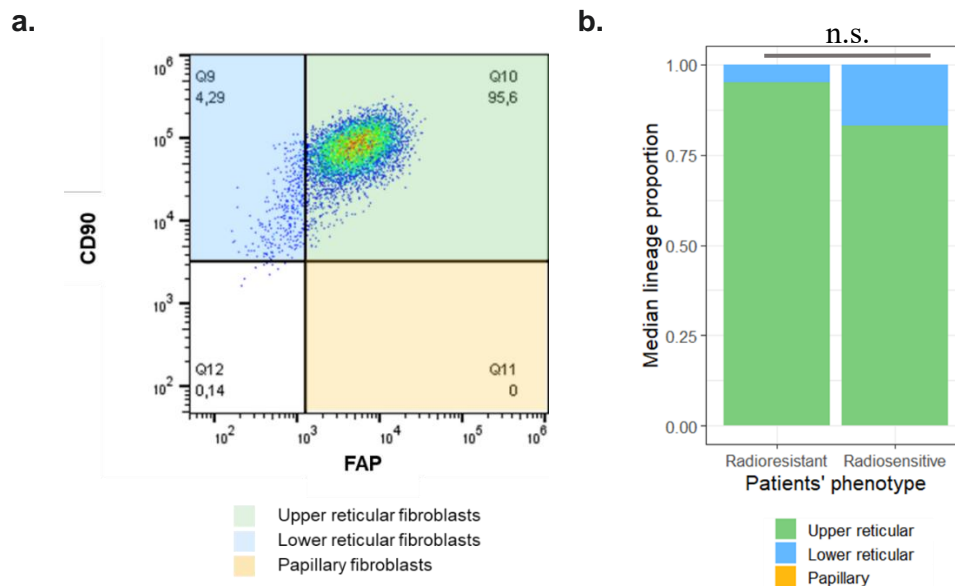


Figure 20. Subpopulation characterisation of primary adult skin fibroblast cultures. a. Lineage gating strategy according to FAP and CD90 staining. b. Median lineage proportion between radiosensitive (n = 2) and radioresistant (n = 3) skin fibroblast cultures. n.s. : not significant.

12.2.3.2. Invasion and collagen production properties are similar in fibroblasts from radiosensitive and radioresistant patients

We characterised the collagen production and the cell invasion properties of 11 primary adult skin fibroblast cultures, 6 derived from radioresistant patients, 5 derived from radiosensitive patients. Experimental values are detailed in Table 12. No significant differences were found in these functions between fibroblasts from radiosensitive and radioresistant patients as measured in this work (Figure 21), suggesting no impairment in collagen production and invasion properties, at basal state, in radiosensitive skin fibroblasts compared to radioresistant skin fibroblasts.

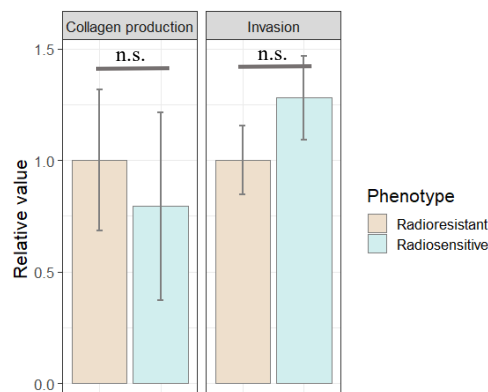


Figure 21. Relative collagen production and invasion of fibroblasts from radiosensitive patients compared to fibroblasts from radioresistant patients. Data are shown as median +/- SEM.

		Radioresistant fibroblasts	Radiosensitive fibroblasts	p-val
Collagen production	<i>n</i>	6	5	
	<i>Absorbance at 540 nm</i>	0.17 (0.03 – 0.36)	0.14 (0.05 – 0.39)	n.s.
Invasion	<i>n</i>	6	5	
	<i>Absorbance at 570 nm</i>	0.98 (0.52 – 1.33)	1.25 (0.77 – 1.85)	n.s.
Migration	<i>n</i>	4	3	
	<i>Migration in 6h (µm)</i>	45.39 (19.84 – 86.64)	74.45 (54.05 – 95.29)	*
Proliferation	<i>n</i>	4	4	
	<i>% of Ki67+ cells</i>	4.39 (2.21 – 7.97)	11.02 (6.06 – 23.33)	**
Apoptosis	<i>n</i>	4	3	
	<u>Basal state (72h)</u>			
	<i>% of live cells</i>	92.5 (76 – 95.8)	77.3 (72.7 – 87.9)	**
	<i>% of early apoptotic cells</i>	0.32 (0.21 – 1.74)	1.04 (0.82 – 1.41)	*
	<i>% of late apoptotic cells</i>	0.37 (0.13 – 1.13)	0.87 (0.44 – 5.92)	*
	<i>% of dead cells</i>	6.09 (3.81 – 21.1)	20.4 (7.91 – 25.8)	*
	<u>8 Gy (72h)</u>			
	<i>% of live cells</i>	79.1 (76.4 – 83)	66.5 (58.2 – 73.6)	**
	<i>% of early apoptotic cells</i>	1.06 (0.81 – 2.5)	3.565 (0.49 – 6.18)	n.s.
	<i>% of late apoptotic cells</i>	0.69 (0.21 – 2.84)	6.03 (0.4 – 12.5)	n.s.
	<i>% of dead cells</i>	18.5 (14.8 – 22.4)	24.4 (18.8 – 28.7)	*
	<u>8 Gy – Basal state</u>			
	<i>% of live cells</i>	-11.525 (-18.1 – -3.2)	-3.7 (-25.55 – -3.2)	n.s.
	<i>% of early apoptotic cells</i>	0.82 (0.62 – 1.96)	-0.34 (-0.65 – 5.19)	n.s.
<i>% of late apoptotic cells</i>	0.1375 (0.08 – 2.22)	-0.115 (-0.41 – 7.43)	n.s.	
<i>% of dead cells</i>	8.84 (8.47 – 17.38)	4.4 (3.95 – 12.91)	n.s.	
DNA repair	<i>n</i>	4	4	
	<u>Number of 53BP1 foci per nucleus</u>			
	<i>Not irradiated – 1h</i>	1.37 (0.76 - 2.09)	1.77 (1.07 - 2.78)	n.s.
	<i>Not irradiated – 4h</i>	2.21 (0.77 - 3.13)	1.79 (0.69 - 2.81)	n.s.
	<i>Not irradiated – 24h</i>	1.59 (0.51 - 2.80)	0.70 (0.37 - 1.34)	n.s.
	<i>2 Gy – 1h</i>	29.80 (27.72- 36.52)	28.93 (27.82 - 32.09)	n.s.
	<i>2 Gy – 4h</i>	9.31 (8.55 - 13.11)	10.69 (10.29 - 12.06)	n.s.
	<i>2 Gy – 24h</i>	3.77 (1.59 - 6.96)	5.74 (1.82 - 8.18)	***

Table 12. Functional characterisation of radioresistant and radiosensitive skin fibroblasts. Results are given as median (range) of each analysed parameter. n.s: not significant, * p < 0.05, ** p < 0.01, *** p < 0.001

12.2.3.3. Radiosensitive fibroblasts migrate faster than fibroblasts from radioresistant patients

We evaluated radiosensitive (n = 3) and radioresistant (n = 4) skin fibroblasts migration through a wound healing assay. Experimental values are detailed in Table 12. We showed that in 6 hours, fibroblasts from radiosensitive patients migrate around 65% more than fibroblasts from radioresistant patients, as illustrated in Figure 22a and 22b.

12.2.3.4. Radiosensitive fibroblasts proliferate more than fibroblasts from radioresistant patients

We evaluated the proliferation of radiosensitive (n = 4) and radioresistant (n = 4) skin fibroblasts with an indirect immunofluorescence Ki67 staining. Experimental values are detailed in Table 12. We found that fibroblasts from radiosensitive patients are 2.5 times more proliferative than fibroblasts from radioresistant patients as shown in Figure 22a.

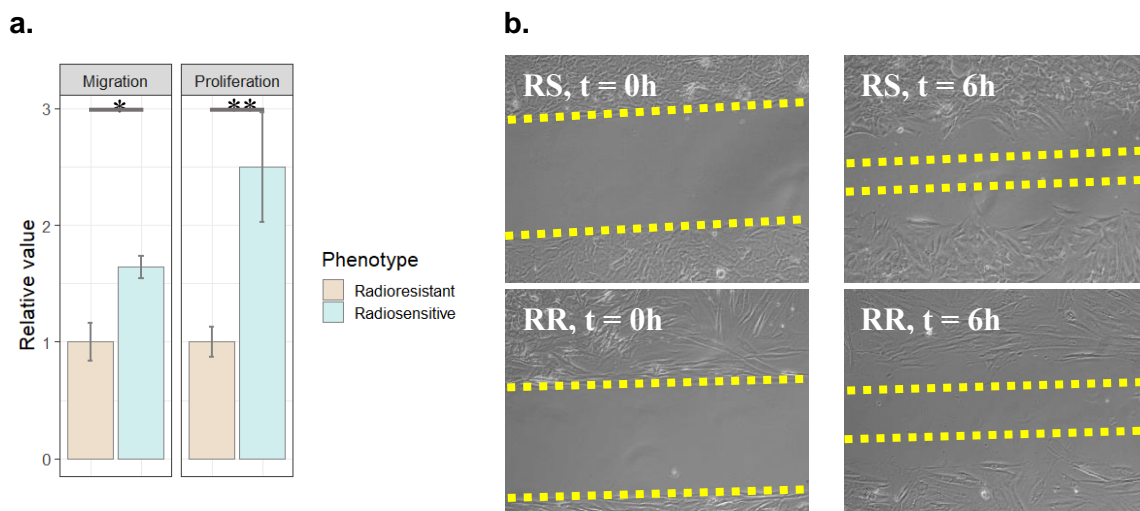


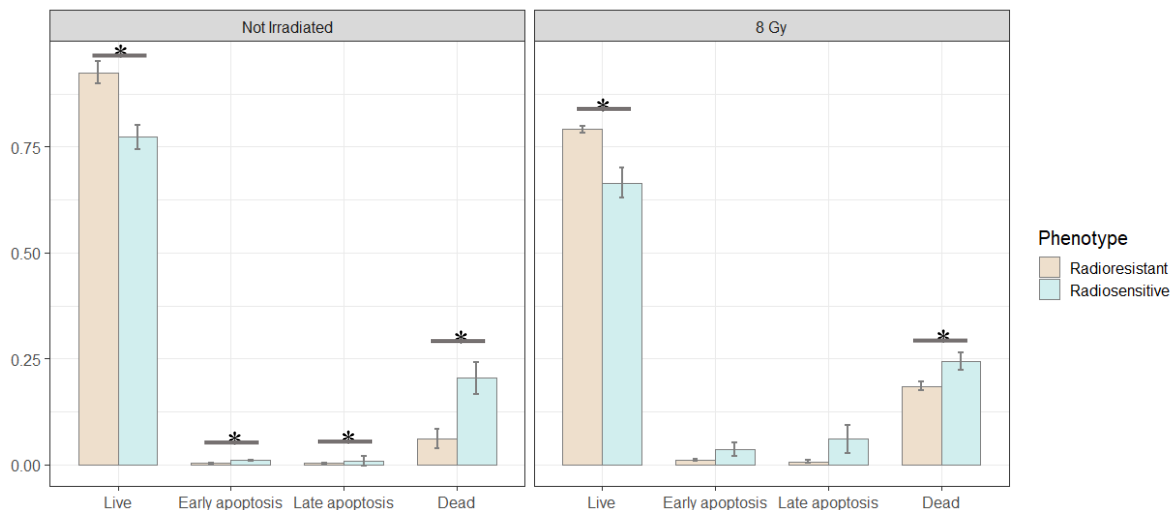
Figure 22. Migration and proliferation of fibroblasts from radiosensitive and radioresistant patients. a. Relative migration and proliferation of fibroblasts from radiosensitive patients compared to fibroblasts from radioresistant patients. Data are shown as median +/- SEM. * p < 0.05, ** p < 0.01 b. Representative results of the wound healing assay. Yellow dotted lines represent the migration front. RR: Radioresistant fibroblasts, RS: Radiosensitive fibroblasts.

12.2.3.5. Radiosensitive fibroblasts undergo more apoptosis

We measured radiosensitive (n = 3) and fibroblasts from radioresistant patients (n = 4) apoptosis at basal state and 72h hours after an 8 Gy irradiation in flow cytometry with an Annexin V-PI assay. Annexin V-/PI- cells are live cells. Annexin V+/PI- cells are undergoing early apoptosis. Annexin V+/PI+ cells are undergoing late apoptosis. Annexin V-/PI+ cells are dead cells. Detailed values are given in Table 12. At basal state, the proportion of live fibroblasts from radiosensitive patients is significantly lower than the one of fibroblasts from radioresistant patients (Figure 23a). The proportions of early apoptotic, late apoptotic and dead

cells are significantly higher in fibroblasts from radiosensitive patients (Figure 23a). Similar results are obtained 72h after an 8 Gy irradiation (Figure 23a). The proportion of live fibroblasts from radiosensitive patients is significantly smaller whereas the proportion of dead fibroblasts from radiosensitive patients is significantly greater than fibroblasts from radioresistant patients' ones (Figure 23a). We do not observe any irradiation-related excess mortality in fibroblasts from radiosensitive patients compared to fibroblasts from radioresistant patients (Figure 23b).

a.



b.

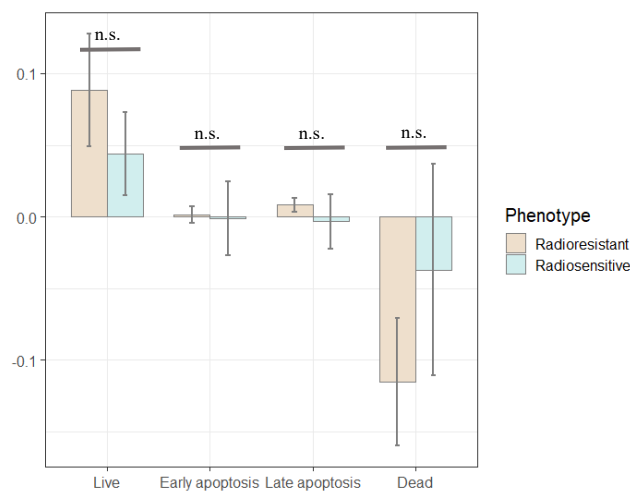
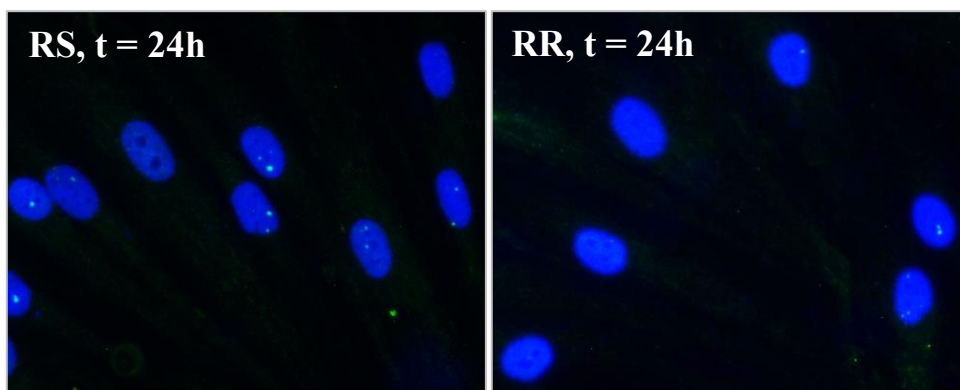


Figure 23. Proportion of live, early apoptotic, late apoptotic and dead fibroblasts from radiosensitive and radioresistant patients, determined by flow cytometry using an Annexin V-PI assay. a. 72h after an 8 Gy irradiation or no irradiation. b. Irradiation-related apoptosis in fibroblasts from radiosensitive and radioresistant patients. * $p < 0.05$, ** $p < 0.01$, n.s.: not significant.

12.2.3.6. Fibroblasts from radiosensitive patients exhibit an impairment in DSB repair

We assessed the DNA repair capacity of radiosensitive (n = 4) and fibroblasts from radioresistant patients (n = 4) using DSB repair kinetics. DSB were labelled with 53BP1, a key protein in DSB repair (Figure 24a). The values are detailed in Table 12. We found no significant difference in the number of DSBs at basal state between fibroblasts from radiosensitive and radioresistant patients (Figure 24b). Thus, basal genomic integrity is similar between the two studied phenotypes. After a 2 Gy irradiation, fibroblasts from radiosensitive patients accumulate a delay in repair over time. A tendency for a higher number of residual DSBs appears as early as 4h post-irradiation to become significant 24 hours post-irradiation with around 2 more DSB per nuclei (Figure 24b). Thus, fibroblasts from radiosensitive patients show a defect in DSB repair compared with fibroblasts from radioresistant patients.

a.



b.

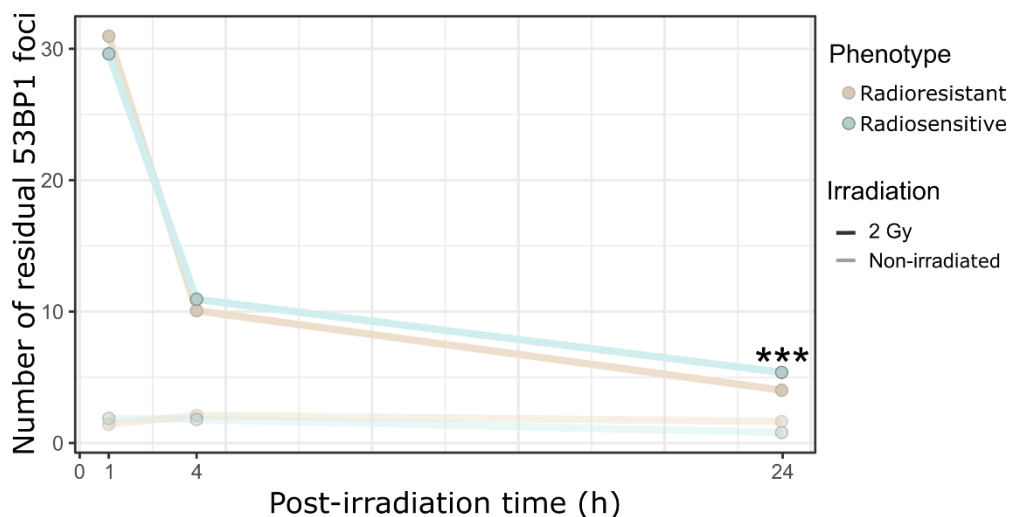


Figure 24. DNA repair assessment through 53BP1 staining of fibroblasts from radioresistant and radiosensitive patients. a. Representative results of 53BP1 staining 24h after a 2 Gy irradiation. Each green focus represents a DNA DSB. Blue structures are DAPI-stained nuclei.

RR: Radioresistant fibroblasts, RS: Radiosensitive fibroblasts. b. Number of residual 53BP1 foci 1h, 4h, and 24h after a 2 Gy irradiation or in control conditions. *** $p < 0.001$.

12.2.4. Discussion

In this work, we functionally characterised radiosensitive and radioresistant skin fibroblasts. Although homogeneous, the overwhelming majority of fibroblasts in our cultures were reticular fibroblasts. As our patients are of advanced age, it is expected that reticular fibroblasts are predominant. (195) However, the near absence of papillary fibroblasts is surprising. Several hypotheses could explain this phenomenon. On the one hand, the virtual absence of papillary fibroblasts could be attributed to a selection induced by the primoculture derivation method used, which could be unfavourable to this cell subtype. However, to date, little data exists on this problem. On the other hand, Janson *et al.* (196) describe a fibroblastic primoculture drift in in vitro culture, leading to the progressive loss of the papillary phenotype favouring of the reticular phenotype for long culture times (passages 16 to 22). As this work was carried out on early passage cells, with minimal culture times, this pitfall should have been avoided. However, the use of fibroblasts from elderly patients could be a factor aggravating this phenomenon of phenotypic drift.

Although not significantly different between the two radiosensitivity phenotypes, the invasion properties of the fibroblasts followed the same trend as the migration assay, i.e. an increase in fibroblasts from radiosensitive patients. This similarity of evolution suggests that the non-significance of the comparison between fibroblasts from radiosensitive and radioresistant patients ($p = 0.10$) is due to a lack of power in our study, resulting from a limited number of patients.

Rognoni *et al.* (197) demonstrated a negative feedback loop between fibroblast ECM deposition/remodelling and proliferation. They suggest that during wound healing, fibroblast migration and proliferation are positively correlated between themselves, and negatively correlated to ECM synthesis. As in their study, migration and proliferation are here positively correlated. Let us consider the radioresistant phenotype as the physiological standard. Its level of migration and proliferation is closely related to its secretory capacity. Thus, according to the model of Rognoni *et al.*, fibroblasts displaying a greater proliferation than radioresistants one would exhibit lower secretory capacities. However, fibroblasts from radiosensitive patients are more proliferative but secrete just as much as fibroblasts from radioresistant patients (Figure 21). This finding suggests a defect in the homeostatic balance between proliferation, migration and extracellular matrix synthesis, which could be involved in the pathophysiology of RISF. It should be noted that SPLICI-Rad study patients did not present fibrosis on their non-irradiated

skin. Thus, this mechanism, if it is at work, only becomes pathological in the event of damage to the skin, requiring repair.

We showed that fibroblasts from radiosensitive patients are more prone to apoptosis, independent of irradiation. These observations seem to be at odds with the data obtained by Ozsahin *et al.* (57), who found lower apoptosis of CD4 and CD8 lymphocytes in patients at higher risk of developing late post-radiotherapy toxicities. As the role of apoptosis in the occurrence of RISF is yet to be deciphered, it is difficult to suggest anything other than the use of different cell models to explain this difference.

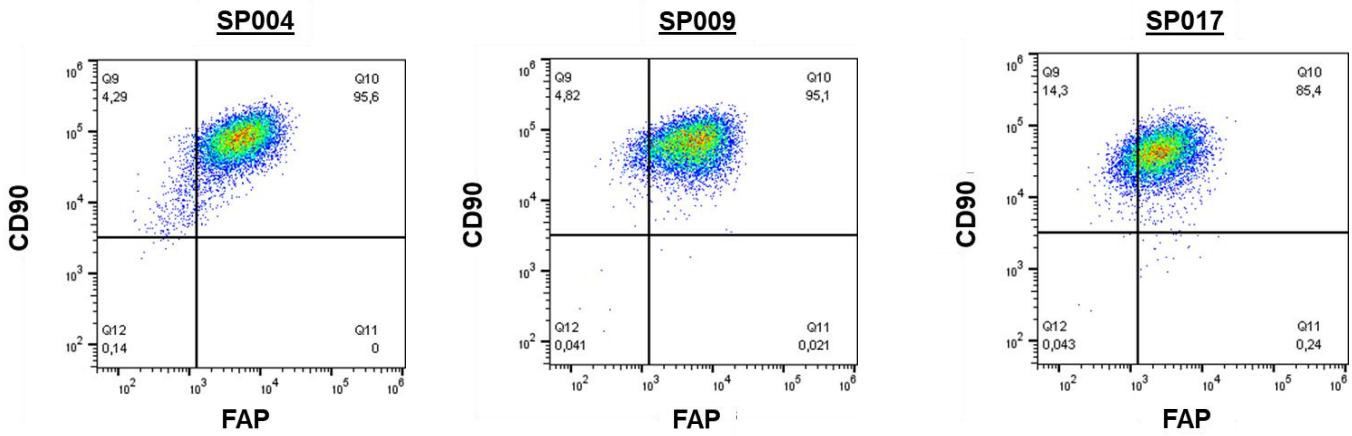
Ionising radiations are known to be genotoxic agents causing DSB and inducing the relocation of the 53BP1 protein to these breaks.(198) Using 53BP1 as a DSB marker, we have shown that fibroblasts from radiosensitive patients display a DNA repair delay, with a median difference of 2 unrepaired DSB 24h after a single 2 Gy irradiation. Although 2 DSB are a rather modest amount of damage to repair for healthy cells, we must keep in mind that radiotherapy schemes classically require the delivery of 2 Gy during five consecutive days, and for several weeks. Thus, this differential of a few breaks can be dramatic on repeated irradiations, completely disrupting cellular homeostasis and contributing to the emergence of RISF. It would be interesting to evaluate the response of fibroblasts after repeated irradiation. Nevertheless, these experiments are logistically delicate, as they depend on the availability of linear accelerators, whose main purpose remains the treatment of patients. The repair defect identified in our study supports the work of Vogin *et al* (191), who proposed another DNA repair defect of skin fibroblasts involving ATM, a major DNA repair kinase required for DSB recognition, to be predictive of the onset of RISF.

12.2.5. *Conclusion*

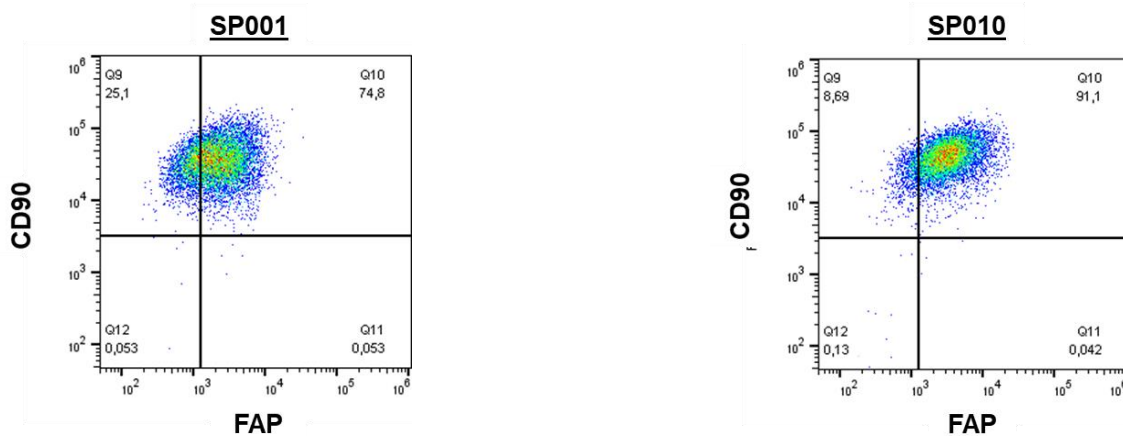
The present study contributes to increase the knowledge on radiosensitive and radioresistant dermal fibroblasts and highlights the possible involvement of DNA repair, cell migration and proliferation in the onset of RISF. This study certainly provides a new source of exploratory pathways for RISF pathophysiology. Its understanding will require further functional explorations, notably through an accurate *in vitro* radiation-induced model, to determine which of the aforementioned physiological differences between fibroblasts from radiosensitive and radioresistant patients could be causal in RISF occurrence. Moreover, dermal fibroblasts are conjunctive cells embedded in a rich extracellular matrix and surrounded by the epidermis and the hypodermis with which they interact greatly, 3D fibroblast cultures in skin models would be of interest to be better understand fibroblasts behaviour.

12.2.6. Supplementary material

a.



b.



c.

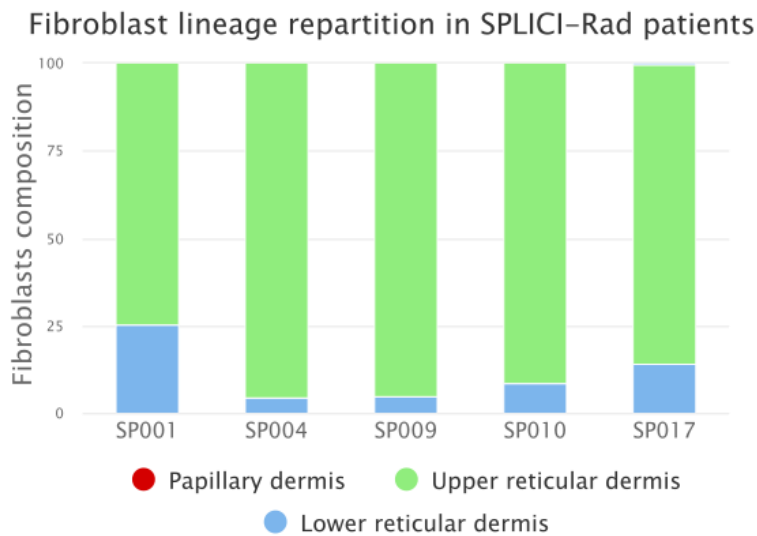


Figure 25. Detail of subpopulation characterisation of primary fibroblast cultures. a. Lineage characterisation of radioresistant primary fibroblasts. b. Lineage characterisation of radiosensitive primary fibroblasts b. Lineage proportion for skin fibroblast culture.

12.3. Complementary results and discussion

For intellectual property concerns, genetic implication cannot be discussed in the previous article. Along with complementary experiments, it will be discussed in the following section.

To approximate early events leading to RISF, we subjected our fibroblasts from radiosensitive and radioresistant patients to a fibroblast activation model consisting of a single 2 Gy irradiation and treatment with TGF β (100 ng/ml), as described in (194). We ensured the effective treatment of our primary cultures by the increase in 53BP1-labelled DSBs (positive control of irradiation) and the decrease in fibroblast migration rate (positive control of TGF β treatment (199)). Whether with irradiation alone, TGF β treatment alone or both at the same time, all differences shown in the basal state are abolished. Two hypotheses could explain this phenomenon. On the one hand, the treatments applied could have too strong effects on cell metabolism compared to inter-phenotypic differences, masking the latter. On the other hand, the model recapitulates the pathophysiology of RISF in a very fragmented way since it includes a one-off treatment (vs. an increase in TGF β activity over long periods), a single irradiation (vs. repeated irradiations) and short experimental times (maximum 3 days vs. several years).

As per cell migration and invasion, migration- and adhesion-related genes are strongly differentially expressed between fibroblasts from radiosensitive and radioresistant patients in our transcriptomic data. Indeed, these genes' expression levels can perfectly discriminate between fibroblasts from radiosensitive and radioresistant patients, suggesting a strong implication of this cellular pathway in fibroblasts' radiosensitivity (Figure 26). Among them, we can find BVES and NDNF which are part of our radiosensitivity transcriptomic signature. While BVES produces a cell adhesion protein (200), NDNF is implicated in neuron migration. (201) However, none of them have been described in fibroblasts yet.

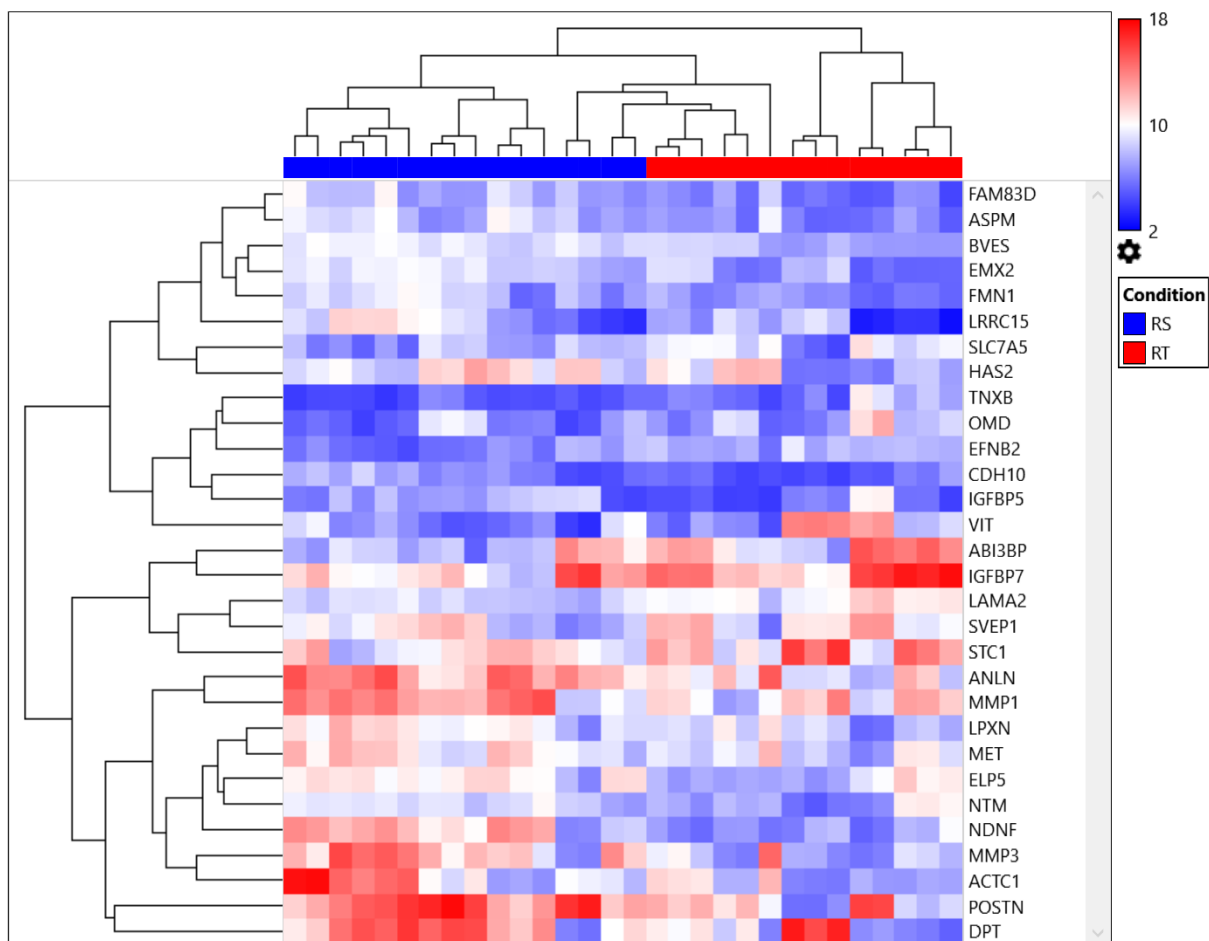


Figure 26. Heatmap of differentially expressed migration- and adhesion-related genes between fibroblasts from radioresistant and radiosensitive patients at basal state ($|FC| > 2.8$, $p\text{-val} < 0.10$, $n_{RR} = 7$, $n_{RS} = 6$)

As described above, extracellular matrix synthesis may be disrupted in fibroblasts from radiosensitive patients. Few genes related to that pathway are strongly differentially expressed between fibroblasts from radiosensitive and radioresistant patients (Figure 27). Among them, MMP1, MMP3, MMP16 and ADAMTS12 are metalloproteinases, proteins that degrade the components of the extracellular matrix such as collagens, fibronectin... (202) As fibrosis is caused by an excess of collagen, one would think that these metalloproteinases would be downregulated in fibroblasts from radiosensitive patients. However, in our data, they are counter-intuitively overexpressed in fibroblasts from radiosensitive patients.

COL11A1, described as highly overexpressed in reticular fibroblasts, is overexpressed in our fibroblasts from radiosensitive patients ($FC = 4.21$, $p = 0.002$). We know that important migration properties are typical of reticular fibroblasts, especially during wound healing. These same reticular fibroblasts are also responsible for the fibrous character of scars. Our fibroblasts from radiosensitive patients migrate faster, have a greater tendency to invasion, express more

COL11A1 and produce the same amount of collagen compared to fibroblasts from radioresistant patients whereas they should produce less given their proliferation. (197) These observations suggest that fibroblasts from radiosensitive patients exhibit a profile of "super" reticular fibroblasts, whose enhanced reticular phenotype could lead to excessive fibrosis, and therefore to RISF.

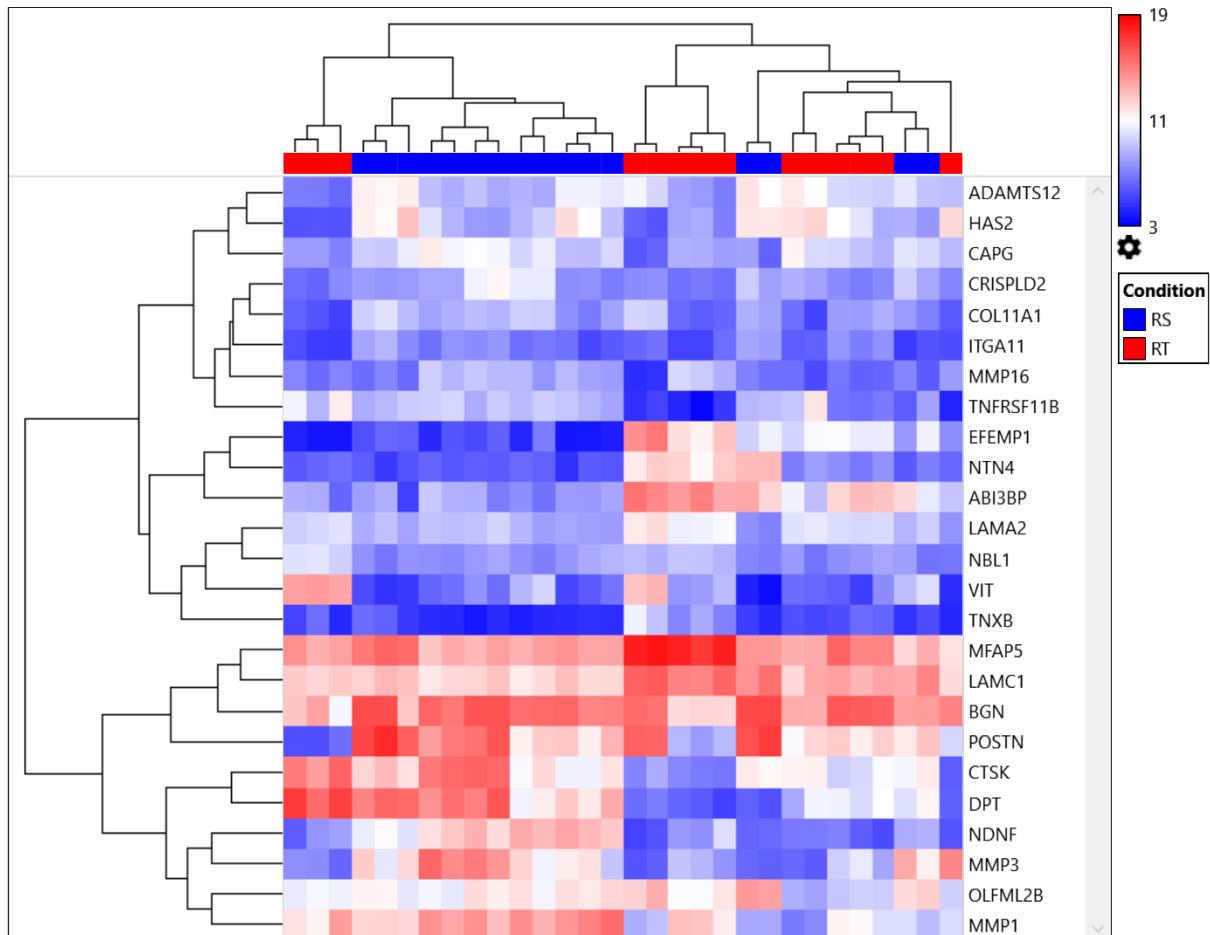


Figure 27. Heatmap of differentially expressed extracellular matrix-related genes between fibroblasts from radioresistant and radiosensitive patients at basal state ($|FC| > 2$, $p\text{-val} < 0.10$, $n_{RR} = 7$, $n_{RS} = 6$).

We showed a higher proportion of apoptotic cells in radiosensitive primocultures at basal state and 72h after an 8 Gy irradiation. We report the overexpression of TNFRSF11B in radiosensitive cells ($FC = 4.55$, $p = 0.03$), also known as TRAIL, which is implicated in apoptosis. The role of TNFRSF11B is debated, with data from the literature suggesting pro-apoptotic (203–208) and anti-apoptotic functions. (209–214) The implication of this gene in apoptosis could be assessed using RNA interference treatment to see if viability is restored to a level similar to that of fibroblasts from radioresistant patients.

12.4. Conclusion

Our study is the first to characterise the physiology of radiosensitive and radioresistant skin fibroblasts, laying the foundation for understanding their functions. It suggests the possible involvement of DNA repair, cell migration and proliferation in the onset of RISF. Most of the proposed impaired pathways are supported by transcriptomic data, reinforcing their relevance in SRIF onset. Although very broad, our study lacks mechanistic pathway explaining the functions defects and their links to RISF. Linking basal radiosensitive and radioresistant functions to RISF onset will require further functional and molecular explorations, notably through the use of an accurate in vitro radiation-induced model. Moreover, dermal fibroblasts are conjunctive cells embedded in a rich extracellular matrix and surrounded by the epidermis and the hypodermis with which they interact greatly, 3D fibroblast cultures in skin models would be of interest to be better understand fibroblasts behaviour.

Discussion and **perspectives**

Invented barely 100 years ago from empiric experiences, RT has emerged as an essential modality for cancer treatment. Yet, without taking anything away from its clinical utility, only little is known about the sensitivity and response to irradiation at the tissue, cellular and molecular levels. This lack of knowledge is a double burden for the patient who is subjected to suboptimal treatments regarding both tumour inactivation and of peri-tumoral healthy tissues protection. Thus, the therapeutic ratio could be increased with better molecular and imaging knowledge.

My PhD project focused on a minute part of this challenge: on the one hand the discrimination of radionecrosis from tumour progression after treatment of brain metastases using stereotactic radiotherapy, on the other hand the search for RISF predictive markers and the functional characterisation of fibroblasts from radiosensitive and radioresistant patients. Although not in the same scientific fields (image analysis and machine learning vs. cellular and molecular biology), these two projects share a common philosophy: implementing a translational approach for the improvement of late radiation-induced toxicities. Both radiomics and molecular biology approaches led to the development of easily usable, non-invasive, and cost-effective models to diagnose and prevent RT late toxicities.

The emergence of targeted therapies and immunotherapy, which are not only effective but also generally rather well tolerated, might lead one to believe that the more toxic cancer treatment modalities will be gradually abandoned. However, both of these treatments are extremely expensive (> 90% of cancer treatments costs in France), and unless there is a revolution in how they are produced, they will remain so. Moreover, medical oncology - unlike RT - has benefited from treatment personalisation (e.g. systematic screening for dihydropyrimidine dehydrogenase deficiency is recommended before starting treatment with 5-fluorouracil, a chemotherapy). While it is reasonable to expect that Western societies with protective social security systems, such as France, will favour the benefits of their sick citizens over their finances, this is unlikely to be the case in poorer countries that cannot afford these therapies. Thus, the more conventional, cost-effective, yet still effective modalities such as radiotherapy will continue to be used. Given their design, our discrimination algorithm and prognostic test of RISF are easily usable, require little medical equipment, are cheap and can be helpful for a large number of patients.

The pursuit of any research work must be coupled with its ethical review. While it is unlikely that the results presented in this manuscript could be diverted to ethically objectionable uses, the design raises more questions. Indeed, like many European studies, the SPLICI-Rad study is only composed of patients of Caucasian origin. Ethnicity plays a role in disease determinants, development and symptoms (see Review), especially in the case of high-

throughput genomic and transcriptomic studies as presented here. Non-Caucasian ethnicities are under-represented in European research, even though they represent an overwhelming majority of the world's population, which may limit the application of scientific findings. I believe that before proposing our test to assess IRS to other populations, it would be best to ensure its relevance and reliability on an ethnically diverse sample.

Both discrimination of radionecrosis from tumour progression after treatment of brain metastases using stereotactic radiotherapy, and search for RISF predictive markers and functional characterisation of fibroblasts from radiosensitive and radioresistant patients were exploratory and conducted on a modest number of patients. Collaborations with Pr Philippe Lambin's team (Mastro Clinic) and the UNITRAD group have been initiated to have access to validation cohorts of several hundred patients. Hence, we will be able to validate our diagnostic *in silico* model and our IRS blood test.

Conclusion

To offer better management of radiotherapy toxicities, this dissertation aimed at i- improving the differential diagnosis between brain metastasis recurrence and RN and ii- unravelling molecular determinants of individual radiosensitivity through its most protean and clinically demonstrative illustration – i.e. RISF.

- i- Through an original pilot study, we demonstrated the benefit of quantitative imaging parameters in the differential diagnosis of modifying brain target lesion after SRT. Indeed, our radiomics model differentiates RN from tumour recurrence with an 85% accuracy. Moreover, our model is early and non-invasive since based on the very first lesion change on follow-up MRI. Easily integrated into imaging software, our model could assist (neuro)radiologists in indistinguishable image interpretation and radiation oncologists in early decision making. Ultimately, our approach may provide a reliable alternative to cerebral biopsies. Due to its modest sample size, this study is a proof of concept that needs to be validated on a larger cohort to assess the robustness of the algorithm. To this end, a collaboration with Prof. Lambin's team (Maastrro Clinic, Maastricht) is in progress.

- ii- Analysis of SPLICI-Rad study (NCT03000764) samples revealed molecular and cellular determinants of radiation-induced skin fibrosis. Indeed, the comparative transcriptome analysis of healthy fibroblasts from radiosensitive and radioresistant patients revealed a signature of individual radiosensitivity. Based on this signature, we developed a prognostic blood test to determine individual radiosensitivity. This test is currently being patented. We also demonstrated the expression and splicing of keratin genes in healthy skin fibroblasts, in a phenotypic specific way. As keratins are considered epithelium-specific, our work opens the way to new keratins functions, especially in conjunctive tissues. Finally, we functionally characterised our fibroblasts, and highlighted a defect in double strand breaks repair 24 hours after a 2-Gy irradiation, as well as cell migration and proliferation differences in fibroblasts from radiosensitive patients compared to fibroblasts from radioresistant patients. Understanding the links between these differences and RISF onset will require further functional explorations, notably through an accurate in vitro radiation-induced model, to determine which of the aforementioned physiological differences between fibroblasts from radiosensitive and radioresistant patients could be causal in RISF occurrence.

References

1. Evans E, Staffurth J. Principles of cancer treatment by radiotherapy. Surgery (Oxford). 2018 Mar 1;36(3):111–6.
2. Lievens Y, Borrás JM, Grau C. Provision and use of radiotherapy in Europe. Molecular Oncology. 2020;14(7):1461–9.
3. Sung H, Ferlay J, Siegel RL, Laversanne M, Soerjomataram I, Jemal A, et al. Global cancer statistics 2020: GLOBOCAN estimates of incidence and mortality worldwide for 36 cancers in 185 countries. CA: A Cancer Journal for Clinicians [Internet]. [cited 2021 Feb 11];n/a(n/a). Available from: <https://acsjournals.onlinelibrary.wiley.com/doi/abs/10.3322/caac.21660>
4. Roentgen WC. [On a new kind of ray (first report)]. Munch Med Wochenschr. 1959 Jul 24;101:1237–9.
5. DESPEIGNES V. Observation concernant un cas de cancer de l'estomac traite par les rayons Rontgen. Lyon Med. 1896;82:428-430 ; 503–6.
6. Becquerel J, Crowther JA. Discovery of radioactivity. Nature. 1948 Apr 17;161(4094):609.
7. Curie E. Marie and Pierre Curie and the discovery of radium. Br J Radiol. 1950 Jul;23(271):409–12.
8. Thariat J, Hannoun-Levi J-M, Sun Myint A, Vuong T, Gérard J-P. Past, present, and future of radiotherapy for the benefit of patients. Nature Reviews Clinical Oncology. 2013 Jan;10(1):52–60.
9. The Treatment of Malignant Disease by Radium and X-Rays: Being a Practice of Radiotherapy. Journal of the American Medical Association. 1949 Jan 29;139(5):342–342.
10. BERGONIE J. De quelques resultas de la radiotherapie et essai de fixation d'une technique radionnelle. C R Acad Sci. 1906;143:983–95.
11. Coutard H. PRINCIPLES OF X RAY THERAPY OF MALIGNANT DISEASES. The Lancet. 1934 Jul 7;224(5784):1–8.
12. Taylor LS. History of the International Commission on Radiological Protection (ICRP). Health Phys. 1958 Sep;1(2):97–104.
13. Tiemann J. [Practical irradiation planning using a 'dedicated system']. Strahlentherapie. 1974 Nov;148(5):463–7.
14. Horiot JC, van der Schueren E, Johansson KA, Bernier J, Bartelink H. The programme of quality assurance of the EORTC radiotherapy group. A historical overview. Radiother Oncol. 1993 Nov;29(2):81–4.

15. Bonadonna G, Brusamolino E, Valagussa P, Rossi A, Brugnatelli L, Brambilla C, et al. Combination chemotherapy as an adjuvant treatment in operable breast cancer. *N Engl J Med*. 1976 Feb 19;294(8):405–10.
16. Veronesi U, Saccozzi R, Del Vecchio M, Banfi A, Clemente C, De Lena M, et al. Comparing radical mastectomy with quadrantectomy, axillary dissection, and radiotherapy in patients with small cancers of the breast. *N Engl J Med*. 1981 Jul 2;305(1):6–11.
17. Veronesi U, Cascinelli N, Mariani L, Greco M, Saccozzi R, Luini A, et al. Twenty-Year Follow-up of a Randomized Study Comparing Breast-Conserving Surgery with Radical Mastectomy for Early Breast Cancer. *New England Journal of Medicine*. 2002 Oct 17;347(16):1227–32.
18. Mohan R, Grosshans D. Proton therapy – Present and future. *Advanced Drug Delivery Reviews*. 2017 Jan 15;109:26–44.
19. Mohamad O, Sishc BJ, Saha J, Pompos A, Rahimi A, Story MD, et al. Carbon Ion Radiotherapy: A Review of Clinical Experiences and Preclinical Research, with an Emphasis on DNA Damage/Repair. *Cancers*. 2017 Jun;9(6):66.
20. Favaudon V. Radiothérapie flash à très haut débit de dose : point sur les avancées récentes. *Cancer/Radiothérapie*. 2019 Oct 1;23(6):674–6.
21. Matsuoka S, Ballif BA, Smogorzewska A, McDonald ER, Hurov KE, Luo J, et al. ATM and ATR substrate analysis reveals extensive protein networks responsive to DNA damage. *Science*. 2007 May 25;316(5828):1160–6.
22. San Filippo J, Sung P, Klein H. Mechanism of eukaryotic homologous recombination. *Annu Rev Biochem*. 2008;77:229–57.
23. Lieber MR. The mechanism of human nonhomologous DNA end joining. *J Biol Chem*. 2008 Jan 4;283(1):1–5.
24. Mirzayans R, Andrais B, Scott A, Wang YW, Murray D. Ionizing radiation-induced responses in human cells with differing TP53 status. *Int J Mol Sci*. 2013 Nov 13;14(11):22409–35.
25. Ciccia A, Elledge SJ. The DNA Damage Response: Making It Safe to Play with Knives. *Molecular Cell*. 2010 Oct 22;40(2):179–204.
26. Rubin P, Casarett GW. Clinical radiation pathology as applied to curative radiotherapy. *Cancer*. 1968 Oct;22(4):767–78.
27. Mohanti BK, Bansal M. Late sequelae of radiotherapy in adults. *Support Care Cancer*. 2005 Oct;13(10):775–80.

28. Sperk E, Welzel G, Keller A, Kraus-Tiefenbacher U, Gerhardt A, Sütterlin M, et al. Late radiation toxicity after intraoperative radiotherapy (IORT) for breast cancer: results from the randomized phase III trial TARGIT A. *Breast Cancer Res Treat*. 2012 Aug 1;135(1):253–60.
29. Dueck AC, Mendoza TR, Mitchell SA, Reeve BB, Castro KM, Rogak LJ, et al. Validity and Reliability of the US National Cancer Institute's Patient-Reported Outcomes Version of the Common Terminology Criteria for Adverse Events (PRO-CTCAE). *JAMA Oncol*. 2015 Nov 1;1(8):1051.
30. Hill-Kayser CE, Vachani C, Hampshire MK, Jacobs LA, Metz JM. An Internet Tool for Creation of Cancer Survivorship Care Plans for Survivors and Health Care Providers: Design, Implementation, Use and User Satisfaction. *J Med Internet Res [Internet]*. 2009 Sep 4 [cited 2021 May 8];11(3). Available from: <https://www.ncbi.nlm.nih.gov/pmc/articles/PMC2762859/>
31. Liu L, O'Donnell P, Sullivan R, Katalinic A, Moser L, de Boer A, et al. Cancer in Europe: Death sentence or life sentence? *Eur J Cancer*. 2016 Sep;65:150–5.
32. Baumann M, Hölscher T, Begg AC. Towards genetic prediction of radiation responses: ESTRO's GENEPI project. *Radiother Oncol*. 2003 Nov;69(2):121–5.
33. Dörr W. Radiobiology of tissue reactions. *Ann ICRP*. 2015 Jun;44(1 Suppl):58–68.
34. Rodemann HP, Blaese MA. Responses of normal cells to ionizing radiation. *Semin Radiat Oncol*. 2007 Apr;17(2):81–8.
35. Withers HR, Taylor JM, Maciejewski B. Treatment volume and tissue tolerance. *Int J Radiat Oncol Biol Phys*. 1988 Apr;14(4):751–9.
36. Burnet NG, Johansen J, Turesson I, Nyman J, Peacock JH. Describing patients' normal tissue reactions: concerning the possibility of individualising radiotherapy dose prescriptions based on potential predictive assays of normal tissue radiosensitivity. Steering Committee of the BioMed2 European Union Concerted Action Programme on the Development of Predictive Tests of Normal Tissue Response to Radiation Therapy. *Int J Cancer*. 1998 Dec 18;79(6):606–13.
37. Andreassen CN, Alsner J. Genetic variants and normal tissue toxicity after radiotherapy: a systematic review. *Radiother Oncol*. 2009 Sep;92(3):299–309.
38. Taylor AM, Harnden DG, Arlett CF, Harcourt SA, Lehmann AR, Stevens S, et al. Ataxia telangiectasia: a human mutation with abnormal radiation sensitivity. *Nature*. 1975 Dec 4;258(5534):427–9.

39. Khanna KK. Cancer risk and the ATM gene: a continuing debate. *J Natl Cancer Inst.* 2000 May 17;92(10):795–802.
40. Ho AY, Fan G, Atencio DP, Green S, Formenti SC, Haffty BG, et al. Possession of ATM sequence variants as predictor for late normal tissue responses in breast cancer patients treated with radiotherapy. *Int J Radiat Oncol Biol Phys.* 2007 Nov 1;69(3):677–84.
41. Chak LY, Gill PS, Levine AM, Meyer PR, Anselmo JA, Petrovich Z. Radiation therapy for acquired immunodeficiency syndrome-related Kaposi's sarcoma. *J Clin Oncol.* 1988 May;6(5):863–7.
42. Amoaku WM, Archer DB. Cephalic radiation and retinal vasculopathy. *Eye (Lond).* 1990;4 (Pt 1):195–203.
43. Mukesh M, Harris E, Jena R, Evans P, Coles C. Relationship between irradiated breast volume and late normal tissue complications: a systematic review. *Radiother Oncol.* 2012 Jul;104(1):1–10.
44. Giaj-Levra N, Sciascia S, Fiorentino A, Fersino S, Mazzola R, Ricchetti F, et al. Radiotherapy in patients with connective tissue diseases. *Lancet Oncol.* 2016 Mar;17(3):e109–17.
45. Takeda Y, Dynan WS. Autoantibodies against DNA double-strand break repair proteins. *Front Biosci.* 2001 Nov 1;6:D1412-1422.
46. Chronic toxicity risk after radiotherapy for patients with systemic sclerosis (systemic scleroderma) or systemic lupus erythematosus: Association with connective tissue disorder severity - ScienceDirect [Internet]. [cited 2021 May 8]. Available from: <https://www-sciencedirect-com.bases-doc.univ-lorraine.fr/science/article/pii/S0167814007006512>
47. Paulino AC, Constone LS, Rubin P, Williams JP. Normal tissue development, homeostasis, senescence, and the sensitivity to radiation injury across the age spectrum. *Semin Radiat Oncol.* 2010 Jan;20(1):12–20.
48. Bernier-Chastagner V, Hettal L, Gillon V, Fernandes L, Huin-Schohn C, Vazel M, et al. Validation of a high performance functional assay for individual radiosensitivity in pediatric oncology: a prospective cohort study (ARPEGE). *BMC Cancer.* 2018 Jul 6;18(1):719.
49. Rube CE, Fricke A, Schneider R, Simon K, Kühne M, Fleckenstein J, et al. DNA repair alterations in children with pediatric malignancies: novel opportunities to identify patients at risk for high-grade toxicities. *Int J Radiat Oncol Biol Phys.* 2010 Oct 1;78(2):359–69.

50. Nahum AE. The radiobiology of hypofractionation. *Clin Oncol (R Coll Radiol)*. 2015 May;27(5):260–9.
51. Toledano A, Garaud P, Serin D, Fourquet A, Bosset J-F, Breteau N, et al. Concurrent administration of adjuvant chemotherapy and radiotherapy after breast-conserving surgery enhances late toxicities: long-term results of the ARCOSEIN multicenter randomized study. *Int J Radiat Oncol Biol Phys*. 2006 Jun 1;65(2):324–32.
52. Girinsky T, Cosset JM. [Pulmonary and cardiac late effects of ionizing radiations alone or combined with chemotherapy]. *Cancer Radiother*. 1997;1(6):735–43.
53. Bentzen SM, Skoczylas JZ, Overgaard M, Overgaard J. Radiotherapy-related lung fibrosis enhanced by tamoxifen. *J Natl Cancer Inst*. 1996 Jul 3;88(13):918–22.
54. Niyazi M, Maihoefer C, Krause M, Rödel C, Budach W, Belka C. Radiotherapy and ‘new’ drugs-new side effects? *Radiat Oncol*. 2011 Dec 21;6:177.
55. Voong KR, Hazell SZ, Fu W, Hu C, Lin CT, Ding K, et al. Relationship Between Prior Radiotherapy and Checkpoint-Inhibitor Pneumonitis in Patients With Advanced Non-Small-Cell Lung Cancer. *Clin Lung Cancer*. 2019 Jul;20(4):e470–9.
56. MI F, M B, N F. Functional Assays for Individual Radiosensitivity: A Critical Review. *Seminars in radiation oncology* [Internet]. 2017 Oct [cited 2021 May 8];27(4). Available from: <http://pubmed.ncbi.nlm.nih.gov/28865513/>
57. Ozsahin M, Crompton NEA, Gourgou S, Kramar A, Li L, Shi Y, et al. CD4 and CD8 T-lymphocyte apoptosis can predict radiation-induced late toxicity: a prospective study in 399 patients. *Clin Cancer Res*. 2005 Oct 15;11(20):7426–33.
58. Granzotto A, Benadjaoud MA, Vogin G, Devic C, Ferlazzo ML, Bodgi L, et al. Influence of Nucleoshuttling of the ATM Protein in the Healthy Tissues Response to Radiation Therapy: Toward a Molecular Classification of Human Radiosensitivity. *International Journal of Radiation Oncology*Biophysics*Physics*. 2016 Mar 1;94(3):450–60.
59. Bergom C, West CM, Higginson DS, Abazeed ME, Arun B, Bentzen SM, et al. The Implications of Genetic Testing on Radiation Therapy Decisions: A Guide for Radiation Oncologists. *Int J Radiat Oncol Biol Phys*. 2019 Nov 15;105(4):698–712.
60. Fu KK, Pajak TF, Trotti A, Jones CU, Spencer SA, Phillips TL, et al. A Radiation Therapy Oncology Group (RTOG) phase III randomized study to compare hyperfractionation and two variants of accelerated fractionation to standard

- fractionation radiotherapy for head and neck squamous cell carcinomas: first report of RTOG 9003. *Int J Radiat Oncol Biol Phys*. 2000 Aug 1;48(1):7–16.
61. Cowan RA, McBain CA, Ryder WDJ, Wylie JP, Logue JP, Turner SL, et al. Radiotherapy for muscle-invasive carcinoma of the bladder: results of a randomized trial comparing conventional whole bladder with dose-escalated partial bladder radiotherapy. *Int J Radiat Oncol Biol Phys*. 2004 May 1;59(1):197–207.
 62. Fried DV, Das SK, Marks LB. Imaging Radiation-Induced Normal Tissue Injury to Quantify Regional Dose Response. *Semin Radiat Oncol*. 2017 Oct;27(4):325–31.
 63. Evans ES, Hahn CA, Kocak Z, Zhou S-M, Marks LB. The role of functional imaging in the diagnosis and management of late normal tissue injury. *Semin Radiat Oncol*. 2007 Apr;17(2):72–80.
 64. Hettal L, Stefani A, Salleron J, Courrech F, Behm-Ansmant I, Constans JM, et al. Radiomics Method for the Differential Diagnosis of Radionecrosis Versus Progression after Fractionated Stereotactic Body Radiotherapy for Brain Oligometastasis. *Radiat Res*. 2020 May;193(5):471–80.
 65. Anscher MS, Kong FM, Andrews K, Clough R, Marks LB, Bentel G, et al. Plasma transforming growth factor beta1 as a predictor of radiation pneumonitis. *Int J Radiat Oncol Biol Phys*. 1998 Jul 15;41(5):1029–35.
 66. Moulder JE, Fish BL, Cohen EP. ACE inhibitors and All receptor antagonists in the treatment and prevention of bone marrow transplant nephropathy. *Curr Pharm Des*. 2003;9(9):737–49.
 67. Delanian S, Porcher R, Balla-Mekias S, Lefaix J-L. Randomized, placebo-controlled trial of combined pentoxifylline and tocopherol for regression of superficial radiation-induced fibrosis. *J Clin Oncol*. 2003 Jul 1;21(13):2545–50.
 68. Delanian S, Baillet F, Huart J, Lefaix J-L, Maulard C, Housset M. Successful treatment of radiation-induced fibrosis using liposomal Cu Zn superoxide dismutase: clinical trial. *Radiotherapy and Oncology*. 1994 Jul 1;32(1):12–20.
 69. Lefaix J-L, Delanian S, Leplat J-J, Tricaud Y, Martin M, Nimrod A, et al. Successful treatment of radiation-induced fibrosis using CuZn-SOD and Mn-SOD: An experimental study. *International Journal of Radiation Oncology*Biophysics*. 1996 May 1;35(2):305–12.
 70. Le Rhun E, Dhermain F, Vogin G, Reyns N, Metellus P. Radionecrosis after stereotactic radiotherapy for brain metastases. *Expert Rev Neurother*. 2016 Aug;16(8):903–14.

71. Levin VA, Bidaut L, Hou P, Kumar AJ, Wefel JS, Bekele BN, et al. Randomized double-blind placebo-controlled trial of bevacizumab therapy for radiation necrosis of the central nervous system. *Int J Radiat Oncol Biol Phys*. 2011 Apr 1;79(5):1487–95.
72. Clarke RE, Tenorio LMC, Hussey JR, Toklu AS, Cone DL, Hinojosa JG, et al. Hyperbaric oxygen treatment of chronic refractory radiation proctitis: a randomized and controlled double-blind crossover trial with long-term follow-up. *Int J Radiat Oncol Biol Phys*. 2008 Sep 1;72(1):134–43.
73. Bey E, Prat M, Duhamel P, Benderitter M, Brachet M, Tromprier F, et al. Emerging therapy for improving wound repair of severe radiation burns using local bone marrow-derived stem cell administrations. *Wound Repair Regen*. 2010 Feb;18(1):50–8.
74. Nussbaum ES, Djalilian HR, Cho KH, Hall WA. Brain metastases: Histology, multiplicity, surgery, and survival. *Cancer*. 1996;78(8):1781–8.
75. Nayak L, Lee EQ, Wen PY. Epidemiology of brain metastases. *Curr Oncol Rep*. 2012 Feb;14(1):48–54.
76. Soffietti R, Abacioglu U, Baumert B, Combs SE, Kinhult S, Kros JM, et al. Diagnosis and treatment of brain metastases from solid tumors: guidelines from the European Association of Neuro-Oncology (EANO). *Neuro Oncol*. 2017 Feb 1;19(2):162–74.
77. Le Rhun É, Dhermain F, Noël G, Reyns N, Carpentier A, Mandonnet E, et al. [ANOCEF guidelines for the management of brain metastases]. *Cancer Radiother*. 2015 Feb;19(1):66–71.
78. Lippitz B, Lindquist C, Paddick I, Peterson D, O'Neill K, Beaney R. Stereotactic radiosurgery in the treatment of brain metastases: the current evidence. *Cancer Treat Rev*. 2014 Feb;40(1):48–59.
79. Williams BJ, Suki D, Fox BD, Pelloski CE, Maldaun MVC, Sawaya RE, et al. Stereotactic radiosurgery for metastatic brain tumors: a comprehensive review of complications. *J Neurosurg*. 2009 Sep;111(3):439–48.
80. Kamada K, Mastuo T, Tani M, Izumo T, Suzuki Y, Okimoto T, et al. Effects of stereotactic radiosurgery on metastatic brain tumors of various histopathologies. *Neuropathology*. 2001 Dec;21(4):307–14.
81. Kohutek ZA, Yamada Y, Chan TA, Brennan CW, Tabar V, Gutin PH, et al. Long-term risk of radionecrosis and imaging changes after stereotactic radiosurgery for brain metastases. *J Neurooncol*. 2015 Oct;125(1):149–56.

82. Le Rhun E, Dhermain F, Vogin G, Reyns N, Metellus P. Radionecrosis after stereotactic radiotherapy for brain metastases. *Expert Rev Neurother*. 2016 Aug;16(8):903–14.
83. Lin NU, Lee EQ, Aoyama H, Barani IJ, Barboriak DP, Baumert BG, et al. Response assessment criteria for brain metastases: proposal from the RANO group. *Lancet Oncol*. 2015 Jun;16(6):e270-278.
84. Stockham AL, Ahluwalia M, Reddy CA, Suh JH, Kumar A, Vogelbaum MA, et al. Results of a questionnaire regarding practice patterns for the diagnosis and treatment of intracranial radiation necrosis after SRS. *J Neurooncol*. 2013 Dec;115(3):469–75.
85. Keek SA, Leijenaar RT, Jochems A, Woodruff HC. A review on radiomics and the future of theranostics for patient selection in precision medicine. *BJR*. 2018 Jul 5;91(1091):20170926.
86. Lucia F, Visvikis D, Vallières M, Desseroit M-C, Miranda O, Robin P, et al. External validation of a combined PET and MRI radiomics model for prediction of recurrence in cervical cancer patients treated with chemoradiotherapy. *Eur J Nucl Med Mol Imaging*. 2019 Apr 1;46(4):864–77.
87. Zhang Z, Yang J, Ho A, Jiang W, Logan J, Wang X, et al. A predictive model for distinguishing radiation necrosis from tumour progression after gamma knife radiosurgery based on radiomic features from MR images. *Eur Radiol*. 2017 Nov 24;
88. Tiwari P, Prasanna P, Wolansky L, Pinho M, Cohen M, Nayate AP, et al. Computer-Extracted Texture Features to Distinguish Cerebral Radionecrosis from Recurrent Brain Tumors on Multiparametric MRI: A Feasibility Study. *AJNR Am J Neuroradiol*. 2016 Dec;37(12):2231–6.
89. Larroza A, Moratal D, Paredes-Sánchez A, Soria-Olivas E, Chust ML, Arribas LA, et al. Support vector machine classification of brain metastasis and radiation necrosis based on texture analysis in MRI. *J Magn Reson Imaging*. 2015 Nov;42(5):1362–8.
90. Alberts B, Johnson A, Lewis J, Morgan D, Raff M, Roberts K, et al. *Molecular Biology of the Cell*. 6e édition. New York, NY: Garland Science; 2014. 1464 p.
91. GENCODE - Human Release Statistics [Internet]. [cited 2021 May 10]. Available from: <https://www.genencodegenes.org/human/stats.html>
92. Rion N, Rüegg MA. LncRNA-encoded peptides: More than translational noise? *Cell Res*. 2017 May;27(5):604–5.

93. Alfeghaly C, Sanchez A, Rouget R, Thuillier Q, Igel-Bourguignon V, Marchand V, et al. Implication of repeat insertion domains in the trans-activity of the long non-coding RNA ANRIL. *Nucleic Acids Res.* 2021 Apr 19;
94. Chen H-C, Cheng S-C. Functional roles of protein splicing factors. *Bioscience Reports.* 2012 Apr 5;32(4):345–59.
95. Dutertre M, Sanchez G, De Cian M-C, Barbier J, Dardenne E, Gratadou L, et al. Cotranscriptional exon skipping in the genotoxic stress response. *Nature structural & molecular biology.* 2010;17(11):1358.
96. Papasaikas P, Valcárcel J. The Spliceosome: The Ultimate RNA Chaperone and Sculptor. *Trends in Biochemical Sciences.* 2016 Jan 1;41(1):33–45.
97. Ding L-H, Shingyoji M, Chen F, Hwang J-J, Burma S, Lee C, et al. Gene expression profiles of normal human fibroblasts after exposure to ionizing radiation: a comparative study of low and high doses. *Radiation research.* 2005;164(1):17–26.
98. Wang X, Arai S, Song X, Reichart D, Du K, Pascual G, et al. Induced ncRNAs allosterically modify RNA-binding proteins in cis to inhibit transcription. *Nature.* 2008 Jul;454(7200):126–30.
99. Lü X, Peña L de la, Barker C, Camphausen K, Tofilon PJ. Radiation-Induced Changes in Gene Expression Involve Recruitment of Existing Messenger RNAs to and away from Polysomes. *Cancer Res.* 2006 Jan 15;66(2):1052–61.
100. Forrester HB, Li J, Hovan D, Ivashkevich AN, Sprung CN. DNA Repair Genes: Alternative Transcription and Gene Expression at the Exon Level in Response to the DNA Damaging Agent, Ionizing Radiation. *Marinus MG, editor. PLoS ONE.* 2012 Dec 28;7(12):e53358.
101. Shkreta L, Chabot B. The RNA Splicing Response to DNA Damage. *Biomolecules.* 2015 Dec;5(4):2935–77.
102. Giono LE, Nieto Moreno N, Cambindo Botto AE, Dujardin G, Muñoz MJ, Kornblihtt AR. The RNA Response to DNA Damage. *Journal of Molecular Biology.* 2016 Jun 19;428(12):2636–51.
103. Holdt LM, Beutner F, Scholz M, Gielen S, Gäbel G, Bergert H, et al. ANRIL expression is associated with atherosclerosis risk at chromosome 9p21. *Arteriosclerosis, thrombosis, and vascular biology.* 2010;30(3):620–7.
104. Liu Y, Sanoff HK, Cho H, Burd CE, Torrice C, Mohlke KL, et al. INK4/ARF Transcript Expression Is Associated with Chromosome 9p21 Variants Linked to Atherosclerosis. *PLOS ONE.* 2009 Apr 3;4(4):e5027.

105. Dorsett Y, McBride KM, Jankovic M, Gazumyan A, Thai T-H, Robbiani DF, et al. MicroRNA-155 Suppresses Activation-Induced Cytidine Deaminase-Mediated Myc-Igh Translocation. *Immunity*. 2008 May 16;28(5):630–8.
106. Li X, Tian F, Wang F. Rheumatoid Arthritis-Associated MicroRNA-155 Targets SOCS1 and Upregulates TNF- α and IL-1 β in PBMCs. *International Journal of Molecular Sciences*. 2013 Dec;14(12):23910–21.
107. Fisher B, Anderson S, Bryant J, Margolese RG, Deutsch M, Fisher ER, et al. Twenty-year follow-up of a randomized trial comparing total mastectomy, lumpectomy, and lumpectomy plus irradiation for the treatment of invasive breast cancer. *N Engl J Med*. 2002 Oct 17;347(16):1233–41.
108. Porock, KristJanson. Skin reactions during radiotherapy for breast cancer: the use and impact of topical agents and dressings. *European Journal of Cancer Care*. 1999 Sep;8(3):143–53.
109. Yarnold J, Vozenin Brotons M-C. Pathogenetic mechanisms in radiation fibrosis. *Radiotherapy and Oncology*. 2010 Oct 1;97(1):149–61.
110. Safwat A, Bentzen SM, Turesson I, Hendry JH. Deterministic rather than stochastic factors explain most of the variation in the expression of skin telangiectasia after radiotherapy. *International Journal of Radiation Oncology*Biology*Physics*. 2002 Jan 1;52(1):198–204.
111. Martin M, Delanian S, Sivan V, Vozenin-Brotons MC, Reisdorf P, Lawrence D, et al. Fibrose superficielle radio-induite et TGF- β 1. *Cancer/Radiothérapie*. 2000 Sep 10;4(5):369–84.
112. Delanian S, Lefaix JL. Réversibilité de la fibroatrophie radio-induite. *La Revue de Médecine Interne*. 2002 Feb 1;23(2):164–74.
113. Weigel C, Schmezer P, Plass C, Popanda O. Epigenetics in radiation-induced fibrosis. *Oncogene*. 2015 Apr;34(17):2145–55.
114. Martin M, Lefaix J-L, Delanian S. TGF- β 1 and radiation fibrosis: a master switch and a specific therapeutic target? *International Journal of Radiation Oncology*Biology*Physics*. 2000 May 1;47(2):277–90.
115. Chan RJ, Webster J, Chung B, Marquart L, Ahmed M, Garantziotis S. Prevention and treatment of acute radiation-induced skin reactions: a systematic review and meta-analysis of randomized controlled trials. *BMC Cancer*. 2014 Jan 31;14(1):53.

116. Ejaz A, Greenberger JS, Rubin PJ. Understanding the mechanism of radiation induced fibrosis and therapy options. *Pharmacology & Therapeutics*. 2019 Dec 1;204:107399.
117. Averbek D, Candéias S, Chandna S, Foray N, Friedl AA, Haghdoost S, et al. Establishing mechanisms affecting the individual response to ionizing radiation. *International Journal of Radiation Biology*. 2020 Mar 3;96(3):297–323.
118. Wynn TA. Fibrotic disease and the T H 1/T H 2 paradigm. *Nature Reviews Immunology*. 2004 Aug;4(8):583–94.
119. Bonner JC. Regulation of PDGF and its receptors in fibrotic diseases. *Cytokine & Growth Factor Reviews*. 2004 Aug 1;15(4):255–73.
120. Cellular basis of radiation-induced fibrosis. *Radiotherapy and Oncology*. 1995 May 1;35(2):83–90.
121. Westbury CB, Yarnold JR. Radiation Fibrosis — Current Clinical and Therapeutic Perspectives. *Clinical Oncology*. 2012 Dec 1;24(10):657–72.
122. Common Terminology Criteria for Adverse Events (CTCAE). 2017;155.
123. Lyngholm CD, Christiansen PM, Damsgaard TE, Overgaard J. Long-term follow-up of late morbidity, cosmetic outcome and body image after breast conserving therapy. A study from the Danish Breast Cancer Cooperative Group (DBCG). *Acta Oncologica*. 2013 Feb 1;52(2):259–69.
124. Bush WS. Genome-Wide Association Studies. In: Ranganathan S, Gribskov M, Nakai K, Schönbach C, editors. *Encyclopedia of Bioinformatics and Computational Biology* [Internet]. Oxford: Academic Press; 2019 [cited 2021 Feb 25]. p. 235–41. Available from: <https://www.sciencedirect.com/science/article/pii/B978012809633820232X>
125. Maréchal A, Zou L. DNA Damage Sensing by the ATM and ATR Kinases. *Cold Spring Harb Perspect Biol* [Internet]. 2013 Sep [cited 2020 May 15];5(9). Available from: <https://www.ncbi.nlm.nih.gov/pmc/articles/PMC3753707/>
126. Ho AY, Fan G, Atencio DP, Green S, Formenti SC, Haffty BG, et al. Possession of ATM sequence variants as predictor for late normal tissue responses in breast cancer patients treated with radiotherapy. *Int J Radiat Oncol Biol Phys*. 2007 Nov 1;69(3):677–84.
127. Andreassen CN, Rosenstein BS, Kerns SL, Ostrer H, De Ruyscher D, Cesaretti JA, et al. Individual patient data meta-analysis shows a significant association between the ATM rs1801516 SNP and toxicity after radiotherapy in 5456 breast and prostate cancer patients. *Radiother Oncol*. 2016;121(3):431–9.

128. Kerns SL, Fachal L, Dorling L, Barnett GC, Baran A, Peterson DR, et al. Radiogenomics Consortium Genome-Wide Association Study Meta-Analysis of Late Toxicity After Prostate Cancer Radiotherapy. *J Natl Cancer Inst.* 2020 Feb 1;112(2):179–90.
129. Angèle S, Romestaing P, Moullan N, Vuillaume M, Chapot B, Friesen M, et al. ATM haplotypes and cellular response to DNA damage: association with breast cancer risk and clinical radiosensitivity. *Cancer Res.* 2003 Dec 15;63(24):8717–25.
130. Andreassen CN, Alsner J, Overgaard M, Overgaard J. Prediction of normal tissue radiosensitivity from polymorphisms in candidate genes. *Radiother Oncol.* 2003 Nov;69(2):127–35.
131. Zschenker O, Raabe A, Boeckelmann IK, Borstelmann S, Szymczak S, Wellek S, et al. Association of single nucleotide polymorphisms in ATM, GSTP1, SOD2, TGFB1, XPD and XRCC1 with clinical and cellular radiosensitivity. *Radiother Oncol.* 2010 Oct;97(1):26–32.
132. Terrazzino S, Deantonio L, Cargnin S, Donis L, Pisani C, Masini L, et al. Common European Mitochondrial Haplogroups in the Risk for Radiation-induced Subcutaneous Fibrosis in Breast Cancer Patients. *Clin Oncol (R Coll Radiol).* 2016;28(6):365–72.
133. Rishishwar L, Jordan IK. Implications of human evolution and admixture for mitochondrial replacement therapy. *BMC Genomics.* 2017 08;18(1):140.
134. Terrazzino S, Cargnin S, Deantonio L, Pisani C, Masini L, Canonico PL, et al. Impact of ATM rs1801516 on late skin reactions of radiotherapy for breast cancer: Evidences from a cohort study and a trial sequential meta-analysis. *PLoS ONE.* 2019;14(11):e0225685.
135. Terrazzino S, Deantonio L, Cargnin S, Donis L, Pisani C, Masini L, et al. DNA Methyltransferase Gene Polymorphisms for Prediction of Radiation-Induced Skin Fibrosis after Treatment of Breast Cancer: A Multifactorial Genetic Approach. *Cancer Res Treat.* 2017 Apr;49(2):464–72.
136. Andreassen CN, Alsner J, Overgaard J, Herskind C, Haviland J, Owen R, et al. TGFB1 polymorphisms are associated with risk of late normal tissue complications in the breast after radiotherapy for early breast cancer. *Radiother Oncol.* 2005 Apr;75(1):18–21.
137. Quarmby S, Fakhoury H, Levine E, Barber J, Wylie J, Hajeer AH, et al. Association of transforming growth factor beta-1 single nucleotide polymorphisms with radiation-induced damage to normal tissues in breast cancer patients. *International Journal of Radiation Biology.* 2003 Jan 1;79(2):137–43.

138. Moullan N, Cox DG, Angèle S, Romestaing P, Gérard J-P, Hall J. Polymorphisms in the DNA repair gene XRCC1, breast cancer risk, and response to radiotherapy. *Cancer Epidemiol Biomarkers Prev.* 2003 Nov;12(11 Pt 1):1168–74.
139. Quarmby S, West C, Magee B, Stewart A, Hunter R, Kumar S. Differential Expression of Cytokine Genes in Fibroblasts Derived from Skin Biopsies of Patients who Developed Minimal or Severe Normal Tissue Damage after Radiotherapy. *Radiation Research.* 2002 Mar;157(3):243–8.
140. Heldin C-H, Westermark B. Mechanism of Action and In Vivo Role of Platelet-Derived Growth Factor. *Physiological Reviews.* 1999 Jan 10;79(4):1283–316.
141. Alsner J, Rødningen OK, Overgaard J. Differential gene expression before and after ionizing radiation of subcutaneous fibroblasts identifies breast cancer patients resistant to radiation-induced fibrosis. *Radiotherapy and Oncology.* 2007;6.
142. Rødningen OK, Børresen-Dale A-L, Alsner J, Hastie T, Overgaard J. Radiation-induced gene expression in human subcutaneous fibroblasts is predictive of radiation-induced fibrosis. *Radiotherapy and Oncology.* 2008;7.
143. Lyngholm CD, Overgaard J, Christiansen PM, Alsner J. Validation of a gene expression profile predictive of the risk of radiation-induced fibrosis in women treated with breast conserving therapy. *Acta Oncologica.* 2015 Oct 21;54(9):1665–8.
144. Andreassen CN, Overgaard J, Alsner J. Independent prospective validation of a predictive test for risk of radiation induced fibrosis based on the gene expression pattern in fibroblasts irradiated in vitro. *Radiotherapy and Oncology.* 2013 Sep 1;108(3):469–72.
145. Azria D, Riou O, Castan F, Nguyen TD, Peignaux K, Lemanski C, et al. Radiation-induced CD8 T-lymphocyte Apoptosis as a Predictor of Breast Fibrosis After Radiotherapy: Results of the Prospective Multicenter French Trial. *EBioMedicine.* 2015 Dec;2(12):1965–73.
146. Azria D, GOURGOU S. In vitro method for predicting the risk of developing a breast late effect after radiotherapy [Internet]. WO2018041960A1, 2018 [cited 2021 Feb 15]. Available from: https://patents.google.com/patent/WO2018041960A1/fr?oq=WO_2018041960
147. Forrester HB, Li J, Leong T, McKay MJ, Sprung CN. Identification of a radiation sensitivity gene expression profile in primary fibroblasts derived from patients who developed radiotherapy-induced fibrosis. *Radiotherapy and Oncology.* 2014 May;111(2):186–93.

148. Application of microarray analyses to identify genes involved in radiation-induced fibrosis. - Abstract - Europe PMC [Internet]. [cited 2021 Feb 15]. Available from: <https://europepmc.org/article/PMC/4233572#free-full-text>
149. Sprung C, McKAY M. Method of Detecting Radiation Exposure and Adverse Toxicity Thereto [Internet]. 2011 [cited 2021 Feb 15]. Available from: <https://patentscope.wipo.int/search/en/detail.jsf?docId=WO2011006214>
150. Patel K. Follistatin. *Int J Biochem Cell Biol.* 1998 Oct;30(10):1087–93.
151. Forrester HB, de Kretser DM, Leong T, Hagekyriakou J, Sprung CN. Follistatin attenuates radiation-induced fibrosis in a murine model. *PLoS One.* 2017;12(3):e0173788.
152. Henderson NC, Sheppard D. Integrin-mediated regulation of TGF β in fibrosis. *Biochimica et Biophysica Acta (BBA) - Molecular Basis of Disease.* 2013 Jul 1;1832(7):891–6.
153. Portela A, Esteller M. Epigenetic modifications and human disease. *Nature Biotechnology.* 2010 Oct;28(10):1057–68.
154. Babalola O, Mamalis A, Lev-Tov H, Jagdeo J. The role of microRNAs in skin fibrosis. *Arch Dermatol Res.* 2013 Nov 1;305(9):763–76.
155. Chung YL, Wang A-J, Yao L-F. Antitumor histone deacetylase inhibitors suppress cutaneous radiation syndrome: Implications for increasing therapeutic gain in cancer radiotherapy. *Mol Cancer Ther.* 2004 Mar 1;3(3):317–25.
156. Weigel C, Veldwijk MR, Oakes CC, Seibold P, Slynko A, Liesenfeld DB, et al. Epigenetic regulation of diacylglycerol kinase alpha promotes radiation-induced fibrosis. *Nature Communications.* 2016 Mar 11;7(1):10893.
157. Liu C-S, Schmezer P, Popanda O. Diacylglycerol Kinase Alpha in Radiation-Induced Fibrosis: Potential as a Predictive Marker or Therapeutic Target. *Front Oncol.* 2020;10:737.
158. Valinciute G, Weigel C, Veldwijk MR, Oakes CC, Herskind C, Wenz F, et al. BET-bromodomain inhibitors modulate epigenetic patterns at the diacylglycerol kinase alpha enhancer associated with radiation-induced fibrosis. *Radiotherapy and Oncology.* 2017 Oct 1;125(1):168–74.
159. FORAY N, GRANZOTTO A, DEVIC C. Methode predictive pour caracteriser la radiosensibilite et la reaction tissulaire d'un patient envers un rayonnement ionisant therapeutique [Internet]. WO2015121596A1, 2015 [cited 2021 Mar 8]. Available from: https://patents.google.com/patent/WO2015121596A1/fr?q=WO_2015121596

160. PEREIRA S. Methode predictive rapide pour caracteriser la radiosensibilite et/ou le risque de toxicite tissulaire d'un individu envers une irradiation [Internet]. WO2018229439A1, 2018 [cited 2021 Mar 8]. Available from: https://patents.google.com/patent/WO2018229439A1/fr?q=WO_2018229439
161. Deschavanne PJ, Debieu D, Fertil B, Malaise EP. Re-evaluation of in vitro radiosensitivity of human fibroblasts of different genetic origins. *Int J Radiat Biol Relat Stud Phys Chem Med.* 1986 Aug;50(2):279–93.
162. GUO GZ, SASAI K, OYA N, SHIBATA T, SHIBUYA K, HIRAOKA M. A significant correlation between clonogenic radiosensitivity and the simultaneous assessment of micronucleus and apoptotic cell frequencies. *International Journal of Radiation Biology.* 1999 Jan 1;75(7):857–64.
163. Abugessaisa I, Ramilowski JA, Lizio M, Severin J, Hasegawa A, Harshbarger J, et al. FANTOM enters 20th year: expansion of transcriptomic atlases and functional annotation of non-coding RNAs. *Nucleic Acids Res.* 2021 Jan 8;49(D1):D892–8.
164. FORAY N, GRANZOTTO A, Devic C. Methode predictive pour determiner la radiosensibilite tissulaire [Internet]. FR3017625B1, 2018 [cited 2021 May 20]. Available from: https://patents.google.com/patent/FR3017625B1/fr?q=FR_3017625
165. Azria D, Lacombe J, Solassol J, MANGE A. Method for determining radiosensitivity [Internet]. WO2014154854A1, 2014 [cited 2021 May 20]. Available from: https://patents.google.com/patent/WO2014154854A1/fr?q=WO_2014154854
166. Schmitz A, Baijer J, Azria D, Kerns S, Perdry H. Method for evaluating individual radiosensitivity and the risk of adverse effects [Internet]. WO2017032865A1, 2017 [cited 2021 May 20]. Available from: https://patents.google.com/patent/WO2017032865A1/fr?q=WO_2017032865
167. Lambin P, Nalbantov GI, Smeets HJM, Voets AM. Method for determining the risk of developing radiation-induced toxicity after exposure to radiation [Internet]. WO2014184028A1, 2014 [cited 2021 May 20]. Available from: https://patents.google.com/patent/WO2014184028A1/fr?q=WO_2014184028
168. Port M, Hérodin F, Valente M, Drouet M, Ostheim P, Majewski M, et al. Persistent mRNA and miRNA expression changes in irradiated baboons. *Sci Rep.* 2018 Oct 18;8(1):15353.
169. COPERNIC project investigators, Granzotto A, Benadjaoud MA, Vogin G, Devic C, Ferlazzo ML, et al. Influence of Nucleoshuttling of the ATM Protein in the Healthy Tissues Response to Radiation Therapy: Toward a Molecular

- Classification of Human Radiosensitivity. *Int J Radiat Oncol Biol Phys*. 2016 Mar 1;94(3):450–60.
170. Azria D, Riou O, Castan F, Nguyen TD, Peignaux K, Lemanski C, et al. Radiation-Induced CD8 T-Lymphocyte Apoptosis as a Predictor of Breast Fibrosis After Radiotherapy: Results of the Prospective Multicenter French Trial. *EBioMedicine*. 2015;2(12):1965–73.
171. Alsner J, Rødningen OK, Overgaard J. Differential Gene Expression before and after Ionizing Radiation of Subcutaneous Fibroblasts Identifies Breast Cancer Patients Resistant to Radiation-Induced Fibrosis. *Radiother Oncol*. 2007;83(3):261–6.
172. Lyngholm CD, Overgaard J, Christiansen PM, Alsner J. Validation of a Gene Expression Profile Predictive of the Risk of Radiation-Induced Fibrosis in Women Treated with Breast Conserving Therapy. *Acta Oncol*. 2015;54(9):1665–8.
173. Tolkien JRR. *The Lord of the Rings*. HarperCollins; 1999. 1664 p.
174. Heckler G, Aigueperse C, Hettal L, Thuillier Q, Chaumont F de, Dallongeville S, et al. Substructure Analyzer: A User-Friendly Workflow for Rapid Exploration and Accurate Analysis of Cellular Bodies in Fluorescence Microscopy Images. *JoVE (Journal of Visualized Experiments)*. 2020 Jul 15;(161):e60990.
175. Hesse M, Zimek A, Weber K, Magin TM. Comprehensive analysis of keratin gene clusters in humans and rodents. *European Journal of Cell Biology*. 2004;83(1):19–26.
176. Qiu B-F, Zhang G-Q, Xu F-M, Xu Q, Xu T. Effect of the transdifferentiation of BECs into myofibroblasts on the pathogenesis of secondary cholestatic hepatic fibrosis. *Exp Ther Med*. 2019 Apr;17(4):2769–76.
177. Ren C, Paronetto F, Mak KM, Leo MA, Lieber CS. Cytokeratin 7 staining of hepatocytes predicts progression to more severe fibrosis in alcohol-fed baboons. *Journal of Hepatology*. 2003 Jun 1;38(6):770–5.
178. Bateman AC, Hübscher SG. Cytokeratin expression as an aid to diagnosis in medical liver biopsies. *Histopathology*. 2010;56(4):415–25.
179. Fitzpatrick E, Mitry RR, Quaglia A, Hussain MJ, deBruyne R, Dhawan A. Serum Levels of CK18 M30 and Leptin Are Useful Predictors of Steatohepatitis and Fibrosis in Paediatric NAFLD. *Journal of Pediatric Gastroenterology and Nutrition*. 2010 Oct;51(4):500–6.

180. Jazwinski AB, Thompson AJ, Clark PJ, Naggie S, Tillmann HL, Patel K. Elevated serum CK18 levels in chronic hepatitis C patients are associated with advanced fibrosis but not steatosis. *Journal of Viral Hepatitis*. 2012;19(4):278–82.
181. Kaswala DH, Lai M, Afdhal NH. Fibrosis Assessment in Nonalcoholic Fatty Liver Disease (NAFLD) in 2016. *Dig Dis Sci*. 2016 May;61(5):1356–64.
182. Hettal L, Rouget R, Thuillier Q, Cérimèle E, Tosti P, François A, et al. Cytokeratin KRT7 and KRT18 gene expression predicts radiation-induced skin fibrosis. *International Journal of Radiation Oncology, Biology, Physics*. Submitted.
183. Chiarelli N, Carini G, Zoppi N, Ritelli M, Colombi M. Transcriptome analysis of skin fibroblasts with dominant negative COL3A1 mutations provides molecular insights into the etiopathology of vascular Ehlers-Danlos syndrome. *PLoS One*. 2018;13(1):e0191220.
184. Driskell RR, Lichtenberger BM, Hoste E, Kretzschmar K, Simons BD, Charalambous M, et al. Distinct fibroblast lineages determine dermal architecture in skin development and repair. *Nature*. 2013 Dec;504(7479):277–81.
185. Mine S, Fortunel NO, Pigeon H, Asselineau D. Aging Alters Functionally Human Dermal Papillary Fibroblasts but Not Reticular Fibroblasts: A New View of Skin Morphogenesis and Aging. *PLOS ONE*. 2008 Dec 30;3(12):e4066.
186. Janson DG, Saintigny G, van Adrichem A, Mahé C, El Ghalbzouri A. Different Gene Expression Patterns in Human Papillary and Reticular Fibroblasts. *Journal of Investigative Dermatology*. 2012 Nov;132(11):2565–72.
187. Woodley DT. Distinct Fibroblasts in the Papillary and Reticular Dermis. *Dermatologic Clinics*. 2017 Jan;35(1):95–100.
188. Nauroy P, Barruche V, Marchand L, Nindorera-Badara S, Bordes S, Closs B, et al. Human Dermal Fibroblast Subpopulations Display Distinct Gene Signatures Related to Cell Behaviors and Matrisome. *Journal of Investigative Dermatology*. 2017 Aug 1;137(8):1787–9.
189. Korosec A, Frech S, Gesslbauer B, Vierhapper M, Radtke C, Petzelbauer P, et al. Lineage Identity and Location within the Dermis Determine the Function of Papillary and Reticular Fibroblasts in Human Skin. *Journal of Investigative Dermatology*. 2019 Feb;139(2):342–51.
190. Haydont V, Neiveyans V, Fortunel NO, Asselineau D. Transcriptome profiling of human papillary and reticular fibroblasts from adult interfollicular dermis pinpoints the ‘tissue skeleton’ gene network as a component of skin chrono-ageing. *Mechanisms of Ageing and Development*. 2019 Apr;179:60–77.

191. Granzotto A, Benadjaoud MA, Vogin G, Devic C, Ferlazzo ML, Bodgi L, et al. Influence of Nucleoshuttling of the ATM Protein in the Healthy Tissues Response to Radiation Therapy: Toward a Molecular Classification of Human Radiosensitivity. *International Journal of Radiation Oncology*Biography*Physics*. 2016 Mar 1;94(3):450–60.
192. Common Terminology Criteria for Adverse Events (CTCAE). 2009;79.
193. Korosec A, Frech S, Lichtenberger BM. Isolation of Papillary and Reticular Fibroblasts from Human Skin by Fluorescence-activated Cell Sorting. *JoVE*. 2019 May 7;(147):59372.
194. Kumar D, Yalamanchali S, New J, Parsel S, New N, Holcomb A, et al. Development and Characterization of an In Vitro Model for Radiation-Induced Fibrosis. *Radiation Research*. 2018 Jan 19;189(3):326–36.
195. Haydont V, Bernard BA, Fortunel NO. Age-related evolutions of the dermis: Clinical signs, fibroblast and extracellular matrix dynamics. *Mechanisms of Ageing and Development*. 2019 Jan 1;177:150–6.
196. Janson D, Saintigny G, Mahé C, Ghalbzouri AE. Papillary fibroblasts differentiate into reticular fibroblasts after prolonged *in vitro* culture. *Exp Dermatol*. 2013 Jan;22(1):48–53.
197. Rognoni E, Pisco AO, Hiratsuka T, Sipilä KH, Belmonte JM, Mobasser SA, et al. Fibroblast state switching orchestrates dermal maturation and wound healing. *Mol Syst Biol* [Internet]. 2018 Aug 29 [cited 2021 May 30];14(8). Available from: <https://www.ncbi.nlm.nih.gov/pmc/articles/PMC6113774/>
198. Anderson L, Henderson C, Adachi Y. Phosphorylation and Rapid Relocalization of 53BP1 to Nuclear Foci upon DNA Damage. *Mol Cell Biol*. 2001 Mar;21(5):1719–29.
199. Dally J, Khan JS, Voisey A, Charalambous C, John HL, Woods EL, et al. Hepatocyte Growth Factor Mediates Enhanced Wound Healing Responses and Resistance to Transforming Growth Factor- β 1-Driven Myofibroblast Differentiation in Oral Mucosal Fibroblasts. *International Journal of Molecular Sciences*. 2017 Aug 1;18(9):1843.
200. Osler ME, Chang MS, Bader DM. Bves modulates epithelial integrity through an interaction at the tight junction. *Journal of Cell Science*. 2005 Oct 15;118(20):4667–78.
201. Kuang X-L, Zhao X-M, Xu H-F, Shi Y-Y, Deng J-B, Sun G-T. Spatio-temporal expression of a novel neuron-derived neurotrophic factor (NDNF) in mouse brains during development. *BMC Neuroscience*. 2010 Oct 25;11(1):137.

202. Bonnans C, Chou J, Werb Z. Remodelling the extracellular matrix in development and disease. *Nat Rev Mol Cell Biol.* 2014 Dec;15(12):786–801.
203. Ji J, Zhu P, Sun C, Sun J, An L, Zhang Y, et al. Pathway of 3-MCPD-induced apoptosis in human embryonic kidney cells. *J Toxicol Sci.* 2017;42(1):43–52.
204. Barathan M, Gopal K, Mohamed R, Ellegård R, Saeidi A, Vadivelu J, et al. Chronic hepatitis C virus infection triggers spontaneous differential expression of biosignatures associated with T cell exhaustion and apoptosis signaling in peripheral blood mononucleocytes. *Apoptosis.* 2015 Apr;20(4):466–80.
205. Altun Z, Olgun Y, Ercetin P, Aktas S, Kirkim G, Serbetcioglu B, et al. Protective effect of acetyl-L-carnitine against cisplatin ototoxicity: role of apoptosis-related genes and pro-inflammatory cytokines. *Cell Prolif.* 2014 Feb;47(1):72–80.
206. Mirzaei MR, Najafi A, Arababadi MK, Asadi MH, Mowla SJ. Altered expression of apoptotic genes in response to OCT4B1 suppression in human tumor cell lines. *Tumour Biol.* 2014 Oct;35(10):9999–10009.
207. Nihrane A, Sezgin G, Dsilva S, Dellorusso P, Yamamoto K, Ellis SR, et al. Depletion of the Shwachman-Diamond syndrome gene product, SBDS, leads to growth inhibition and increased expression of OPG and VEGF-A. *Blood Cells Mol Dis.* 2009 Feb;42(1):85–91.
208. Gao B, Sun W, Wang X, Jia X, Ma B, Chang Y, et al. Whole genome expression profiling and screening for differentially expressed cytokine genes in human bone marrow endothelial cells treated with humoral inhibitors in liver cirrhosis. *Int J Mol Med.* 2013 Nov;32(5):1204–14.
209. Emery JG, McDonnell P, Burke MB, Deen KC, Lyn S, Silverman C, et al. Osteoprotegerin is a receptor for the cytotoxic ligand TRAIL. *J Biol Chem.* 1998 Jun 5;273(23):14363–7.
210. Song L, Sun Z, Kim D, Gou W, Strange C, Dong H, et al. Adipose stem cells from chronic pancreatitis patients improve mouse and human islet survival and function. *Stem Cell Research & Therapy.* 2017 Aug 30;8(1):192.
211. Huang T-C, Lee P-T, Wu M-H, Huang C-C, Ko C-Y, Lee Y-C, et al. Distinct roles and differential expression levels of Wnt5a mRNA isoforms in colorectal cancer cells. *PLoS One.* 2017;12(8):e0181034.
212. Jin X, Wu X-X, Jin C, Inui M, Sugimoto M, Kakehi Y. Delineation of apoptotic genes for synergistic apoptosis of lexatumumab and anthracyclines in human renal cell carcinoma cells by polymerase chain reaction array. *Anticancer Drugs.* 2012 Apr;23(4):445–54.

213. Silva JC, Ferreira-Strixino J, Fontana LC, Paula LM, Raniero L, Martin AA, et al. Apoptosis-associated genes related to photodynamic therapy in breast carcinomas. *Lasers Med Sci.* 2014 Jul;29(4):1429–36.
214. Higgs JT, Jarboe JS, Lee JH, Chanda D, Lee CM, Deivanayagam C, et al. Variants of Osteoprotegerin Lacking TRAIL Binding for Therapeutic Bone Remodeling in Osteolytic Malignancies. *Mol Cancer Res.* 2015 May;13(5):819–27.

Résumé

En Europe, on estime que le cancer a touché 4,4 millions de nouveaux patients et a été à l'origine de près de 2 millions de décès en 2020. Environ 50 % de tous les patients européens atteints de cancer recevront une radiothérapie (RT). Bien qu'il s'agisse d'un outil indispensable au traitement des patients, la RT peut s'accompagner de toxicités secondaires légères à sévères. Il existe un véritable défi dans la prévention, le diagnostic et la gestion des toxicités secondaires induites par la RT. D'une part, nous avons développé un algorithme capable de discriminer la progression tumorale de la radionécrose cérébrale, deux lésions très similaires à l'imagerie, après RT stéréotaxique d'oligométastases cérébrales. D'autre part, nous avons étudié les déterminants moléculaires de la fibrose cutanée radio-induite. Nous avons développé un test pronostic pour prédire la propension des patientes à développer des toxicités tardives avant d'avoir reçu leur traitement par RT. Nous avons également posé les premières bases de la compréhension des différences physiologiques entre les fibroblastes cutanés des patientes à risque et ceux des patientes sans risque de développer des toxicités tardives après RT.

Abstract

In Europe, 4.4 million new cancer cases and almost 2 million cancer deaths occurred in 2020. About 50% of all European cancer patients will receive radiotherapy. Although a necessary tool in patients care, radiotherapy can be accompanied by mild to severe secondary toxicities. There is a real challenge in the prevention, diagnosis and management of secondary toxicities induced by radiotherapy. On the one hand, we developed an algorithm able to discriminate between tumour recurrence and radionecrosis, two very similar lesions on imaging, after stereotactic irradiation of brain metastases. On the other hand, we studied the molecular determinants of radiation-induced skin fibrosis. We developed a prognostic test to predict patients' outcome before radiotherapy and laid the first bricks to understand the physiological differences between at-risk and non-at-risk patients' skin fibroblasts.